UNIVERSITÀ DEGLI STUDI ROMA TRE
Dipartimento di Fisica "Edoardo Amaldi"
Dottorato di ricerca in fisica - XIX ciclo

Systematic study of the response and calibration of the Monitored Drift Tubes of the ATLAS Muon Spectrometer

Silvestro Di Luise

Coordinator

Prof. Orlando Ragnisco

Supervisor

Prof. Filippo Ceradini

January 2007

Contents

Paste decades of research in both theoretical and experimental high energy physics have lead to the so called Standard Model (SM) of particle physics which represents the today knowledge of nature's building blocks and forces on a sub-atomic scale. However there are still questions to be answered in the SM frame, such as the existence of the Higgs boson, a foundamental step in the explanation of the origin of the particle masses. Moreover experimental confirmations of the most appealing theoretical extensions of the SM, such as "Super Symmetry" need more performing experimental facilities to be investigated.

The next generation of hadron collider experiments at CERN has the potential to make precision tests of the model and to search for signatures of physics beyond the Standard Model in fact with the start of the Large Hadron Collider (LHC) operation, sheduled for the 2007, which will provide proton-proton collions at 14 TeV an unprecedented quantity of new physics phenomena will become experimentally accessible.

The ATLAS detector is conceived to be sensisitve to an as large as possible variety of final states signatures. High momentum muons are among the most promising and reliable signatures in the high energy collision events at the LHC. This led to the design of a high resolution muon spectrometer with stand-alone triggering and momentum measurement capability over a wide area of the kinematic phase space. Momentum determination is based on the magnetic deflection of muons trajectory in an air-core toroidal magnet field. The track reconstruction is performed in three measurement stations mainly made of high pressure drift tubes (MDT).

Discovery physics, as well as high-statistics precision measurements, will require extraction of clean signals with the ATLAS detector. This demands precise and stable in-situ calibration of the different subdetectors.

The purpose of the work presented here is the study of the performance of the drift tubes of the ATLAS muon spectrometer.

In particular, the analysis is focused on the development and optimization of the calibration tecnique, the study of the systematics involved and of the impact on the spatial resolution. That is the subject of the chapters from four to seven.

It follows an analysis aimed the check for any evidence of degradation in the MDT preformance as a consequence of the extended exposure of the detector to the large particle flux during the accelerator operation.

The first two chapters are dedicated to the description of the research program, the main characteristics of the experimental apparatus and the physical motivatons which have driven both the accelerator and the detector design with emphasis in the ATLAS Muon Spectrometer. The third chapter reviews the principles of operation of the drift tubes motivating the choice of the operating parameters of the ATLAS MDTs and the problematics related to the signal extraction. An overview of the experimental setups, the software tools and the analysis tecniques used can be found in chapter four.

Chapter 1

Physics program at the LHC and the experimental apparatus

1.1 Introduction

The Standard Model (SM)is the theory which better describes elementary particle interactions. Within the SM, particles are divided in spin 1/2 matter fields (leptons and quarks) and spin 1 gauge bosons which mediate particle interactions.

	Fermions			Bosons	
Leptons (l)	$\begin{pmatrix} \nu_e \\ e \end{pmatrix}$	$\begin{pmatrix} \nu_\mu \\ \mu \end{pmatrix}$	$\begin{pmatrix} \nu_\tau \\ \tau \end{pmatrix}$	$\begin{pmatrix} \gamma \\ Z, W^\pm \end{pmatrix}$	$SU_T(2) \times U_Y(1)$
Quarks (q)	$\begin{pmatrix} u \\ d \end{pmatrix}$	$\begin{pmatrix} c \\ s \end{pmatrix}$	$\begin{pmatrix} t \\ b \end{pmatrix}$	$(\ g_{cc'} \ )$	$SU_C(3)$

The Standard Model is a renormalizable gauge theory based on the symmetry

$$SU_T(2) \otimes U_Y(1) \otimes SU_C(3)$$

where T is the weak isospin, Y is the hypercharge and C is the color. The unified theory of electromagnetic and weak interactions relies on the symmetry $SU_T(2) \otimes U_Y(1)$ and processes are described in terms of γ, Z^0 and $W^\pm$ bosons exchange. Quantum Chromodynamics (QCD) is a non abelian gauge theory based on a $SU_C(3)$ color symmetry which describes hadronic interactions. The gauge bosons of the color field are 8 *colored* gluons.

To reproduce observations on weak decays and to allow CP violation within the Standard Model, the quarks which participate in weak interaction have to be mixed introducing a mixing matrix (Cabibbo, Kobayashi, Maskawa CKM) [1][2] defined by

$$\begin{pmatrix} d' \\ s' \\ b' \end{pmatrix} = V_{CKM} \begin{pmatrix} d \\ s \\ b \end{pmatrix} = \begin{pmatrix} V_{ud} & V_{us} & V_{ub} \\ V_{cd} & V_{cs} & V_{cb} \\ V_{td} & V_{ts} & V_{tb} \end{pmatrix} \begin{pmatrix} d \\ s \\ b \end{pmatrix} \tag{1.1}$$

and described in terms of 3 parameters and one complex phase for a total of four free parameters.

In the Standard Model particles are massless because mass terms in the lagrangian are not invariant; to generate the observed particle mass spectra, the breaking of the electroweak symmetry is required. This can be done by the Higgs mechanism [3] which makes use of one isodoublet field: three Goldstone bosons among the four degrees of freedom are absorbed to build up the longitudinal components of the massive $W^{\pm}$ and Z bosons; the last degree of freedom corresponds to a physical scalar particle, the Higgs boson. The present knowledge on the Higgs particle mass is shown in fig. 1.1 [4]. Although there is yet no direct evidence of the Higgs boson, a global Standard Model fit to the electroweak data yields information about the Higgs boson mass m_H: m_H=88^{+60}_{-37} GeV corresponding to a 95% CL upper limit of m_H<206 GeV. The 95% CL lower limit of 114 GeV from the direct searches at LEP2 [5] is also shown. Despite of its numerous successes in explaining the present data, the Standard Model will not be tested completely before the Higgs boson has been experimentally observed and studied. This particle has to be searched in a mass range from the present experimental limit up to the limit of 1 TeV imposed by the stability of the theory.

The experimental behaviour of the coupling constants suggests a possible unification (*Grand Unification Theory*, with all forces described by a single coupling constant) at an energy scale Λ_{GUT} of the order 10^{14}-10^{16} GeV. Trying to extend the Standard Model up to Λ_{GUT} presents two major problems. The first is the so called *naturalness*

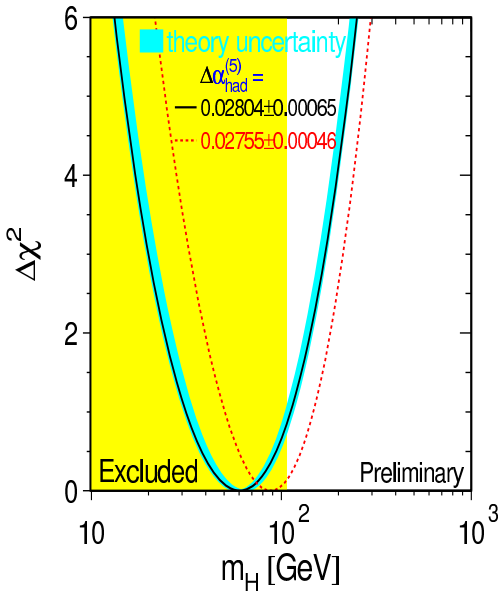

Figure 1.1: The χ^2 of the fit to electroweak data as a function of the Higgs mass [4].

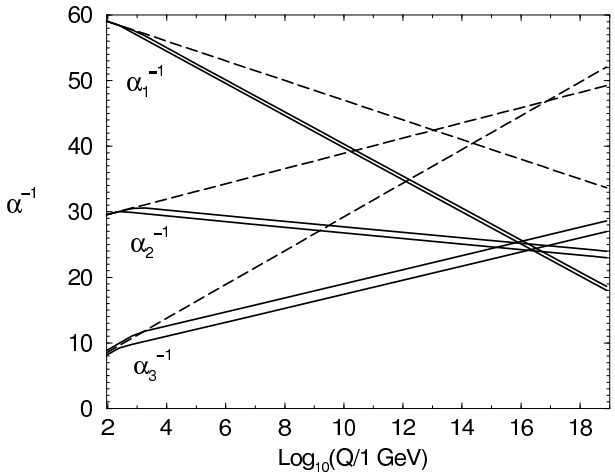

Figure 1.2: Evolutions of the inverse gauge coupling $\alpha_i^{-1}(Q^2)$ in the Standard Model (dashed lines) and in the $MSSM$ (solid line) [6].

problem: the Higgs mass diverges quadratically with Λ (cancellations at all orders would be required). The second is that *GUT* predictions for the coupling constants are incompatible with the Standard Model. To overcome these problems, different theories have been proposed as an extension of the Standard Model. The most promising is *SUperSYmmetry* which is based on the assumption that a particle, boson or fermion, has a partner (*sparticle*) with inverted statistics. In this assumption two problems are solved at once: supersymmetric particle loops cancel exactly the quadratic divergences and contribute to the running of the gauge coupling constants correcting the discrepancies with *GUT* theories (fig. 1.2). The Minimial Supersymmetric extension of the Standard Model (*MSSM*) [6] is based on the same symmetry as the *SM* and contains the minimum number of particles. *MSSM* requires two isodoublets of Higgs fields to cancel anomalies and to give mass to fermions and introduces 5 bosons (Sec. 1.4).

1.2 Physics program at the LHC

The Large Hadron Collider (LHC) [13] is a proton proton collider under construction at CERN in the existing LEP tunnel. It has been designed for a center of mass energy of 14 TeV and for a luminosity of $10^{34}\ cm^{-2}\ s^{-1}$. The two proton beams will circulate in

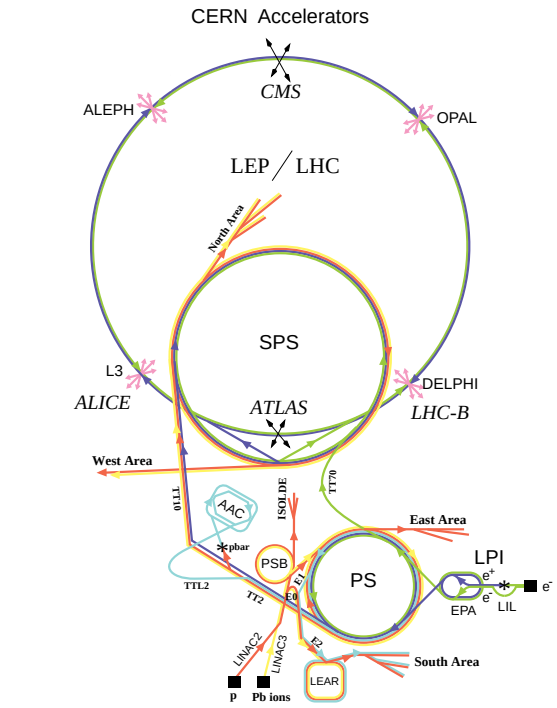

LEP: Large Electron Positron collider
SPS: Super Proton Synchrotron
AAC: Antiproton Accumulator Complex
ISOLDE: Isotope Separator OnLine DEvice
PSB: Proton Synchrotron Booster
PS: Proton Synchrotron

LPI: Lep Pre-Injector
EPA: Electron Positron Accumulator
LIL: Lep Injector Linac
LINAC: LINear ACcelerator
LEAR: Low Energy Antiproton Ring

LHC nominal parameters	
Beam energy	7 TeV
Magnetic field of the dipoles	8.33 T
Bunch spacing	24.95 ns
Number of bunches	2808
Radius of the bunch at the interaction point	16 μm
Bunch length	7.7 cm
Number of particle in a bunch	$1.1{\cdot}10^{11}$
Luminosity	$10^{34}\ cm^{-2}s^{-1}$
Crossing angle	300 μrad
Circulating current	0.56 A
Energy lost per round	7 keV
Total radiated power per beam	3.8 kW

Table 1.1: LHC nominal parameters

two different beam lines contained in the same cryogenic and mechanical structure. To accelerate the protons to the injection energy of 450 GeV, the Super Proto Synchrotron (SPS) and its pre-accelerators are used (fig. 1.2). The 1232 magnets foreseen along the beam line are 14.6 m long and will have a magnetic field of 8.33 T. The beams will collide with an angle of 300 μrad to avoid multiple collisions between the bunches near the interaction vertex. As the bunches will be 7.7 cm long and will have a radius of 16 μm at the crossing point, the spread of the position of the interaction vertex is expected to be 5.6 cm (r.m.s) along the beam line.

The Large Hadron Collider will offers a large range of physics opportunities.

The most important issue is the quest for the origin of the spontaneous symmetry breaking mechanism in the electroweak sector of the Standard Model. A possible manifestation of the spontaneous symmetry breaking mechanism is the existence of a Higgs boson or of a family of Higgs particles in the case of the minimal supersymmetric extension of the Standard Model.

The search of supersymmetric particles as of any other signal of new physics (for example, new heavy gauge bosons up to 5-6 TeV) is another relevant part of the physics program.

Already at initial lower luminosity the LHC will be a high rate b and t quark factory. The cross section for $b\bar{b}$ pairs production is expected to be 0.5 mb, about 1% of the total cross section. This means about $5{\cdot}10^{12}$ events per year at a luminosity of 10^{33} cm^{-2} s^{-1}. A wide program of B-physics studies can thus be performed including a precise measurement of CP violation and the determination of the parameters of the CKM matrix. The 10^7 $t\bar{t}$ pairs delivered per year with a luminosity of 10^{33} cm^{-2} s^{-1} will allow a precise top quark mass measurement in different channels and the search for rare decays.

Proton-(anti)proton cross sections for several processes are shown in fig. 1.3 as a function of the center of mass energy [7]. At the LHC energy, non diffractive p-p inelastic cross section is assumed to be 70 mb. This means an average of 20 collisions per bunch crossing at the design luminosity.

The largest fraction of these collisions are non interesting inelastic collisions (the so called *minimum bias* events) characterized by a small average transverse momentum of the produced particles ($< p_T >= 500\ MeV$). On the other hand, processes of interest have a smaller cross section; for example the cross section for Higgs production is about 10 pb. This gives a hint on the importance for the experiments that will operate at the LHC of an adequate detector granularity to avoid *pile-up* and of a very high background rejection capability of the trigger system.

1.3 Higgs boson search

In fig. 1.4 the expected cross-sections for each individual process for SM Higgs boson production at the LHC are shown as a function of the Higgs mass M_H [8]. The Higgs

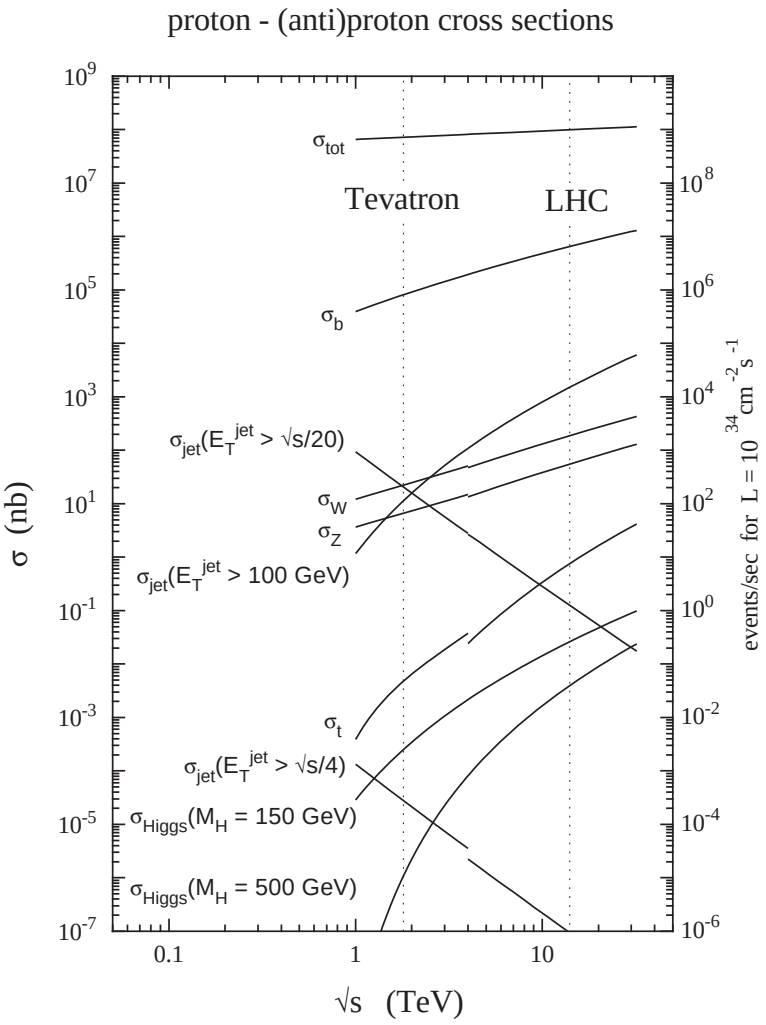

Figure 1.3: Proton-(anti)proton cross sections for several processes as a function of the center of mass energy [7].

boson is produced mainly via gluon-gluon fusion with a cross section larger than 10 pb for M_H up to 400 GeV. The second dominant production process for M_H>100 GeV is the vector boson fusion (VBF). The associated production of SM Higgs with other heavy particles (W, Z, $t\bar{t}$ pairs) is relevant for M_H<200 GeV.

The Higgs branching ratios and total width are shown in fig. 1.5 and 1.6 as a function of the Higgs mass [9]. The decays useful for Higgs detection in different M_H ranges are those with large branching ratio and detection efficiency and low background contamination. The mass range goes from the lower limit of 114 GeV set by LEP2 [5] and the upper limit of 1 TeV required for the stability of the theory.

The strategy adopted for the Higgs searches depends on M_H [18]:

- Low mass region (M_H<130 GeV). $H \rightarrow b\bar{b}$ has a branching ratio close to 1 but the signal to background ratio due to QCD background is smaller than 10^{-5}. This

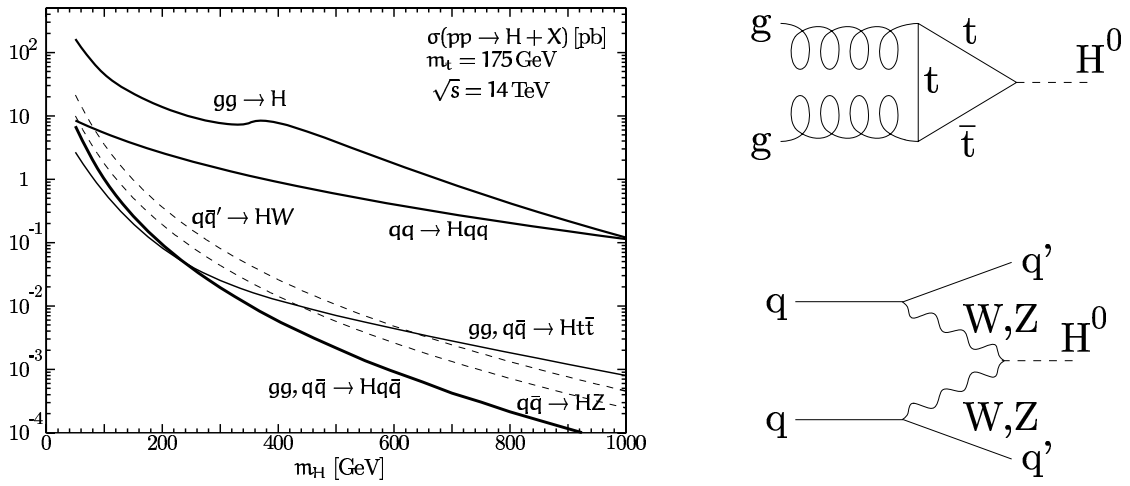

Figure 1.4: Higgs boson production cross-section at the LHC for the various process as a function of the Higgs mass M_H. The diagram of the two dominating processes (gluon-gluon fusion and vector boson fusion) are shown on the right.

decay mode may be used in the associated production of the Higgs with a W, a Z or a $t\bar{t}$ pair; in these cases the high p_T leptons from gauge bosons or top decay can be used to select the events.

The $H \rightarrow \gamma\gamma$ channel has a small branching ratio (about 10^{-3}) but the expected signal to background ratio of 10^{-2} makes this channel interesting.

- Intermediate mass region (130 $GeV < M_H < 2M_Z$). The most powerful channels are $H \rightarrow ZZ^{(*)} \rightarrow 4l$ and $H \rightarrow WW^{(*)} \rightarrow l\nu l\nu$. The leptons are required to reduce the background.

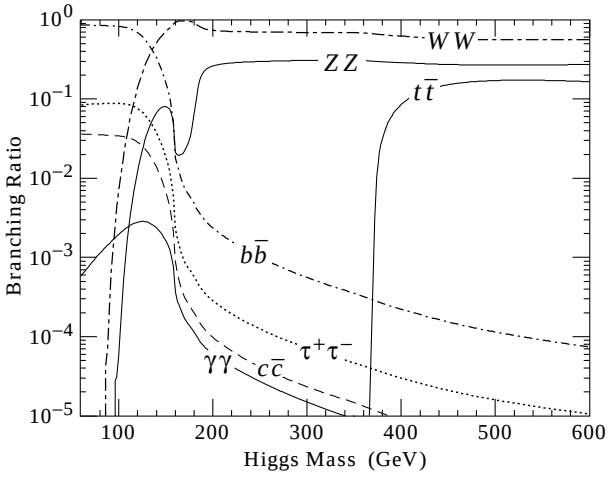

Figure 1.5: Higgs branching ratios as a function of M_H.

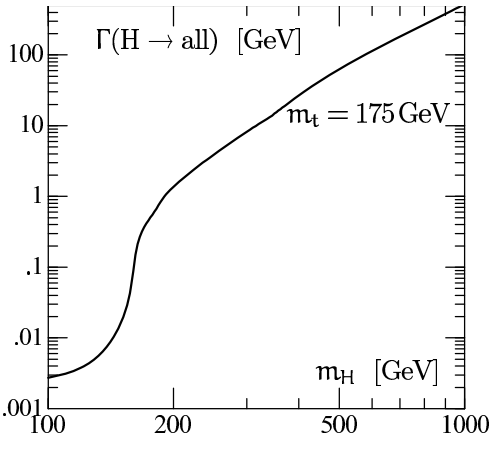

Figure 1.6: Total Higgs width Γ_H as a function of M_H.

- High mass region (M_H>$2M_Z$). The discovery should be feasible in the channel $H \to ZZ \to 4l$. The sources of background for this process are mainly two: $t\bar{t} \to Wb+W\bar{b} \to l\nu+l\nu\bar{c}+l\nu+l\nu c$ and $Zb\bar{b} \to lll\nu cl\nu\bar{c}$ but the signal can be detected requiring an high invariant mass for two lepton pairs.

  For very large masses (M_H>500 GeV) the production cross section decreases and the channels $H \to ZZ \to ll\nu\nu$ and $H \to WW \to l\nu 2jets$ have to be used to increase the statistics.

The statistical significance (defined as $N_S/\sqrt{N_B}$, where N_S and N_B are the number of signal and background events) is shown in figure 1.7 as a function of the Higgs mass for the different decay modes.

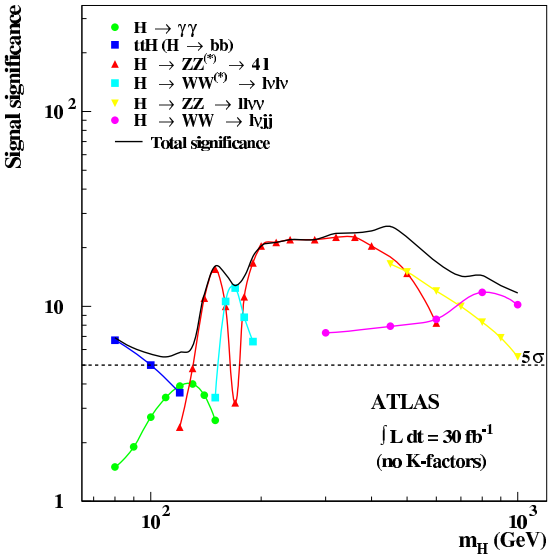

Figure 1.7: Statistical significance for the discovery of a SM Higgs boson in different channels [18].

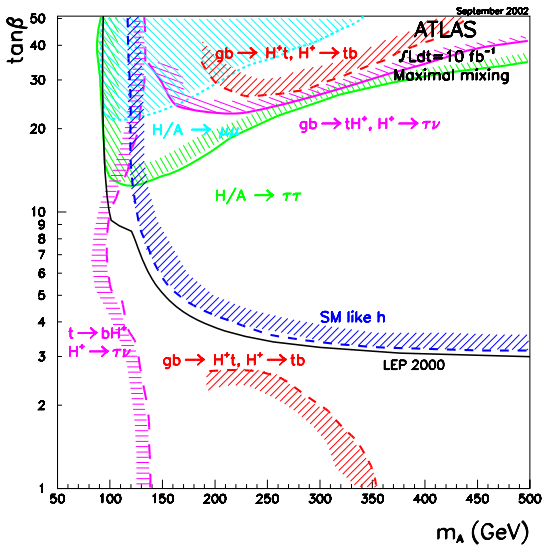

Figure 1.8: 5σ contours in the $M_A/tan\beta$ plane for the $MSSM$ Higgs [12].

1.4 Supersymmetric particles and Higgs boson in the MSSM

If supersymmetric particles exist, they will be produced and detected at the LHC in a mass range up to 2 TeV. They will in turn decay to the lightest supersymmetric particle (LSP) which is stable and hardly interacting with matter. The search for supersymmetric particles thus sets stringent limits on missing energy measurement.

The simplest supersymmetric extension of the Standard Model requires two doublets with vacuum expectation value v_1 and v_2 to implement the mechanism of spontaneous symmetry breaking.

The physical particle spectrum contains two neutral scalar bosons (h and H), two charged Higgs bosons ($H^{\pm}$) and one pseudoscalar (A). The mass of the lightest boson (h) depends on the ratio v_2/v_1=$tan\beta$, on the top mass and on the masses of the other supersymmetric particles. At large $tan\beta$ and with m_{top}=174 GeV, m_h<130 GeV and this limit reduces for lower $tan\beta$. If a single Higgs particle will be found with a mass larger than 130 GeV, supersymmetric theories will be ruled out.

The plane of the two free parameters M_A and $tan\beta$, in the range $0<M_A<500$ GeV and $0<tan\beta<50$, can be explored with some specific decay channels like $A/H\rightarrow\tau\tau$ and with SM Higgs like channels as $h/H\rightarrow\gamma\gamma$ (fig. 1.8). The most promising results to be the channel $A/H\rightarrow\tau\tau$. It is required a very good τ identification capability and a good resolution in missing energy measurement. The selection of these events is based on the detection of the lepton coming from a τ; the other τ can decay into hadrons (higher branching ratio) or into leptons. To reduce the background from $pp\rightarrow b\bar{b}X$ followed by $b\rightarrow jet$ and $\bar{b}\rightarrow\mu$, an isolated high p_T lepton, a jet with $E_T^j>40\ GeV$ and missing energy ($E_T^{miss}>20\ GeV$) are required.

1.5 ATLAS: an outlook of the experiment

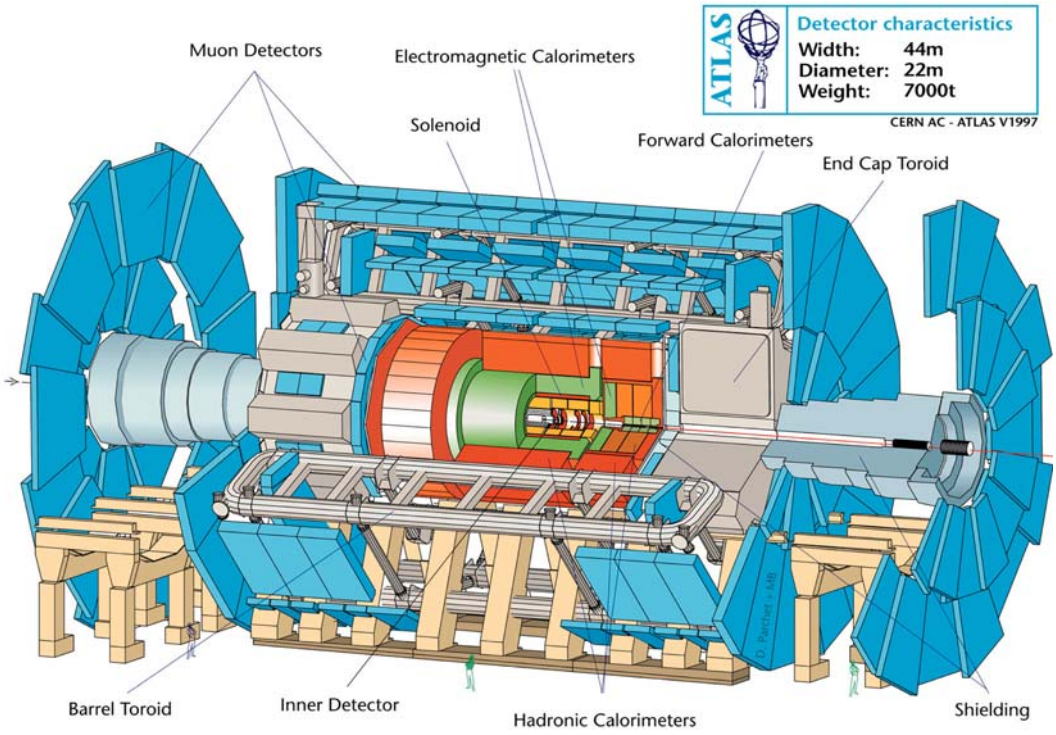

Figure 1.9: Three-dimensional view of the ATLAS detector. The subdetectors and the magnet system are shown.

The ATLAS (A Toroidal LHC ApparatuS) [14] collaboration proposed a general

purpose experiment designed to exploit the full discovery potential of the LHC outlined in the previous Sections. The main goals that have driven the design of the detector are:

- A calorimeter system that can identify and measure electrons and photons, measure energy and direction of particles and jets and that is hermetic for missing energy measurements.
- An inner tracking system for lepton momentum measurement, for b-quark tagging and for enhanced electron-photon identification.
- A muon system for muon identification and momentum measurement for very high energy muons.
- A selective trigger to confront the high background environment.
- A large geometrical acceptance.
- Radiation resistance to allow operation for more than ten years of data taking.

In fig. 1.9 a three-dimensional view of the ATLAS detector is shown. Starting from the beam line, the detector is made of an inner tracker contained in a superconducting solenoid that generates a field of 2 T, of an electromagnetic and hadronic calorimeter and of the Muon Spectrometer which consists of layers of muon chambers in a toroidal air-core magnet. A global reference system is defined with the beam line as z axis and the y axis pointing in the upward direction. In the x-y plane, the R coordinate is the distance from the beam line and ϕ is the azimuthal angle ($0<\phi<2\pi$). The polar angle θ in the R-z plane is in the range $0<\theta<\pi$; the pseudorapidity η is defined as $\eta=-\ln(\tan(\theta/2))$.

In the following can be found a brief decsription of the Inner Detector and of the Calorimeter system.

The Muon Spectrometer will be the subject of the next Chapter.

Inner detector

The inner detector [15] has been designed to match the following requirements:

- Tracking capability up to $|\eta|<2.5$.
- Transverse momentum resolution $\frac{\Delta p_T}{p_T}<30\%$ at p_T=500 GeV and $|\eta|<2$
- High efficiency (95%) for isolated tracks with $p_T>5$ GeV

An overview of the inner detector is given in figure 1.10. Its outer radius is R=115 cm and it is about 7 m long. It is divided in three zones; in the central ($|z|$<80 cm, $barrel$) detectors are placed in rings centered on the beam line while in the forward regions ($end-caps$) they are arranged in wheel orthogonal to the beam line.

- Semiconductor Tracker (SCT). It is made of silicon detector segmented in pixels (2 layers in the barrel region and 8 wheels in the end caps) or in strips (4 layers in the barrel). Single point resolution is 13 μm.

- Transition Radiation Tracker (TRT). It is made of drift straw tubes filled with a Xenon gas mixture with a single point resolution of 170 μm; polypropylene radiators are provided to generate transition radiation which gives additional electron identification ability.

Each track with $|\eta|$<2.5 is reconstructed with 6 precise points in the SCT and at least 36 points in the TRT.

Calorimeters

The ATLAS calorimeter [16][17] has been designed to meet the different demands of the LHC physics program while operating in a very high luminosity environment. This system must be capable of reconstructing the energy of electrons, photons and jets as well as measuring missing transverse energy.

The calorimeter is shown in fig. 1.11. A barrel cryostat around the inner detector cavity contains the barrel electromagnetic calorimeter and the solenoidal coil which supplies a uniform field in the inner tracking volume. This coil is placed in front of

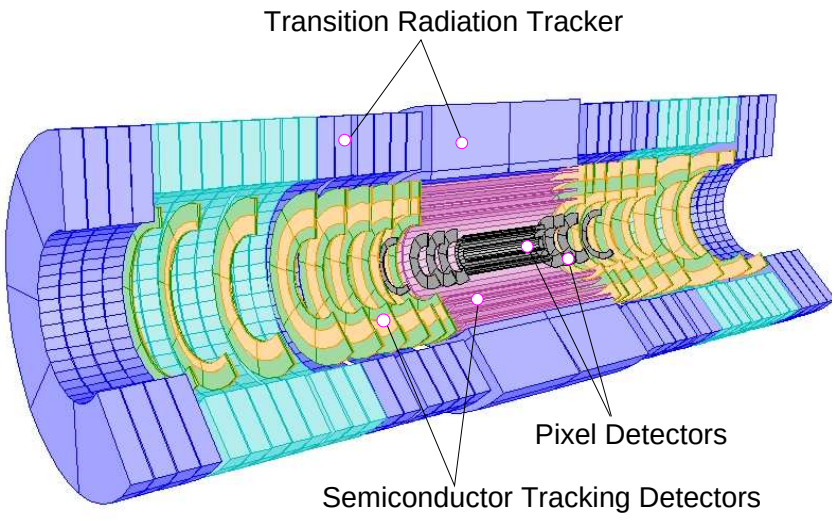

Figure 1.10: Layout of the inner detector.

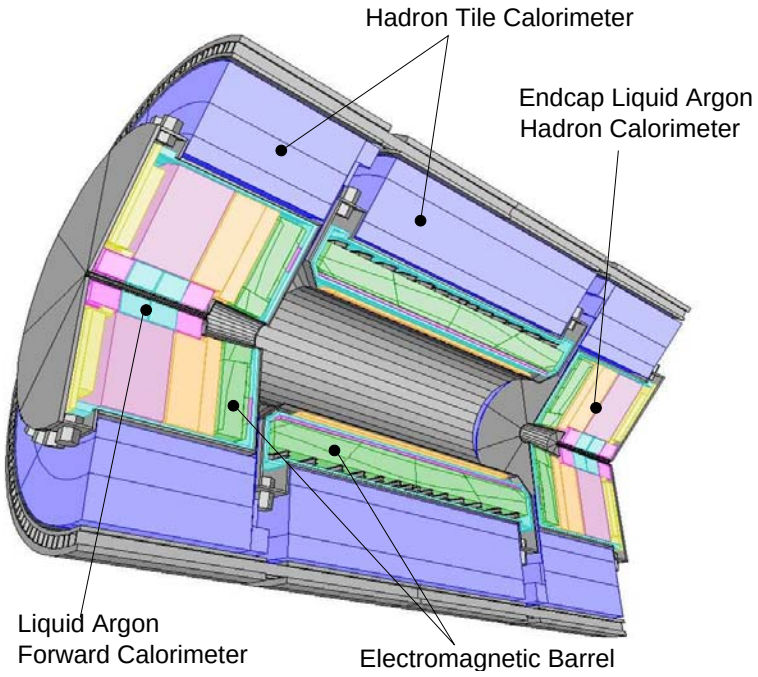

Figure 1.11: Three dimensional view of the calorimeter system.

the electromagnetic calorimeter. Two end-cap cryostats enclose the electromagnetic and hadronic end-cap calorimeters as well as the integrated forward calorimeter. The barrel and extended barrel hadronic calorimeters are contained in an outer support cylinder, acting also as main solenoid flux return. The outer radius of the calorimeters is 4.23 m. The electromagnetic calorimeter uses lead absorbers in liquid Argon; it is implemented in an '*accordion*' geometry. Angular resolution is expected to be 40 $\mu rad/\sqrt{E(GeV)}$ while energy resolution will be $\frac{\sigma_E}{E}$=10%/$\sqrt{E(GeV)}$ $\oplus$1%. The hadronic calorimeter in the barrel region uses iron absorbers with scintillator plates staggered in planes perpendicular to the beam axis. At larger rapidities, where higher radiation resistance is required, the adronic calorimeter is based on the use of liquid Argon. The expected combined energy resolution is $\frac{\sigma_E}{E}$=50%/$\sqrt{E(GeV)}$ $\oplus$3% in the barrel and $\frac{\sigma_E}{E}$=100%/$\sqrt{E(GeV)}$ $\oplus$10% in the end caps.

At η=0, the total thickness of the calorimeters is about 11 interaction lengths.

Chapter 2

The ATLAS Muon Spectrometer

An overview of the requirements that have driven the design of the ATLAS muon spectrometer [19] is presented in the first part of the Chapter. It follows a description of the apparatus and of the trigger system.

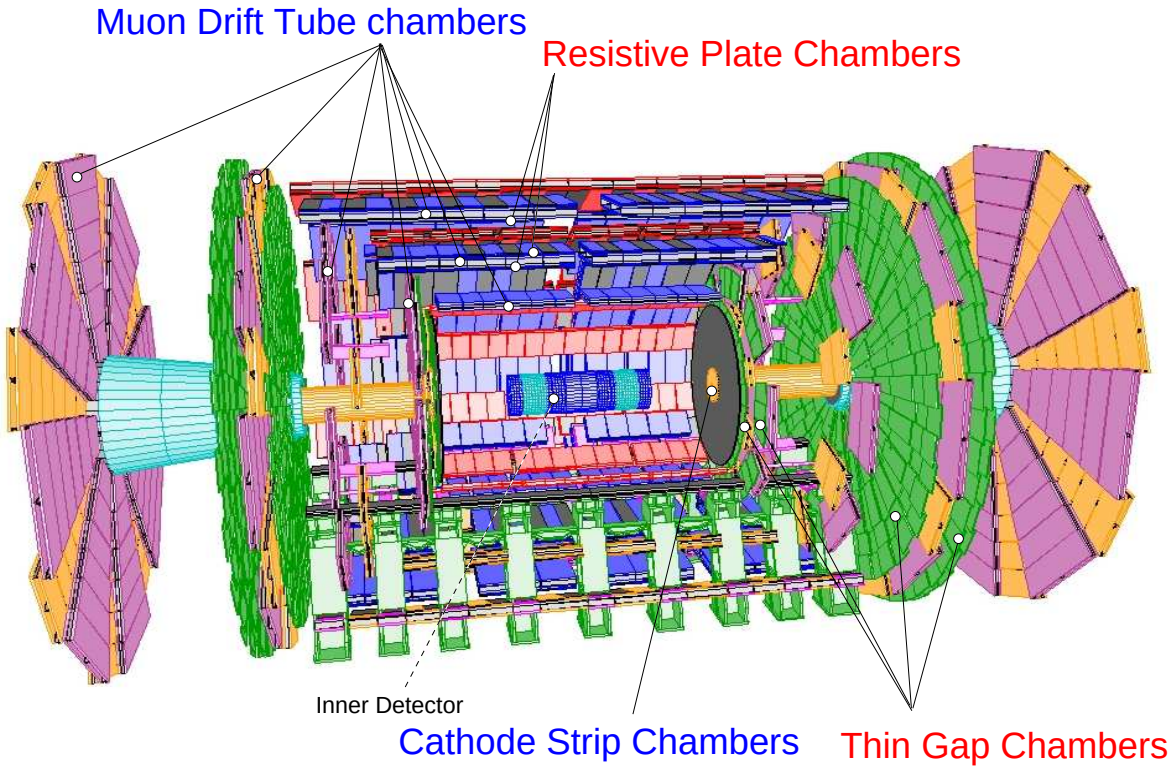

Figure 2.1: The muon spectrometer of the ATLAS detector. Muon Drift Tubes (MDT) and Cathode Strip Chambers (CSC) are *precision chambers* while Resistive Plate Chamber (RPC) and Thin Gap Chambers (TGC) are *trigger chambers* (see text for details).

The muon spectrometer (fig. 2.1) covers the largest fraction of the ATLAS volume with its dimensions of 22 m in external diameter and 44 m in length.

Charged particles trajectories are deflected by the means of a toroidal magnetic field of 0.6 T on average. The particle position is measured at different points. Knowing the field map, the muon momentum can be derived from the *sagitta* of the track fitted to the points. Two different kind of detectors are present: the *precision chambers*, to measure the coordinate in the bending plane and the *trigger chambers* used as trigger device and to measure the coordinate along the magnetic field line (the "second coordinate").

2.1 Physics Motivations

The desired performance of the spectrometer are defined by the main physical processes present in the ATLAS research program [18]. For example:

1. The Standard Model decay

   $$H \rightarrow ZZ^* \rightarrow \mu\mu ll$$

   is dominant for Higgs masses from 120 GeV/c^2 to 180 GeV/c^2. In this range the natural mass width is of about 1 GeV/c^2. Considering also the high background associated to this process it was found that the mass resolution should be of the order of 1% to achieve a significant signal sensitivity.

   This implies a transverse momentum[1] resolution $dp_t/p_t \leq 2\%$, according to the latest estimations.

   In this channel muons are produced with momenta between 5 GeV/c and 50 GeV/c.

   Similar requirements are valid for the MSSM decay

   $$H^0, A \rightarrow \mu^+\mu^-$$

   which is dominant in the mass range from 100 GeV/c^2 and 200 GeV/c^2 and for $\tan\beta > 20$.

   Moreover, a high detection efficiency in a large pseudorapidity range is particularly important, in fact, due to the muons momentum, a good hermiticity in the forward region is required.

2. Possible extensions of the Standard Model can be pursued searching for $Z' \rightarrow \mu^+\mu^-$ and all muonic decays of heavy supersymmetric particles. In this kind of processes, the decaying particle can have a mass as high as 5 TeV/c^2 and produce muons with momentum in the TeV/c range. A resolution dp_t/p_t of

[1] The momentum component orthogonal to the magnetic field line.

about 10% is considered a good value for an unambiguous determination of the muon (curvature) sign.

3. For beauty particle studies good performance are needed in the reconstruction of muons from the B decay chain whose typical momentum is lower than 30 GeV/c.

2.2 Performance requirements and technical motivations

The main requirements that have to be met to maximize the overall detector performance and their impact on the spectrometer design are outlined here.

- The transverse momentum p_t of a charged particle moving in a uniform magnetic field $\vec{B}$ is related to the *sagitta* S of the trajectory, defined in the fig. 2.2, by the

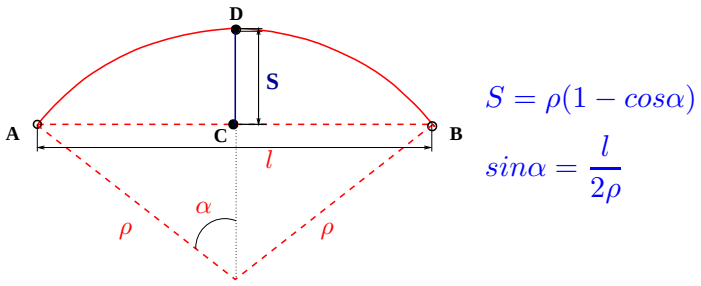

Figure 2.2: The sagitta S of the circular trajectory with curvature radius ρ through the points A,D and B is the shortest distance $\overline{CD}$ from the real trajectory and the undeflected path $\overline{AB}$ [29].

equation

$$S = \frac{0.3Bl^2}{8p_t} \tag{2.1}$$

where the length l is measured in meter, B in Tesla and p_t is the momentum perpendicular to $\vec{B}$ measured in GeV/c([2]). The error on the sagitta, σ_S, can be assumed proportional to the single point resolution[3]. Therefore from the 2.2:

$$\frac{dp_t}{p_t} = \frac{\sigma_S}{S} \propto \frac{\sigma(r)}{S} = \sigma(r)\,\frac{p_t}{0.3Bl^2}. \tag{2.3}$$

[2]From fig. 2.2: $\alpha \sim l/2\rho$ for $l << \rho$. Since the curvature radius $\rho = \frac{p_t}{0.3B}$ follows

$$S = \rho(1 - cos\alpha) \simeq \rho(1 - (1 - (\frac{1}{2}\alpha^2)\,) = \frac{\rho\alpha^2}{2} \simeq \frac{0.3Bl^2}{8p_t}. \tag{2.2}$$

[3]Assuming the positions r_A, r_D and r_C of the points in fig. 2.2 have been measured with (the same) resolution $\sigma(r)$, the sagitta can be calculated as $S = r_D - \frac{1}{2}(r_A + r_B)$ and the associated resolution $\sigma_S^2 = \sigma(r)^2 + 2 \cdot \frac{1}{4}\sigma(r)^2 = \frac{3}{2}\sigma(r)^2$.

Hence the momentum resolution degrades linearly with increasing p_t but improves for high B field and larger radial size (lever arm) of the tracking volume.

The measurement points used for the track reconstruction (on the bending plane), the "super points", are usually chosen as the center of the muon chamber traversed by the particle (fig. 2.8). The super points coordinates are thus determined using the information available from the single drift tubes (Sec. 2.4.1).

The point resolution $\sigma(r)$ in the 2.3 sums up the contributes due to the intrinsic tube resolution the multiple scattering and the alignment precision.

The apparatus must allow for a resolution dp_t/p_t of few percent in the low momentum region (see e.g. point 1 of the previous Section) where the resolution is dominated by energy loss (up to 20 GeV/c) and multiple scattering. This was a decisive argument for choosing an air core magnet system with the lowest possible amount of matter.

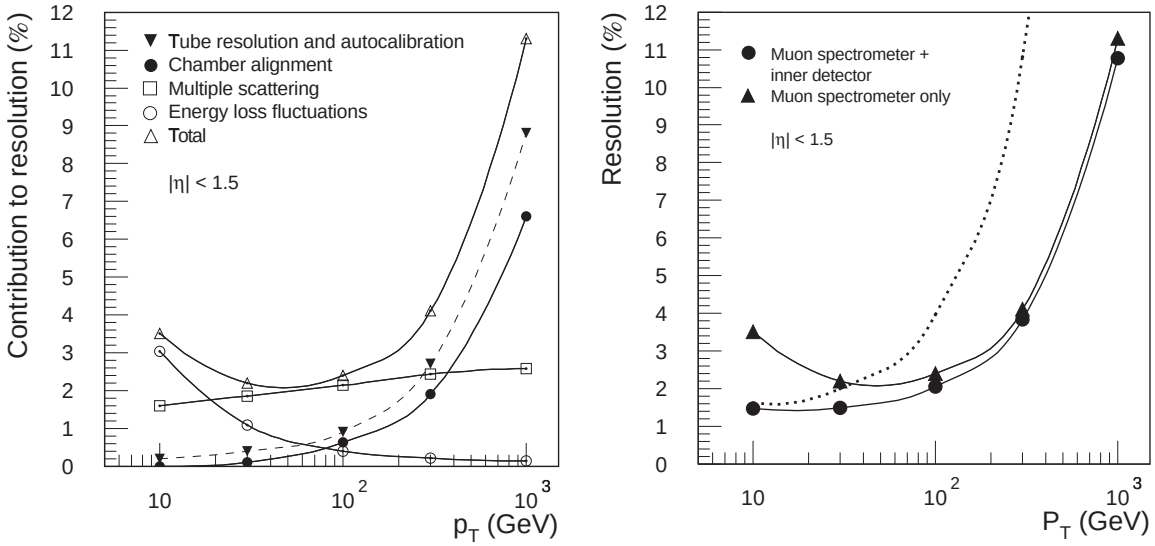

Figure 2.3: *Left.* Contribution to the standalone transverse muon momentum resolution assuming a single tube resolution of 80 μm. Above 300 GeV/c the dominant contribution comes from the single tube resolution, followed by the chamber alignment. *Right.* Muon momentum resolution combining the measurements of both the spectrometer and the inner detector. The dotted line corresponds to the inner detector standalone tracking. For momenta above 100 GeV/c the Muon Spectrometer standalone performance almost equals the combined one.

As demonstrated in fig. 2.3 a resolution between 2% and 3.5% is achievable in the

momentum range from 10 GeV/c to 2000 GeV/c. Using also the measurement points provided by the inner detector the 2% value is possible from 3 GeV/c to 100 GeV/c.

Since the inner detector (standalone) resolution is better for momenta lower than 20 - 30 GeV/c, in the B physics studies (see for example point 3 of the previous Section) the muon chambers are used mainly at trigger level (described further). The implication for the muon system is that pattern recognition should work even for the "softest" muons reaching the spectrometer which have a momentum of about 3 GeV/c.

The goal of a resolution $dp_t/p_t \approx 10\%$ for $p_t = 1\,TeV/c$, as reported in the point 2 of the previous Section, can be achieved only through the combination of the bending power and of the precision of the detector in the sagitta measurement (eq. 2.3). Therefore such requirement strongly influenced the definition of the main detector characteristics.

The term Bl^2 in 2.3 suggests that a large tracking cavity and an intense magnetic field are needed. To generate a magnetic field of few Telsa over the large spectrometer volume a current of the order of 10 kA must be provided. Such currents can be considered only in the context of superconducting magnets. The number of lines crossed by a muon track in toroids is constant and the bending power increases at higher pseudorapidities (Sec. 2.3) hence a toroidal magnetic field has the property that the transverse momentum resolution is constant over a wide range of pseudorapidity. A drawback of this configuration is that the bending does not take place in the plane transverse to the beam axis therefore the precise knolwdge of the primary interaction point (20 μm wide at LHC) cannot be exploited.

With $B = 0.6\ T$ and $l = 4.5\ m$, from 2.2 results a sagitta of 500 μm for a momentum of 1 TeV/c. This means the sagitta must be determined with a precision $\sigma_S = S \cdot dp_t/p_t$ of about 50 μm (eq. 2.3). For high momentum muons multiple scattering is negligible and the resolution is dominated by the intrinsic tube resolution and the alignment precision as shown in fig. 2.3. It can be demonstrated that a tube resolution of about 80 μm is necessary. As a consequence the accuracy of the relative positioning of the chambers and the mechanical precision of the chamber assembly has to match the spatial resolution of the drift tubes. This ask for a dedicated alignment system and specific chamber construction demands (a description of the spectrometer is given in the next Section).

- A reconstruction of the track in the non-bending plane projection (second coordinate plane) with a point resolution of about 10 mm is required for a safe track reconstruction and reliable momentum determination.

- In general all the physics measurements benefit from a high rapidity coverage

and good hermiticity. An example is given in point 2 of the previous Section; high hermiticity is also important to avoid fake missing energy detection which may suggests the presence of neutrinos or stable super-symmetric particles.

The ATLAS spectrometer covers the range $|\eta| < 2.7$. Two chamber technologies are used: the Monitored Drfit Tubes in the central rapidity region while for $|\eta| > 2$ Cathode Strip Chamber with higher granularity and rate capability are used since they have to operate in a higher background rate and particle density.

- Trigger selectivity: transverse momentum thresholds of 10 - 20 GeV/c are adequate for high-mass states, which will be in the focus of LHC physics at nominal luminosity. Lower thresholds of $p_t \sim 5$ GeV/c are required for CP violation and beauty physics.

- Trigger coverage: adequate trigger efficiencies can be obtained with a pseudorapidity coverage smaller than that of the precision chambers. The actual requirements are mostly determined by processes at the opposite ends of the LHC mass scale: the need for good acceptance for rare high mass Higgs particles, and the need for very high statistics to study small rate asymmetries due to CP violation in the B sector. A trigger coverage corresponding to $|\eta| < 2.4$ is found to be sufficient.

- Bunch-crossing identification: the LHC bunch-crossing interval of 25 ns sets the scale for the required time resolution of the first-level trigger system (Sec. 2.4, 2.5).

- The ATLAS experiment is forseen to meet the whole physics program after at least 10 years of operation. The necessity to operate for many years in a high background and particle flux without performance degradation implies severe constraints on the detector condition of operation. Therefore a gas which does not suffer from aging effect is mandatory. Moreover a fine segmentation helps to reduce occupancy to a good track reconstruction capability. The background operation condition are described in the next Chapter.

2.3 The magnetic system

The ATLAS magnetic system consists of a central solenoid and three toroid magnets. The central solenoid produces a field of 2 T in the Inner Detector region.

Each of the three toroids, one in the barrel and two in the endcap region, is made out of 8 coils assembled radially around the beam axis (fig. 2.4). The barrel toroid extends over a lenght of 25 m with an inner diameter of 9.4 m and outer dimeter of 20 m. The two endcap toroids, inserted at the two ends of the barrel, have a length of 5 m; inner and outer diameter are respectively 1.6 m and 10.7 m. The barrel coils

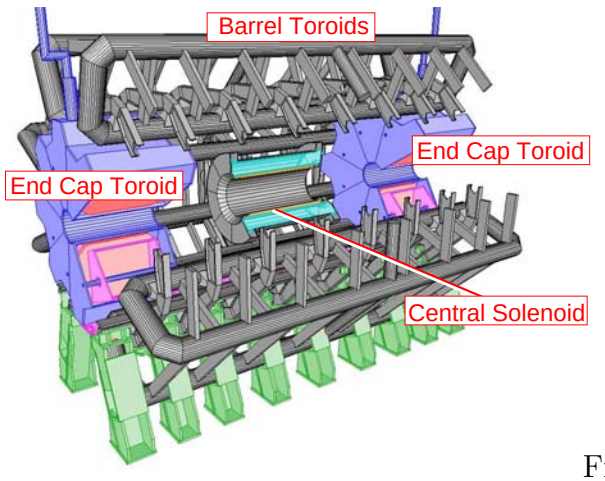

Figure 2.4: The ATLAS magnetic system.

are contained in individual cryostats while in the endcaps they are assembled in a single large cryostat. The results is a field configuration (fig. 2.5) where the field lines surround the detector azimuthally. The average value is 0.6 T. The bending power $\int \vec{B} \cdot \vec{dl}$ at $\phi = 0$ varies from 2 Tm for $|\eta| = 0$ to 9 Tm for $|\eta| = 2.7$ (fig. 2.5).

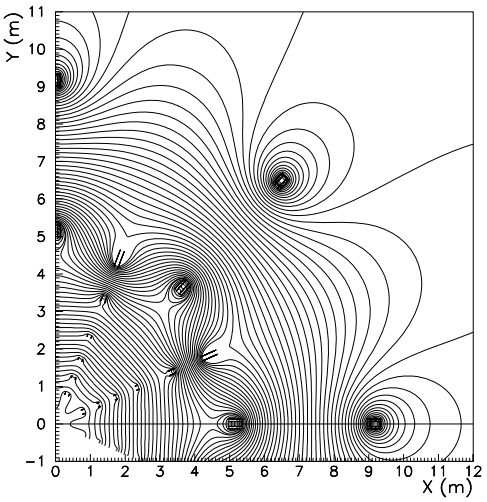

(a) Magnetic field map for a fixed η in the transition region. The field lines are shown in a plane perpendicular to the beam axis. The interval separating consecutive lines is 0.1 Tm.

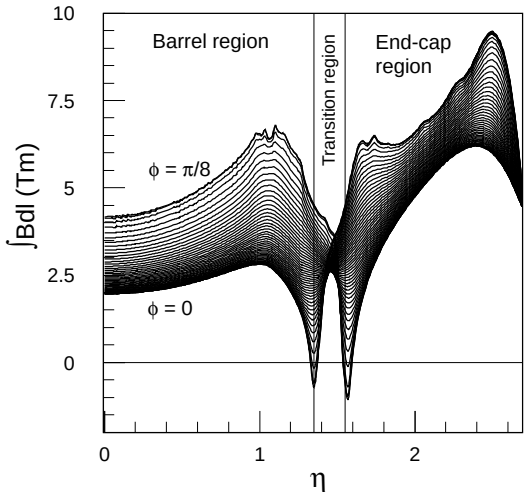

(b) Toroid bending power $\int \vec{B}\vec{dl}$ of the azimuthal field component integrated between the first and the last muon chamber as a function of pseudorapidity for different values of ϕ.

Figure 2.5: Characteristics of the toroidal magnetic field.

2.4 Apparatus description

The ATLAS Muon Spectrometer is made up of three main modules: the barrel region and two endcap regions (fig. 2.1, 2.6).

In the barrel ($|\eta| < 1$) chambers are arranged in three cylinders, usually referred as stations, concentric with the beam axis. The inner station (BI:Barrel Inner) is located at distance of about 5 m while the middle (BM) and the outer stations (BO) are positioned at radii of about 7.5 m and 10 m respectively (fig. 2.1, 2.6). Usually a chamber is labelled with a three letter code according to the its position, fig. 2.7. If the chamber spans the region between two toroid coils, it's of type L (Large), then it can be labelled as BIL, BML or BOL. Instead if it is in the line with a toroid coil it's a type S (Small) chamber: BIS, BMS or BOS[4].

In this η-region the inner and the outer stations are outside the toroid coils hence the particles position are measured near the inner and outer field boundaries, and inside the field volume. An example is shown in fig. 2.8.

The end-cap chambers cover the pseudo-rapidity range $1 < |\eta| < 2.7$ and are arranged in four disks at distances of 7 m, 10 m, 14 m and $21 - 23$ m from the interaction point (fig. 2.1, 2.6). In this η-region the chambers are arranged to determine the momentum with the best possible resolution from a point-angle measurement.

[4]Other labels are used to identify "special" chambers: for example in the bottom part of the spectrometer some chambers, the BOFs, have an irregular shape to leave room to the spectrometer supports.

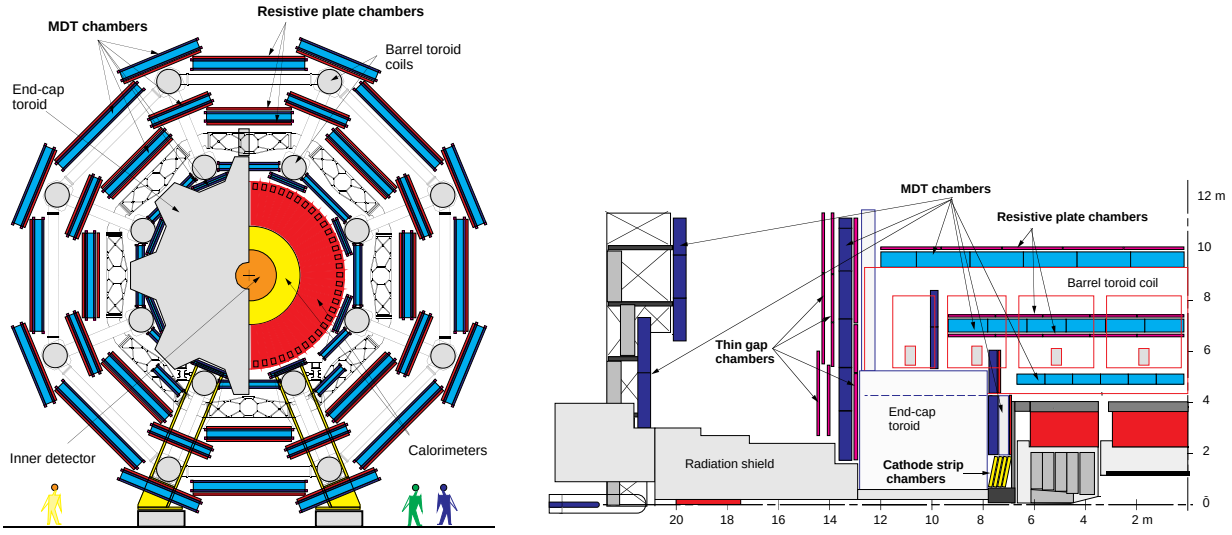

Figure 2.6: *Left*. Transverse view of the ATLAS Muon Spectrometer. *Right*. Side view of one quadrant of the spectrometer.

The whole spectrometer consists of two type of chambers and four different technologies:

- **Precision Chambers**. For the precision measurement of muon tracks in the principal bending direction of the magnetic field, Monitored Drift Tube (MDT) chambers are used except in the innermost ring of the end-cap inner station ($2 < |\eta| < 2.7$).

  In the innermost ring of the end-cap inner station (fig. 2.6) Cathode Strip Chambers (CSC) are employed to cope with the higher particles flux. The CSC are

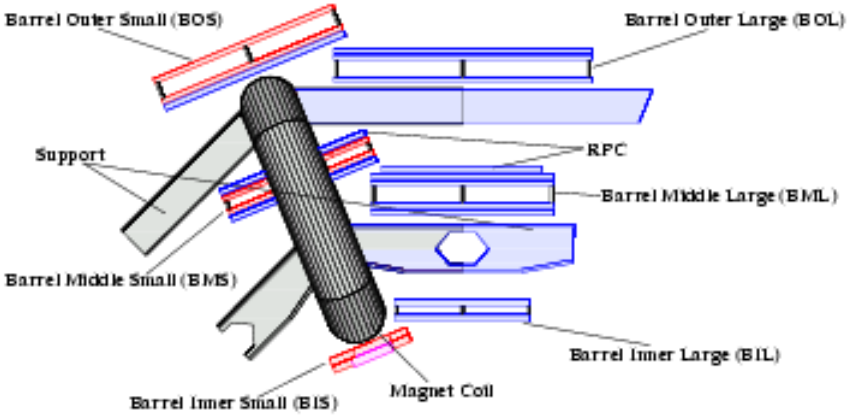

Figure 2.7: Definition of the chambers identifcation label in the barrel sector.

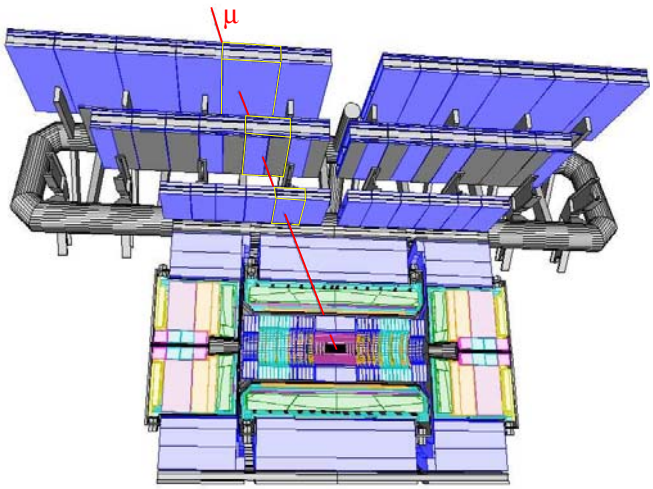

Figure 2.8: Event display of a muon traversing the inner detector, the calorimeters and three barrel stations.

multi-wire proportional chambers with cathode strip rea-dout and with a symmetric cell in which the anode-cathode spacing is equal to the anode-wire pitch. A spatial resolution of 60 μm has been measured. A transverse coordinate is obtained from the strips parallel to the anode wires, which form the second cathode of the chamber.

- **Trigger Chambers**. These chambers provide the trigger function, the bunch-crossing identification (par. 2.5) and the measurement of the second coordinate.

  In the barrel this information is provided by three stations of Resistive Plate Chambers (RPC). They are located on both sides of the middle MDT station, and either directly above or directly below the outer MDT station (fig. 2.6, 2.7, 2.12). An RPC consists of a pair of parallel bakelite plates of high resistivity with a well defined distance; the gap between the two plates is filled with a gas mixture on the basis of tetrafluoroethane ($C_2H_2F_4$). A voltage of about 10 kV is applied across the gap; this causes primary ionization electrons produced by a traversing particle to multiply while drifting towards the anode. Signals are read out via capacitive coupling by a set of metal strips on the outside of the bakelite plates. Typical spatial and time resolutions are 1 ns and 10 mm respectively. These values are adequate for identification of the muon hits with the associated bunch crossing and rough muon transverse measurements at trigger level (Sec. 2.5)

  Each chamber is made of two rectangular detector layers, each one read out by two orthogonal series of pick-up strips: the η-strips are parallel to the MDT wires and provide the measurements of the trigger detector in the bending plane; and the ϕ-strips, orthogonal to the MDT wires, provide the second coordinate measurement which is important for the off-line pattern recognition.

  In the end-caps, three stations of Thin Gap Chambers (TGC), located near the middle MDT station will be installed. The TGC have a structure similar to multi-wire proportional chambers, with the difference that the anode-wire pitch (1.8 mm) is larger than the cathode-anode distance (1.4 mm). The electric field configuration and the short drift distance provide for a good time resolution and a fast response. Signals from the anode wires, arranged parallel to the MDT wires, provide the trigger information together with read-out strips arranged orthogonal to the wires, that also provide a measurement of the second coordinate.

2.4.1 The MDT chambers

A schematic drawing of an MDT chamber is shown in fig. 2.9.

It consists of three (e.g. type BM,BO chambers) or four (e.g. type BI) layers (a *multilayer*) of cylindrical aluminium drift tubes on each side of a supporting frame. The tubes diameter is of about 3 cm.

The four-layer chambers are located in the innermost muon detector stations where the background hit rates are the highest. An additional drift tube layer makes the pattern recognition in this region more reliable. The distance between (spacer width) the two multilayers is about 170 mm for the inner stations and 317 mm for the middle and outer stations.

The drift tubes, named MDT (Monitored Drift Tubes), are the basic unit of the chamber, they are filled with a noble gas based mixture and have a thin wire running along the cylinder axis which serves as anode when high voltage is applied between the wire and the tube wall. Such a detector can be used for precise position measurements as described in detail in the next Chapter.

The barrel chambers are of rectangular shape with areas of 1.5 m^2 to 12 m^2 and length between 1 m and 6 m([5]). Instead, the disk like shape of the end cap stations implies a trapezoidal chamber geometry. The tapering angles are 8.5^o for the smaller and 14^o for the larger chambers. The endcap chamber areas range from 1 m^2 to 10 m^2.

[5]On one end of the chamber, the tubes are connected to the high voltage and on the other end to the read-out electronics. The denominations readout (RO) and high voltage (HV) is also used to distinguish between the chamber ends (fig. 2.9). The supporting frame is a light-weight aluminium structure holding the drift tube layers. It consists of three crossplates (RO, MI and HV, fig. 2.9) oriented perpendicularly to the tube axis, i.e. in z-direction in the chamber coordinate system. The crossplates are connected by two longbeams oriented parallel to the tube axis, i.e. in x-direction. The multilayers are glued to the crossplates.

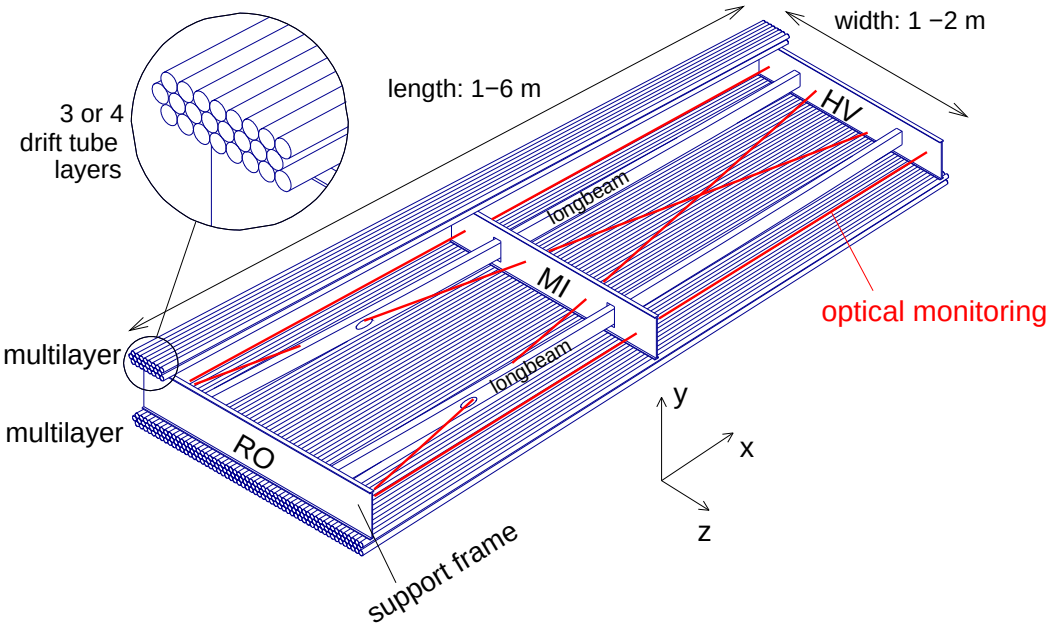

Figure 2.9: Scheme of the MDT chambers layout.

There are in total 380000 MDTs in ATLAS assembled into 1194 chambers.

In order to achieve the desired resolution (see previous Section) wires are positioned inside each tube and the MDTs are glued togheter following a special assembly procedure. The wire-tube eccentricity is below 10 μm. Considering also the relative assembly accuracy of MDTs within a chamber the anode wires are positioned inside a chamber with 20 μm accuracy.

Internal alignment

Chamber deformation due to temperature changes and gravitational forces are measured continuously during the operation of ATLAS by means of light rays (fig. 2.9). A LED at one end of the chamber is used together with a lens mounted on the middle cross plate to project an encoded chess-board pattern mask onto a CCD camera at the other chamber end. Changes in the chamber geometry will result in a movement or rotation of the image; by analysing the CCD data this can be corrected for during the track reconstruction process. The system described is known as 'in-plane alignment'. The continuous recording of the chamber shape, is a core feature of the ATLAS Muon Spectrometer, this explains the adjective "Monitored" used to identify the ATLAS drift tubes.

The local chamber alignment (in-plane alignment) precision in lower then 10 μm.

2.4.2 The global alignment system

Displacements of the chambers position up to several millimeters are expected to be found with respect to the nominal designed position, moreover, relative chamber movements (of the same size) can be expected when the toroid magnet is switched on or because of temperature variations.

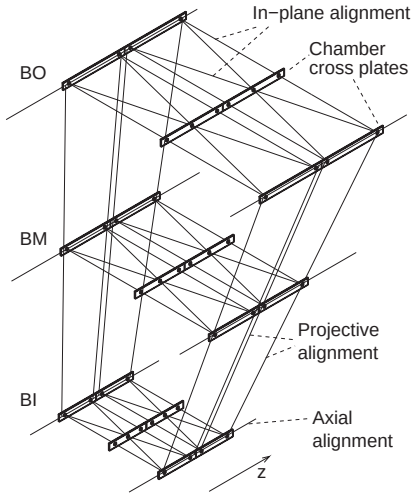

Figure 2.10: Muon chamber alignment for the barrel region. All chambers are arranged such that the lines connecting their corners point towards the interaction point ('projective towers'). A set of optical alignment rays is used to monitor chamber movements. Axial lines run parallel to the beam axis while projective lines connect different stations. Adjacent chambers are additionally connected by so called proximity sensors (not shown).

Equally important to the measurement of the individual chamber shapes (discussed in the previous Section) is therefore the monitoring of the total muon spectrometer geometry.

This so-called 'global alignment system' is, as the in-plane, based on optical sensors connected by light rays. The barrel chambers are arranged such that they form projective towers, as shown in fig. 2.10: the hypothetical lines connecting the corners of an inner, middle and outer station chamber point towards the interaction point. Adjacent chambers are optically linked by proximity sensors; axial lines are parallel to the beam axis and connect chambers within a station. A set of projective alignment rays finally provides a connection of the three stations themselves[6].

The global alignment system allows for a relative positioning accuracy of MDTs within a chamber lower then 30 μm.

2.5 The Trigger Strategy

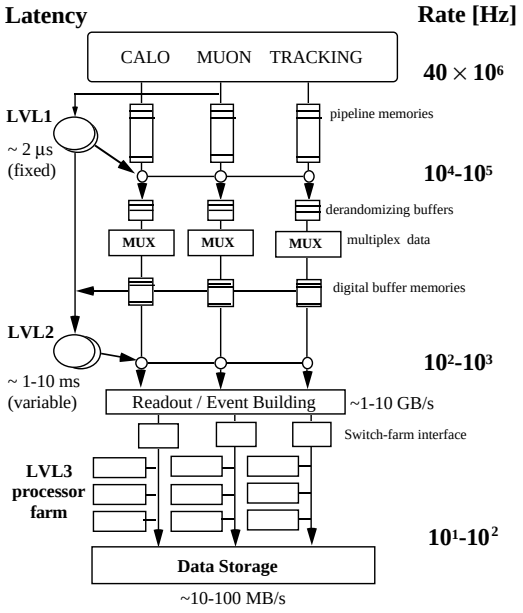

Figure 2.11: The ATLAS three level trigger architecture.

The rate with which events accour at the LHC is given by the bunch crossing frequency of 40 MHz (one every 25 ns), multiplied by the number of proton-proton collisions per bunch crossing (25 on average). For a luminosity of 10^{34} $cm^{-2}s^{-1}$, the event rate is 10^9 Hz.

[6]In the endcap region the situation is slightly more difficult since the vacuum vessels of the endcap toroids block the line of sight between some of the stations. In addition to the elements described above for the barrel, a system of rigid reference bars is therefore used. These are cylindrical metal tubes which are themselves equipped with an optical system to monitor their deformation. Sensors mounted on the alignment bars are then utilized to interconnect the individual chambers and stations.

The data-acquisition will be able to store events with a rate of 100 Hz (corresponding to about 50 MB/s).

The task of the trigger is to reduce the interaction rate from 10^9 Hz to 100 Hz selecting efficiently only the events of interest for the physics objectives (the Higgs production rate, for example, is 0.1 $\frac{events}{s}$).

The bunch-crossing period of 25 ns is much shorter than the maximum response of the MDT[7] and thus association of the event with the correct bunch crossing identification is essential to reconstruct correctly muon tracks and to correlate data from different subdetectors.

In the trigger architecture of the ATLAS experiment, data from different sectors of different subdetectors are processed in parallel to speed up the procedure. Three trigger levels of increasing accuracy and complexity are used to select the events; informations from the previous levels are used to reduce the amount of data to be processed (fig. 2.11).
The Level-1 trigger uses data with reduced-granularity from the trigger chambers. The Level-2 trigger uses full-granularity and full-precision data from the trigger and the precision chambers but examines only regions of the detector area flagged by the Level-1 trigger as "regions of interest" (RoI) . The Level-3 trigger uses the full event data for the final selection of events for offline analysis.

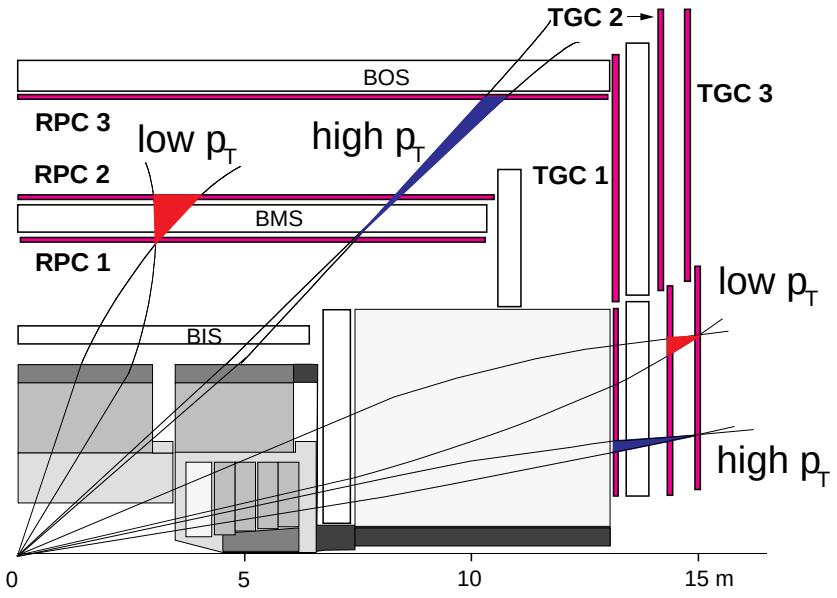

Figure 2.12: Scheme of the first level muon trigger.

- **Level-1** First level trigger accepts data at the rate of 40 MHz with a latency of 2 μs. Criteria of selection are the multiplicity of muons, electromagnetic clusters

[7]Dominated by the maximum drift time which is about 700 ns (Ch. 3).

and jets as well as global information like missing transverse energy. After this trigger selection the event rate is reduced to 75 kHz.

For the case of the Level-1 muon trigger two scenarios are forseen (fig. 2.12). When the LHC will operate at high luminosity (10^{34} $cm^{-2}s^{-1}$) the amount of data can only be coped with if a sufficiently high muon momentum thershold is chosen: the so colled high-p_t trigger accepts muons with $p_t > 20GeV/c$. For low luminosity runs (10^{33} $cm^{-2}s^{-1}$) momenta down to 6 GeV/c are accepted. This is the low-p_t trigger.

In the barrel region the low-p_t trigger request is satisfied if, in the stations RPC1 and RPC2 (fig. 2.12), a combination of hits (in both coordinates) can be found which fulfills the condition that the hits in RPC2 lie within a tolerance window from the straight line defined by the hit in RPC1 and the interaction region. No hits in RPC3 are required since low energy particles are likely to be deflected before reaching the outer station. For the endcap low-p_t trigger analogous hit combination is required in TGC3 and TGC2 stations.

For the high-p_t trigger an additional hit, within a coincidence window, is required in the station RPC3 (barrel) or TGC1 (end-cap).

- **Level-2** The second level is designed to reduce the Level-1 trigger rate to a about 1 kHz. To achieve the required rate reduction of a factor 100, the Level-2 trigger must process data from the trigger detectors and combine them with data from the tracking chambers. Level-2 processing is restricted to the Regions of Interest in the η-ϕ space defined by Level-1 informations.

  In the muon spectrometer, the p_t resolution of the first level can be improved using data from the precision chambers to measure momentum with a fast algorithm.

- **Level-3** Performs a global analysis combining information from different subdetectors. Events which meet the final criteria are stored.

Chapter 3

Monitored Drift Tubes

3.1 Description

The basic components of an ATLAS drift tube [19] are shown in fig. 3.1.

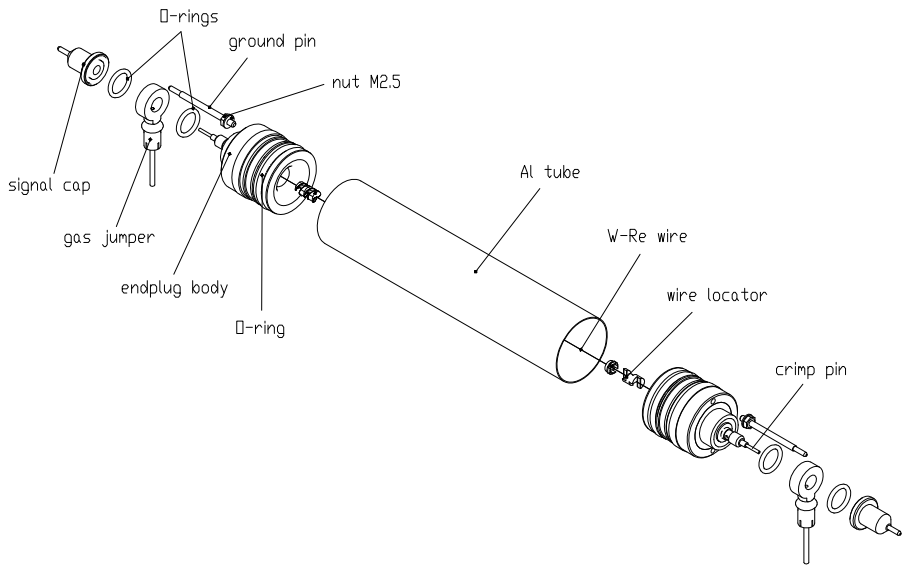

Figure 3.1: Schematic view of an ATLAS Monitored Drift Tube.

Each MDT consists of a thin wall (0.4 mm) aluminium tube with 29.97 mm outer diameter, a gold plated tungsten-rhenium wire with a diameter of 50 μm placed along the tube axis and two endplugs which close the MDT at both ends. Each endplug consists of a body of modified polyphenylenether re-enforced with glass fibres, an accurately machined outer aluminium ring and a high precision central brass insert. The endplugs, besides making the gas sealing, provide also electrical insulation between the high voltage anode wire and the outer tube wall. They further fix the position of the wire with respect to the aluminium tube and allow the connection of the MDT to the

gas distribution and front-end electronics. The precisely machined outer surface of the endplug is used during assembly of the individual MDTs to control the relative position of the wire with respect to the tube axis to the required 10 μm accuracy. The main parameters are listed in tab. 3.1.

Parameter	Nominal value
Outer tube radius	14.985 mm
Wall thickness	400 μm
Tube material	Al
Tube length	from 180 to 520 cm
Anode wire radius	25 μm
Anode wire material	W-Re alloy (93:7)
	gold plated 3% by weight
Anode wire resistance	40 Ω/m
Anode wire tension	350 g
Tube-wire eccentricity	10 μm (r.m.s.)

Table 3.1: Basics MDT construction parameters.

3.2 Principles of operation

Drift tubes are gas filled ionization detectors operating in proportional mode. The anode wire is supplied with a high voltage, typically in the kV range, while the metallic tube wall is grounded. Electron and ion pairs created by a ionizing particle traversing the gas drift towards the anode and the cathode respectively in the radially symmetric electric field

$$E(r) = \frac{V}{ln\frac{b}{a}} \cdot \frac{1}{r}, \tag{3.1}$$

where V is the anode wire potential, b the tube inner radius and a the wire radius. Close to the wire the electric field is high enough for the drifting electrons to gain sufficient kinetic energy to cause secondary ionization; the total number of electron-ion pairs increases by a factor G known as "gas gain" or "gas amplification". For the ATLAS MDTs an Ar:CO_2 $(93:7)$ gas mixture is adopted, the nominal potential is $3080\,V$ and the operating absolute pressure is 3 bar; the gas gain is $2{\times}10^4$.

In the section are described the physical processes involved in the signal generation in a drift tube [20, 21, 22, 23, 24, 25, 28].

3.2.1 Ionization

Muons The average energy loss by a charged particle, heavier than electron, traversing

a thickness dx of material is given by the Bethe-Block fomula

$$-dE/(\rho dx) = Kz^2 \cdot \frac{Z}{A} \cdot \frac{1}{\beta^2} \cdot \left(\frac{1}{2} ln \frac{2m_e c^2 \beta^2 \gamma^2 T_{max}}{I^2} - \beta^2 \right), \tag{3.2}$$

where K is a constant equal to 0.31 $MeV g^{-1} cm^{-2}$, ρ is the density, Z the atomic number, A the mass number of the absorbing material. I is equal to ZI_0 if I_0 is the mean ionization potential per electron of the absorbing material ; β and γ are the relativistic parameters of the particle of charge ze. T_{max} is the maximum kinetic energy which can be transferred in a single collision to a free electron.

Neglecting the dependence of T_{max} on the particle mass, the energy loss depends only on the particle velocity: it decreases as $1/\beta^2$ reaching the minimum value at $\beta \sim 0.96$, and increases slowly for $\beta \to 1$ ([1]). For energies greater than few hundred MeV all the particles are at the minimum of ionization (said to be *mip*s or minimum ionizing particles) and loose the same amount of energy per unit length. For most material the minimum $dE/\rho dx$ is approximatively equal to 2 $MeV/(g\ cm^2)$.

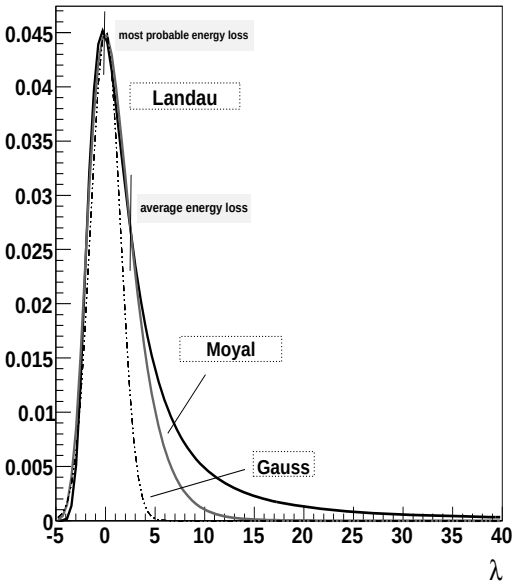

Figure 3.2: Landau and Moyal distributions. A gaussian fit to the maximum is also drawn.

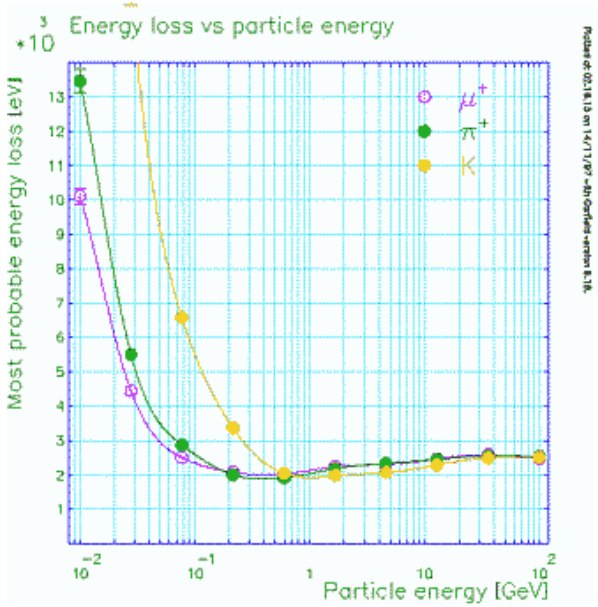

Figure 3.3: Simulation of the most probable energy loss in 1 cm of Argon for different particles.

In case of thin absorbers, like gases, the total energy deposition is given by a small amount of interactions hence fluctuations around the average can be significant. The

[1]The increase in the energy loss for momenta higher than 10 GeV/c or so ("relativistic rise"), due to the logarithmic term in the Bethe-Block formula, is saturated because of "polarization effects" (not taken into account by the 3.2). In gases saturation occurs around few hundred GeV/c at a value which is about 1.5 times minimum ionization.

energy loss distribution in thin media follows a Landau distribution [20] which is well approximated by the Moyal analytic formula [21, 22]

$$f(\lambda) = \frac{1}{\sqrt{2\pi}} e^{-\frac{1}{2}(\lambda + e^{-\lambda})}, \ \lambda = \frac{E - E_p}{\xi}. \tag{3.3}$$

The function depends on the single parameter E_p: the most likely energy loss. The parameter λ represents the normalized energy deviation from E_p being $\xi = Kz^2 \cdot Z/A \cdot \rho/\beta^2 \cdot x$ the first term of the Bethe-Block formula (3.2). As shown in fig. 3.2, Moyal approximation underestimates the Landau tail at high energy losses. In figure 3.3 is reported the most probable energy loss distribution in Argon at normal condition (NTP ([2])) for different particles with energy ranging from 10 MeV to 100 GeV produced with the GARFIELD [41] (Sec. 4.4) simulation program.

Charged particles, in a gaseous absorber, loss their energy mainly through excitation and ionization of the atoms of the material itself. In the former case an electron can be released whether the excited atom returns to the ground state emitting an Auger electron or a photon which ionizes the gas via photoelectric effect. The total average number n_{tot} of ion pairs produced per unit length can be espressed as the ratio

$$n_{tot} = \Delta E / W_i \tag{3.4}$$

Gas	Z	δ (g/cm^3)	I_0 (eV)	W_i (eV)	$dE/d(\rho x)$ (MeV/gcm^2)	dE/dx (keV/cm)	n_p (cm^{-1})	n_{tot} (cm^{-1})
H_2	2	$8.38 \cdot 10^{-5}$	15.4	37	4.03	0.34	5.2	9.2
He	2	$1.66 \cdot 10^{-4}$	24.6	41	1.94	0.32	5.9	7.8
N_2	14	$1.17 \cdot 10^{-3}$	15.5	35	1.68	1.96	(10)	56
O_2	16	$1.33 \cdot 10^{-3}$	12.2	31	1.69	2.26	22	73
Ne	10	$8.39 \cdot 10^{-4}$	21.6	36	1.68	1.41	12	39
Ar	18	$1.66 \cdot 10^{-3}$	15.8	26	1.47	2.44	29.4	94
Kr	36	$3.49 \cdot 10^{-3}$	14.0	24	1.32	4.60	(22)	192
Xe	54	$5.49 \cdot 10^{-3}$	21.1	22	1.23	6.76	44	307
CO_2	22	$1.86 \cdot 10^{-3}$	13.7	33	1.62	3.01	(34)	91
CH_4	10	$6.70 \cdot 10^{-4}$	13.1	28	2.21	1.48	16	53
C_4H_{10}	34	$2.42 \cdot 10^{-3}$	10.8	23	1.86	4.50	(46)	195

Table 3.2: Properties of some gases used in drift detectors. See text for parameters description. Values are given at NTP.

of the total average energy loss per length ΔE and the effective energy W_i needed to produce a single pair[3]. This value sums up both primary ion pairs, produced in

[2]Normal Tempearature and Pressure conditions: 293.15 K, 1 $atm \equiv 1.013$ $bar \equiv 760$ $Torr$.

[3]This value is greater than the ionization potential of the gas since, during the ionization process, part of the energy can be dissipated by excitation of the inner shells of the gas atom.

the collisions of the particle itself, and secondary ion pairs, produced by those primary electrons ejected with energy sufficient to provoce further gas ionizations. Electrons have energies mostly in the range 10-100 eV (the ionization potential of Argon is 15 eV), that means their range in the gas volume is of the order of 10 μm (fig. 3.5); hence ionization electrons can be treated as grouped in clusters localized around the primary ionization points along the particle trajectory.

In tab. 3.2 are listed some useful experimental values. Measurements reported in fig. 3.4(a) suggest that the average number of primary ion pairs (n_p) is roughly proportional to the atomic number of the medium.

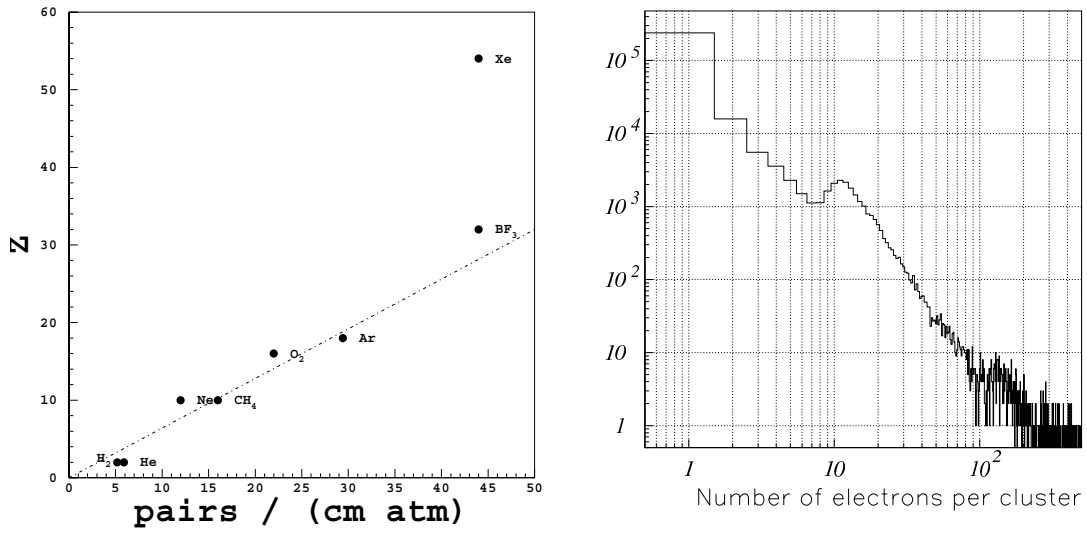

(a) (b)

Figure 3.4: (a) Number of primary ionizing events with rispect to the atomic number of the medium. (b) Electron cluster size distribution for 100 GeV muons in $Ar : CO_2$ (93:7) NTP.

Using the data from tab. 3.2 and the 3.4, the following values can be derived for a $(93 : 7)$ mixture of $Ar : CO_2$ under normal conditions:

$n_{tot} = (2440/26) \times 0.93 + (3010/33) \times 0.07 \simeq 97$ ion pairs/cm,
$n_p = 29.4 \times 0.93 + 34 \times 0.07 \simeq 29.7$ ion pairs/ cm.

The average distance between clusters is therefore of about $1/30\ cm \simeq 300\ \mu m$ and each cluster contains 3 electrons on the average at normal condition. Fig. 3.4(b) shows the cluster size distribution for the same mixture and for 100 GeV muons: the great majority of the collisions release a single electron but a long tail is present as direct

consequence of the Landau tail in the energy loss distribution.

Because of the discrete and statistical nature of the ionization process, the MDT signal generated by a traversing muon shows different maxima, related to the individual clusters (fig. 3.6), in particular for those passing closer to the wire where drift distances difference between track clusters are enhanched.

The effect of the ionization statistics on the particle position measurements will be discussed further in the Chapter.

electron range, δ-electrons Fig. 3.5 shows the average number of electrons emitted above a certain energy threshold in 1 cm of Argon. In the electron energy range 0.1-1 keV the typical value of the cross sections of electons in the gas medium is $10^{-15} - 10^{-16}$ cm^{-2} (fig. 3.8) which implies a mean free path between collision of few microns. Considering also the large mass difference between the target and the projectile the original direction of the emitted electron is randomized after few collisions. Therefore, the actual range travelled by a inization electron cannot be estimated integrating the Bethe-Block formula 3.2. The effective range deduced from measurements

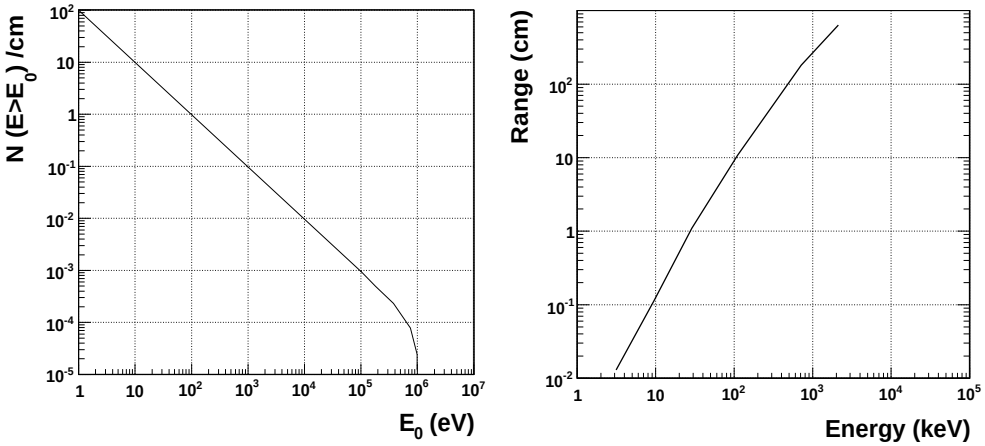

Figure 3.5: *Left*: Number of electrons ejected at an energy $E \geq E_0$, as a function of E_0, in 1 cm of Argon at nominal conditions by a 1 GeV/c proton. *Right*: Range of electrons in Argon, at nominal conditions, as a function of the electron energy itself.

turns out to be indeed two o three order o magnitude smaller. Results are reported in fig. 3.5 for energies above few keV. From the two plots of fig. 3.5 results that a 1 keV electron, which has a range of about 100 μm, is emitted every 10 minimum ionizing particles. Since the average energy loss in Argon is 2.5 keV/cm the further ionization they induce may distorce the center of gravity of the charge produced by the original track. This sets an intrinsic limit in the accuracy on the position achievable with a gas detector of the order of 10 μm. An increase in the gas density do not improve the position accuracy since the reduction in the practical range is compendated by an increase in the number of electron produced at any energy. Electrons emitted with an

energy above few keV are usually called δ-electrons. Due to the higher energy of the incident inizing particle, δ-electrons are emitted almost perpendicularly to the incident track. They represents the small percentage of the ionizing events, corresponding to the Landau distribution tail, a large fraction of the muon energy is transferred to an electron in a single collision and are energetic enough to travel macroscopic distances in the gas and produce a secondary track significatively distinguishable from the original one. On the average, 0.01 electrons per centimeter are emitted, in Argon at normal condition, with energy of 30 keV that means a range of about 1 cm (3.5). A δ-electron can also to be produced in the tube wall. In both cases the secondary track can pass closer to the wire than the original ionizing particle trajectory. The consequence is a reduced reconstruction efficiency.

photons The interaction process depends strongly on the photon energy. Below 1.02 MeV the dominant processes are the photoelectric effect and the Compton scattering (which may occur both in the gas and in the tube wall). Above this value, pair production is the most probable process. If the photoconversion occurs, likely up to 20 keV or so, the whole photon energy is transferred to a single electron. The spatial range is of few millimiters. This means that the MDT signal caused by a low energy photon interaction presents a single peak shaped structure as shown in fig. 3.6.

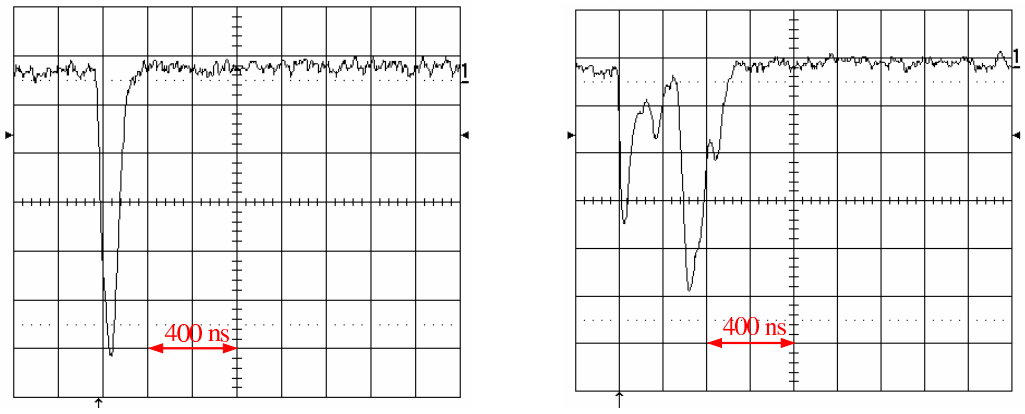

Figure 3.6: *Left*: MDT signal generated by 22 keV photons from a ^{109}Cd source. *Right*: MDT signal generated by a muon.

For a photon energy $E_\gamma \sim 100$ keV, instead, the favourable interaction is the Compton pocess. In this case, the scattered electron has a high probability to receive an energy

$$E_e < E_e^{max} = E_\gamma \cdot \frac{2\gamma}{1+2\gamma}, (\gamma = E_\gamma / m_e c^2)$$

sufficient to traverse the whole tube and ionize the gas originating a signal similar to

the muon (fig. 3.6). Similar considerations can be made for photon interaction in the gamma conversion energy range.

neutrons The products of the neutron interaction in the gas , in the tube wall or in the surrounding material are responsible of the ionization. Three processes are possible, depending on the neutron energy. Neutron capture, most probable for thermal neutrons (up to 100 eV), and conseguence photon emission and interaction. For fast neutrons (1 keV - 10 MeV) the recoil of gas nuclei with its associated inization produces a detectable signal. At higher energies (greater than 100 MeV), charged particles, mainly protons, produces in anelastic neutron collisions are the source of the signal.

3.2.2 Diffusion and Drift

Electrons and ions, produced in the ionization process, quickly loose their energy by multiple collisions with the gas molecules up to the thermal energy $\varepsilon = \frac{3}{2}kT$ ($\simeq 40\ meV$ at the room temperature) being k the Boltzman constant and T the temperature in Kelvin. The energy distribution is given by the Maxwell-Boltzmann function $F(\varepsilon) \propto \sqrt{\varepsilon} \cdot e^{-\varepsilon/kT}$. A point-like cluster, produced at time $t = 0$ in $\vec{r}_0$, in the absence of any external field, starts to diffuse by multiple collisions according to the continuity equation:

$$\frac{\partial n(\vec{r},t)}{\partial t} - D \cdot \nabla^2 n(\vec{r},t) \tag{3.5}$$

where n is the particle density and D is the diffusion coefficient of the gas. Therefore, at the time $t > 0$, the particles are distributed in the space according to a Gaussian with center $\vec{r}_0$ and width

$$\sigma^D = \sqrt{6Dt} \qquad (\sqrt{2Dt} \quad \text{in one dimension}). \tag{3.6}$$

In general, the average mean free path between collisions is

$$\lambda = \frac{1}{N\sigma(\varepsilon)} \tag{3.7}$$

if $\sigma(\varepsilon)$ is the collision cross section and $N = \frac{N_A}{A}\rho$ (N_A: Avogadro constant) is the number of molecules per volume.

If charges are exposed to an electric field $\vec{E}$, a drift motion along the field lines is superimposed over the disordered diffusion motion.

The usual expression for the drift is velocity is

$$\vec{v}_{drift} = \mu \cdot \vec{E}. \tag{3.8}$$

The quantity

$$\mu = \mu(\varepsilon, E, \rho) \tag{3.9}$$

is the charge mobility. The mobility is proportional to the average time between collisions τ (3.16): it depends on the particle energy, hence on the electric field strength $E = |\vec{E}|$ also, it is directly proportional to the mean free path (3.14) thus inversely proportional to the gas density; the scaling

$$\mu(\rho) = \mu(\rho_0)\, \rho_0/\rho \tag{3.10}$$

holds between the values at the two different densities ρ_0 and ρ.

If also a magnetic field $\vec{B}$ is present (as it happens when particle momentum measurements is required) the drift velocity follows the line of the force $\vec{F} = e(\vec{E} + \vec{v}_{drift} \times \vec{B})$ and the angle between $\vec{v}_{drift}$ and $\vec{B}$ is called *Lorentz angle*.

For particles diffusing with thermal energy, the following relation exists between the mobility and the diffusion coefficients (Nernst-Townsend formula):

$$\frac{D}{\mu} = \frac{kT}{e}. \tag{3.11}$$

From 3.6, 3.8 and 3.11 results that the diffusion width of thermal ions and electrons, over a distance $L = v_{drift} \cdot t$, is independent on the nature of the ion and the gas (thermal limit):

$$\sigma^D = \sqrt{\frac{2kTL}{eE}}. \tag{3.12}$$

The microscopic picture

A simple microscopic model of the particle motion in the gas can be formulated. Between two collisions the drift velocity $\vec{v}_{drift}$ of a particle with charge e and mass m is the sum of the random thermal velocity $\vec{v}_r$, the component $\vec{v}_d$ acquired, in the drift (field) direction, since the previous scattering, and the velocity $\vec{v}_E(t)$ due to the electric field $\vec{E}$ acceleration during the time t:

$$\vec{v}_{drift} = \vec{v}_r + \vec{v}_d + \vec{v}_E = \vec{v}_r + \vec{v}_d + \frac{e}{m}\vec{E}\, t. \tag{3.13}$$

It is assumed $t \leq \tau$ where τ is the average time between collisions:

$$\tau = \frac{\lambda}{v_{rel}} = \frac{1}{N\sigma\, v_{rel}}. \tag{3.14}$$

The quantity v_{rel} is the average relative velocity of the drifting particle and the gas particles in the laboratory frame.

The random thermal contribution $\vec{v}_r$ vanishes once averaged over angles (i.e. over many collisons) and can be neglected. If E is fixed, an equilibrium condition is reached

when the momentum gained between two encounters is lost in the next collision. The equilibrium condition is

$$m\,\vec{v_E}(\tau) = f_p\, m\,(\vec{v}_d + \vec{v}_E(\tau)). \tag{3.15}$$

The quantities in 3.15 are assumed averaged over many collisons. The factor f_p is the average fractional momentum loss in the scattering in the field direction Form 3.13, 3.15 results:

$$\vec{v}_{drift} = \vec{v}_d + \vec{v}_E = \vec{v}_E \frac{1-f_p}{f_p} + \vec{v}_E = \frac{\vec{v}_E}{f_p} = \frac{e}{m}\,\tau\,\frac{1}{f_p}\cdot\vec{E}. \tag{3.16}$$

This relation justifies the expression 3.8.

Deriving an explicit expression for the relative velocity v_{rel} in the 3.14, the mobility depends on the energy through the scattering cross section σ only. The total energy of a particle moving with instantaneous velocity v is made up of the thermal energy and the energy received from the electric field (ε_E):

$$\varepsilon = \frac{1}{2}mv^2 = \frac{3}{2}kT + \varepsilon_E. \tag{3.17}$$

Two limiting cases can be distinguished according to the field strength.

- Low field limit: $\varepsilon_E << 3/2\,kT$.

  In this case both the gas molecules velocity v_{gas} and the drifting particle velocity v are comparable and the relative velocity can be calculated by the equipartition of energy

  $$v_{rel}^2 =< |\vec{v} - \vec{v}_{gas}| >^2 = v^2 + v_{gas}^2 = 3kT\left(\frac{1}{m} + \frac{1}{M}\right) = 3kT/m^* \tag{3.18}$$

  where M is the mass of the molecules of the media and

  $$m^* = \left(\frac{1}{m} + \frac{1}{M}\right)^{-1} \tag{3.19}$$

  is the reduce mass of the two colliding bodies.

  The scattering can be considered elastic in the energy range considered.

  The factor f_p has the following (non relativistic) expression in case of elastic scattering:

  $$f_p = \frac{M}{M+m}\,(1 - \overline{cos\,\theta}) = \frac{m^*}{m}\,(1 - \overline{cos\,\theta}) \tag{3.20}$$

  (θ is the scattering angle). In the following the scattering will be assumed isotropic: $\overline{cos\,\theta} = 0$ (which is a good approximation for electrons but not always for ions especially at high momenta). Using 3.14, 3.16 and 3.20:

  $$v_{drift} = \frac{e}{m^*}\,\tau\cdot E = \left(\frac{1}{m^*}\right)^{\frac{1}{2}}\left(\frac{1}{3kT}\right)^{\frac{1}{2}}\frac{e}{N\sigma}\cdot E. \tag{3.21}$$

  It follows that mobility is rather constant in the low field limit (fig. 3.7).

- High field limit: $\varepsilon_E >> 3/2kT$. In this case $\varepsilon \simeq \varepsilon_E$ and $v_{rel} \simeq v$. The velocity v reaches the equilibrium value when the energy acquired from the field E between two encounters is lost in the next collision:

$$eE \cdot v\tau = f_E\,\varepsilon = f_E\,\frac{1}{2}mv^2 \tag{3.22}$$

where f_E is the fraction of the total energy ceded to the gas. From 3.16 and 3.22:

$$v^2_{drift} = \frac{e}{m^* N\sigma}\left(\frac{1}{2}\frac{f_E}{f_p}\right)^{\frac{1}{2}} \cdot E. \tag{3.23}$$

It follows that mobility is approximatively proportional to $1/\sqrt{E}$ in the high field limit (fig. 3.7).

____ * ____

It can be demonstrated that the mean displacement σ_D in one direction after a large number $n = t/\tau$ of isotropic scatterings is given by

$$\sigma^2_D = n\,\frac{2}{3}\lambda^2 = \frac{2}{3}\frac{\lambda^2}{\tau}\,t. \tag{3.24}$$

From comparison to 3.6, D the coefficient D is the part proportional to $2t$:

$$D = \frac{\lambda^2}{3\tau} = \frac{v^2_{rel}}{3}\,\tau. \tag{3.25}$$

For particles diffusing with thermal energy, relations 3.18 and 3.21 can be used, and the 3.25 becomes $D = kT/e\,\mu$ which is the 3.11.

Ions

Measured values for the mean free path, velocity, and diffusion coefficient of several ions are listed in tab. 3.3.

gas	$\lambda(cm)$	v (cm/s)	D (cm$^2/s$)
H_2	1.8×10^{-5}	2.0×10^5	0.34
He	2.8×10^{-5}	1.4×10^5	0.26
Ar	1.0×10^{-5}	4.4×10^4	0.04
O_2	1.0×10^{-5}	5.0×10^4	0.06
H_2O	1.0×10^{-5}	7.1×10^4	0.02

Table 3.3: *Mean free path, velocity and diffusion coefficient for ions in their parent gas (normal conditions).*

For electric field strength normally used for drift chambers the ion mobility is almost independent on the electric field. As shown in fig. 3.7, Argon mobility is constant up

to values of the reduced electric field $E/p \sim 20\,V/(cm\,Torr)$([4]) that means up to a distance $\sim 100\,\mu m$ from the wire at the nominal MDT voltage. In fact, a great fraction of the energy aquired by the ions on a mean free path, is lost in the collision with the gas molecules because of the small mass difference. Therefore their energy remains almost thermal and only a small fraction is due to the field. For a mixture of n different gases, the mobility μ_i of the ion i is given by (Blanc's law):

$$\frac{1}{\mu_i} = \sum_{k=1}^{n} \frac{c_k}{\mu_{ik}}, \tag{3.26}$$

where c_k is the concentration by volume of the gas k and μ_{ik} is the mobility of the ion i in the gas k. Measured mobilities of different ions in their own gas or in a different one can be found in tab. 3.4.

If different type of ions are present, those with higher ionization potentials are neutralised after 10^2-10^3 collisions by the capture of electrons from atoms with lower ionization potentials. Mean free paths are of the order of 10^{-5} cm, only one kind of ions is thus left after a drift length of about $5 \cdot 10^{-2}/k$ cm if k is the percentage of the lowest ionization potential molecules.

Gas	Ion	Mobility $(cm^2V^{-1}s^{-1})$
He	He^+	10.42
Ne	Ne^+	4.10
Ar	Ar^+	1.53
Kr	Kr^+	0.96
Xe	Xe^+	0.57
CO_2	$[CO_2]^+$	1.09
CH_4	$[CH_4]^+$	2.26
Ar	$[CO_2]^+$	1.72
Ar	$[CH_4]^+$	1.87

Table 3.4: Measured mobilities for different ions (normal conditions).

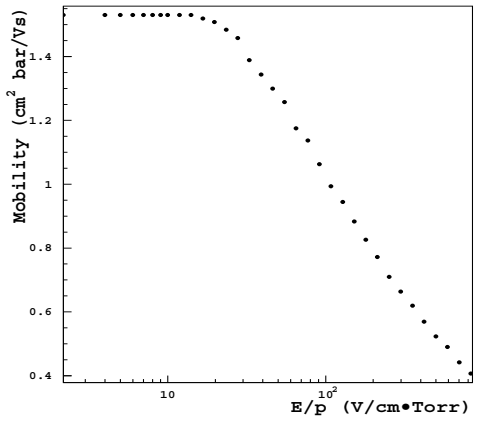

Figure 3.7: Mobility for Ar^+ ions in Ar with respect to the reduced electric field E/p.

Electrons

In an electric field, electrons can gain much more energy between two collisions compared to ions because they are lighter and they have a longer mean free path. Moreover, the small mass implies that they lose less energy when colliding elastically with the gas molecules. For these reasons electrons can reach random energies several orders of

[4]The equivalent field at 1 atm is obtained by multiplying by 760.

magnitude higher than the thermal one. In a simplified model the drift velocity can be written as

$$v_{drift} = \frac{e}{2m_e} E\tau, \tag{3.27}$$

where $\tau(E, \varepsilon)$ is the average time between collisions. The collision cross section and, on the consequence τ, depends critically on the electron energy and the electric field. In fact, electron energy can easily pass the threshold of inelastic excitation of the gas molecules; in this case, the drift velocity (the mobility) becomes a function of the energy loss associated with such process.

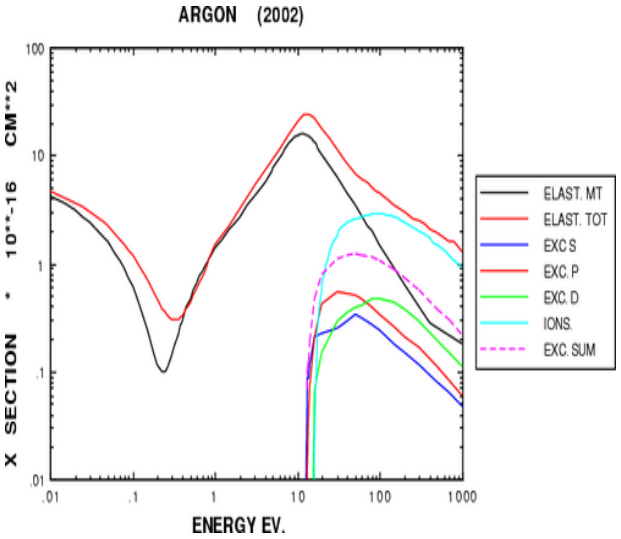

Figure 3.8: Collision cross section for electrons in Argon as function of the energy.

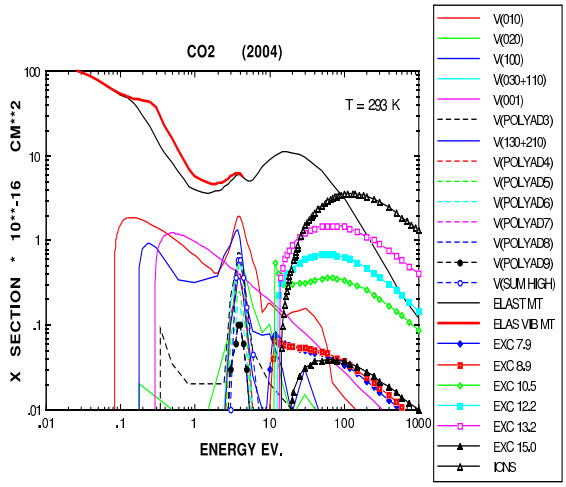

Figure 3.9: Collision cross section for electrons in CO_2.

A characteristic phenomenon which may occour for electrons in the eV range is the Ramsauer effect. At these energies electrons wavelength are comparable to bound electron orbits in the molecules of the gas and quantum mechanical effects arise which make the atoms nearly 'transparent' to electrons, i.e. leads to a minimun in the collision cross section. An example of this behaviour is given by the cross section of electrons in Argon (fig. 3.8). The energy distribution will favour those energies for which the interaction cross section is lower. An increase in the energy in fact implies an increase in the probability of scattering with the subsequent energy loss. This tends to keep electron energy close to the cross section minimum. This effect leads to a saturation of the drift velocity which remains almost constant with increasing electric field (fig. 3.10 for pure Argon).

The major consequence of the sensitive dependece of the cross section on the energy is that drift velocity can vary cosiderably with small changes in the gas composition since one gas may have a large scattering cross section where another has a minimum. This happens for example for mixture of Argon with polyatomic gases. In fig. 3.9 is shown the cross section for carbon dioxide. Figure 3.10 instead shows some examples

of drift velocity versus the electric field for different gases and compositions.

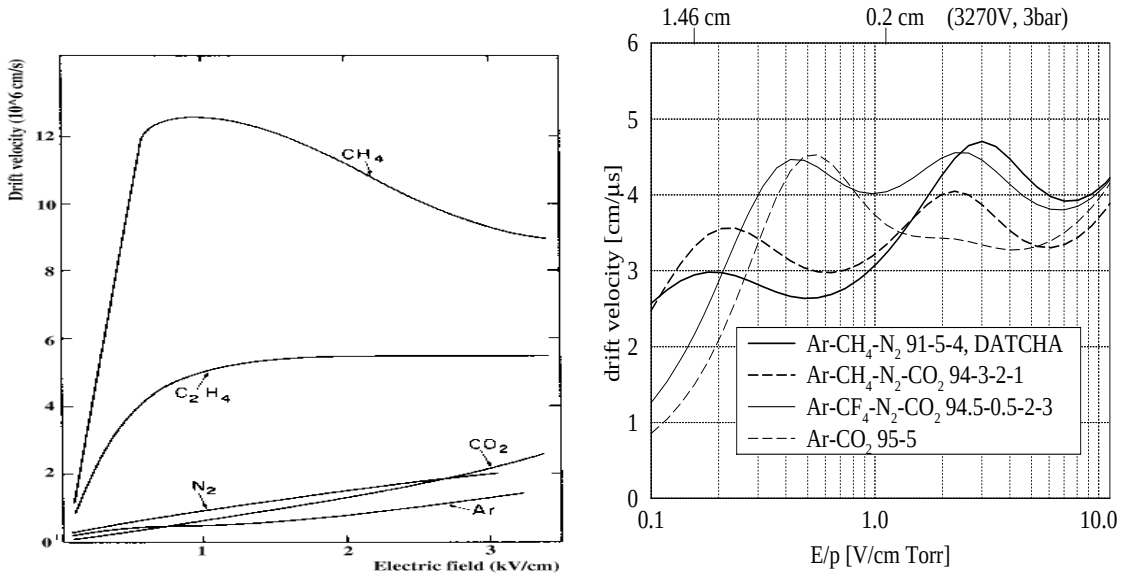

Figure 3.10: Drift velocity for several gases.

Drift velocities of the order of 10^6 cm/s can be attained before saturation sets in. On the average, the electrons drift velocity is three order of magnitude higher than the ions velocity.

3.2.3 Ionization amplification. Gain

While drifting towards the anode, electrons gain more and more energy between two consecutive collisions due to the increasing electric field strength. When their kinetic energy is such to cause gas ionization an avalanche multiplication process sets in.

If α is defined as the average number of electron-ion pairs produced per unit length ($\alpha = N_p\sigma_i$ if N_p is the number of molecules per unit volume and σ_i the inization cross section for electrons), a given number N of pairs is then augmented to $N + dN$ over the length dr where

$$dN = \alpha \cdot N \cdot dr. \tag{3.28}$$

For a given gas mixture, the coefficient α (first Townsend coefficient) depends strongly on the electric field and gas density. The final number N of electrons in the avalanche is obtained by integrating 3.28 between the point $r{=}r_0$ where the multiplication starts (and N_0 electron-ion pairs are present) and the wire surface ($r{=}a$):

$$N = N_0\, e^{\int_{r_0}^{a} \alpha(E(r))\, dr} = N_0\, e^{\int_{E(r_0)}^{E(a)} \alpha(E)\, \frac{dr}{dE}\, dE}. \tag{3.29}$$

The quantity $G = N/N_0$ is usually called *gain* and represents the amplification factor of the drift tube.

Because of the nature of the underlying phenomena involved, the amplification is a statistical process. Fluctuations $g = G/\bar{G}$ around the mean value $\bar{G}$ (given by the 3.29) are well described, for a cylindrical geometry, by a Polya distribution:

$$f(g) \propto g^{\Theta} \cdot e^{-(\Theta+1)\,g}. \tag{3.30}$$

The parameter Θ ($0 < \Theta < 1$) is related to the fraction of electrons whose energy exceeds a threshold energy for ionization and depends on the gas properties and on the field geometry [27].

Equation 3.29 can be integrated assuming α to be proportional to the electric field. Measurements state this is a good approximation for heavy noble gases between 10^3 and 10^4 V/cm, a typical range for drift detectors near thin wires. The result is (Diethorn's formula):

$$G = \left[\frac{E(a)}{E_{min}(\rho)}\right]^{\frac{ln2 \cdot a \cdot E(a)}{\Delta V}}. \tag{3.31}$$

The minimum field E_{min} at which the multiplication can start is given by the ratio of the energy required to ionize the molecules of the media to the mean free path between collisions. Therefore E_{min} is proportional to the gas density ($E_{min} = E_{min}(\rho_0)\,\rho/\rho_0$ if $E_{min}(\rho_0)$ is the value given a the density ρ_0). The quantity $e\,\Delta V$, instead, is the average energy required to liberate an electron in the gas. The field at the wire surface ($E(a)$) can be calculated from the 3.1.

Gain measurements for different values of the applied voltage are shown in 3.11 for several Ar:CO_2 mixture at 3 bar [26]. For the 93:7 choice, aperated at 3080 V, the gain is about $2 \cdot 10^4$. Fits to the measured points give the following values of the Diethorn parameters:

$$\Delta V = 34\,V,\ E_{min} = 24\,kV/cm$$

for ρ_0 at 1 *bar* and 295 K (errors are about 10%). From the E_{min} value and the 3.1 results that $r_0 \simeq 200\,\mu m$.

Mode of operation

In 1 cm of Argon at NTP about 100 electrons are released by a minimum ionizing particle. A signal consisting of such a little amount of charge is impossible to detect since the electronic read-out noise is orders of magnitude higher (Sec. 3.3.2). Hence ionization amplification is necessary. In order to be useful, however, field geometry must be cosidered also. If, for example, the electric field is uniform between cathodes, the detected signal will depend on the avalanche length. For events with the same energy deposit, the signal amplitude will then vary with position and proportionality between energy and signal amplitude is lost. Moreover, spark break down rate would

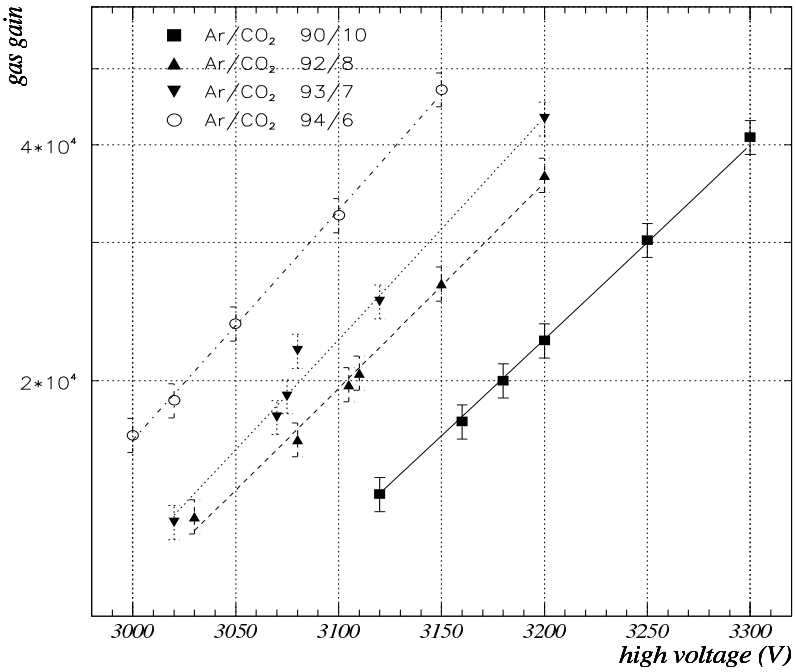

Figure 3.11: Gas gain for different $Ar : CO_2$ mixtures.

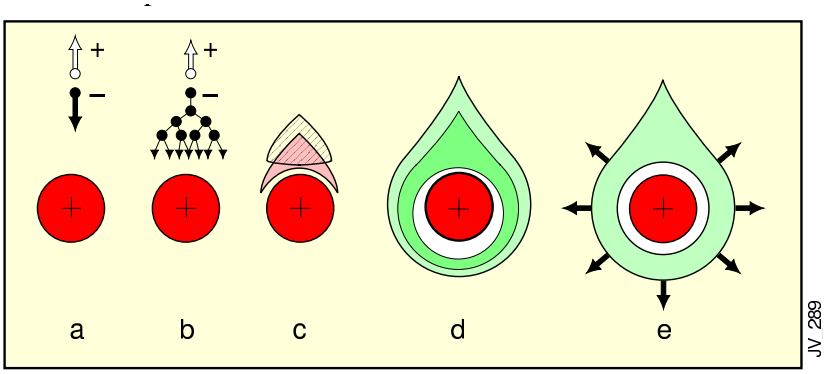

Figure 3.12: Avalanche development steps. Ions separate from electrons as the avalanche approches the anode. The drop-like shape surrounding the wire is due to lateral diffusion.

be very high along the whole drift path making the detector operation stable only for low value of the gain.

These limitations are overcome in a cylindrical geometry where the electric field, thanks to the $1/r$ dependence, is relatively weak along the drift path besides close to the wire surface. Electrons produced in the primary ionization simply drift along the field lines until the proximity of the anode (typically few wire radii) where the condition for the avalanche to start is met. Fig. 3.12 illustrates the time development

of the avalanche. Gain as high as 10^5 can be achieved with this kind of detectors before proportionality is lost. The maximun value depends strongly on the gas used.

3.2.4 Development of the signal

The signal on the elctrodes is induced by the movement of the charges.

Considering an electron drift velocity of 5 $cm/\mu s$ and that the drift path of the electron avalanche is only as big as the amplification zone ($\sim$ 100 μm), the whole multiplication process lasts few nanoseconds. Therefore electrons induce a very short signal and the size and time development of the whole signal is determined mostly by the ion drift.

If the anode is kept at the constant potential V, the current signal I induced on an electrode by a carge q in $\vec{r}(t)$ moving with velocity $\vec{v}(\vec{r})$ in the field $\vec{E}(\vec{r})$ can be conveniently calculated using the Ramo's theorem [23]:

$$I(\vec{r}(t)) = -\frac{q}{V} \cdot \vec{v} \cdot \vec{E}. \tag{3.32}$$

With $\vec{E} = \frac{V}{ln(b/a)} \frac{1}{r} \hat{r}$ and $\vec{v} = \mu \vec{E}$, 3.32 becomes

$$I(r) = \frac{qV\mu}{(ln\frac{b}{a})^2} \cdot \frac{1}{r^2}. \tag{3.33}$$

The ion mobility can be assumed to be constant outside the avalanche region (Sec. 3.2.2). In this approximation, if the ion is produced at the distance r_0 from the wire, the time it takes to move from r_0 to r is

$$t(r) = \int_{r_0}^{r} \frac{dr'}{v(r')} = \frac{ln(b/a)}{\mu V} \int_{r_0}^{r} r'\, dr' = \frac{1}{2} \frac{ln(b/a)}{\mu V} \cdot (r^2 - r_0^2). \tag{3.34}$$

from which follows

$$r^2(t) = \frac{2\mu V}{ln(b/a)}(t + t_0), \qquad t_0 = \frac{r_0^2}{2\mu V} ln(b/a). \tag{3.35}$$

The time t_{max} needed to reach the tube wall is then

$$t_{max} = t(b) = \frac{ln(b/a)}{2\,\mu V}(b^2 - r_0^2). \tag{3.36}$$

Substituting 3.35 in 3.33:

$$I(t) = \frac{q}{2ln(b/a)} \cdot \frac{1}{t + t_0}, \qquad 0 \le t \le t_{max}. \tag{3.37}$$

The current induced by a single ionization cluster of n_p electrons, in the approximation that the whole charge multiplication occurs at the point r_0 is obtained setting

$$q = e\, n_p\, G. \tag{3.38}$$

Assuming $\mu \simeq 1.53\ cm^2/(Vs)$, $a = 25\,\mu m$, $b = 1.46\,cm$, $V = 3080\ V$, q=e=1.61 $\times$ $10^{-19}\ C$; $G = 2 \cdot 10^4$ and $n_p = 3$, $r_0 \simeq 70\ \mu m$ for Argon at 3 bar results that:

$$t_0 \simeq 30\,ns,\ \ t_{max} \simeq 1.3\,ms \text{ and } I(0) \simeq 0.26\,\mu A. \tag{3.39}$$

The 3.37 implies that the rise of the voltage signal $V(t)$ is very fast:

$$V(t) \propto \int I\,dt \propto ln\left(1 + \frac{t}{t_0}\right). \tag{3.40}$$

This can be seen also from the espression of the fraction of the total charge integrated over the time t:

$$\frac{Q(t)}{Q(t_{max})} = \frac{\int_{t_0}^{t} I(t')\,dt'}{\int_{t_0}^{t_{max}} I(t')\,dt'} = \frac{\ln\left(1 + \frac{t}{t_0}\right)}{\ln\left(1 + \frac{t_{max}}{t_0}\right)}. \tag{3.41}$$

Using the values in 3.39, it can be estimated that half of the total charge is integrated already after a time $t \simeq 6\,\mu s \simeq 5 \cdot 10^{-3}\,t_{max}$. According to the t_0 definition the fraction increases with decreasing anode wire radius.

3.2.5 Gas mixtures

One of the basic properties of a detector gas mixture is the stability of the operation at high gain and low voltage.

The principal component of a desirable gas is usually a noble gas such as Argon. Noble gases allow multiplication at relatively low electric fields. In fact they do not have molecules: this means that electrons are easily accelerated as they mostly undergo elastic collisions with little loss of energy, and that the inelastic collisions are dominated by ionization rather than excitation processes. Moreover electrons can easily be absorbed in complex molecules.

Argon is usually preferred since it gives more primary ionisation than He or Ne and is more affordable than Kr or Xe.

A gas detector filled with a noble gas only, however, does not allow stable operation. During the avalanche process many Ar atoms are excited and decay emitting UV photons (e.g. with an energy of 11.6 eV). These photons can strike the cathode (Aluminium has a ionisation threshold of 6 eV) and eject photoelectrons which give rise to another avalanche. There is therefore a positive feedback and a continuous discharge sets in. A chamber filled with pure Ar suffers from such breakdown at relatively low gain. Some kind of gases can be added in order to *quench* the secondary avalanches. Polyatomic gases have many non-radiative vibrational and rotational excited states over a wide energy range. If a chamber contains a fraction of such a gas, its molecules will absorb energy from excited Argon atoms by colliding with them or by dissociating into smaller molecules. Since $\sigma_{emission} << \sigma_{collision}$ the UV photon emission is eliminated or quenched. The presence of a quenching gas can allow an enormous increase in stable

gain achievable. Carbon dioxide (CO_2) Isobutane (C_4H_{10}), methane (CH_4) as well as many hydrocarbons and alcohols belong to this type of gases.

Symptoms of an imperfect quenching is, for example, the presence of spurious signal pulses at $t \simeq t_{max}$ (after pulsing) with the consequent increase of the dead time and resolution reduction.

3.3 Electronics

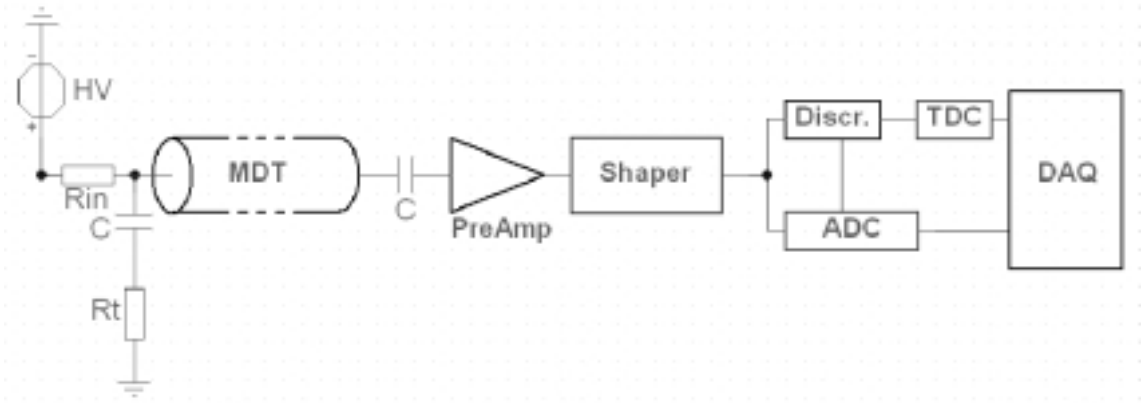

Figure 3.13: MDT electronics scheme.

Fig 3.13 shows a schematic view of the electronics of an MDT. On one side of the tube (HV side) the high voltage is provided to the anode wire while the tube wall is grounded. The current signal is read at the other side of the tube (RO side), amplified, shaped and then presented to a discriminator. The logical output signal of the discriminator is sent to a TDC which measures the time difference between the pulse and the signal provided by an external trigger. An ADC chip integrates the discriminated signal over a defined time window (*gate*). Such a circuit allows drift time measuments in fact, if the pulse comes from a triggering muon then the TDC time is equal to the drift time plus a constant due to signal propagation time in the electronics. The TDC information can be used for position measurements as discussed further.

As reported at the end of the Sec. 3.2.4 the signal induced in the tube is characterised by a very short rise time. Atlas MDT are used for precise position mesurements, therefore, high timing resolution is required. This means that the relevant information is mostly contained in the early portion of the pulse. It is not convenient either to use the entire signal since it will introduce events pile-up effects and a large dead time in the read-out chain reducing the high event rate capability of the system. The long signal tail is shorten by means of a double differentiator circuit (the shaper module in the figure) which attenuates the low frequency components.

In the next pragraphs the various steps involved in the signal processing are descibed in more detail.

3.3.1 The tube circuit

A simple model of an MDT tube, including also the High Voltage (HV) distribution and part of the on-chamber read-out electronics, is shown in figure 3.14. The resistor

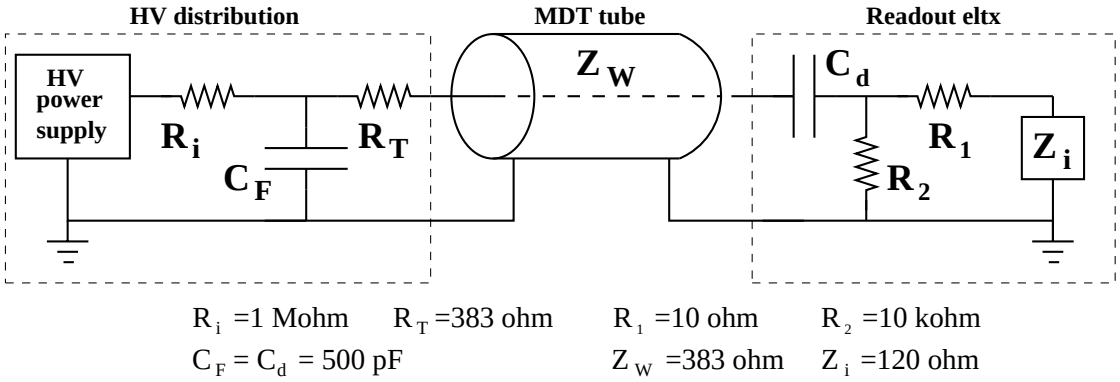

Figure 3.14: A simple model of the tube. The HV distribution and part of the on-chamber read-out electronics is also drawn.

R_i=1 $M\Omega$ is the HV protection resistor it limits the current in case of breakdown. The capacitor C_F=500 pF is a filter connected to ground which minimizes the HV induced noise. R_T=383 Ω is the termination resistor, equal to the tube impedance in order to avoid signal reflections. C_d = 500 pF is the HV decoupling capacitor, R_2=10 $k\Omega$ is a protection resistor, on the read-out side, Z_i=120Ω is the input impedance of the amplifier. The tube characteristic impedance is $Z \simeq \sqrt{L/C}$=380 Ω, where L=$\frac{\mu}{2\pi} ln(b/a)$ and C=$\frac{2\pi\epsilon}{ln(b/a)}$ are the capacitance and the inductance per unit length (for gases ϵ=ϵ_0 and μ=μ_0).

The voltage at the output of the front-end electronics is shown in figure 3.15(b) [31].

3.3.2 Read-out

The full read-out chain is made in three different steps:

1. Amplification, shaping and discrimination of the tube signal.
2. Time to digital conversion and charge to digital convertion.
3. Electronics initialization and chamber data collection.

The first two steps are performed by two different chips (ASD [31] and AMT [32]) both mounted on a front-end board (*mezzanine*) which is connected to the tubes via a two

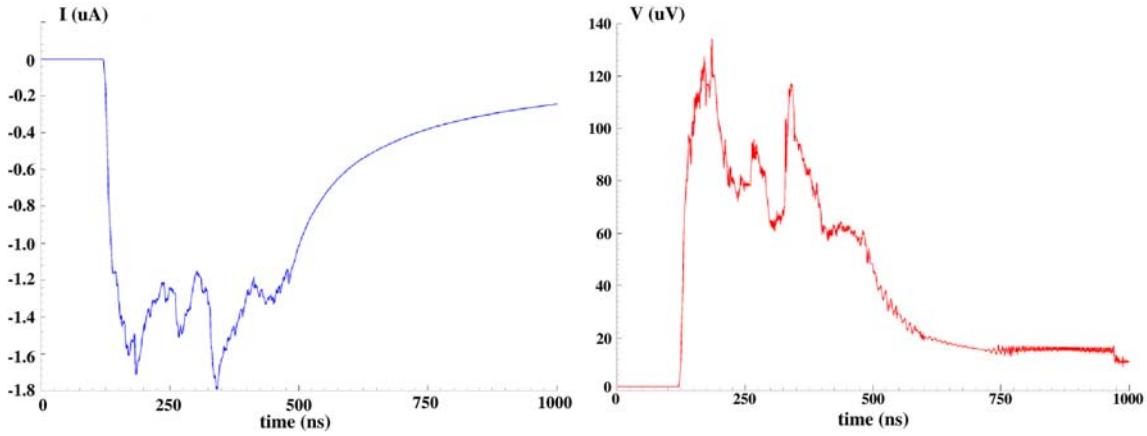

(a) Current (μA) induced on an MDT wire as seen at the tube signal pin.

(b) Voltage signal (μV) induced at the amplifier input.

Figure 3.15: Current and voltage signal induced by a charged particle at the input of the read-out electronics.

layer printed circuit board (the "hedgehog") which is mounted directly onto the ends of the tubes. The hedgehog couples the electronics capacitively to the wires and provides a discharge protection for the amplifier input. For a MDT of the type BIL, for example, 6×4 tubes, 6 in each of the 4 layers of a multilayer, are read out-via one hedgehog and

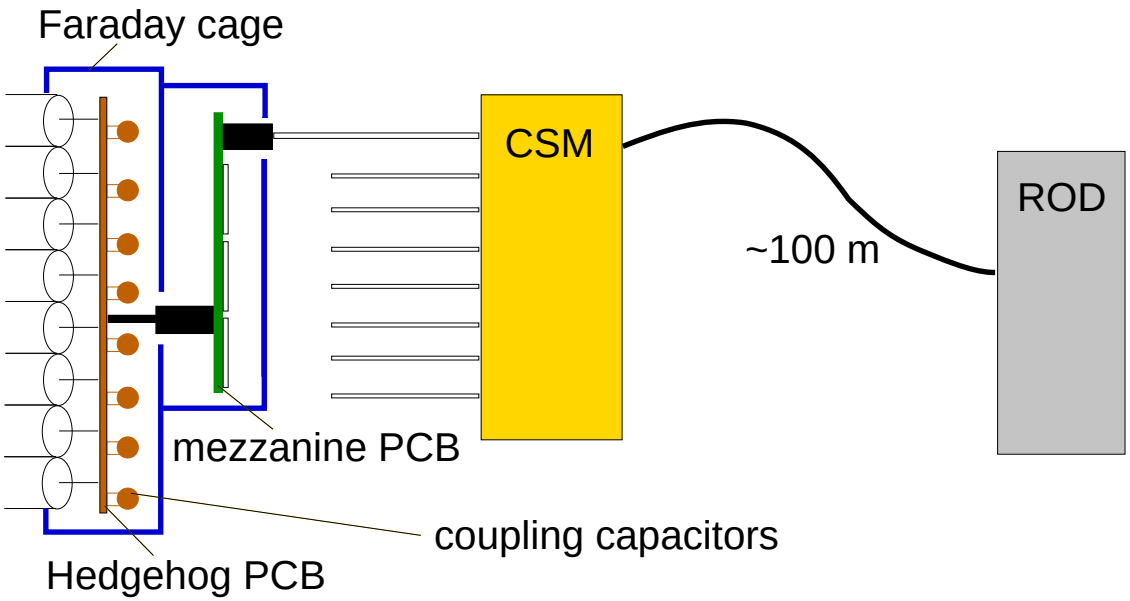

Figure 3.16: Scheme of the MDT read-out system.

one mezzanine board. The high voltage is connected to the tubes via different hedgehog boards at the opposite end of the tubes. Both ends of each multilayer are enclosed by a Faraday cage. The different mezzanines of each chamber are then read by the CSM (Chamber Service Module) which is a board mounted directly on the chamber. The CSM provides the interface between the on-chamber read out electronics and the Data Acquisition System (DAQ). In the ATLAS detector, the data will be delivered from the CSM by about 100 m long optical fibres to the Readout Driver modules (ROD). A scheme of the read out layout id shown in fig. 3.16

The ROD board performs both data collection and initialization of the parameters of the ASD and AMT chips. A description of the read-out chain and of the software used for this purpose is given in Chapter 4.

A block diagram of the ASD (Amplifier, Shaper, Discriminator) chip is given in fig. 3.17 while in tab. 3.5 the most relevant analog specification of the ASD are given.

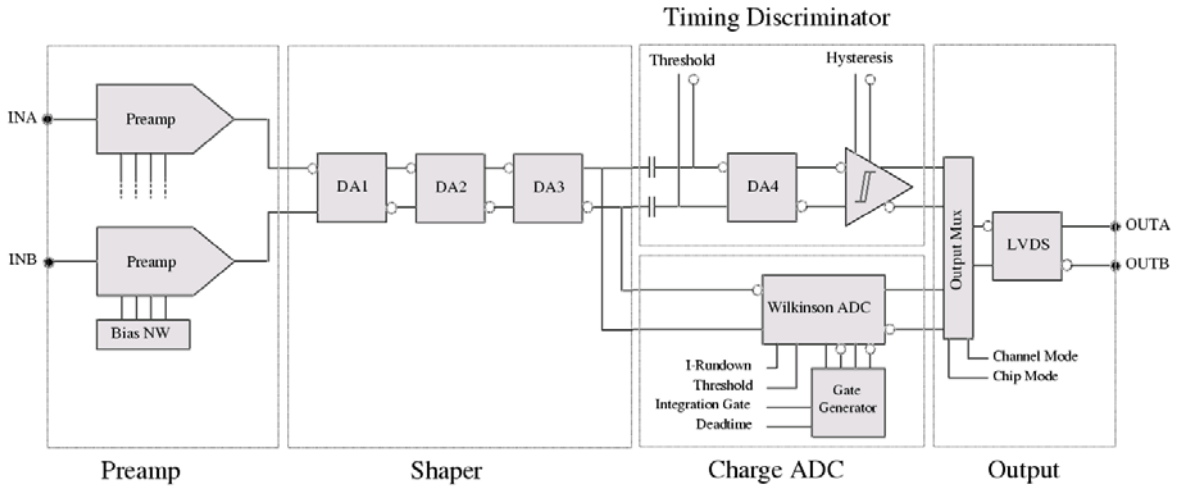

Figure 3.17: Block diagram of the ASD chip.

Each tube is connected to a preamplifier (a second preamplifier is inserted to provide DC balance for the subsequent stages and a common-mode rejection of noise). The amplified signal is sent to a series of three differential amplifiers (DA1, DA2, DA3) that provide signal gain and implement bipolar shaping. Bipolar shaping was chosen to prevent baseline shifts caused by the foreseen high ionization level.

Input impedance	$Z_I = 120\ \Omega$
Noise	ENC=6000 e r.m.s.
Shaping function	bipolar
Shaper peaking time	$\tau_s = 15\ ns$
Sensitivity at shaper output	12 mV/fC (delta pulse into terminated MDT)

Table 3.5: ASD analog specifications.

The output of the shaper is split and sent to an ADC and to a discriminator. The ADC integrates the signal in a given time gate and stores the charge in a capacitor that is then discharged with a constant "run down" current. The discharge time is proportional to the pulse charge. The leading edge timing and the pulse width are read and converted into digital data by the AMT TDC.

The signal is also sent to a discriminator which commutes when the signal is higher than a programmable threshold to measure the leading edge of the signal. A useful way to parametrize the threshold of the discriminator is in term of number of primary electrons N_{thr}. Converting N_{thr} in the value of the voltage requires the knowledge of the amplifier response as a function of frequency. The response function is the output of the device when the input is a current signal $q\delta(t)$. For the ASD it is 12 mV/fC (tab. 3.5). As the amplifier has a limited bandwidth, the response function is a curve with a finite rise time τ_s (*peaking time*) of about 15 ns. For an input current given by 3.37 the corresponding sampled charge is

$$Q(\tau_s) = \int_{t_0}^{\tau_s} I(t')\, dt' = \frac{eN_{thr}G}{2ln\frac{b}{a}} ln\left(1 + \frac{\tau_s}{t_0}\right) = eN_{thr}Gf(\tau_s) \tag{3.42}$$

where G is the gas gain and $f(\tau_s)$=0.031 (for t_0=30 ns, see 3.39). For a gas gain of $2{\cdot}10^4$ we have Q=0.25 fC (3 mV signal) per primary electron.

The value of the threshold N_{thr} has to be fixed taking into account the electronic noise which can be expressed in terms of ENC (Equivalent Noise Charge) for a direct comparison with the signal. ENC is the amplitude, expressed in equivalent electrons, of a signal equal to the r.m.s of the electronic noise. In the ASD the noise level is 6000 electrons (tab. 3.5). In order to have the amplitude of ionization signals larger than the noise,

$$N_{thr}Gf(\tau_s) > ENC \tag{3.43}$$

must hold for a given threshold. This expression relates threshold and gas gain; the choice of their value will be discussed in the next Chapter. .

In the final stage of the ASD chip, the signals are sent to an LVDS cell that converts them into external low level signals. These signals are then sent to the AMT TDC chip which is also mounted on the mezzanine board.

A simulation of the signal in the different stages is shown in figure 3.18 [31].

In fig. 3.18(a) the output of the pre-amplifier is shown while in fig. 3.18(b) the bipolar output of the shaping system is shown. In fig. 3.18(c) a threshold of 60 mV has been applied. In figure 3.18(d) the final signal and the discriminator output is shown.

The AMT TDC chip is a 24 channel programmable TDC. All detector front end electronics is clocked at the LHC frequency of 40 MHz; as the TDC works with a 5-bit interpolator, the least count is 25/32=0.78125 ns. This TDC measures the starting time of the signal with respect to an external trigger received through the CSM; the width of the signal can be measured as it can also be related to the charge collected by the ASD.

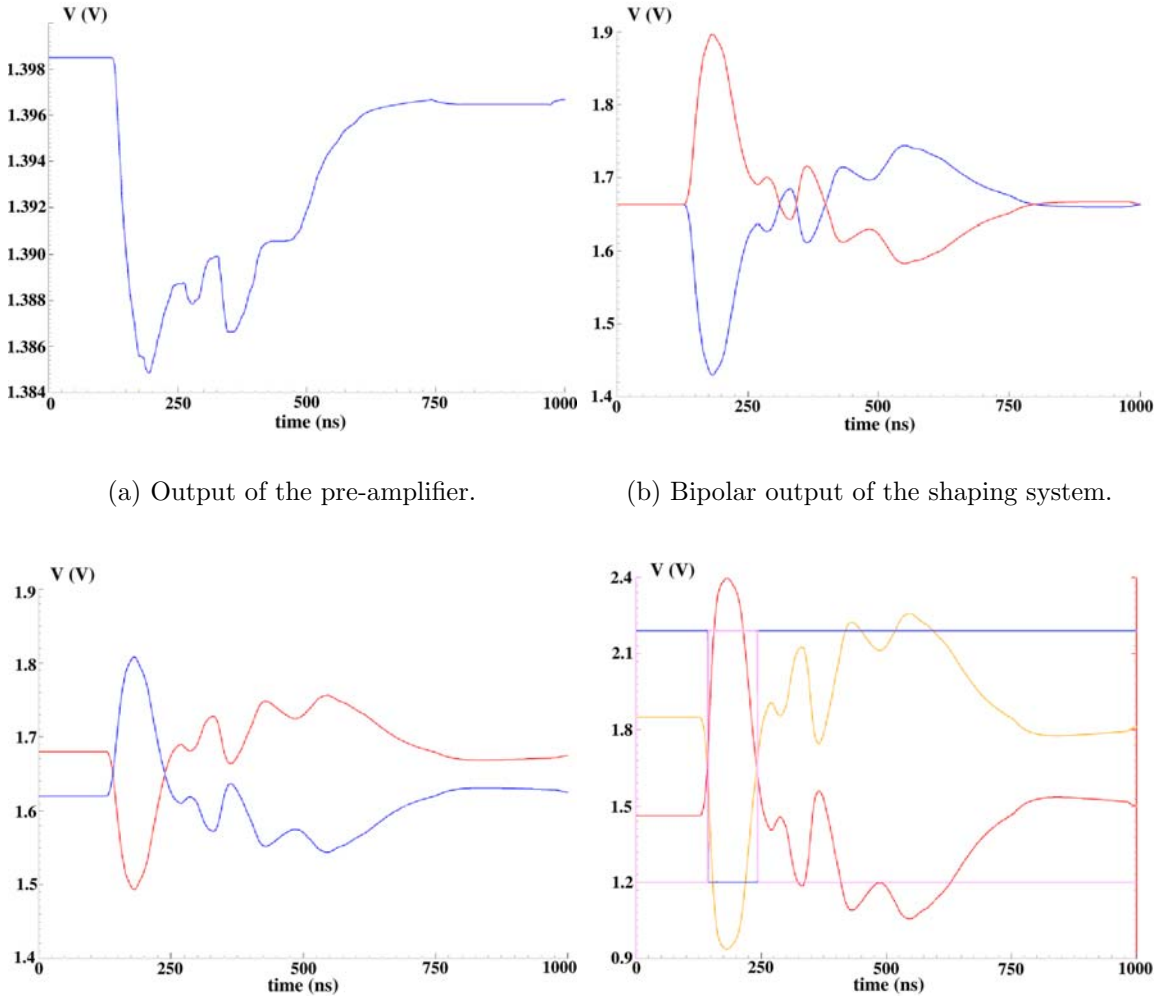

(a) Output of the pre-amplifier.

(b) Bipolar output of the shaping system.

(c) Bipolar signal with a 60 mV threshold applied.

(d) Final signal and discriminator output.

Figure 3.18: Simulation of the signal in the different stages of the ASD chip.

Further information about the ADC and TDC operation will be given in in the chapter 4.

3.4 Background environment

The enormous rate of proton-proton collisions at the Large Hadron Collider (10^9 collisions per second) is one of the major challenges for the LHC experiments. The large amount of particles produced at the interaction point makes the wire aging, radiation damage, activation of detector parts, and radiation-induced backgrounds in the

detector a major concern and has a critical impact on the design of the whole system.

The expected background condition defines parameters such as the rate capability of single tubes and the aging properties, granularity and redundancy of the trigger logic, the pattern recognition efficiency, and are an important input for the choice of the baseline gas and the front-end electronics [34].

The background sources in the Muon Spectrometer can be classified into two main categories:

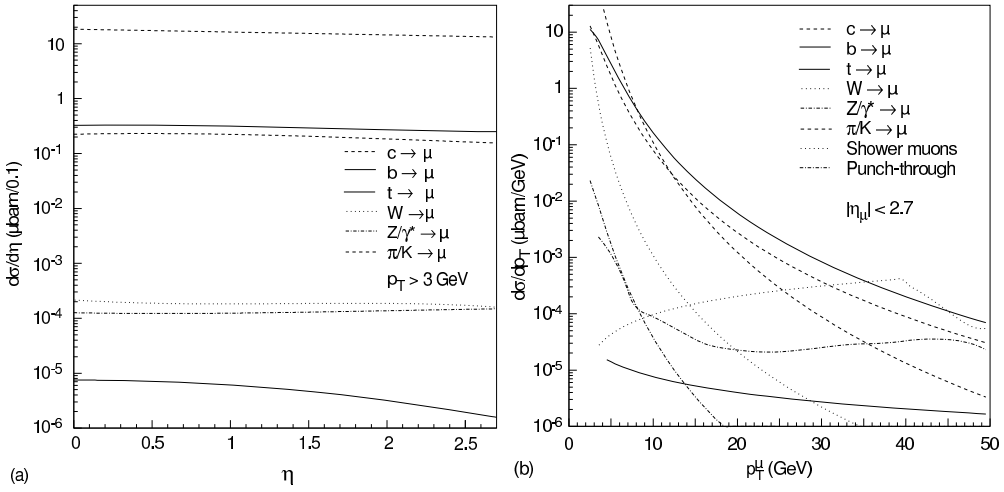

Figure 3.19: Simulate inclusive cross section for primary collision products: (a) as a function of the psudorapidity integrated over $3 < p_t < 50\ GeV/c$ and (b) as a function of p_t integrated over $|\eta| < 2.7$.

- **Primary backgound** Primary collision products penetrating into the Muon Spectrometer through the calorimeters, are correlated in time with the $p-p$ interaction. As shown in fig. 3.19 the sources of primary background are semileptonic decays of light ($\pi, K \rightarrow \mu X$) and heavy (c, b, $t \rightarrow \mu X$) flavours, gauge Boson decays ($W, Z, \gamma^* \rightarrow \mu X$), shower muons and hadronic punch-through. At small p_t (less than 10 GeV/c), the largest source of background are muons from π/K decays in flight; depending on pseudorapidity, muons with momenta from 3 GeV/c to 6 GeV/c will be absorbed in the calorimeters. At moderate p_t (above 10 GeV/c), *top* and Z decays also give a sizeable contribution.

  From the point of view of the particle rate the primary background is negligible compared to the uncorrelated background, which is discussed in the next point. The maximum expected particle flux due to the primary background is of the order of 10 Hz/cm^2 in the innermost precision chamber.

- **Radiation background** When high energy particles from the interaction point enter the detector material and machine elements (beam pipe, calorimeter, shield-

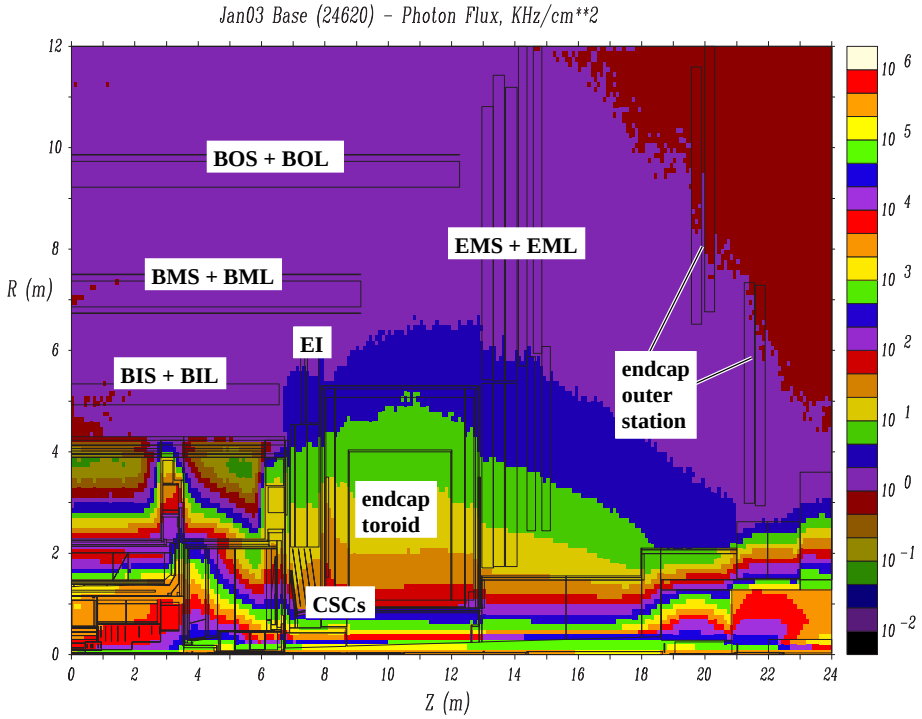

Figure 3.20: Photon flux (kHz/cm^2) in an ATLAS quadrant (GCALOR simulation).

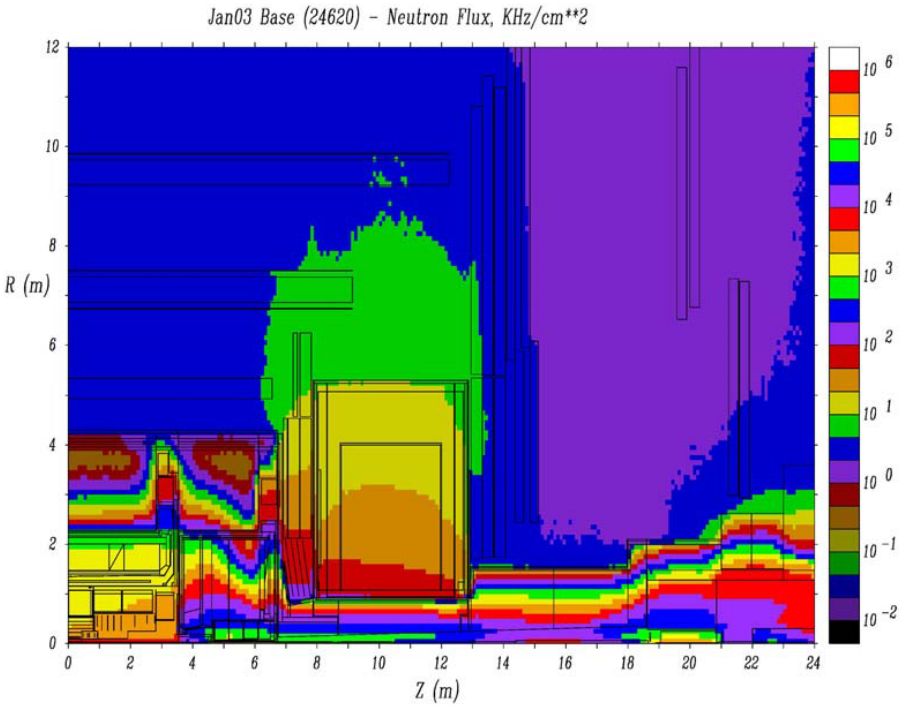

Figure 3.21: Neutron flux (kHz/cm^2) in an ATLAS quadrant (GCALOR simulation).

ing material etc.), they begin to shower. If the material is thick, the shower development will continue until most charged particles have been absorbed; the remnants are mostly neutrons and associated photons. Electromagnetic showers are absorbed very rapidly, while neutrons travel long distances, losing their energy gradually. Nuclear capture of thermal neutrons frequently results in the production of photons via (n,γ) reactions. The typical photon energies from these processes range from 100 keV to up to some MeV.

Neutrons produced in the showering process are scattered many times before being captured, giving rise to a rather uniform background radiation in the muon spectrometer. This background enters into the spectrometer from all directions and is not any longer correlated in time time to the primary $p-p$ interaction.

Figures 3.20 and 3.21 show the expected flux of photons and neutrons obtained with the GCALOR (Jan03 version) Monte Carlo. The maximum flux is of about 10 kHz/cm^2 for photons and 5 kHz/cm^2 for neutrons.

The particle flux is higher in the inner layer of the forward regions since most of the hadrons are produced at small angles with respect to the beam axis.

3.4.1 Expected counting rate

The radiation background affects the muon system mainly by generating uncorrelated noise hits in the chambers with the consequent pattern recognition degradation, space-charge build-up and aging.

The counting rate is an estimator of the rate at which drift tubes in the muon system will count in response to the background particle rates. It can be evaluated as:

$$\gamma \times \varepsilon_\gamma + n \times \varepsilon_n + p + \pi + \mu + 0.25 \times e \tag{3.44}$$

where γ, n, π, μ, e stand for the particles flux while ε_γ, ε_n are the photon and neutron chamber sensitivity[5]. The sensitivities to charged particles is taken as 100 %. The electron flux is multiplietd by a factor 0.25 to avoid double counting of electrons produced in photon interaction in the surrounding materials [34]. Since all these quantities depend on the energy in the 3.44 is implicit the convolution with the individual particle energy distibution. Figures 3.22 and 3.23 show particle flux and sensitivity for neutron and photons as a function of the energy.

Average values used for the estimations are 8×10^{-3} and 5×10^{-4} for the sensitivity to photons and neutrons respectively.

Despite the low sensitivity the relative contribution to the counting rate is dominated by neutral particles because of their higher flux with respect to charged particles.

In particular, photons contribute for about 70% while neutrons contribute at 10% level.

[5]Efficiency for a particle to produce a detectable signal (hit) in the chamber.

The evaluated count rate is reported in fig. 3.24 for the different spectrometer stations. For the $MDTs$ it ranges from about 10 Hz/cm^2 in the middle of the barrel to about 100 Hz/cm^2 for $|\eta| \sim 2$([6]).

MDT chambers have been designed to handle up to 5 times the estimated counting rate. In fact, several sources of uncertanties have to be taken into account: due to the limited knowledge of the shower processes in the calorimeters and of the (n,γ) cross-section, the simulated photon and neutron fluxes might be wrong by a factor of 2.5; chamber sensitivities could be in error by a factor of 1.5 from comparison between different simulation programs and measurements; finally the uncertainty in the $p-p$ cross-section and in the multiplicity of the particles produced in the primary collision is estimated to be $\pm 30\%$.

A conservative linear superposition of these uncertainties yields a factor of five. The ATLAS muon instrumentation is therefore designed to operate at a nominal luminosity of $10^{34} cm^{-2} s^{-1}$, allowing for a safety factor of five on the background rate.
Consequently the highest background rates for one MDT is assumed to be 500 Hz/cm^2.

3.4.2 Accumulated charge

During the ionization amplification process, described in 3.2.3, the great amount of drifting charges present in a restricted region (the avalanche) around the anode, can prime chemical reactions with the conseguent deposit of molecular compounds on the wire. This leads to a progressive deterioration of the tube performance and might finally compromise the tube operation. This phenomenon, usually called aging, is described in detail in Ch. 8. The aging of a given drift tube, after the period of operation ΔT, is therefore proportional to the total charge Q produced in gas during the interval ΔT. The quantity Q is usually expressed in unit of length and can be written as

$$Q = R \cdot d \cdot \bar{n}_e \cdot G \cdot e \cdot \Delta T \tag{3.45}$$

where R is the counting rate per unit area as defined in the previous paragraph, d is the tube diameter, $\bar{n}_e$ is the average number of primary ionization electrons (e is the electron charge) and G is the gas gain.

According to the information given in 3.4.1 the quantity $\bar{n}_e$ can be evaluated in the approximation that all background particles are photons; the photon energy can be assumed to be in the MeV range. In that case ionization due to photon interaction is similar to the ionization caused by a charged particle: in $Ar : CO_2$ (93:7) at 3 bar the number of primary electrons produced per unit length is $\Delta n/\Delta x \sim 300\, p.e./cm$ (Sec. 3.2.1). Hence the average number of primary electrons released is proportional to the average distance travelled in the tube by the ionizing particle:

$$\bar{n}_e = \frac{2\int_0^R \sqrt{R^2 - b^2} db}{R} \cdot \frac{\Delta n}{\Delta x} \sim 1000 \text{ electrons.} \tag{3.46}$$

[6] for the CSC it can be as high as 300 Hz/cm^2.

In the above equation R is the tube radius and b is the track distance from the wire.

In 10 years of LHC operation ($\Delta T = 10^8\, s$), with a background counting rate of 500 Hz/cm^2 (Sec. 3.4.1),

$$Q = 500\frac{Hz}{cm^2} \cdot 3\, cm \cdot G \cdot 1000\, e \cdot 10^8\, s = G \cdot 2.4 \cdot 10^5 \frac{C}{cm}. \tag{3.47}$$

Operating the chamber at a gain of $2 \cdot 10^4$ the accumulate charge in 10 years will be about 0.5 C/cm.

Therefore from the knowledge of the tube aging, which depends on the gas and on the operating conditions, with respect to the accumulated charge is possible to derive the expected lifetime of the detector for a fixed gain (Ch. 8).

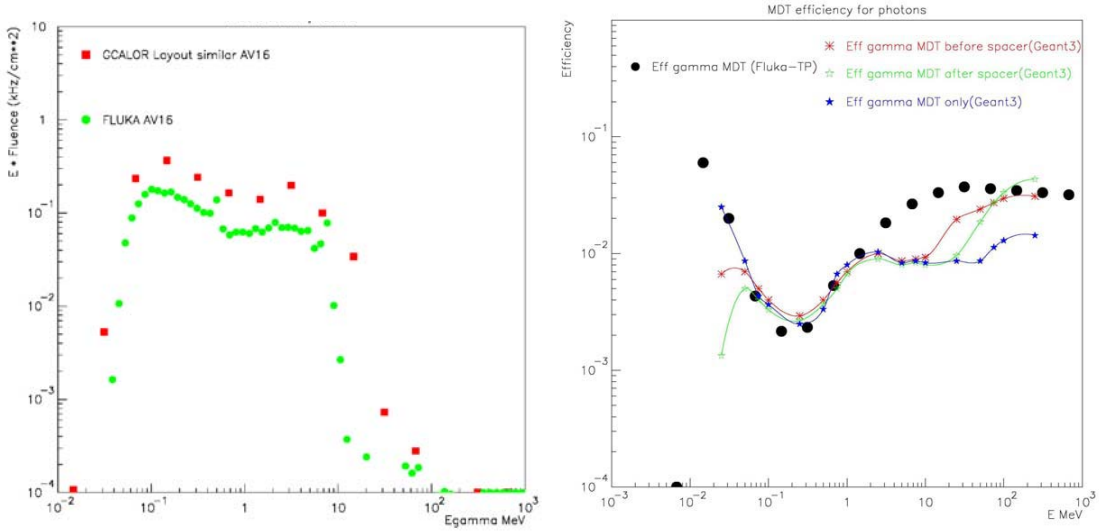

(a) (b)

Figure 3.22: (*a*) Photon flux as predicted by FLUKA and GCALOR Monte Carlo (nominal luminosity). (*b*) MDT efficiency for photons. The efficiency below 100 keV is due to photo-electric effetc in the gas while the rising around 1 MeV is due to the Compton scattering in the tube wall (Sec. 3.2.1).

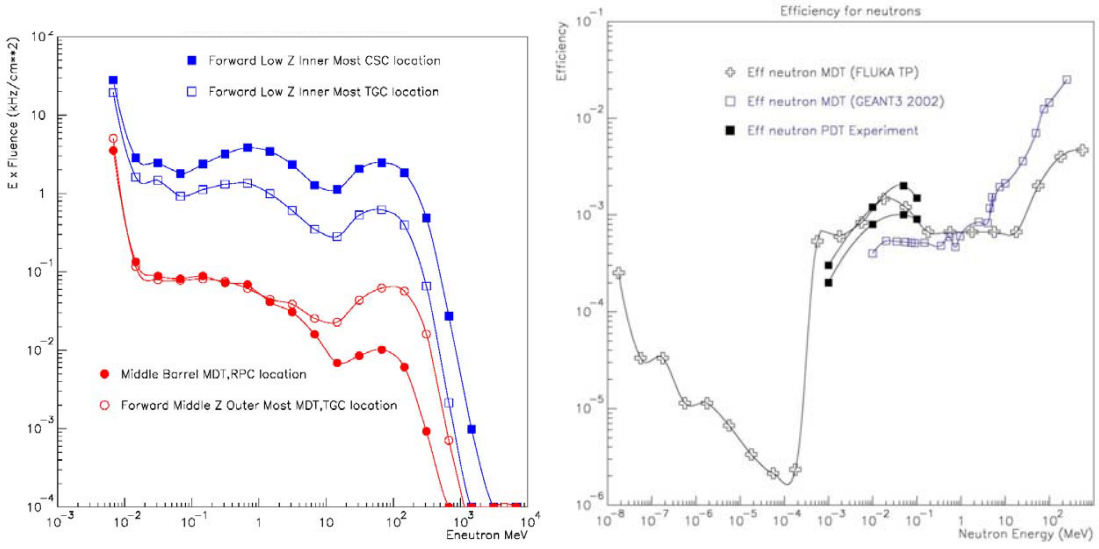

(a) (b)

Figure 3.23: (*a*) Neutron flux in the various region of the Muon Spectrometer as predicted by GCALOR Monte Carlo. All neutrons with energy below 10 keV are collapsed in the single bin (nominal luminosity). (*b*) MDT efficiency for neutrons. The rise around 1 keV (detection threshold) is due to the recoil of gas nuclei(Sec. 3.2.1).

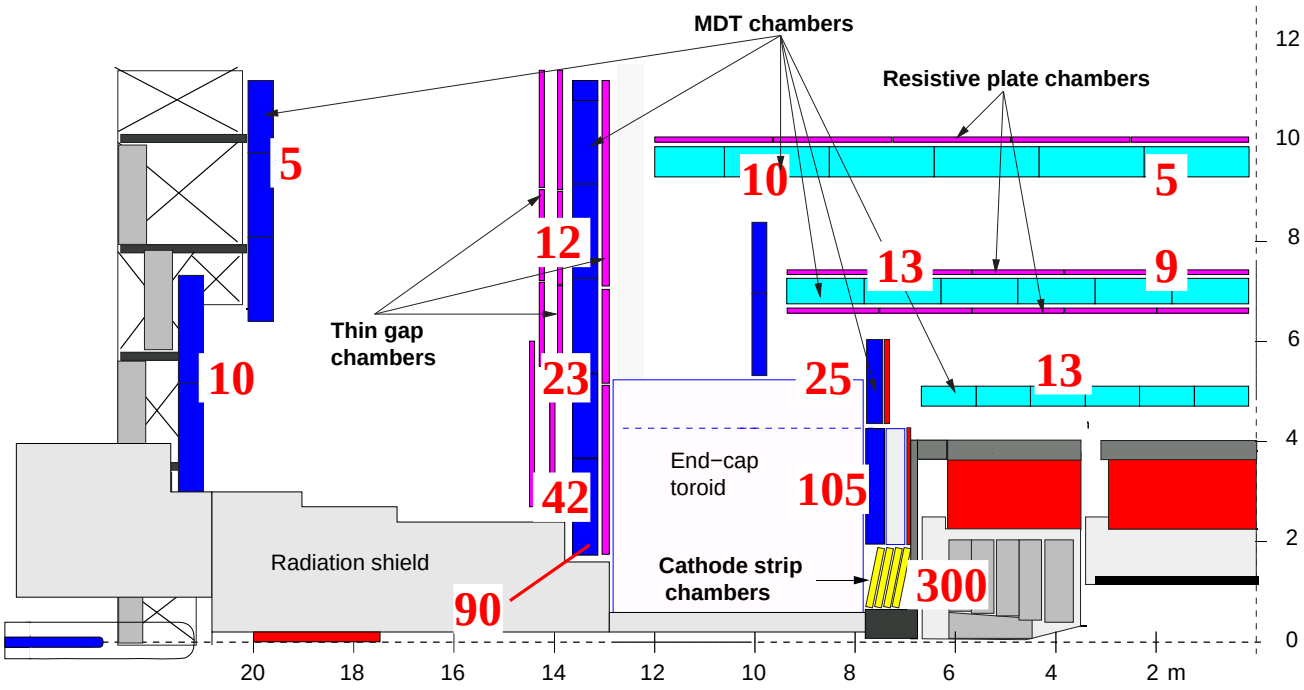

Figure 3.24: Background count rate (Hz/cm^2) in the precision chambers of the Muon Spectrometer at the nominal luminosity [28].

Chapter 4

Experimental setups, datasets and tools

Different experimental setups and datasets have been used for the studies presented in this work.

- In the present chapter the MDT test stand built in the Roma Tre laboratory and the CERN SPS test beam stand are described. The main differences between the two setups, that is to say the experimental probe (cosmic rays versus energetic monochromatic muons/pions) and the trigger devices, make them the suitable environments for analysis concerning the calibration an the resolution of the MDTs. An introduction to the analysis procedures and software tools used and developed for the analysis is also given.

- Another dedicated setup, developed for purposes of ageing studies, is described in the chapter 8.

4.1 Roma Tre MDT test site

The construction, assembly and test of a significant fraction of all the the MDT chambers (namely BIL and BML) of the ATLAS experiment has been committed to the INFN institute. Half of the MDT BIL chambers (62 in number) have been host in Roma Tre site ([52]) for the last part of the assembly and for the final control. In fact, each chamber, to be installed in the experiment, has to fulfill specific requirements in terms of mechanical precision, gas tightness, electrical stability, noise level and uniformity of response. In the Roma Tre test site they are equipped with the gas distribution system, the high voltage distribution and the on-chamber front end electronics. Then they undergo the Quality Assurance Quality Control ($QAQC$), a set of well defined tests conceived to monitor the detector functionality (more details in [52, 49]).

The test stand consists mainly of a gas distribution system, a high voltage distribution system and a trigger hodoscope. The gas system guarantees a high stability of

the operating conditions as well as the monitor of pressure, temperature, composition and flux of the gas.

MDTs are operated with $Ar{:}CO_2$ (93:7) at 3 *bar* absolute pressure.

In the next sections, the read-out electronics and the trigger, which are relevant for the presented work, are described in more detail.

4.1.1 Read-out electronics and DAQ

The read-out system used consists of 24-channel mezzanine boards, containing the Amplifier-Shaper-Discriminator (ASD) chip and the AMT-1 TDC chip, connected to the VME Chamber Service Module CSM0 [37] that performs AMT and ASD initialization and read-out. Between the CSM0 (which can serve up to 18 boards) and the mezzanines there is an adapter [38] that provides the boards with the proper low voltage power supply and rearranges the signals to and from the CSM0. The scheme of the setup is shown in figure 4.1. In the final configuration, instead, the CSM is a board mounted directly on the chamber (see 3.3.2, fig. 3.16).

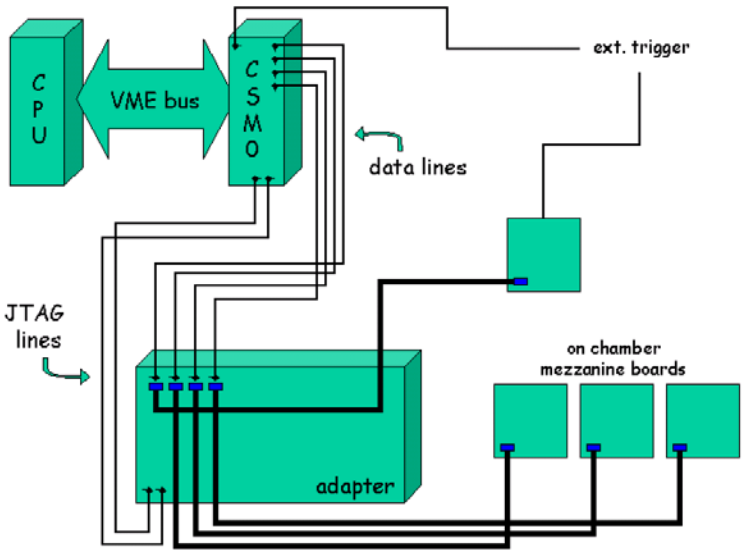

Figure 4.1: Hardware setup of the read-out electronics.

Each mezzanine board is connected to the adapter which in turn is linked to the CSM0 trough several RJ45 cables; there is an RJ45 cable for each mezzanine for the DS-link data connection and 2 Ethernet cables, the JTAG lines, for the initialization protocol (described below) transmission.

Three different steps are required to read-out the mezzanine boards with the CSM0:

1. CSM0 initialization

2. Configuration of TDC and ASD on the mezzanine board

3. Data read-out

After the reset of the CSM board a series of instructions to set the parameters needed for the system operation (as the JTAG transmission rate) are set and serial operations are enabled.

The mezzanine board is programmed using a serial bus with a JTAG protocol. The bus is accessed via VME. A setup string, the JTAG string, containing all the required parameters [32] is loaded from an external ASCII file and is sent to the mezzanine boards. The first parameter (first 8 bit of the string) provides the setting for the DAC which controls the ASD threshold value; this value can be varied from -254 mV to 256 mV in steps of 2 mV: for example, the value 108 corresponds to a threshold of -254+108×2=-38 mV. The ADC integration gate can be chosen between 8 and 45 ns in step of 2.5 ns. The default value is 15 ns. The default discharge ($run\ down$) current value is 4.5 μA and can range from 2.4 μA to 7.3 μA in steps of 0.7 μA. Other programmable parameters control the TDC time measurement. The meaning of these parameters is explained in figure 4.2.

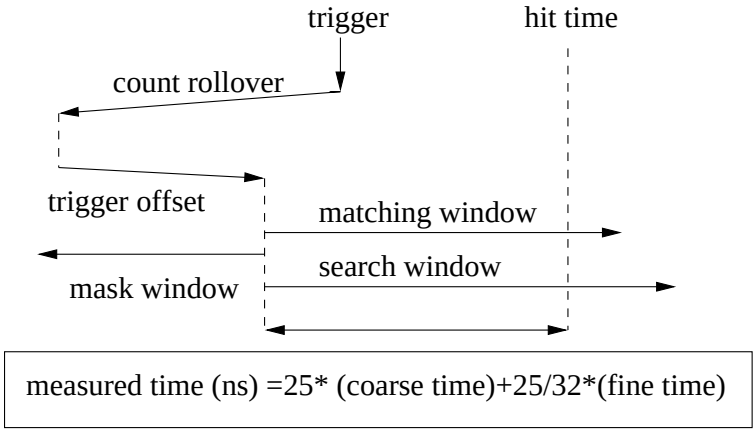

Figure 4.2: Definition for the time measurements parameters.

The *match window* defines the time interval in which hits are considered to match the trigger while the *search window* controls the window in which hits are measured. The *count rollover* and the *trigger offset* parameters fix the starting point of the various time windows with respect to the trigger signal. The *mask window* defines a time window before the trigger time where to look for hits that may have obscured hits in the matching window. All these parameters are given in coarse time counts (25 ns). The behaviour of the TDC must also be programmed by choosing to measure the time on the *leading edge*, on the *trailing edge* or to measure the width of the signal (*time over threshold*). The default choice is to measure the leading edge of the signal.

Once the configuration has been performed, incoming triggers are enabled and data collection can start.

The CSM0 receives a signal from an external trigger device and distributes it to the TDC in an asynchronous way (on the first falling edge of the internal clock of the

AMT parameters (μs) and settings	
matching window	1.575
search window	1.6
mask window	0.5
count rollover	102
trigger offset	100
Time Measurement	Leading Edge

ADC parameters	
integration gate	15 ns
threshold	-38 mV
run down current	10 μA

CSM following the trigger signal). Having no information on the internal clock (which in the experiment will be related to the machine timing) it is necessary to measure the time between the trigger and the clock edge sending the same trigger signal in a channel of a TDC connected to the same CSM0. The number of words in the event has to be retrieved from the proper register and then the data registers can be read. Data are stored in the event raw data file and then analyzed with dedicated software tools as described in the following.

4.1.2 Trigger

Two cosmic ray hodoscopes are available as trigger device for the MDT chambers.

The RPC hodoscope

This hodoscope [35] has been built for the test and certification of the BIL chambers.

The hodoscope provides an almost uniform illumination of the whole BIL chamber surface and allows the simultaneous operation of three chambers which can be positioned in the hodoscope at three different heights (with an accuracy of about 0.1 mm). Three planes of RPC measure the coordinate along the drift tubes and provide a fast trigger with a time resolution of about 1 ns. The distance between the lower two planes is 12 cm and they are separated by 5.5 cm of lead to stop particles with energy lower than about 120 MeV. The third plane is at a distance of 2.4 m from the top lower plane. A scheme of the layout is shown in figure 4.3.

Each RPC covers a surface of 48×124 cm^2. Six RPCs for each plane, for a total trigger surface of 288×124 cm^2 as shown in fig. 4.4. are necessary to cover the whole length of the chamber.

The electrodes of the RPCs are segmented in strips normal to the drift tubes of 2.9 cm pitch. One end of the strips is connected to the electronics board which receives the signals from 16 adjacent strips; each plane is divided in 6 read-out slices. It contains the amplifiers and discriminators and the logic to form a fast-OR signal which is split

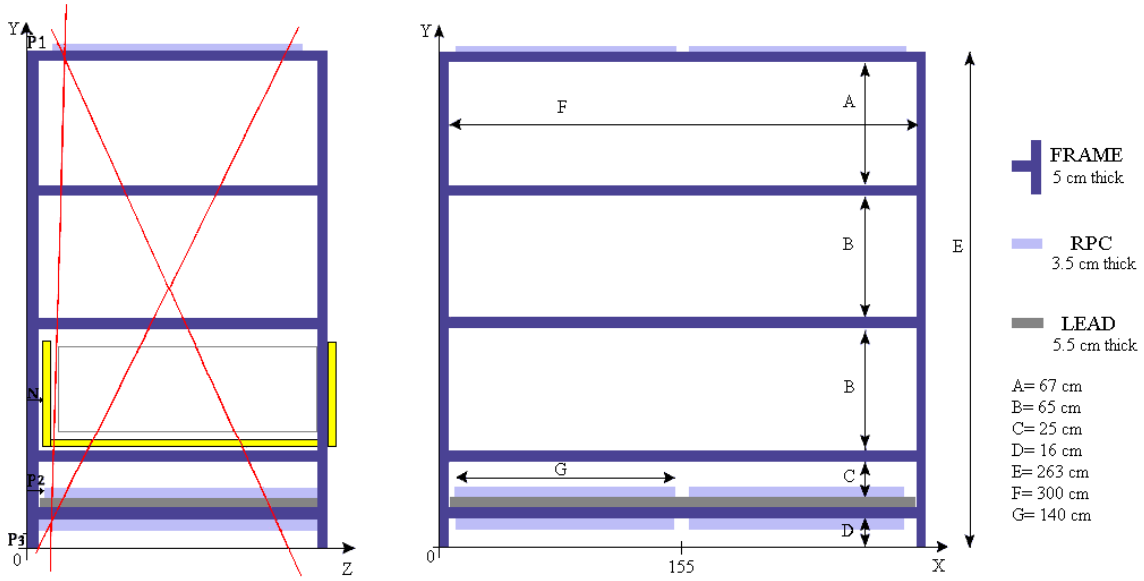

Figure 4.3: Scheme of the hodoscope.

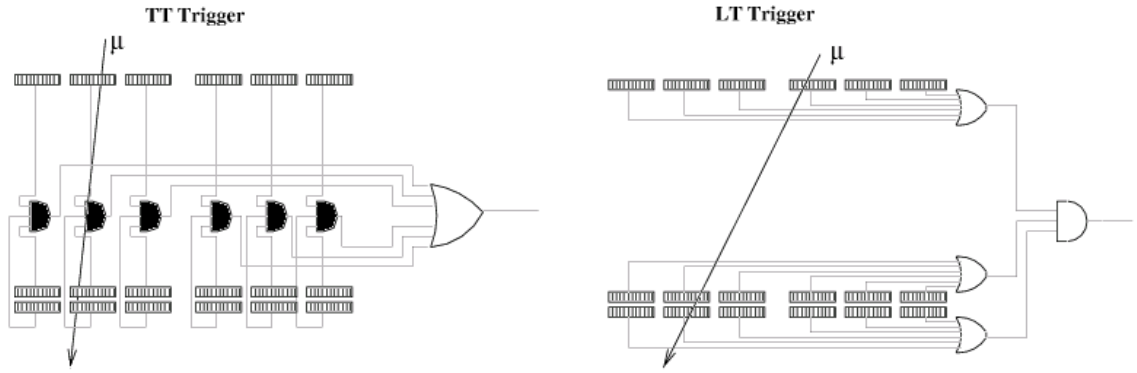

Figure 4.4: The two trigger logics implemented starting from the 18 fast-OR signals.

and sent to a TDC and to the trigger logic to form the global trigger.

Two different trigger logics (see figure 4.4) have been implemented starting from the 18 fast-OR signals. A large acceptance trigger (LT), made with the coincidences of the three planes, selects an aperture of about $\pm 40°$ around the vertical in the plane parallel to the wires. A tight acceptance trigger TT, made with the OR of the six threefold coincidences, defines vertical sectors with aperture of about $\pm 12°$. The LT rate is about 80 Hz and the TT rate is about 15 Hz.

The scintillator hodoscope

A system of four scintillator bars has been built to be used as an alternative trigger device for the data taking with the MDT chambers. The scintillator type is UPS89, based on Polystirene. Each bar covers a surface of $120 \times 20\ cm^2$ and is read out at both ends by two photomultiplier tubes (PMT)[1]. The scintillators thickness is 1 cm.

A possible trigger layout, made up of two trigger planes, is drawn in fig. 4.5.

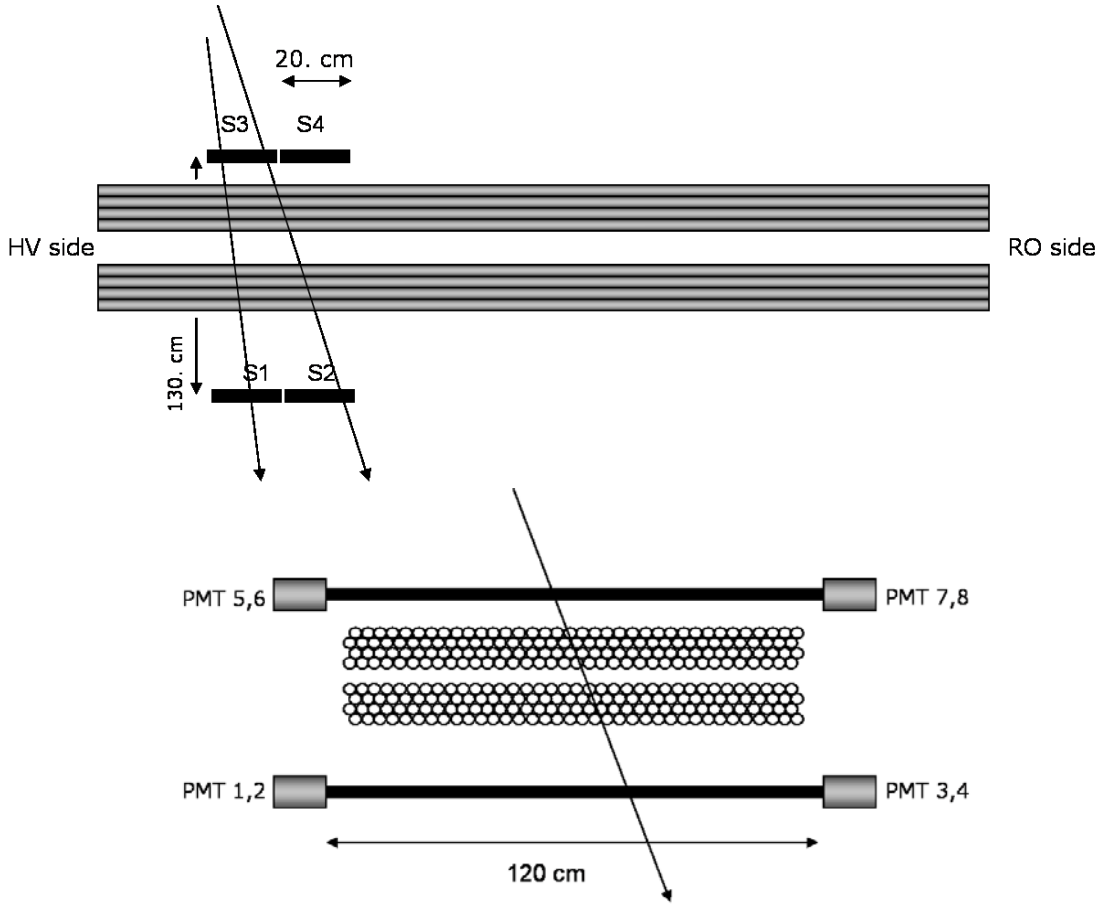

Figure 4.5: An example of a scintillator hodoscope layout.

The trigger logic used is:

$$(S_1\, OR\, S_2)\, AND\, (S_3\, OR\, S_4)$$

where S_i is the signal originated by the coincidence of two PMTs of the same scintillator number i (i.e. PMT 1 and 3, PMT 6 and 8 and so on) (fig. 4.5). Since the trigger time is provided by the last PMT signal which arrives at the coincidence unit, the two lower PMTs (numbered as 1 and 2) are delayed in time by an equal arbitrary quantity

[1]Model Photonis XP2262

in order to avoid event-by-event unknown fluctuations of the trigger time itself and the consequent uncertainty on the hit time measurement.

In this configuration the trigger rate measured is of about 10 Hz.

The scintillators are movable and can be placed along the tubes at different positions.

The relative distance between the planes and the trigger logic (i.e.: $S_1\, AND\, S_3$) can be chosen so that to vary the geometrical acceptance of the hodoscope as needed. This can be exploited to select muons traversing the chamber in a restricted range along the wire direction. An application is reported in 6.3.

The RPC trigger plane is segmented as well in that direction (fig. 4.4), nevertheless each sector is longer compared to a single scintillator slab, moreover a uniform response between sectors is not garanteed because of delays due to differences in the electronics equipment (i.e. cables connections) and response.

4.2 Test Beam Setup

An extensive set of tests of the ATLAS Muon Spectrometer has been performed at the H8 beam line at the CERN SPS accelerator. The beam is made up of either muons or pions with energies from 20 GeV to 350 GeV. The main aim of the test is to allow a carefully study of the MDT drift properties and a better understanding of the calibration constants: definition and determination algorithms, study of the systematics effects and evaluation of their impact.

The entire Test Beam (TB) setup is made up of several modules of the ATLAS Muon chambers, the hadron TILE calorimeter and the electromagnetic Liquid Argon Calorimeter.

A schematic top view of the experimental layout for the muon chambers is drawn in fig. 4.6.

The H8 Muon stand reproduces an ATLAS slice of the barrel and a sector of the endcap, fully instrumented with the front-end electronics and equipped with the alignment system. The barrel-like stand consists of six MDT chambers[2], two for each type:

2 inner (BIL),

2 middle (BML),

2 outer (BOL).

An additional BIL chamber, named

[2]In the end-cap stand there are six MDTs as well: two inner (EI), two middle (EM) and two outer (EO). Three TGC units (one triplet and two doublets) are also present. A CSC chamber has been installed later between the barrel and the end-cap stand and integrated in the data taking. These type of chambers have not been used for the presented studies.

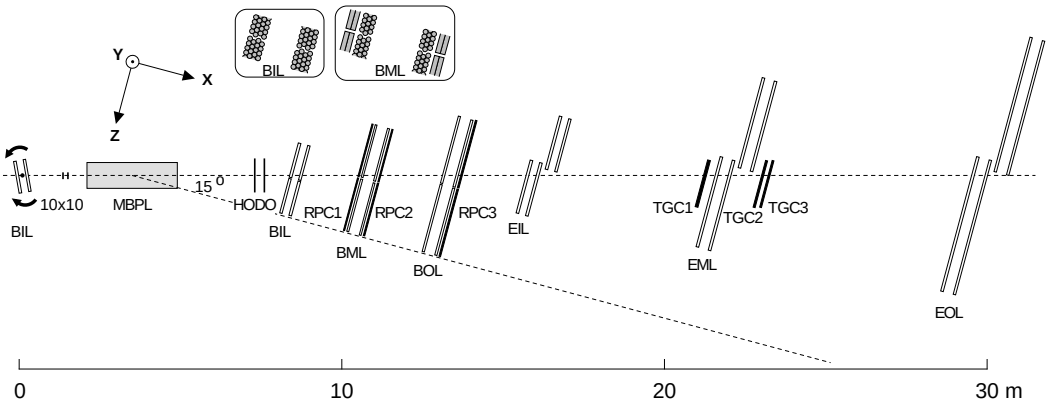

Figure 4.6: Schematic view of the muon chambers setup in the H8 area. MDT tubes are perpendicular to the plane of the figure. The beam axis is parallel to the plane of the figure.

$BILrot$,

is placed on a rotating support. The support can be operated remotely and a rotation up to $\pm 15^o$ around the chamber axis (parallel to the wire direction) is possible. Some sample were taken while keeping the chamber in rotation in order to enlarge the range of the track incidence angle.

A magnet was also installed bewtween the $BILrot$ and the barrel stand and used to bend the beam on the horizontal plane (orthogonal to the MDT wires).

4.2.1 Electronics

All the chambers are equipped with the read-out electronics that will be used in the ATLAS detector. Therefore the CSM is an on-chamber board which receives the trigger and the 40 MHz clock from the Time Trigger Control system (TTC) via optical link. It collects the the data from all the mezzanines and send them via optical link to two prototypes of the Muon Read Out Derive (MROD) which are VME board controlled by the ATLAS DAQ system. An additional mezzanine board was used to encode the time of the trigger signal since this is not synchronous to the CSM clock. The front end electronics is initialized through a JTAG bit string.

4.2.2 Trigger

Two types of trigger have been used. The first is a coincidence of two scintillators covering an area of about 10×10 cm^2 (the 10×10 trigger) to select the core of the beam. The time resolution of the scintillator is about 0.7 ns. In the second, the trigger signal is the coincidence of two larger scintillator planes covering an area of about 60×100 cm^2 and the veto of the 10×10 trigger (the *hodoscope* trigger). In this way, muons in the beam halo, covering a larger fraction of the muon setup, can be selected.

4.2.3 Data Samples

The data used were taken with the chambers operated at the nominal ATLAS conditions: Ar:CO_2 (93:7) gas mixture at 3 bar absolute pressure, high voltage at 3080 V. Three different dicriminator thresholds have been used: 36 mV, 40 mV and 44 mV. Runs when the BILrot chamber was rotating have been selected for the present analysis; the energy of the beam particles was greater than 100 GeV. These samples are suitable for the space-time relation calculation. In the runs taken with the 10×10 trigger the beam spot illumintes 2-3 tubes. The temperature of each chambers has been measured in different positions and at regular time intervals.

4.3 From data decoding to track fit

In the analysis of MDT data, a series of operations have to be performed to reconstruct tracks from the read-out data. For each triggered event the data file contains the list of the hits of event itself. A hit is identified by

- a tube identifier,
- the TDC measurement associated to the tube (*raw time*),
- ADC measurement (*raw charge*).

In the standard procedure the main operations are:

t_0 determination

The t_0 is the drift time associated to a particle crossing a given tube at a distance $r = 0$ from the wire. This value has to be measured for each tube and subtracted to the raw time measurement in order to have the correct drift time ossociated to the hit. This drift time can be converted into a drift radius assuming an $r(t)$ relation.

pattern recognition and track fit

Track reconstruction requires the selection of the hits that can be associated to form a track (*pattern recognition*) and the fit with a line tangent to the $drift\ circles$ (circles centered on the wire with radius equal to the drift radius).

autocalibration

The actual $r(t)$ of an MDT is not know *a priori*. It depends on several parameters (such as gas composition, density, electronic threshold, cfr. Ch.3) and therefore must be derived time by time to fully exploit the precision of the drift tubes. The determination of the $r(t)$ relation requires a dedicated analysis; it is done using data from the chamber with an iterative procedure (*autocalibration*) which allows to find the correct

$r(t)$ relation.

The analysis presented in this work has been performed using the CALIB program [39]. CALIB is a package (developed in Roma Tre and Roma "La Sapienza") for the analysis of MDT data and in particular for the autocalibration of the chambers and for the evaluation of the resolution and of the efficiency. As will be shown in the next chapters, CALIB has been used successfully in various setup like the H8 test beam, the Roma Tre cosmic test site and also on simulated data.

A complete description of the CALIB package, sub-packages, of the data files needed, of the datacards and of the procedures for installing, compiling and running the program are provided in [39]. In the next two sections the data decoding and the track finding task are described while the t_0 determination, autocalibration and other specific algorithms are treated in the next chapters.

4.3.1 Data decoding and geometry handling

In the various setups the data acquisition system is different. For each data format, a different data decoding has been implemented; anyway the bulk of the decoding is the association of a hit (time measurement and sampled charge for a given electronic channel) to a tube of the chamber. This association depends on the electronics and on the chamber type. A description of the inner structure of the chambers (in terms of number of tubes, tube length, distances between multilayer) and of their relative positions is required for a correct positioning in space of the tube. Two different geometry description systems are available in the software package.

One is based on dedicated data files (GeoFile) which contain all the relevant informations; this is useful when dealing with few chambers and allows a fine tuning of the parameters (for example to easily take into account tomograph measurements of the chambers).

The other system is based on the AMDB detector description [40] and is used when the setup becomes more complicated (like the H8 setup or for data simulated in the whole spectrometer).

Once a data entry has been fully decoded a new hit is added to a list which will contain all the hits of the event.

4.3.2 Pattern recognition and track fit

The pattern recognition is a procedure to find the tracks associated to a given hit list.

As outlined in Ch. 2, an MDT chamber is made of two multilayers of 3 or 4 layers of

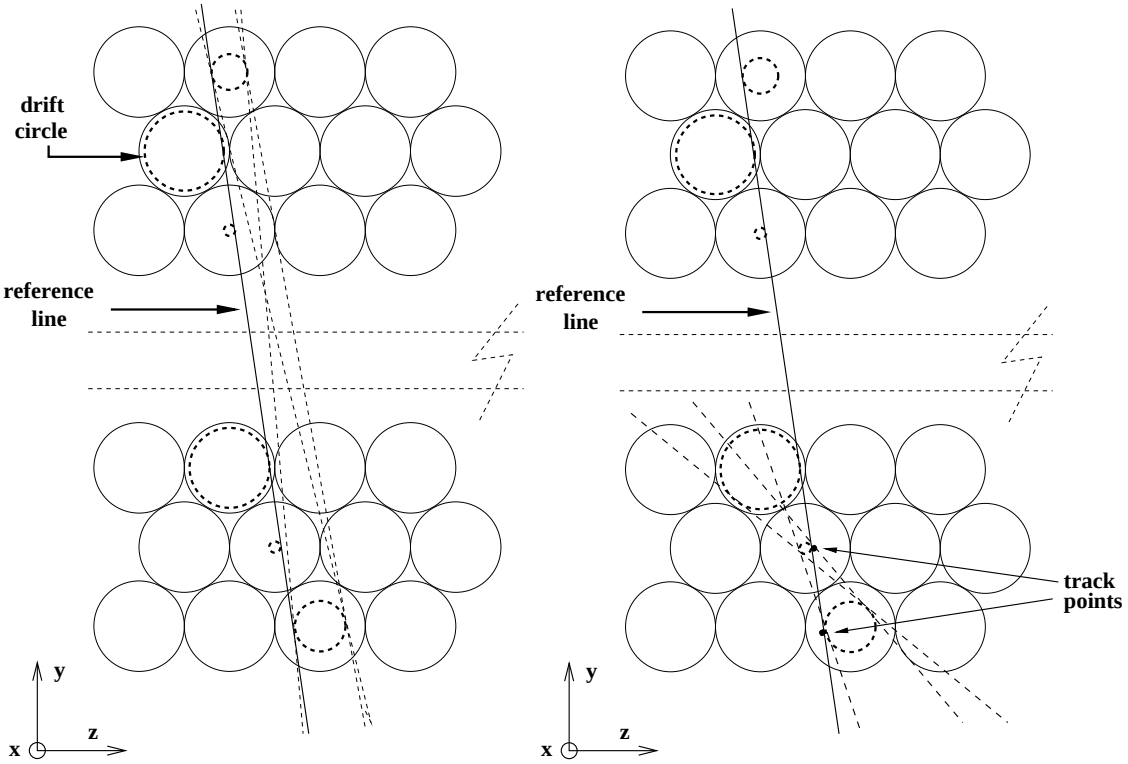

(a) Definition of the reference line

(b) Definition of the first two track points

Figure 4.7: Description of the track element calculation. An example of a fit to the hits within two multilayers of three layers is given.

tubes that are fixed on an aluminium structure (*spacer*). The pattern recognition and track fit procedure can be applied to a chamber or to the two multilayers separately; this depends on the requirements of the application and will be discussed in the following.

Pattern recognition is performed in two steps.

- At initialization, a list of reference patterns, the *Candidate Tracks*, are created taking tubes that are aligned in a given angular range (which is programmable by the user). A comparison (at tube level with no use of drift information to speed up the procedure) between tubes in an event and the *Candidate Tracks* is made to quickly understand which hits can be associated to the same track.

- Once hits have been selected, a fit to the drift circles, the *track fit* (described below), is done and the track is accepted or rejected on the basis of a χ^2 test. If the track is not accepted, the hit which gives the higher contribution to the χ^2 can be removed from the list and the fit is done again. The maximum number of hits that can be removed is user-defined as well. When the track is accepted, the two parameters of the line, their errors, the χ^2 of the fit and the pointers to the hits used are registered and are available for later use. The centers of the tubes

are given in a global reference system (taking into account the position of the chamber). The global system is chosen to have the y and the z axis on the drift plane and the x axis along the tubes.

Once n tubes within a chamber (the same applies considering one multilayer) have been associated to a *Candidate Track* a dedicated ierative algorithm, describe in detail in the Ch. 5 is applied to determine the parameters of the track (track fit):

- The four possible tangents to the first and last drift circles are computed.
- Among these straight lines, the one having the smallest χ^2 with respect to the other drift circles is chosen as the *reference line* (see fig. 4.7(a)).
- Then, the points of closest approach to the reference line of the remaining drift circles are used as *track points* (fig. 4.7(b)).
- To each *track point* is assigned an error defined by the tube resolution function and the parameters of the new reference line is obtained fitting the *track points*.
- the last two steps are iterated until the desired precision in reached.

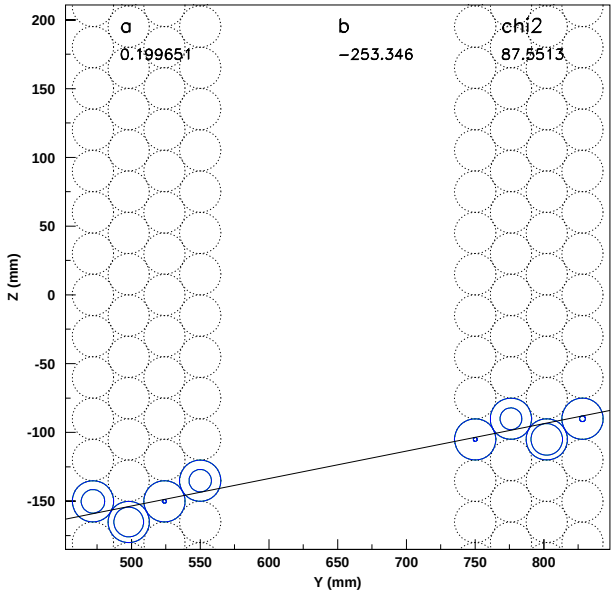

Figure 4.8: A track reconstructed with a BIL chamber. The parameters of the fitted function $z = a \cdot y + b$ and the χ^2 of the fit are also reported.

In the event display of figure 4.8 is shown an example of a track reconstructed in a BIL chamber.

4.4 GARFIELD simulation program

The GARFIELD Monte Carlo program represents the most accurate simulation of the physics processes and the electronics which characterize the behaviour of a drift detector.

Actually it is made up of three packages: HEED[42], MAGBOLTZ[43] and GARFIELD[41] itself.

The HEED program computes the energy loss of fast charged particles in gases, taking, optionally, delta electrons and multiple scattering into account. The program can also simulate absorption of photons in the gas through photo-ionization.

The MAGBOLTZ program, computes electron transport parameters, for example the mobility and the Townsend and the diffusion coefficients (Ch. 3), for a large variety of gases and mixture of gases. The program is based on the numerical solution of the Boltzmann transport equation. The principals initialization parameters are the gas composition, temperature, pressure and the electric(magnetic) field range.

GARFIELD is a program for the simulation of two and three dimensional drift chambers. It is interfaced to HEED and MAGBOLTZ and computes field maps, electron and ion drift lines, drift time maps and arrival time distribution, signal induced on the wires by drifting electrons and ions and the electronics response.

Examples of simulations performed with GARFIELD are given in plots shown throughout Ch. 3.

4.4.1 Choice of the parameters

In this section a brief description of the main settings chosen to configure the program is reported. The specifications are summarized in tab. 4.1.

The computing time of the MAGBOLTZ progrma is not negligible, therefore the two most critical values in this respect, namely `n-e` and `coll`, must be inizialized according to the specific needs as described in what follows. The program will compute the transport properties for discrete values of the reduced electric field are regurarly distributed within a given range adjusted via the `e/p-range` parameter. The values reported in the table corresponds to the reduced electric field at the MDT anode and cathode surface. The number of points is set through the `n-e` parameter. On one hand its value must be large enough so as to represents any fine structure that may be present in the transport properties. On the other hand, an excessively large number of points may lead to oscillations in the interpolation and to a larger computing time (which increases linearly with respect to

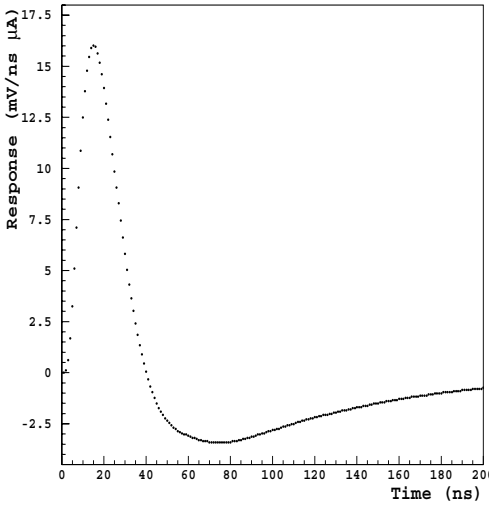

Figure 4.9: Th transfer function provided in input to the simulation.

Magboltz	
Parameter	*Value*
`coll`	10
`e/p-range` $(V/cm \cdot Torr)$	0.14718-85.9527
`n-e`	40
Garfield	
Parameter	*Value/Status*
`gain`	2×10^4
`polya`	0.38
`diffusion`	on
`window` (μs)	0 - 0.78125
`step` (μs)	0.00078125

Table 4.1: Main parameter settingd specicified for the MAGBOLTZ and GARFIELD inizialization.

this parameter). Dedicated estimations suggest 40 logaritmically spaced points as the optimal choice for the kind of simulation presented here (i.e. arrival time distributions, space-time relation etc.). The logaritmic spacing has been chosen in order to better characterize the drift tube region where the field variation is more rapid.

The parameter `coll` specifies the number of collisions, in multiplies of 960000, to be used to compute the transoport propeties at each electric field point. It is worth noticing that the CPU time consumption increases linearly with respect to these parameter while the statistical accuracy of the drift parameters calculation improves with its square root. The chosen value of 20 leads to a statistical error of 0.2% on the drift velocity, 2% on the transverse diffusion and 3.5% on the longitudinal diffusion.

MAGBOLTZ only computes the electron transport properties, not the ions one. The ion mobility can be fixed to a constant value or, if the dependence on the electric field is not negligible, can be provided in tabular form as a function of the reduced electric field. The mobility of the $Ar : CO_2$ (93:7) gas mixture has been approximated with the mobility of pure Argon (Ar^+/Ar) (Sec. 3.2.2). The values provided are the ones reported in the graph of fig. 3.7. For temprature and pressure values different from the nominal ones the mobility has first to be scaled according to the relation 3.10.

The GARFIELD program simulates the drift of the ionization electrons by taking into account both the diffusion and the attachment in the gas for the given gas mixture and operation (pressure, temperature) conditions. The effect of delta electron can be simulated as well. A Polya distribution with parameter $\theta = 0.38$

was used to describe the statistical fluctuations of the gas amplification (the `gain` parameter) around the mean value which was fixed to the nominal value 2×10^4 (Sec. 3.2.3).

The signal propagation along the anode wire and the properties of the front-end electronics (ASD) have been taken into account by folding the raw current signal $I(t)$ with the transfer function of a MDT and an ASD amplifier-shaper circuit (Sec 3.3). The transfer function of a bipolar shaper circuit with 15 ns peaking time has been provided in tabular form. The values are shown in fig. 4.9.

Signals are computed in the time range from 0 to 0.78125 μs and sampled every 0.78125 ns (adjusted through the parameters `window` and `step`) which corresponds the AMT TDC chip resolution.

The output of the current signal convolution is a voltage signal $V(t)$ (fig. 4.9) as seen by the discriminator. The TDC time associated to the passage of a ionizing particle is defined as the time at which the signal $V(t)$ crosses a given threshold, in multiplies of 0.78125 ns. The value of the threshold has to be defined as needed.

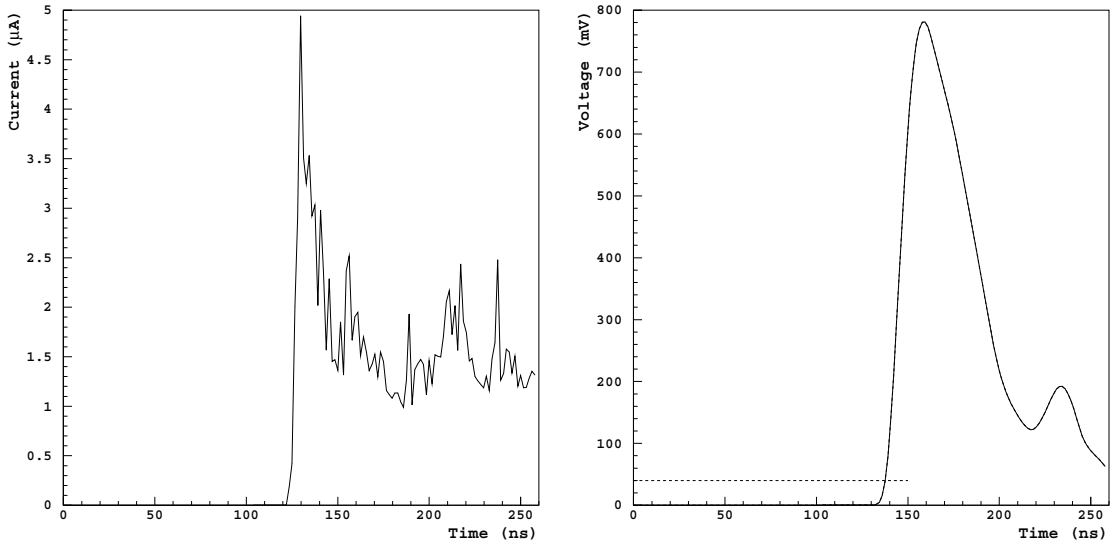

Figure 4.10: $Left$: a typical current signal induced by a 200 GeV muon traversing the tube at a distance of 5 mm to the wire ($Ar : CO_2$ 93 : 7, 3 bar, 293 K). $Right$: the same signal after the convolution with the transfer function of fig. 4.9. The dashed line corresponds to a 40 mV threshold.

4.5 A Monte Carlo for MDT tracking studies

A Monte Carlo simulation program has been developed with the purpose of a systematic and accurate study of the calibration and tracking with an MDT chamber.

Originally the program has been written to study the impact on the resolution of

- multiple scattering in the tubes wall
- trigger induced time jitter

and for

- reconstruction algorithm validation
- miscalibration studies.

It has also been conceived to exploit the accuracy of the GARFIELD simulator and to allow for a direct comparison of the results with the experimental data.

In fact, it can be optionally interfaced with both the GARFIELD program and the CALIB package.

The simulation chain can be outlined as follows:

1 Particle generation. The traversing particle can be generated according to an arbitrary momentum and angular distribution function.

For comparison with the Roma Tre test site measurements, a simulation of the momentum and angular distribution of the cosmic rays has been implemented (Ch. 7).

2 Trigger acceptance check. For computing time saving, by default, the production vertex of the particle is distributed (e.g. uniformly) on the trigger surface which is upstream with respect to the detector. Then particles which are not in the trigger geometrical acceptance are rejected.

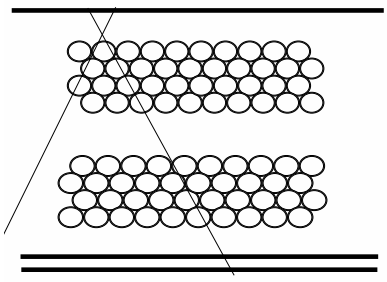

3 Transport. The accepted particle is then transported through the chamber volume. This means that, for each tube encoutered, the deflection of the trajectory due to multiple scattering in the tube wall is calculated. When the particle is inside the tube volume the *impact parameter*, that is the distance with respect to the wire (the tube center), is calculated and stored. The deflection of the direction of a particle (of unitary charge) travelling with momentum p a thickness l of Aluminium (radiation length $X_0 \simeq 89$ mm) can be simulated assuming a Gaussian distribution of the deflection angle θ_{ms}[10]([3]):

$$\theta_{ms} = \frac{13.6MeV}{\beta cp} \cdot \sqrt{\frac{l}{X_0}} \cdot \left(1 + 0.038 \cdot ln(\frac{l}{X_0})\right). \tag{4.1}$$

This is done for each traversed tube until the particle exits the chamber volume. Multiple scattering in the gaseous medium can be neglected (for Argon $X_0 \sim 100$ m at normal conditions). Once the transport simulation is

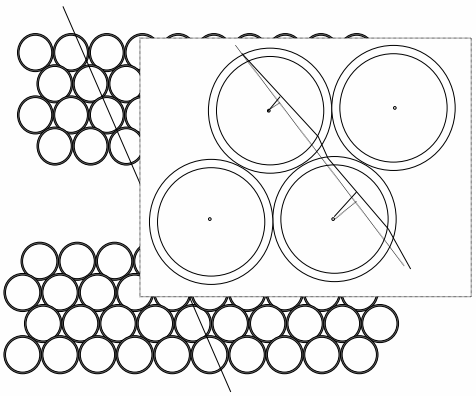

finished, a list of the crossed tubes and the associated impact parameters is available.

4 Hit generation. Once the impact parameter is determined it must be converted into a drift time (i.e. arrival time). Two options:

a GARFIELD is invoked for the drift time calculation. In this way the intrinsic time resolution of the drift tube is automatically taken into account.

b the radius is converted into a drift time interpolating a user defined $r(t)$ relation table. In this case a parametrization

[3]the formula is valid (i.e. 10% accuracy) in the range $10^{-3} < l/X_0 < 10^2$, which is respected since the distance l equals at least the the tube wall radial thickness which is 0.4 mm. A more detailed simulation for the scattering has been also used interfacing the program with the GEANT simulation. No significant discrepancies have been observed relatively to the accuracy of the performed analysis.

$$f_{res} = f_{res}(r)$$

of the gas resolution f_{res} with respected to the radius r must be provided as well. Before the conversion, the impact parameter r_i is smeared through the transformation

$$r_i \rightarrow r_i + \sigma_{gauss} \cdot f_{res}(r_i)$$

where σ_{gauss} is a random number distributed according to a Gaussian function with mean equal to zero and unitary standard deviation. By default, negative radii are changed into positive.

Optionally, the following effects can be simulated.

Trigger delay: each hit time calculated in one of the two ways described above is then augmented by a quantity corresponding to the time the signal takes to reach the read out electronics of the hodoscope. This time depends, on an event-by-event basis, on the impact point of the track on the downstrem trigger plane and on the signal propagation velocity (provided by the user).

Tube t_0: This option implies that a tube dependent time shift is added to the simulated hit times. A list of the t_0 value to be associated to each tube must be provided by the user.

Electronic noise: If this option is selected spurious (non physical) hits are added to the hit list unless they occour at a later time with respect to a physical hit simulated in the same tube. For each tube the probability to give a noise hit is calculated according to the desired noise level. The time associated to the hit is by default uniformly distributed within the time window.

δ-electrons: the δ-electrons production is simulated generating a secondary track with a defined probability. The production point is extracted unifirmly along the track portion comprised in the tube cavity and in the tube wall. The emission angle is 90° (Sec. 3.2.1) and the direction randomized among the two sides of the track. If the δ-electron track distance to the wire is inferior with respect to the original one a new arrival time for the tube is computed. The unknown parameter, the overall production probability of a δ-electron in the tube volume, can be estimated through a tuning on the experimental data (Sec. 5.3).

5 Event data production. After the end of the previous step a list of the crossed tubes and the associated times is available. These generated hits are then written in a format which is readable by the same data decoding and analysis programs, e.g. CALIB, used to process the experimental data.

Steps from 2 to 4 are described in detail in the next Chapter.

Chapter 5

Autocalibration

5.1 The time response of the detector

Drift tubes are used for drift time measurements: the time interval between the passage of the particle in a tube and the time the induced signal cross the threshold of the discriminator (Ch. 3). The first is usually measured by an external time reference signal, that can run asynchronously, e.g. the trigger in experiments with a long-spill beam extraction, or can be synchronized, e.g. with the bunch crossing in experiments at a collider. What is actually measured is the *raw time*, t_m:

$$t_m = t_{part} + t_{drift} + t_{delay} - t_{trig} \tag{5.1}$$

Here t_{part} is the time the particle hit the tube, t_{drift} is the electron drift time in the gas, $t_{delay} = t_{wire} + t_{ele}$ is the propagation time of the tube signal; it sums up the propagation time along the anode wire and the delay due to the read-out electronics. The reference signal (trigger) time

$$t_{trig} = t_{part} + t_{flight} + t_{trig,prop} + t_{trig,ele} + t_{phase} \tag{5.2}$$

is the time at which the trigger gives the start pulse to the TDC connected to the tube. It is the sum of several contributions. The time of flight (t_{flight}) of the particle from the tube to the trigger detector plane; $t_{trig,prop}$ and $t_{trig,ele}$, which are the propagation time of the signal inside the trigger plane and the trigger read-out electronics.

Finally t_{phase} is the time interval between the trigger signal and the reference clock edge. During operation with proton-proton collisions, that means in the presence of a synchronous trigger (with a clock frequency of 40 MHz), all delays due to signals propagation will be constrained by the detector geometry and the muon time of flight. Therefore for high momentum muons, t_{phase} will only depend on the position of the drift tube in the detector. The situation is different when

the MDTs are operated in asynchronous mode, e.g. in a test beam, or when the experiment is triggered with cosmic rays.

Equation 5.1 can be written as:

$$t_m = t_0 + t_{drift} \tag{5.3}$$

The quantity t_0 is a constant of the tube. It has small variations among tubes connected to the same electronic circuits, or tubes close in space. In fig. 5.1 is shown a typical distribution of the measured time t_m, usually called drift time distribution obtained with a high momentum muon beam. Because of the

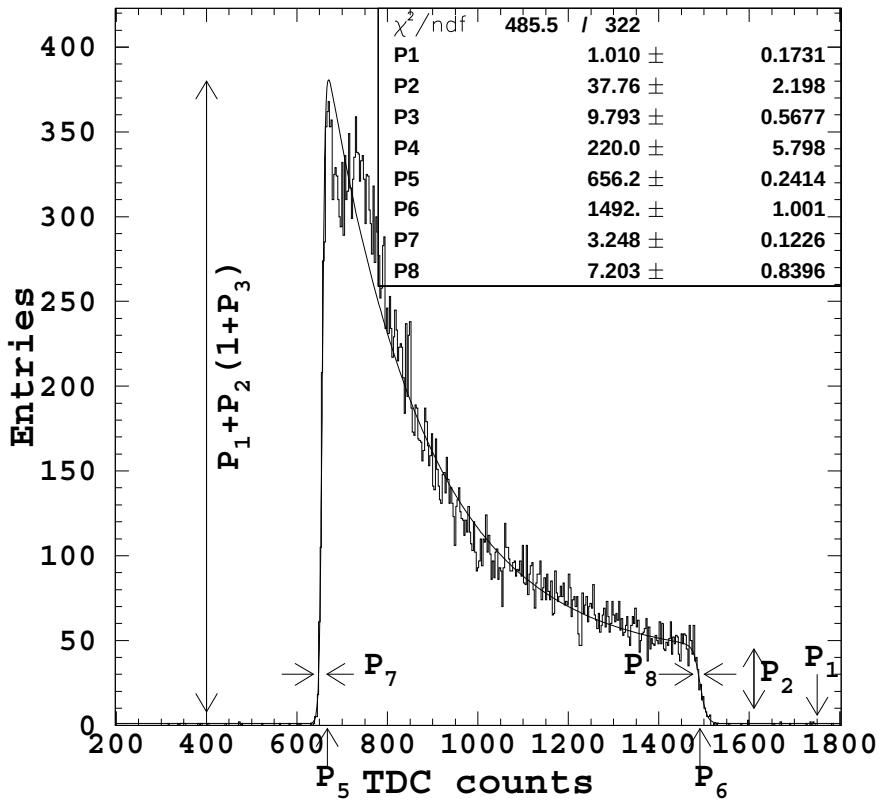

Figure 5.1: Typical drift time distribution at nominal operating conditions and the fitted function 5.4. The meaning of the parameters is explained in the text. A TDC count corresponds to 0.78125 ns.

behavior of the drift velocity which reaches its maximum value close to the anode wire and decreases for larger distances, the drift-time spectrum rises sharply at early times reaching a maximum, then drops continuously for later times. The spectrum ends with another less sharp edge The distribution can be fitted with

the empirical function:

$$f(t) = p_1 + \frac{p_2\left(1 + p_3 e^{-\frac{t-p_5}{p_4}}\right)}{\left(1 + e^{\frac{-t+p_5}{p_7}}\right)\left(1 + e^{\frac{t-p_6}{p_8}}\right)}. \tag{5.4}$$

The parameter p_1 is the uncorrelated (here assumed flat) background, p_2, p_3 and p_4 describe the shape of the central portion of the distribution; p_5 and p_6 are the turning points of the rising and of the trailing edge respectively; p_7 and p_8 describe the rising and trailing edges time width. Muons that are correlated in time with the beam trigger contibute only to the so called *physical time window* of the distribution which is assumed to be comprised between p_5 and p_6. The parameters p_5 and p_6 are generally taken as the definition of t_0 and t_{max}, the time associated with a particle traversing the tube close to the internal wall. The maximum drift time is therefore

$$\Delta t_{drift} = t_{max} - t_0 \simeq p_6 - p_5. \tag{5.5}$$

With an asynchronous trigger, t_{phase}, according to the uniform distribution properties, will contribute to the distribution with a time jitter of r.m.s. width of $25/\sqrt{12} = 7.2$ ns, much larger than the intrinsic resolution of the drift tube. In the measurements at the test beam (Sec. 4.2) or at the production test sites (Sec. 4.1) this effect was eliminated by reading event by event the trigger time with the same TDC used in the MDT front-end electronics. But this method cannot be easily implemented in the standard data acquisition of the experiment when reading the whole detector and thus the t_{phase} uncertainty is unavoidable when triggering asynchronously with cosmic rays.

5.1.1 t_0 determination

The aim of the tube t_0 determination is to syncronize the starting time of the disrtibution for all the MDT tubes.

The t_0 in the 5.3 is usually measured by fitting the parameter p_5, the turning point of rising edge of the function 5.4, described in Sec. 5.1.

Despite the value obtained by a fit procedure does not corresponds to the start of the physical drift window, all drift times are related to that value ($t_{drift} = t_m - t_0$), hence a systematic shift will be reabsorbed in the definition of the $r(t)$ relation.

This consideration justifies the search for a different definition of t_0, for example, in order to improve the accuracy of this parameter, definined as the stability with respect to the sample size variation.

From the 5.4 derives that the parameter p_5 is strongly correlated to the others and that the t_0 can be calculated by fitting only the rising portion of the distribution,

with the Fermi-Dirac function

$$F(t) = p_1 + \frac{F_0}{1 + e^{-\frac{t-t_0}{\Delta T}}}. \tag{5.6}$$

In this case (which can be gneralized to the 5.4) a generic new definition of the t_0 is the time t'_0 at which the function 5.6 equals a fraction f of F_0: $F(t'_0) = f \cdot F_0$, is

$$t'_0 = t_0 - ln(\frac{1}{f} - 1)\Delta T \tag{5.7}$$

that can be rewritten as

$$t'_0 = t_0 - \gamma \Delta T. \tag{5.8}$$

As expected, if $f < 0$ then $\gamma > 0$ and $t'_0 < t_0$. So a new t_0 can be expressed as a displacement of the "Fermi-Dirac t_0" (eq. 5.6) or of the "standard t_0" (eq. 5.4) by a quantity proportional to the rise time ΔT (p_7 in the 5.4) of the distribution. The proportional factor γ is usually named the t_0 *correction factor*.

Hence four methods can be compared (clearly 1 and 3 are a particular case, $\gamma = 0$, of the other two):

1. standard t_0 (parameter p_5 in the 5.4),
2. displaced standard t_0, according to the 5.8,
3. Fermi-Dirac t_0 (eq. 5.6),
4. displaced Fermi-Dirac t_0 according to the 5.8.

The analysis is describe in the following.

- The single tube drift time distribution of fig. 5.1, obtained with about $2 \cdot 10^4$ events, has been used as reference for generating drift time distributions. A thousand independend runs with $2 \cdot 10^3$, $5 \cdot 10^3$, 10^4 and $5 \cdot 10^4$ events have been generated.
- For each run, the generated drift time distributions have been fitted with both the functions 5.4 and 5.6. Moreover, since for the Fermi-Dirac the time range of the fit is not defined unambiguously, several time intervals, in multiples of ΔT. have been fitted with the 5.6.
- the values of the fitted parameter have then been inserted in the 5.8 to calculate different t_0 by varying the correction factor γ in the range $[0, 3]$.
- Finally the resulting distributions have been fitted with a Gaussian and the derived widths taken as a measure of the spread of the relative t_0 definition.

As shown in fig. 5.2(left) the minimum spread of the Fermi-Dirac t_0 is reached for and upper integration limit equal to $t_0 + 5\Delta T$ and a correction factor of about 1.3. Distributions are fitted with a parabola. It can be noticed that all the curves

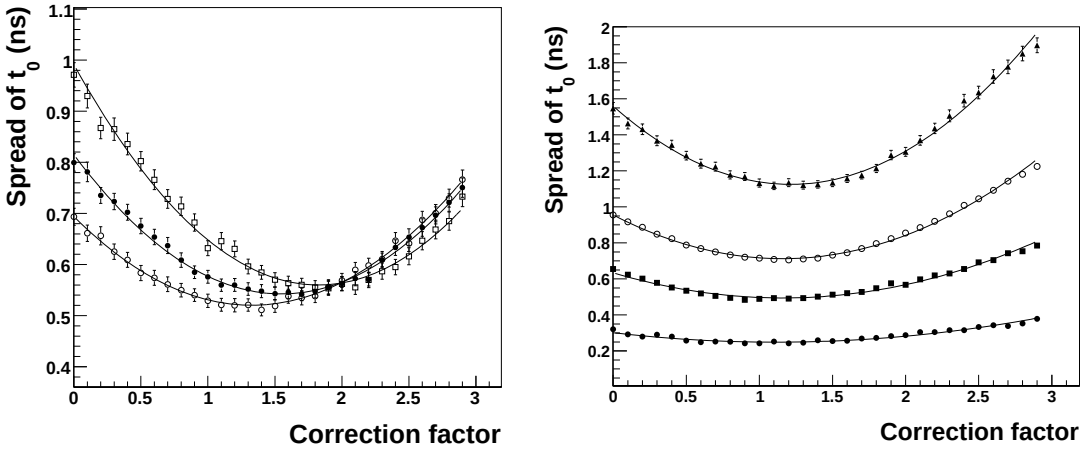

Figure 5.2: *Right* : spread of the Fermi-Dirac t_0 as a function of the correction factor for the sample of 10^4 events. Different families of points corresponds, from top to bottom, to an upper integration limit equal to $t_0 + 3\dot{\Delta}T$, $t_0 + 4\dot{\Delta}T$ and $t_0 + 5\dot{\Delta}T$. The parabolic fits cross each other for a correction factor of 2 as explained in the text (*note* 2). $Left$: spread of the standard t_0 as a function of the correction factor. Different families of points corresponds, from top to bottom, to samples of $2 \cdot 10^3$, $5 \cdot 10^3$, 10^4 and $5 \cdot 10^4$ events.

meet for $\gamma = 2$. This feature will be explained further in the *note* 2. The spread of the standard t_0 instead, is shown in fig. 5.2(right) for the different data samples size. The spread is minimum for a correction factor $\gamma \sim 1.3$ as well.

All the results are summarized in the plot 5.3(left) where, for each definition of the t_0 the best determination (minimum spread) is reported as a function of the sample size (the spread is observed to scale approximatively as $1/\sqrt{N}$ if N os the size of the sample).

It results that the displaced standard t_0 assures the higher accuracy. The spread is lower than a *ns* for samples of at least 5000 events.

The value of about 1.3 is derived in the *note* 1 below.

note 1

From the 5.8 the relation between the error on t'_0 and the errors on the fitted parameters is

$$\sigma^2_{t'_0} = \sigma^2_{t_0} + \gamma^2 \ \sigma^2_{\Delta T} - 2\gamma \ cov_{t_0,\Delta T} \tag{5.9}$$

which can be minimized with respect to the free parameter γ:

$$\frac{\partial \sigma^2_{t'_0}}{\partial \gamma} = 2 \ \gamma \ \sigma^2_{\Delta T} - 2 \ cov_{t_0,\Delta T} = 0 \tag{5.10}$$

that is to say

$$\gamma = \frac{cov_{t_0,\Delta T}}{\sigma^2_{\Delta T}}. \tag{5.11}$$

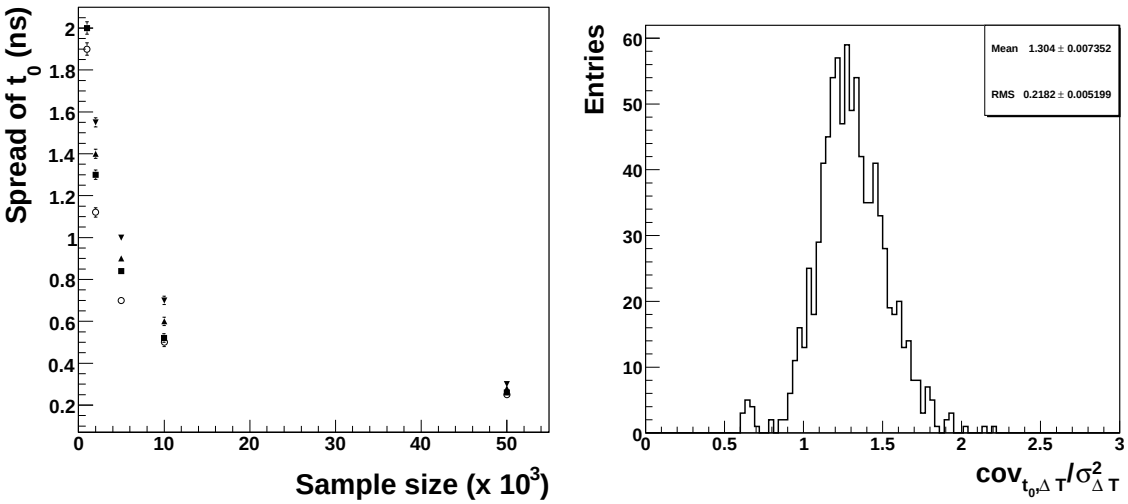

Figure 5.3: *Left*: Spread of the t_0 as a function of the sample size for the different definitions: displaced standard (open dots), displaced Fermi-Dirac (squares), Fermi-Dirac (triangles) and standard. *Right* : distribution of the correction factor of the equation 5.11 for the $5 \cdot 10^4$ sample events.

Hence, the minimum of the variance of t'_0 is

$$\sigma^2_{t'_0} = \sigma^2_{t_0} - \frac{cov^2_{t_0,\Delta T}}{\sigma^2_{\Delta T}} \tag{5.12}$$

if t'_0 itself is defined as

$$t'_0 = t_0 - \frac{cov_{t_0,\Delta T}}{\sigma^2_{\Delta T}} \cdot \Delta T. \tag{5.13}$$

The mean value of the variable γ in the 5.11, as shown in fig. 5.3, equals the one derived empirically from the distributions in fig. 5.2.

note 2

The t_0 can be defined as the parameter p_5 of the 5.4. This parameter is strongly correlated to the others, in particular, it is influenced by the function used to fit the central part of the spectrum: there is a double peak at the maximum of the distribution (e.g. fig. 5.1) which is poorly parametrized by the exponential at the numerator of the 5.4. This makes p_5 sensitive, for example, to sample size variation. the time range of the fit is not defined unabiguously. This introduce a bias in the determination of t_0, the turning point of the 5.6. Since maximum of the 5.6 is given mostly by the parameter F_0 (assuming, for simplicity, $p_1 = 0$) its value may vary significantly with the range chosen for the fit. In the example shown in fig. 5.4(left) a value of 192 ± 6 if found, increasing the range to later

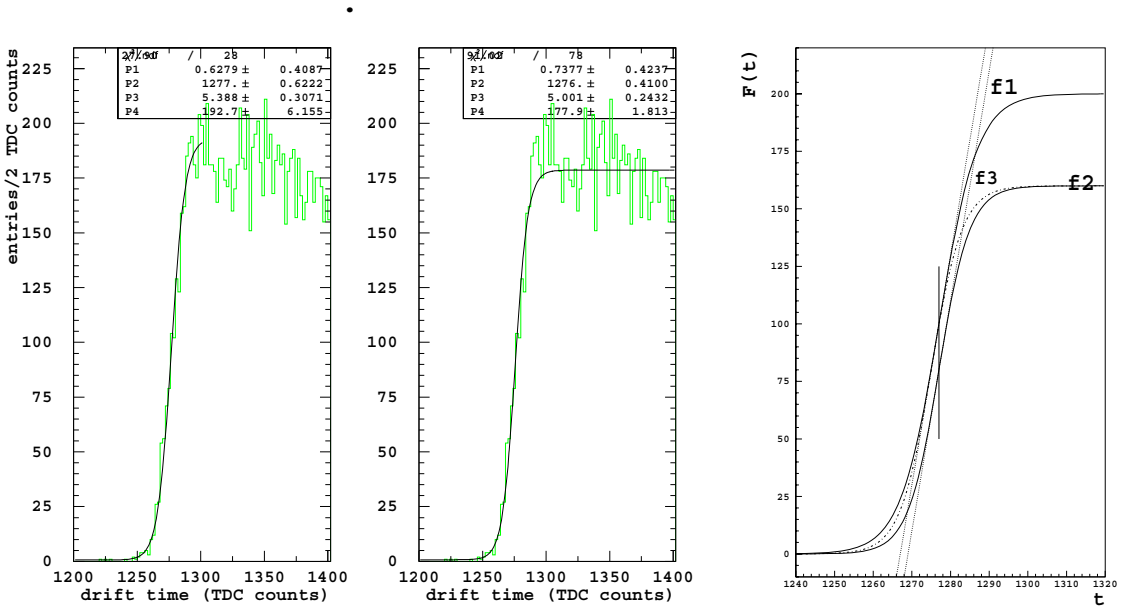

Figure 5.4: (*Left and Center*) Fit results for two different choices of the range. (*Right*) Curves f_1 and f_2 have the same slope and t_0 but different A parameter (eq. 5.14). Curve f_3 concides with f_1 in the rising edge: has the same slope but different t_0 and A. Tangents in $t = t_0$ are also drawn.

times the fitted value for F_0 is 177 ± 1 (center). The slope of the rising edge is proportional to F_0, in fact

$$\frac{dF(t)}{dt}|_{t=t_0} = \frac{F_0}{4\Delta T} \tag{5.14}$$

hence if F_0 varies by a factor, say k, the rise time parameter ΔT will be varied by the same factor to keep the slope unchanged as for the curves f_1 and f_2 in fig. 5.4(right). Those have the same slope and the same t_0 but are shifted along the abscissa. To make the rising edge of f_2 to coincide to the rising edge of f_1 the t_0 of the former function must be shifted to earlier times: curve f_3. As can be derived from the parameters of the two fits reported in 5.4 the found slope is the same but the t_0s differ (by about one TDC count) as a consequence of the different plateau F_0. Quantitatively (see also fig. 5.4(right)): the tangent $s(t)$ to $F(t)$ at $t = t_0$ is

$$s(t) = \frac{F_0}{4\Delta T} \cdot (t - t_0) + \frac{F_0}{2} \tag{5.15}$$

and intersetcs the time axis at $t - t_0 = -2\Delta T$; if $F_0 \to F_0' = kF_0$ and $\Delta T \to \Delta T' = k\Delta T$ $(k < 1)$ then 5.15 becames $s'(t) = F_0/4\Delta T \cdot (t - t_0) - kF_0/2$ which vanishes at $t - t_0 = -2k\Delta T$. Hence, the t_0 has to be shifted by the quantity $-2\Delta T(1 - k)$. Since a typical value for the lower limit of k is 0.9 and 4 TDC counts for ΔT the consequent t_0 variation is of about 1 TDC count. The 5.15

suggests that the quantity

$$t_0 - 2\Delta T \tag{5.16}$$

is invariant with respect to the tranformation $F_0 \rightarrow kF_0$:

$$t_0' - 2\Delta T' = t_0 - 2\ (1-k)\ \Delta T - 2k\Delta T = t_0 - 2\Delta T. \tag{5.17}$$

This explained the crossing point at $\gamma = 2$ for the curves in fig. 5.2.

5.1.2 Chamber response monitor. Noise

Parameters from the fit to a drift time distribution are useful for monitoring chamber response and performance. A typical hit tube distribution for a cosmic

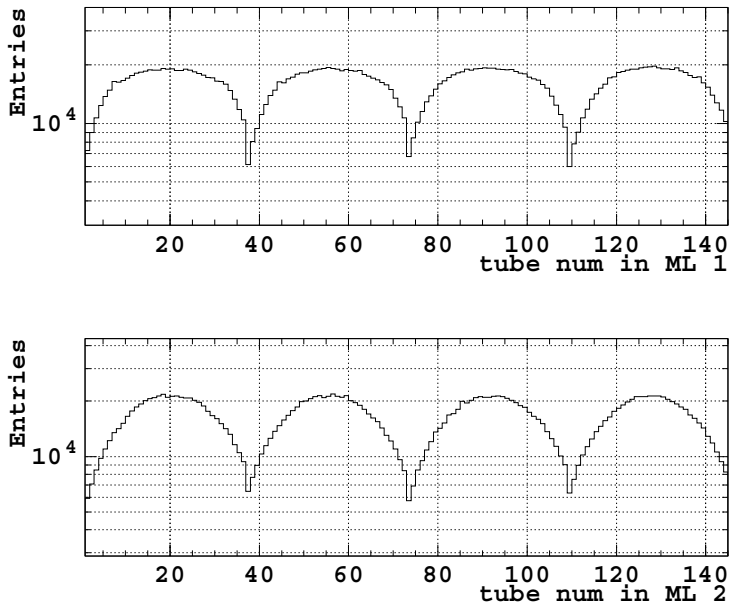

Figure 5.5: Tube hit distributuion on a sample of cosmic muon triggers.

muon trigger data sample (Sec. 4.1) are shown in figure 5.5. The shape of the hit distribution is determined by the angular coverage of the RPC hodoscope. The uniformity of the distributon assures that no dead or extremely inefficient electronics channels are present. Distribution of the parameters p_7, of the fit χ^2 and $\Delta t_{drift} = t_{max} - t_0$ (5.5) (fig. 5.6) can reveal significant deviations from the reference mean values.

The maximum drift time Δt_{drift}, in particular, is very sensitive to the gas properties: density (pressure and temperature) and composition. The tube Δt_{drift} distribution is shown in fig. 5.7 for two different cases. In the upper plot the distribution is not uniform and a "triplet" serial structure is visible. This behavior is

due to the gas distribution system layout: groups of three tubes of the same layer are supplied in parallel and the gas flows serially whithin each group. This may lead, expecially at the beginning of the gas supply, to an uneven gas density and composition inside the tubes belonging to the same group (lower density means higher drift velocity or shorter maximum drift time). The lower plot shows the same distribution once a uniform pressure whitin the chamber is reached. Gas leak or contamination can affect the Δt_{drift} distribution as well.

In fig. 5.8, instead, is shown the correlation between the average t_{max} of a BIL chamber and the temperature for different runs during the Test Beam data taking campaign. The GARFIELD (Sec. 4.4) simulation was used to compute t_{max} for a temperature of 27 $^{\circ}C$ and for different $Ar : CO_2$ mixtures. The composition that reproduce the data better is (93.5 : 6.5). It should be noticed, in this respect, that while the gas composition is verified to be stable in time (through the monitor of the drift parameters), the absolute gas mixture, as produced by the gas system, is not accurately known. A linear fit to the data in fig. 5.8 gives a variation of the maximum drift time with respect to the temperature of 2.5 ± 0.1 ns/K.

Noise

Entries outside the physical time window are due to uncorrelated hits from particle background in the experimetal hall or to electronic noise. The rate f_{random}

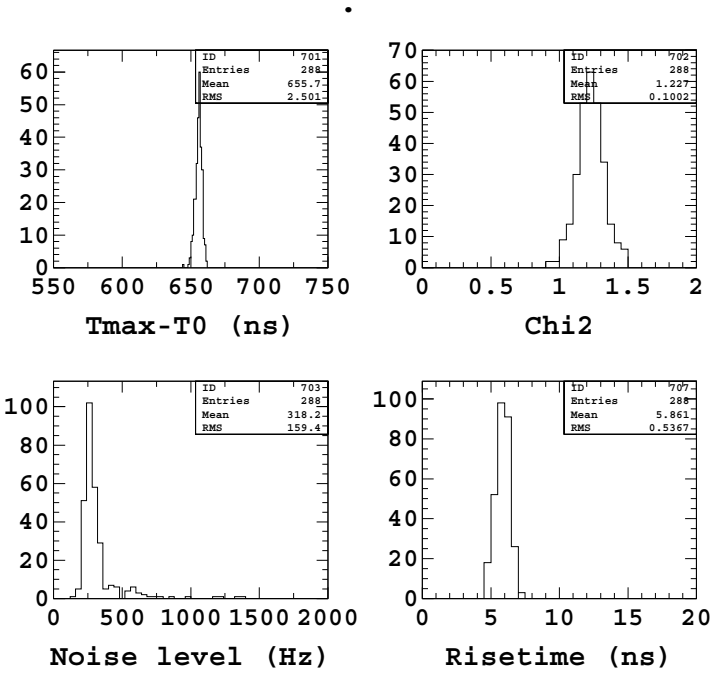

Figure 5.6: Distribution of fit parameters related quantities.

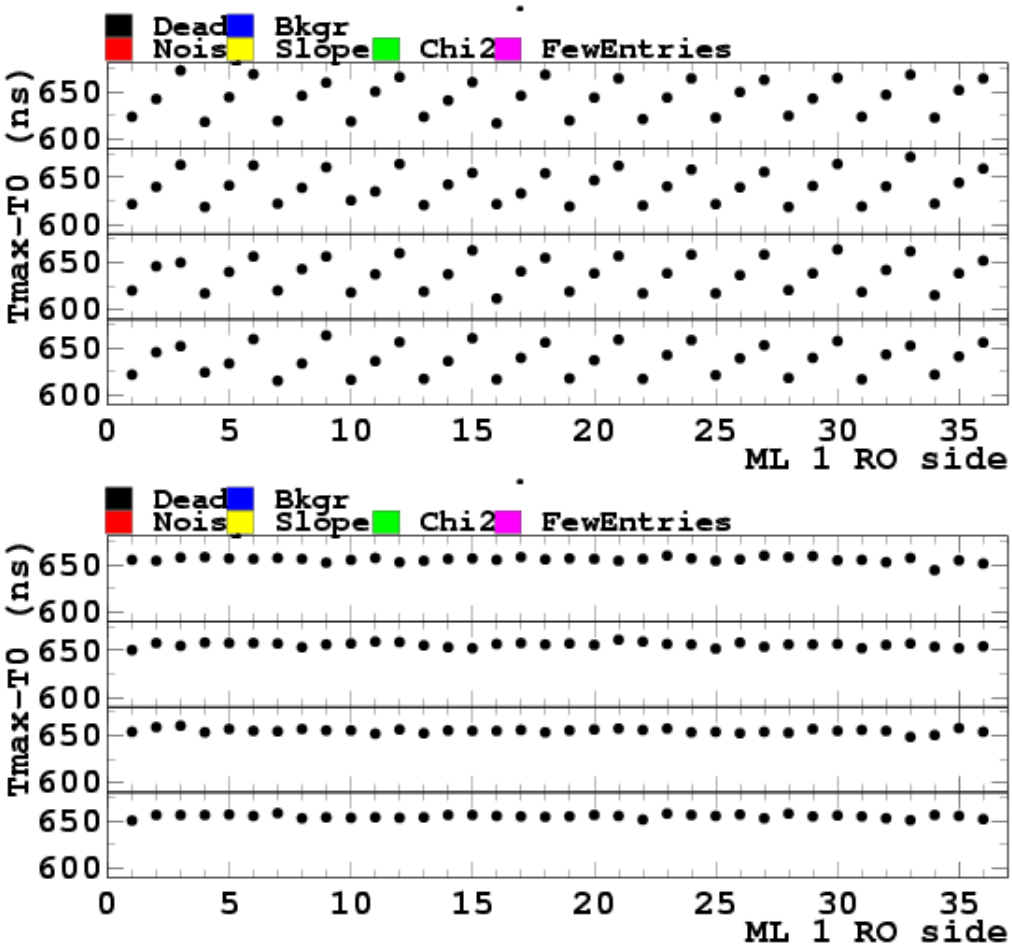

Figure 5.7: Maximum drift time distribution for uneven (*top panel*) and even (*bottom panel*) gas condition over the tubes (36) of the four layer of a multilayer.

of such random hits can be estimated as

$$f_{random} = \frac{n_{out}}{\Delta t_{out}} \frac{1}{N_{trig}} \tag{5.18}$$

where n_{out} is the number of entries outside the physical time window in the interval Δt_{out} and N_{trig} is the number of triggers. Parameter p_1 in the 5.4 is related to the noise rate since $n_{out} = p_1 \cdot \Delta t_{out}/\Delta t_{bin}$ (Δt_{bin} is the bin width). Typical noise distribution is shown in fig. 5.6.

5.2 Autocalibration

As anticipated in 4.3, in order to fully exploit the accurate mechanical properties of the chambers and the good spatial resolution that can be achieved with the drift tubes, a precise knowledge of the $r(t)$ relation is needed. The $r(t)$ relation

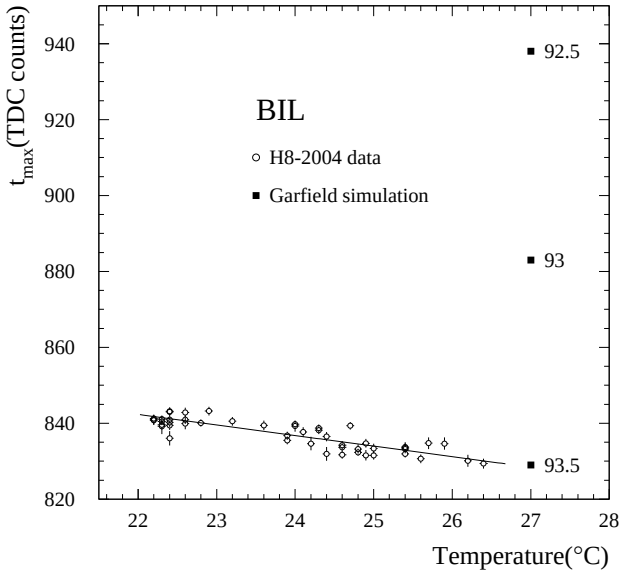

Figure 5.8: Observed drift spectrum length temperature dependence for the BIL chamber and simulated points for different gas composition at 27 $°C$.

depends on the operation conditions as pressure, temperature and local value of the magnetic field; therefore it can be different for tubes in different regions of the spectrometer. It is mandatory to have a procedure to measure and monitor $r(t)$ functions for chambers installed in the experiment.

The autocalibration aims at finding the space-time relation using only data from a chamber.

The method presented here is based on the assumption of straight line tracks.

- The t_0 of each tube has to be known (see previous section) so the drift time t^i_{drift} of a given hit, with associated measured time t^i_m, can be derived from the 5.3.
- The algorithm needs an input $r(t)$ which is used to convert drift times, t^i_{drift}, into drift radii $r_i = r(t^i_{drift})$. For each event, if a valid pattern of hits (candidate track) is found (Sec. 4.3.2), a fit to the line tangent to the drift circles (of radius r_i) is performed. The procedure is described in Sec. 5.3.
- Each fitted track is used to compute its *residuals* with respect to the drift circles used in the fit. The residual is the distance of closest approach between the track and a given drift circle, defined by a center (the wire coordinates) and a (drift) radius (fig. 5.9). The drift time range is divided in bins whose width is chosen to be 7.5 ns. Residuals distribution are produced for each time slice.

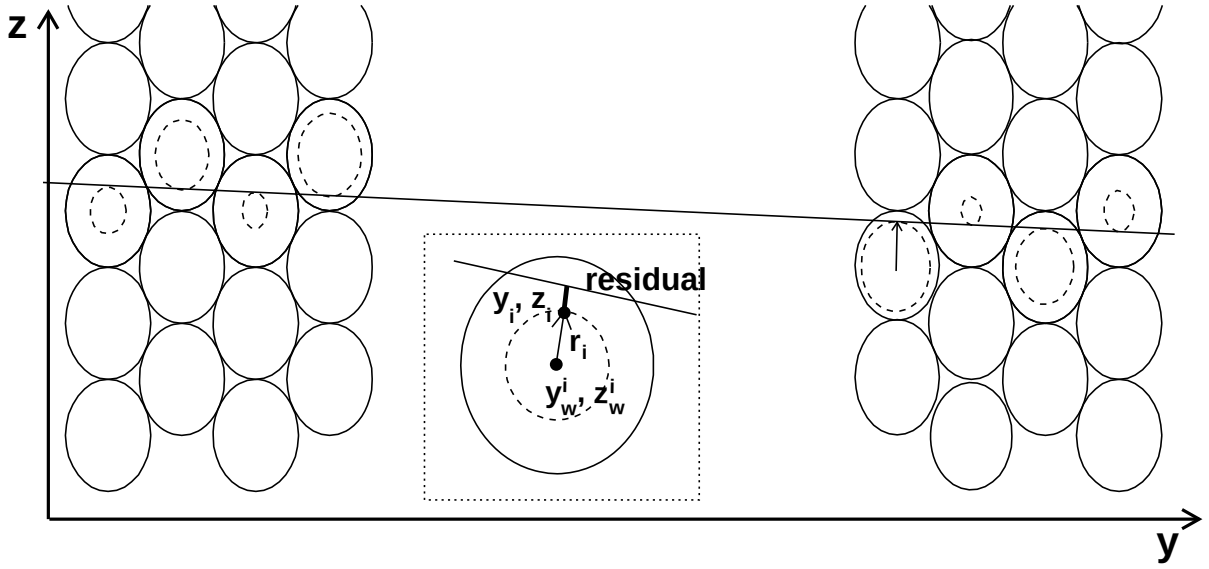

Figure 5.9: Representation of the residual, the drift radius, the wire coordinates and the track point of a track with respect to a generic hit i.

- The mean value of the residual distribution for each time slice is used to correct the initial $r(t)$ relation, which is therefore represented in tabular form.
- The procedure is iterated until the $r(t)$ relation reaches a prefixed accuracy or requiring that the i-th iteration doesn't differ from the (i-1)-th one within errors. In general, at each iteration a χ^2 cut is imposed on the reconstructred track.

5.3 An iterative method for geometrical distance linear least square fitting of circles

In this Section is presented a method developed to perform a fast fit of the tangent line to a pattern of circles.

In fig. 5.9 is represented the track of a muon traversing the 8 layers of an MDT chamber and the drift circles of the generated hits. The equation of a line in the plane perpendicular to the wires can be written as (fig. 5.9)

$$z = a\ y + b. \tag{5.19}$$

The determination of the coefficients a and b translates into the problem of the linear least-squares orthogonal distances fitting of circles. The χ^2 function to be

minimized is therefore defined as follows:

$$\chi^2(a,b) = \sum_{i=1}^{N} \omega_i \left[\frac{|a\ y_w^i + b - z_w^i|}{\sqrt{1+a^2}} - r_i \right]^2 = \sum_{i=1}^{N} \omega_i \cdot \delta_i^2. \tag{5.20}$$

The ratio in the parenthesis is the distance of the line (5.19) to the point (y_w^i, z_w^i). The sum runs over the N hits associated to the track (*i.e.* in the pattern). For each hit, (y_w^i, z_w^i) are the coordinates of the tube center (the wire), r_i is the corresponding drift radius and ω_i is the weight associated to the hit. The quantity δ_i, the residual, is the distance between the track and the circle of radius r_i centered at (y_w^i, z_w^i) (fig. 5.9).

The minimization of the (5.20) leads to a system of two equations

$$\partial\ \chi^2/\partial\ a = 0,\ \partial\ \chi^2/\partial\ b = 0 \tag{5.21}$$

wich are non-linear with respect to the unknown parameters a and b.

A linear approximation of the system can be derived once a good guess of the coefficients a, b is provided. The problem is then solved iteratively.

The first estimation of the track line is performed computing the four possible tangents to the first and the last drift circle of the pattern. Among these lines, is chosen the one giving the smallest χ^2 computed with the function (5.20) using the remaining hits. The parameters of the selected track, say (a_0, b_0), are then used to compute the *track point* (x_i, y_i) of each hit i: the point, belonging to a circle with radius r_i, of closest approch to the track.
Formulated in terms of the track points $y_i = y_i(a_0, b_0)$, $z_i = z_i(a_0, b_0)$, the problem reduces to the orthogonal distance (i.e. the geometrical distance) least-square fitting of points. The quantity to be minimized becomes

$$\chi^2_{t.p.}(a,b) = \sum_{i=1}^{N} \omega_i\ \frac{(a\ y_i + b - z_i)^2}{1+a^2} \tag{5.22}$$

and the system (5.21) can be solved analitically. The extended algebra is reported in the Appendix .1. The second equation gives[1]

$$b = \bar{z}\ - a\ \bar{y}. \tag{5.23}$$

Where $\bar{z} = \sum \omega z / \sum \omega$ and $\bar{y} = \sum \omega y / \sum \omega$ are the weighted average of the z and y points coordinates. The first equation instead leads to a quadratic form in a whose solutions can be written as

$$a_\pm = -A \pm \sqrt{A^2+1} \tag{5.24}$$

[1]Hereinafter the summation symbol may be omitted, *e.g.* $\sum_{i=1}^{N} \omega_i z_i y_i \equiv \sum \omega z y$.

defining

$$A = \frac{1}{2}\frac{(\sum \omega z^2 - \sum \omega \cdot \bar{z}^2) - (\sum \omega y^2 - \sum \omega \cdot \bar{y}^2)}{\sum \omega \cdot \bar{y}\bar{z} - \sum \omega yz}. \tag{5.25}$$

The two couples of possible parameters, $a_\pm$ and $b_\pm = \bar{z} - a_\pm\ \bar{y}$, as expected, correspond to two mutually perpendicular tracks, in fact

$$a_+ = -1/a_-.$$

The one that gives the smallest value of (5.22) correspons to the physical solution.

The right solution can be derived also through a consideration wich will be useful in the following. For tracks almost parallel to the y axis, the problem is not different from the usual least square fit, which minimize the vertical (algebraic) distance. That means that in the limit $a << 1$ or $A << 1$ the two methods has to lead to the same solution. In the requested approximation holds

$$a_\pm = -A \pm A\ \sqrt{1 + \frac{1}{A^2}} \simeq -A \pm A\ \left(1 + \frac{1}{2}\frac{1}{A^2}\right) \tag{5.26}$$

and $z \simeq \bar{z}$. Only $a_+ \simeq 1/2A$ gives the expected solution (see next section).

The track parameters derived this way, are then used to calculate a new set of track points to be intorduced in the (5.23) and the (5.25) and obtain a better estimation for a and b. The procedure is repeated until the correction is smaller than 0.1 μrad and 0.1 μm for the slope

$$m = arctg(a)$$

and the intercept b respectively. The number of iterations needed is less than 3 in the 95% of the cases.

5.3.1 Statistical uncertainty

The statistical error of the angular coefficient does not depend on the reference system. Thus the algebra can be simplified taking a rotated system with the y axis coincident to the fitted track direction. This case corresponds to the approximation $a << 1$ which implies $a = 1/2A$ as reported in the previous section. The results can be derived directly also: the (5.22) equals the χ^2 function of the standard case of vertical (algebraic) distance minimization. Furthermore, the translation to the barycenter system ($y_i \to y_i - \bar{y}$) can be applied in order to have $\bar{y} = 0$. In such a system, from the (5.22) and (5.21) results

$$\partial\chi^2/\partial a \underset{a^2\to 0}{=} a \cdot \sum \omega y^2 + b \cdot \sum \omega y - \sum \omega zy \underset{\bar{y}=0}{=} a \cdot \sum \omega y^2 - \sum \omega zy = 0. \tag{5.27}$$

which implies, considering also the (5.23),

$$a = \frac{\sum \omega z y}{\sum \omega y^2}, \quad b = \bar{z} = \frac{\sum \omega z}{\sum \omega}. \tag{5.28}$$

From the (5.28) the error propagation gives

$$\sigma_a^2 = \frac{\sum \omega^2 y^2 \sigma_z^2}{(\sum \omega y^2)^2}, \quad \sigma_b^2 = \frac{\sum \omega^2 \sigma_z^2}{(\sum \omega)^2}. \tag{5.29}$$

The error on b is minimum when calculated in the barycenter system, in fact, considering that a and b are decoupled (see (5.27),(5.28)) the error on b in a generic system, shifted by Δy along the y axis, is $\sigma_{\bar{z}}^2 + (\Delta y)^2 \cdot \sigma_a^2$. Unless otherwise stated all the quantities are referred to the system of the barycenter.

In the (5.29) σ_{z_i} is the spatial resolution of the point (y_i, z_i), that is to say $\sigma_{z_i} \equiv \sigma(r_i) \equiv \sigma_i$ the tube resolution calculated at the drift distance $r = r_i$, as shown in Fig. 5.9. The dependence of the resolution on the drift radius can be

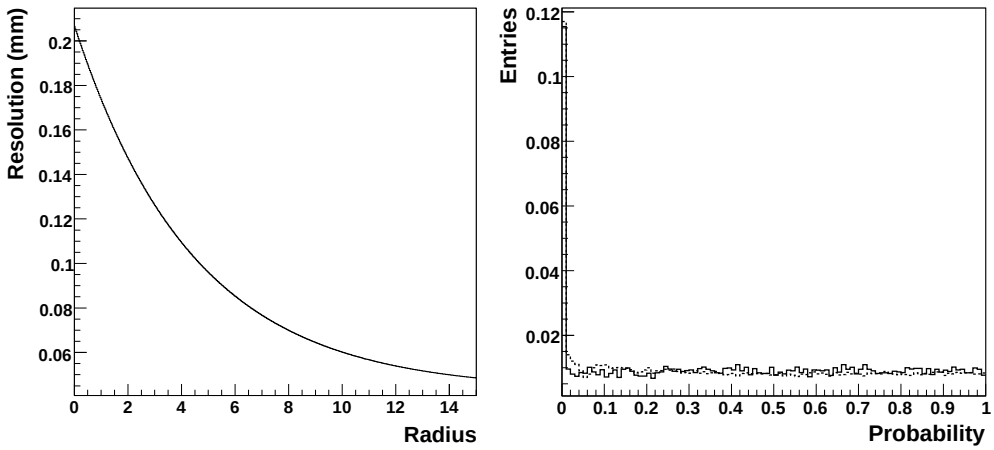

Figure 5.10: *Left*: Tube resolution as a function of the drift radius. *Right*: Track fit probability distribution for Monte Carlo (bold) and data (dashed).

fitted with an exponential function

$$\sigma(r) = p_1 + p_2 \cdot e^{-\frac{r}{p_3}}. \tag{5.30}$$

The values of the three parameters calculated from a fit to the Test Beam data are $p_1 = 0.0431$, $p_2 = 0.164$ and $p_3 = 4.432$. The measurement is described in the Ch. 7. The curve is reported in 5.10.left. Close to the wire is $\sigma(r = 0) = p_1 + p_2 \simeq 200\ \mu m$ and $\sigma \simeq p_1 \simeq 50\ \mu m$ close to the tube wall. The distribution of the χ^2 fit probability distribution is shown in Fig. 5.10.right. The bold line is produced with the Monte Carlo simulation using the resolution (5.30) and weights $\omega = 1/\sigma^2$ (as justified below) while the dashed line correpsonds to the

Test Beam data. The peak at low probabability is due to the δ-ray production. In the Monte Carlo the δ-electrons production (Sec. 4.5, 3.2.1) probability has been tuned in order to reproduce the same ratio between the total entries and the entries in the first bin (χ^2 probability lower than 1%) of the distribution observed in the data. The method gives a δ-electron emission probability of about 3%.

Requiring $\partial\sigma_b^2/\partial\omega_i = 0$ it can be demonstrated that the choice of the weights which minimize the statistical error is $\omega_i \propto 1/\sigma_i^2$ and the (5.29) can be written as

$$\sigma_a^2 = \frac{1}{\sum \omega y^2}, \quad \sigma_b^2 = \frac{1}{\sum \omega}. \tag{5.31}$$

In the case of a constant radial resolution $\sigma(r) = \bar{\sigma}$ it is $\sum \omega = N\bar{\sigma}^2$ therefore

$$\sigma_{ave} = \frac{1}{\sqrt{\frac{1}{N}\sum \frac{1}{\sigma^2}}}. \tag{5.32}$$

is a good estimator of the average tube resolution. The distribution of the quantity (5.32) from the experimental data has a statistical mean of $0.072 \pm 0.005\ mm$. From the (5.32) follows also that the average tube resolution can be calculated from the functional form $\sigma(r)$:

$$\sigma_{ave} = \frac{1}{\sqrt{\frac{1}{R}\int_0^R \frac{1}{\sigma^2(r)}\ dr}} \tag{5.33}$$

where $R = 14.6\ mm$ is the inner tube radius. Using the expression (5.30) with the measured parameters and the (5.33) $\sigma_{ave} = 0.071\ mm$. With a constant resolution $\bar{\sigma}$ the 5.31 become

$$\sigma_a^2 = \frac{\bar{\sigma}^2}{\sum y^2}, \quad \sigma_b^2 = \frac{\bar{\sigma}^2}{N}. \tag{5.34}$$

Relations (5.34) assuming $\bar{\sigma} = \sigma_{ave} = 0.072\ mm$ can be used for a rough (conservative) estimation of the angular (slope) and spatial resolution of the detector. The spatial resolution is defined as the resolution on the parameter b in the barycenter system and is also referred to as the resolution at the super point. Defining Δy_{ML} the distance between the y position of the centers of two outermost tubes it is $\sigma_m \simeq \sigma_a \simeq \sqrt{2}\,\sigma_{ave}/\Delta y_{ML} \sim 0.28\,mrad$ and $\sigma_b \simeq \sigma_{ave}/\sqrt{8} \sim 0.025\,mm$ for an 8 layers chamber ($\Delta y_{ML} \simeq 350\ mm$).

The slope and super point resolution has been studied in detail with the simulation described in 4.5. The resolution on the track parameters m (i.e. $arctg(a)$) and b has been defined as the gaussian width of the distribution of the difference between the generated value of the parameter and the one fitted using the

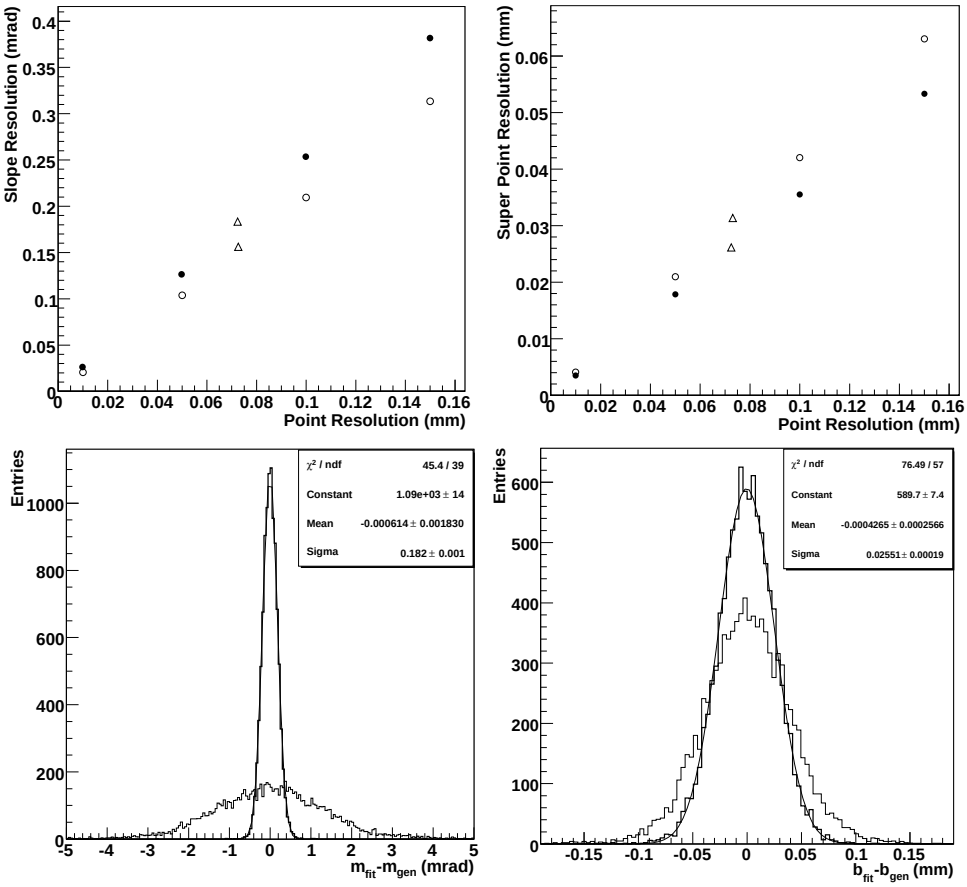

Figure 5.11: *Top Left* : Resolution on the track slope as a function of the resolution for a 8 layers (full dots) and 6 layers (open dots) layout. The triangle are the results of the extrapolation of the (average) point resolution from the slope resolution calculated using the parametrization 5.30 as input to the simulation. *Top Right* : analogous results for the resolution on the super point. *Bottom Left* : Distribution of the difference between the generated track slope and the reconstruced one. The resolution used is parametrization 5.30 fitted to Test Beam data. The narrowest distribution corresponds to a fit over the two multilayers of a 8 layers layout. The wider to a fit over one multilayer (4 layers) only. *Bottom Right* : analogous results for the resolution on the super point.

algorithm described the previous section. Fig. 5.11 shows the slope and super point resolution as a function of the tube resolution, assumed as a constant, for both the chamber layouts, 8 and 6 layers (Sec. 2.4.1). It is reported also the results using the measured resolution function (5.30) with the quoted parameters measured at the Test Beam. It can be noticed that this case would correspond to the behaviour of a chamber with a constant resolution equal to the average one (eq. 5.33). The effect of the delta rays distorces only the tails of the shown dis-

tributions. Tracks with one hit per layer only have been selected. As expected an 8 layers chamber allows a better point resolution thanks to the higher number of measurement layers while a 6 layers chamber is characterized by a better angular resolution thanks to the larger distance between the two multilayers. If only hits from one multilayer are used the slope resolution is worsened by a factor of 7 (4 layers multilayer) while the superpoint resolution scales by a factor $\sqrt{8}/\sqrt{4}$ only (fig. 5.11.bottom).

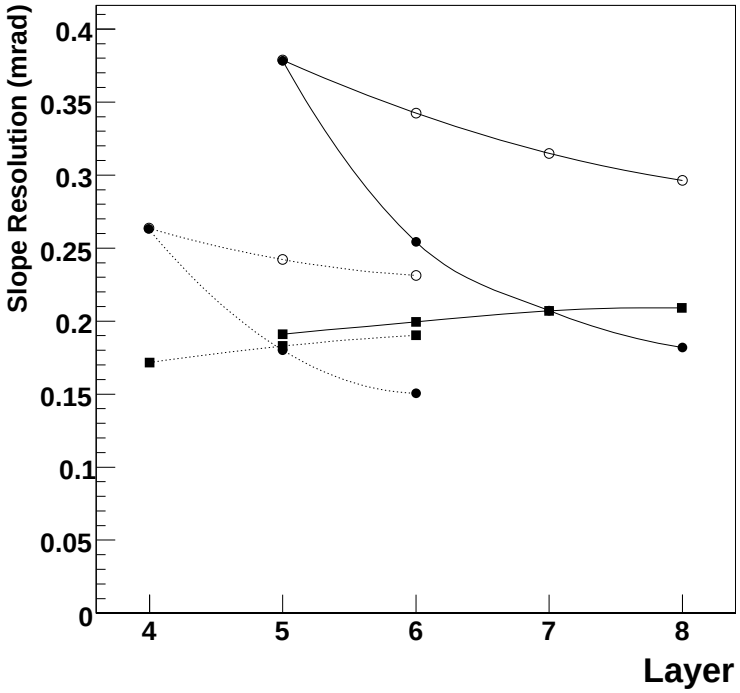

Figure 5.12: Points connected by the continuous line refers to an 8 layers chamber while the points connected by the dashed lines to a 6 layers layout. Full dots report the results for segments having increasing number of hits as indicated in the layer number in the abscissa. Open dots describe the case when only one hit on the layer indicated in the abscissa is added. Thus these segments has always 5 or 4 hits depending on the layout. Squared markers describe the configuration which occour if the hit on the layer indicated on the abscissa is skipped. Thus these segments has always 7 or 5 hits depending on the layout.

The effect on the angular resolution of the number of hits differs depending of their geometrical disposition (configuration) whithin the chamber. The effect can be drawn from the synoptical graph of fig. 5.12 which covers the most frequent possibilities. Details can be found in the caption. These results can be used to choose the better strategy in the pattern selection according to the needs.

5.3.2 Least square weights

In the Ch. 7 will be displayed a method to derive the resolution function $\sigma(r)$ using the results of the track fit itself.

Hence, the resolution function is not know at the track fitting stage and cannot be set $\omega \propto 1/\sigma^2$. If constant weight $\omega = \omega_c$ is assumed, from the 5.28, the value of the parameters a,b is independend on ω_c

$$a = \frac{\sum zy}{\sum y^2}, \quad b = \frac{\sum z}{N} \tag{5.35}$$

and the errors as well (eq. 5.29):

$$\sigma_a^2 = \frac{\sum y^2\sigma^2}{(\sum y^2)^2}, \quad \sigma_b^2 = \frac{\sum \sigma^2}{N^2}. \tag{5.36}$$

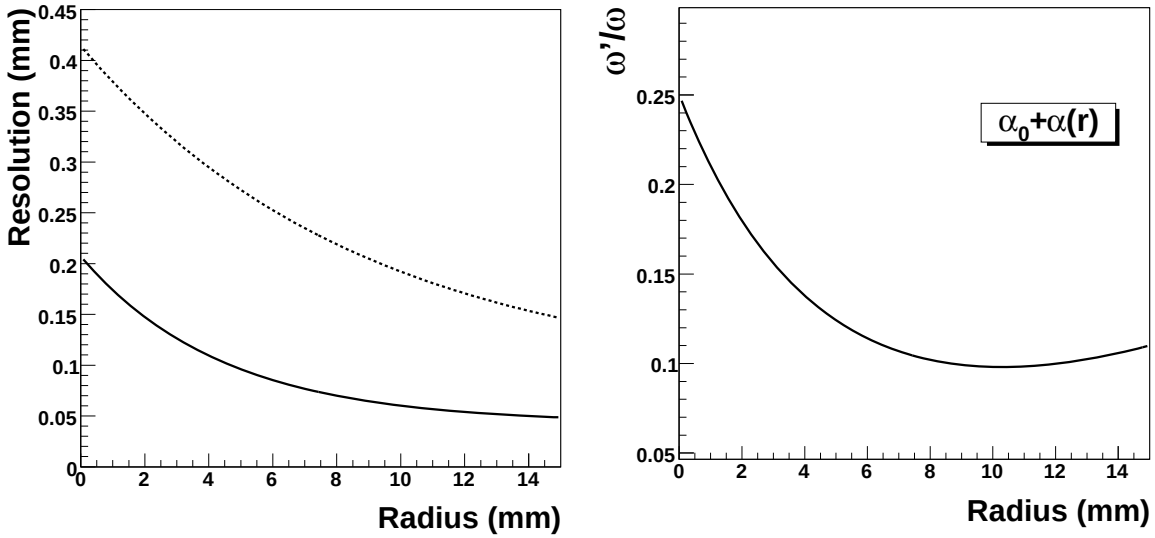

Figure 5.13: *Left* The "true" resolution, used at generation level, (bold line) and a resolution used as the weight (dashed line) for the fit. It is obtained multiplying the true parameters by a factor of 2. *Right* the ratio of the two corresponding weight functions.

In most of the cases it is possible to guess a resolution σ' similar to the, "true", physical one σ. The difference between the two corresponding weight function can be written in the form

$$\frac{\omega'}{\omega} = \alpha_0 + \alpha(r)$$

where $\alpha(r)$ takes into account the non proportionality component between $\omega' = 1/\sigma'^2$ and $\omega = 1/\sigma^2$. Hence the parameter b, for example, is the sum of two contributions:

$$b = \frac{\alpha_0 \sum \omega z}{\alpha_0 \sum \omega + \sum \alpha\omega} + \frac{\alpha\omega \sum z}{\alpha_0 \sum \omega + \sum \alpha\omega}$$

In fig. 5.13 it is shown the ratio ω'/ω for a pessimistic assumption about the resolution: the function dawn has been obtained by multiplying the true parameters (eq.5.30) by a factor of two. It can be observed that $\alpha(r)$ assumes values of the order of 10^{-1} (from 0.1, that is the constant term α_0, to 0.25 or so) therefore the term $\alpha\ \omega$ in the last equation is a second order correction. It will be showed in the next Sections that for a reasonable choice of the parametrization the the actual value of the weights has a minor effect on the calibration.

5.4 Simulation results

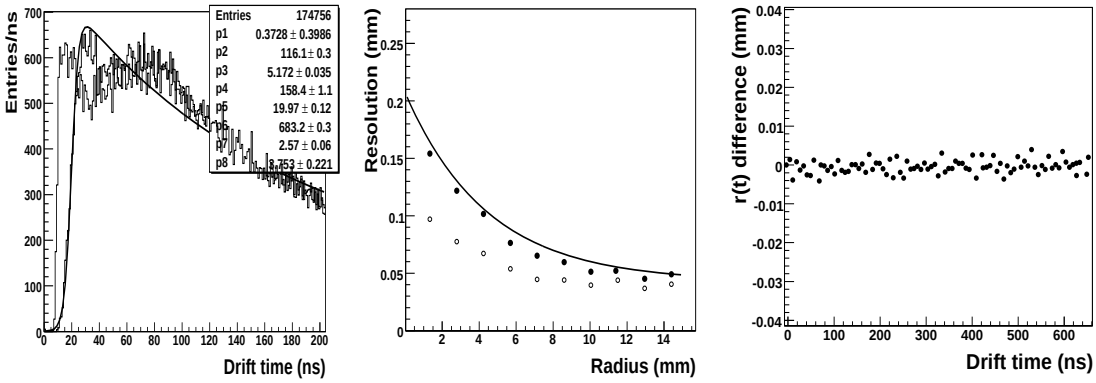

Figure 5.14: *Left*. First part of the simulated drift spectrum for the case of two different discriminator thresholds. *Central*. Resolution corresponding to the two thresholds (points). Resolution curve from a fit to the experimental data is also shown for comparison. *Right*. Difference in the space-time relation obtained with the autocalibration method with respect to the relation used at the simulation level.

The autocalibration algorithm was validated with the simulation program described in Sec. 4.5. As reported in Sec. 5.1.2 the gas composition setting in GARFIELD was tuned so as to reproduce the drift spectrum length observed in the data. The computation of the drift time needs the value of the discriminator threshold to be specified. It was decided to set the threshold value by requiring the simulated drift time spectrum to have a rising time compatible with the one measured from the data. From the 5.14 can be verified that the chosen value for the threshold implies a rise time of about 2.6 ns, to be compared to 3.5 tdc counts of the experimental spectrum 5.1. A further check is the comparison between the resolution calculated from the simulation and the measured one (Sec. 7). The result obtained for an arbitrary lower value of the threshold is also shown for comparison. A sample of 10^5 tracks within the angular range $a = [-0.3, 0.3]$ was then generated and used as input to the calibration. The resulted $r(t)$, after 20

iterations (see next sections), was compared with the expected "true" space-time relation[2]. As shown in fig. 5.14 differences between the two $r(t)$ are at the micon level.

5.5 Systematics

The basic procedure followed for the autocalibration is outlined in the Sec. 5.2 while the details of the track (segment) fit are reported in Sec. 5.3. A sample of type $BILrot$ (about 10^5 segments) taken with the Test Beam setup (Sec. 4.2) has been used for the following considerations.
Unless otherwise stated the track fit is performed using both the multilayers and the correction to the $r(t)$ are calculated separately for the two multilayers. In fact the $r(t)$ of the two multilayers could in general differ because of different operating (mostly gas related) conditions.
The results obtained processing all the events of the indicated sample, with 8 hits (one per layer), accepting tracks with angular spread $a = [-0.3, +0.3]$ (corresponding to $[-17^o, 17^o]$, the maximum value allowed for the rotating BIL), $\chi^2/ndf < 10$, and using the optimized $t_0's$ fit (as decribed in Sec. 5.1.1) is taken as refence. Fig. 5.15(top), relatively to the reference, shows the average of the residual distribution in the various time slices: these are the values of the correction to apply to the $r(t)$ relation. It can be seen that after 5 iterations the correction is below 5 μm. In fig. 5.15(bottom) the residual distribution is shown as a function of the drift time. The larger spread for small drift times reflects the behaviour of the resolution near the wire (Ch. 7). The obtained $r(t)$ is shown as well. For a given choice of the parameters of the autocalibration algorithm the minimum mumber of iterations needed depends on the initial $r(t)$ relation used. The $r(t)$ used to produce the plot of fig. 5.15, for example, does not differ from the calculated one for more than 0.5 mm.
A useful parameter to describe the progress of the calibration is the "convergence factor" $\mu(i)$, defined, for a given iteration i, as the quadratic average of the $r(t)$ corrections

$$\mu(i) = \sqrt{\frac{\sum_{j=1}^{N}(\delta r_{ji})^2}{N}} \tag{5.37}$$

where j runs over the N time bins. The behaviour of the convergence μ with increasing iterations, fig. 5.16, shows an exponential decreasing behaviour which turns into a plateau for a value of the convergence of about 10^{-4} mm. The convergence is therefore quite rapid as can be observed from the plot of the "radius

[2]The tabular form of true $r(t)$ was obtained dividing the drift time range in slices 7.5 ns wide and taking for each bin the average value of the time (simulated) and the corresponding (generated) radius.

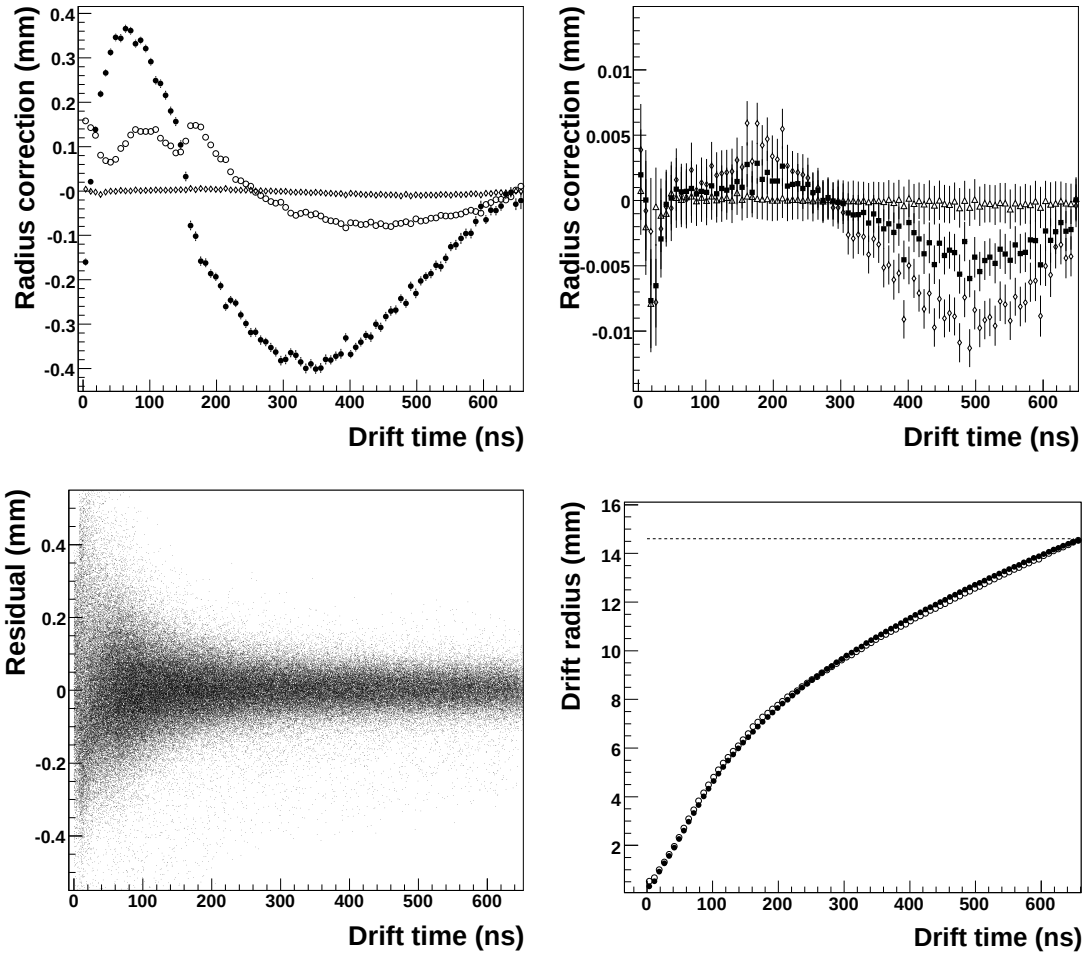

Figure 5.15: *Top Left*.Distribution of average residuals after, from bottom to top, the iteration 1, 2 and 5. Analogous distribution after the iteration 5,6 and 10 is shown in the plot on the right. *Bottom Left* Residuals distribution (iteration 10). *Right* Resulting $r(t)$ (for the first multilayer) relation with 1 (open dots) and 10 (full dots) iterations.

trajectories": the variation of the radius r_i of a given time slice i with respect to the iteration, or the convergence. To each radius is subtracted its final (last iteration) value so as to represents all the time slices on the same vertical scale. Each radius converges monotonically to its asymptotic value. Variation are indeed below few microns for $\mu < 10^{-3}$ mm.

In the following a study on the dependence of the $r(t)$ relation on:

- number of events processed,
- correction factor,

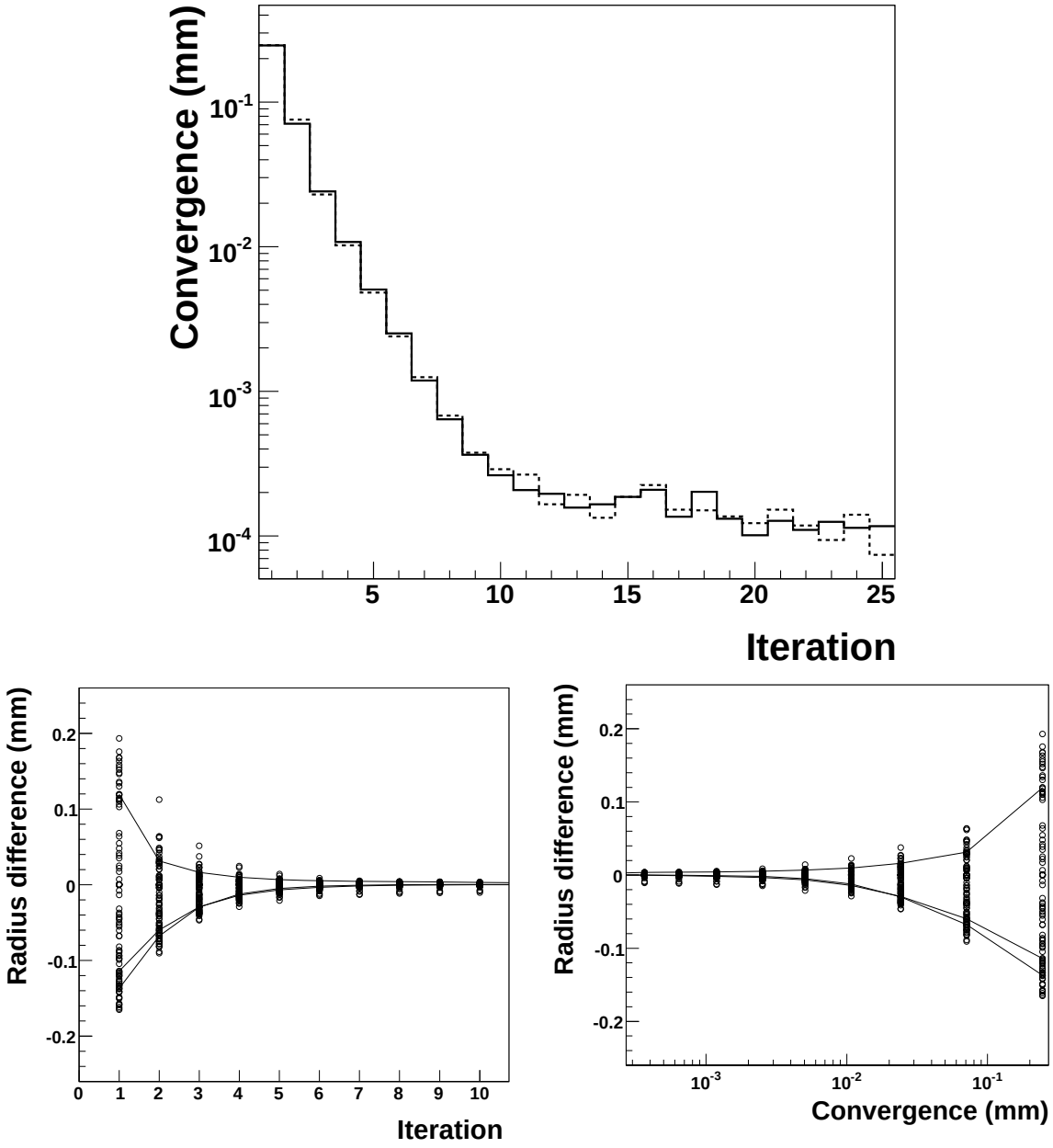

Figure 5.16: *Top*: Convergence factor as a function of the iteration for the two multilayers separately. *Bottom*: Trajectory of the radii (see text) as a function of the iteration number ($Left$) and of the convergence factor ($Right$).

- input resolution function,
- tube $t_0's$,
- track angular spread,

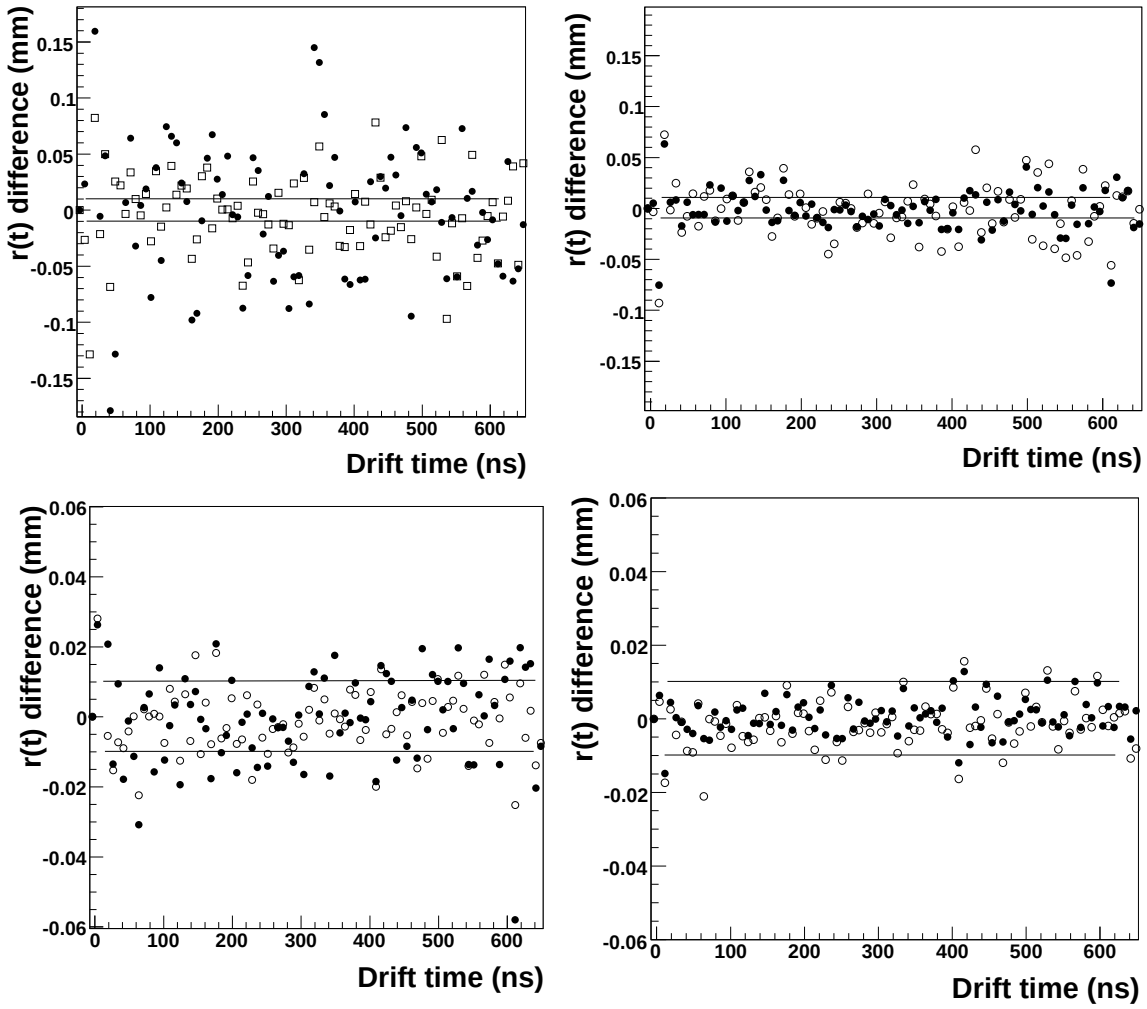

Figure 5.17: r(t) differences for various sample sizes with respect to the reference r(t). *Top*: 1000 and 2000 (full dots) events, 3000 and 5000 (full dots). *Bottom*: 10^4 and $2 \cdot 10^4$ (full dots), $3 \cdot 10^4$ and $4 \cdot 10^4$ (full dots). Lines delimit the area where the difference is lower than 10 μm.

is summarized. For all $r(t)'s$ (reference one included) the minimum number of iteration is fixed by requiring a distribution of the average residuals (i.e. the correction to be applied to the $r(t)$) is within few μm, that means, by requiring the convergence 5.37 to be lower than few μm. In what follows the events of a subsample are uniformly distributed over the whole sample of origin in order to avoid systematic effects related to possible variations of the operating conditions during the data taking.

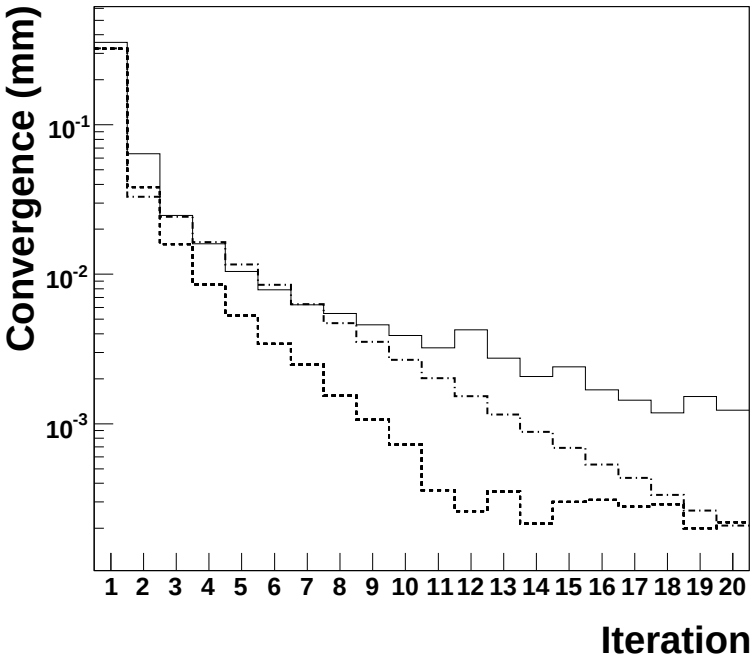

Figure 5.18: Convergence with respect to the value of the factor α (see text). The central curve corresponds to the reference ($\alpha = 1$). The lower(upper) curve corresponds to $\alpha = 1.5$ ($\alpha = 0.5$).

5.5.1 Sample size

In fig. 5.17 are shown the differences in the calculated radius for each time slice with respect to the reference $r(t)$ for different sizes of the processed sample. With 10×10^3 events differences are within 20 μm and within $10\mu m$ using at least 30×10^3 events.

5.5.2 Correction factor

In general, at each iteration, the correction to be applied to a given radius (5.2) can be multiplied by a factor α (which in the standard procedure is unitary). Convergence speed is very sensitive to this factor as shown in fig. 5.18. and reaches a minimum for the empirical value $\alpha \sim 1.5$ where the number of iterations needed is almost half of the number nedeed in the case $\alpha = 1$ to reach the same convergence.

5.5.3 Input resolution

In order to perform the track fit, a resolution function (i.e. an assumption about the least square weights, see Sec. 5.3.2) has to be provided to the autocalibration algorithm. The reference $r(t)$ is calculated using the resolution measured from the data (Ch. 7). A comparison with the $r(t)$ obtained using both a higher

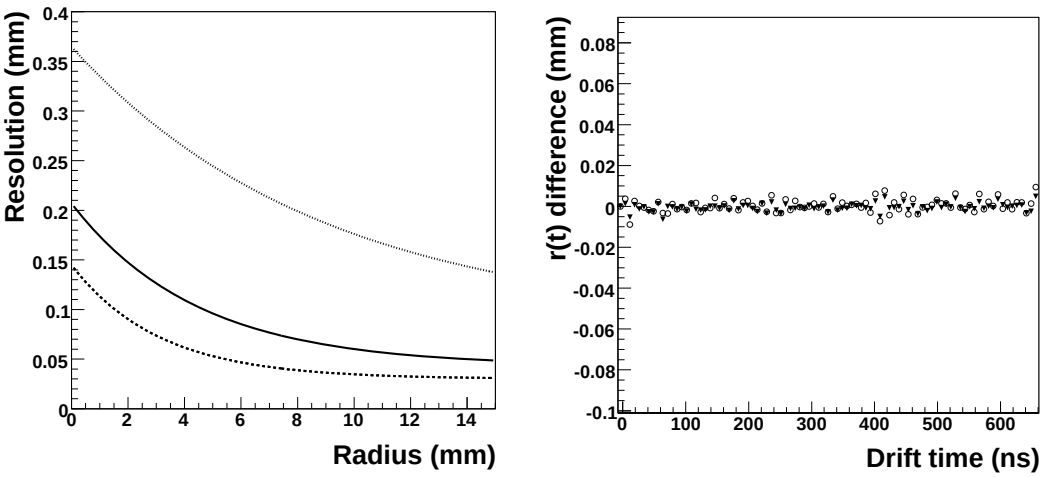

Figure 5.19: On the left plot the middle curve is the resolution function used to determine the reference $r(t)$. On the right plot the $r(t)$ difference, with respect to the reference $r(t)$, using the two parametrizations (upper and lower curve) in the left plot. Full dots correspond to the worse (upper) resolution function.

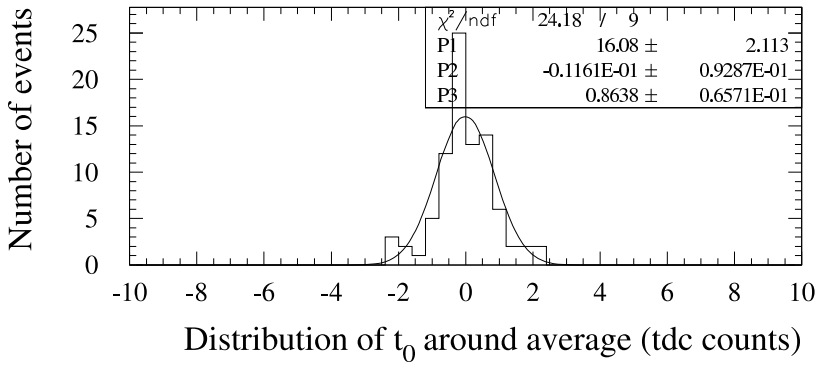

Figure 5.20: Distribution of the $t_0's$ in a chamber.

and a lower resolution (reported in fig. 5.19(left)) is shown in fig. 5.19(right). For very general assumptions about the resolution function, differences in the calculated $r(t)$ are neglibile.

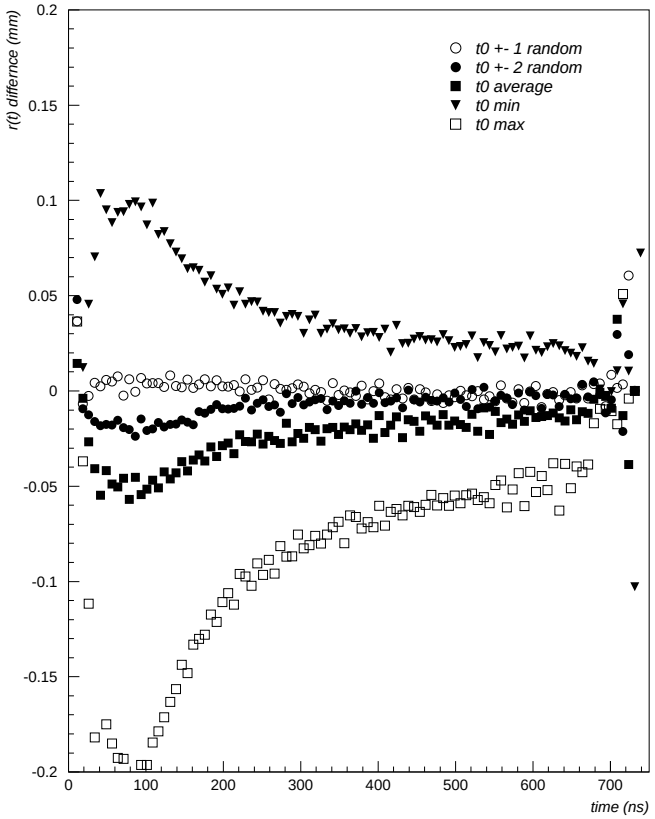

Figure 5.21: Differences with respect to the refrence $r(t)$ when the t'_0s are smeared (see text) and when a unique value corresponding to the average, the maximum or the minimum one is assumed. The shape is typical of a shift along the time axis (Sec. 6.2.1).

5.5.4 tube t_0

The precision in the determination of the t_0 of a single tube has been studied in the Sec. 5.1.1. Fig. 5.20, instead, shows a typical distribution of the t'_0s within the chamber. Tube-to-tube variation have a spread of about 1 TDC count as well. It is useful to quantify the sensitivity of the autocalibration algorithm to the t'_0s definition adopted and to the tube dependent t'_0s variation. Fig. 5.21 reports the differences, with respect to the reference, of the $r(t)'s$ calculated by smearing the fitted t'_0s adding at random ± 1 TDC count or zero TDC counts. The same is repeated by adding ± 2, ± 1 or zero TDC counts. The former operation does not vary the $r(t)$ by more then $10\mu m$ while the latter causes a deviation up to $20\mu m$ close to the wire. The effect is larger if the average t'_0s is used for all the tubes. The discrepancies are as high as 100 μm if the maximum or the minimum value of the t'_0s is assumed. The drift-spectrum-like shape of the observed differences

is due to a relative shift along the time axis as explained in Sec. 6.2.1.

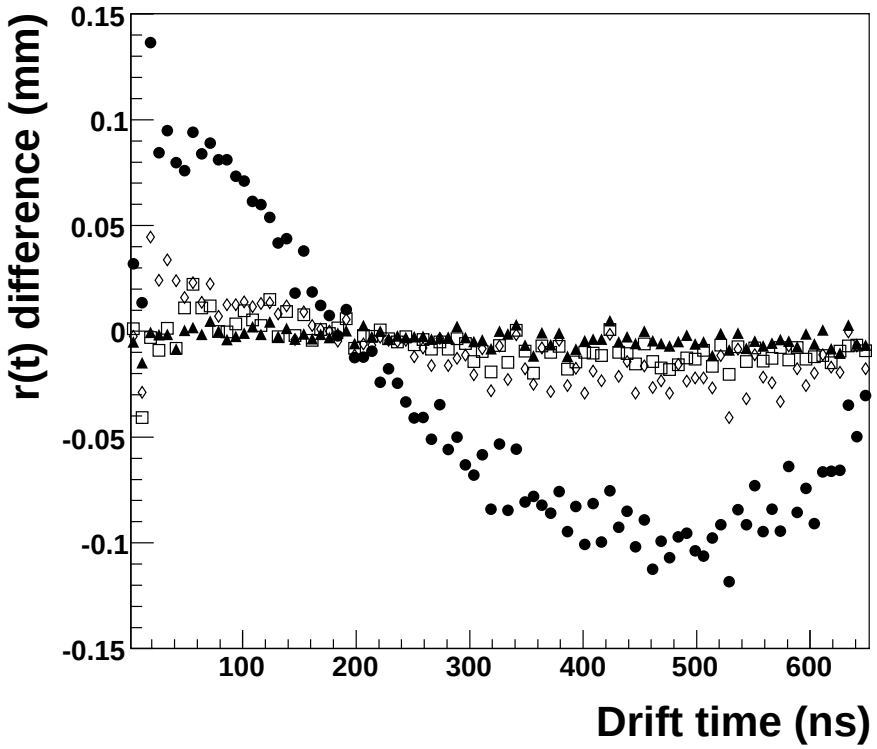

Figure 5.22: Difference between the $r(t)$ calculated using tracks with slope $a = [-0.05, +0.05]$ (full dots), $a = [-0.05, +0.05]$ (diamonds), $a = [-0.1, +0.1]$ (squares), $a = [-0.15, +0.15]$ (triangles) with respect to the reference $r(t)$ ($a = [-0.3, +0.3]$)

5.5.5 Angular spread

The track incident angle has an important impact on the results of the autocalibration as shown in fig. 5.22. An angular aperture of at least ± 0.15 in the parameter a of the track is required (corresponding to $\pm 8.5^o$) for an accuracy of 10 μm and ± 0.1 for $20 \mu m$. The samples analyzed have the same number of events. The systematics caused by almost parallel tracks is due to the fact that they correlate a unique set of drift radii and the autocalibration is not constrained enough.

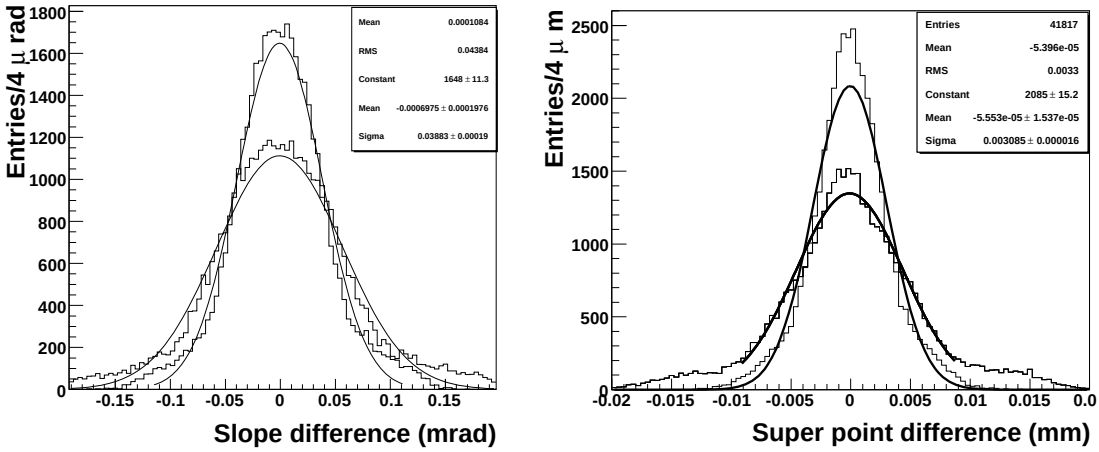

Figure 5.23: Differences between the slope (left) and the super point (right) obtained fitting the same pattern of hits with a good $r(t)$ and a distorted $r(t)$. Different distributions correspond to different value of the distortion parameter A (see text). Results are summarized in fig. 5.24.

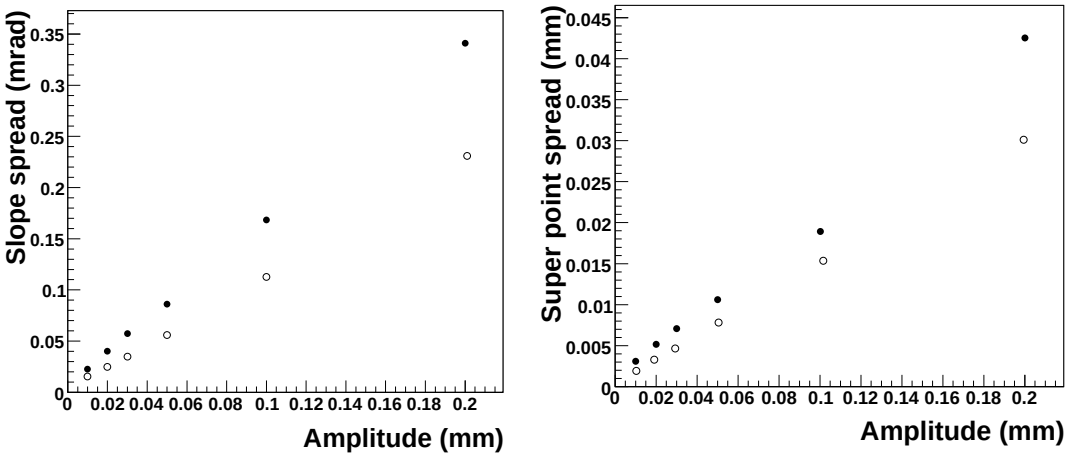

Figure 5.24: Width of the distribution of the differences between the slope (left) and the superpoint (right) obtained fitting the same pattern of hits with a good and a distorted $r(t)$ as a function of the distortion parameter A. Open dots corresponds to a monotonic distortion of amplitude A (see text).

5.6 Impact on the track parameters

The direct conseguence of a poor (wrong) calibration, say miscalibration, of the $r(t)$ relation is a systematically imprecise conversion of the drift times into radii, hence a distortion of the drift circles to be used for a subsequent track fit.

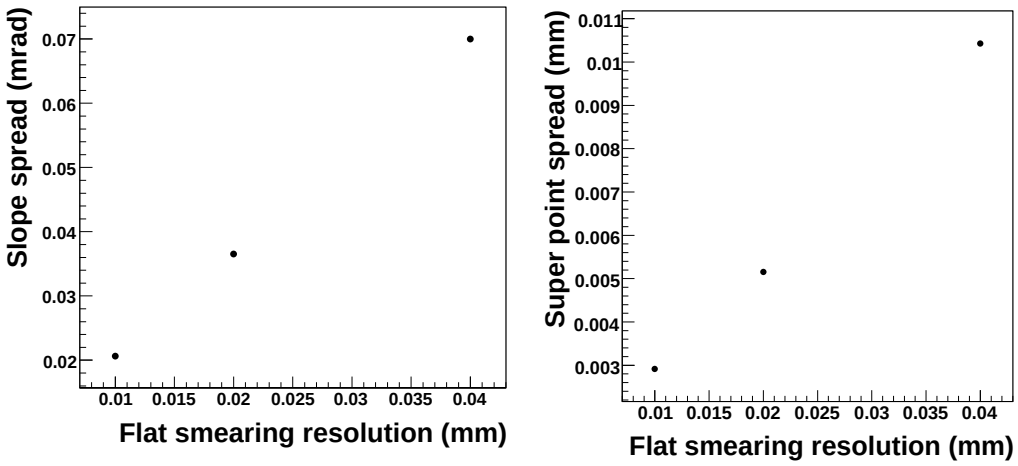

Figure 5.25: Width of the distribution of the differences between the slope (left) and the superpoint (right) obtained fitting the same pattern of hits with a good $r(t)$ and an $r(t)$ distorted through a uniform smearing of the radius in a range which is twice the value indicated in the abscissa and centered around zero.

From the results presented in the previous Section follow that the differences with repsect to the "best" $r(t)$ can be divided into two main categories. The first is represent by differences distibuted almost randomly with no dependence on the drift time; examples can be found in fig. 5.17. It will be discussed at the end of the section.

The second type of differences it is characterized clear depencence on the drift time, generally a sinusoid-like shape. The large discrepancy observed in fig. 5.22, for example, can be parametrized with a sinusoid with an amplitude A of about 0.1 mm and a turning point around 200 ns or, equivalently, at a radius $r = R/2$ (where R is the tube radius, this can be deduced from the fig. 5.15). Therefore a distortion which vanishes at $r = 0$, $r = R/2$ and $r = R$. A way to quantify the effect of the usage of a badly determined $r(t)$ on the track fit is to compare, event-by-event (segment-by-segment), the parameters calulated in such a way with the parameters calculated using the reference $r(t)$ (the data used is the same Test Beam sample analysed so far).

In fig. 5.23 the distribution of the differences for the slope and the super point are shown for different values of the amplitude A. It can be noticed that the mean of the distributions is centered around zero. The width, instead, increases linearly with the distortion as shown in fig. 5.24. For the slope, for example, the contribution due to the systematic of the miscalibration cannot be neglected with respect to the statistical uncertainty for A larger than 0.03 mm (see Sec. 5.3.1). In the fig. 5.24 it is reported also the result for a sinusoidal distortion $r = 0$ and $r = R$ (i.e. monotonic, similar to the patterns shown in fig. 5.21).

Regarding the differences of the type reported in fig. 5.17: they can be interpreted as a uniform smearing of the radius with an r.m.s. idependent on the drift time. Results are reported in fig. 5.25. For distortions uniformly distributed in the range $[-0.04\ mm, 0.04\ mm]$ (see fig. 5.17) the contribution to the broadening of the super point resolution is of about 0.01 mm and 0.07 $mrad$ for the slope.

Chapter 6

Global Time Fitting Algorithm

6.1 Description

Let be assumed the t_0 in equation (5.3) is not known either because of the t_{phase} uncertainty or because it is not measured at all.

A modified fitting algorithm can then be conceived once considered that

1. any two hits associated to the same track cannot differ, in time, by more then the maximum drift time of the tube, Δt_{drift};
2. small variations of t_0's have a negligible effect on the resultant track parameters. In fact, in a regular array of staggered drift cells, they contribute only at second order. Moreover, it is woth noticing that the t_0 differences are characteristics of the tubes or of group of tubes connected to the same electronics board, and, if not negligible, can be determined by measuring directly the relative time delay of the signals and account for them in the algorithm.

Thus, according to (5.3) the difference between two raw times of any two physical hits, 1 and 2, is

$$t_{m,1} - t_{m,2} = t_{drift,1} - t_{drift,2} + t_{0,1} - t_{0,2} \simeq t_{drift,1} - t_{drift,2}. \qquad (6.1)$$

From equation (6.1) it is not possible a unique conversion of the raw time $t_{m,i}$ into a drift radius since each individual $t_{drift,i}$ will be undetermined by a common *time offset* in the physical time window as illustrated in fig. 6.1. The following algorithm has been applied to determine the time offset, t_{offset}.

1. A valid pattern is identified as in the standard procedure outlined in Sec. 4.3; it results in a list of raw times $t_{m,i}$ associated to the track.

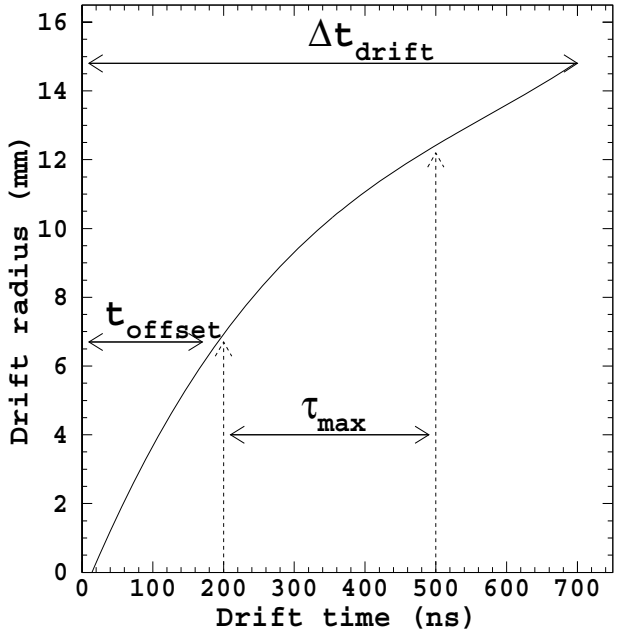

Figure 6.1: The $r(t)$ relation determined with the autocalibration. The vertical lines indicate, for a single event, $\tau_{min} + t_{offset}$ and $\tau_{max} + t_{offset}$ respectively; all the other hits of the event lie between these limits. t_{offset} is found event-by-event fitting the track.

2. It is checked that the difference between the largest and the smallest time in the list is smaller than the maximum drift time, $t_{m,max} - t_{m,min} < \Delta t_{drift}$. If this is not the case, the time with the largest difference from the average (usually a noise hit) is removed from the hit list. The procedure is repeated until the inequality is met for all hits.
3. A new list is formed subtracting the minimum value: $\tau^i = t_{m,i} - t_{m,min}$; hence $\tau_{min} \leq \tau^i \leq \tau_{max}$ with $\tau_{min} = 0$ and $\tau_{max} = t_{m,max} - t_{m,min}$.
4. Assuming an $r(t)$ relation, all the possible sets of radii $r(t_{offset}), \ldots, r(\tau^i + t_{offset}), \ldots, r(\tau_{max} + t_{offset})$ are obtained by varying the time offset in the range $0 < t_{offset} < \Delta t_{drift} - \tau_{max}$ (see Fig. 6.1).

   Each set of radii (i.e. each t_{offset}) leads to a possible value of the quantities a, b and χ^2 as the result of the minimization of the expression 5.20. The correct t_{offset} and, consequently, the best pair of a and b parameters, is defined as the value which gives the smallest χ^2.

The last step is optimized using a binary search algorithm. It is an iterative procedure implemented computing the $\chi^2(t_{offset})$ at the boundaries of a t_{offset} range. The range is reduced by a factor of two at each iteration and centered

around the local minimum. In this case, $8-10$ trials are sufficient on the average as illustrated in fig. 6.2. The speed of each trial can be optimized also choosing a proper value of the correction factor α (see 5.5). The precision with which t_{offset} is found in this way is of about 1 ns. The steps from 2 to 4 substitute the standard

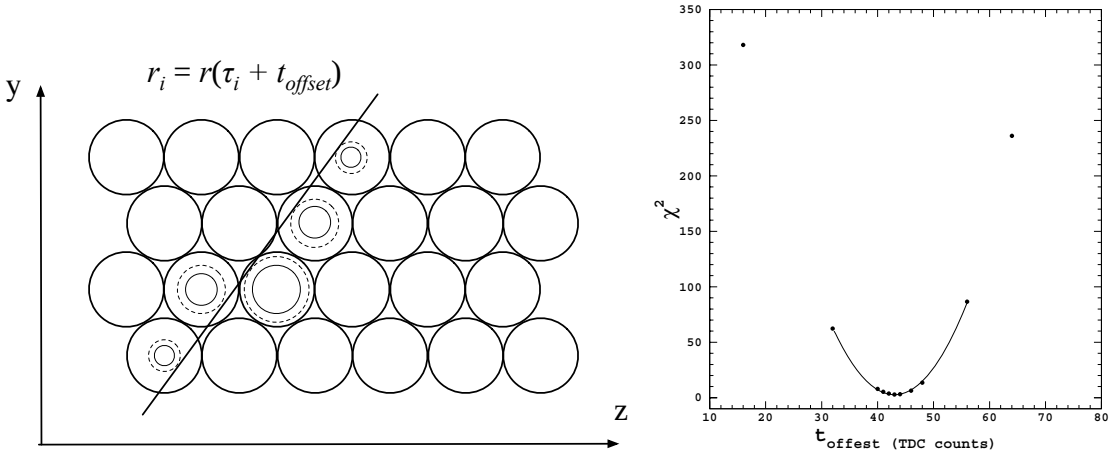

Figure 6.2: Left: the χ^2 of (**??**) is minimized by adding a common delay t_{offset} to the time measurements τ_i. This is like varying the associated drift circles to fit a tangent straight line.
Right: minimization of the χ^2 with 10 trials.

fitting algorithm and can be used for autocalibration and for tracking without the a priori knowledge of the tubes t_0's or in presence of a large trigger time jitter. A good precision in the determination of the track *time zero* can be obtained in this way without the need of large statistics, as for the fit of fig. 5.1; moreover, the knowledge of the track time offset can be exploited to extract other information about the track, e.g. for the measurement of the t_{delay} term of equation (5.1) which, in turn, is related to the position of the track along the tube (Sec. 6.3.3).

6.2 Validation of the method

The method has been validated by analyzing the Test Beam data sample (4.2.3). The trigger was provided by a system of small scintillators (10×10 cm^2) (see 4.2.2). with a time resolution of $\sim$0.7 ns. In these conditions, all time jitter contributions in (5.2) due to the time of flight, t_{flight}, of the particle from the scintillators to the MDT, and the propagation time, $t_{trig,prop}$, of the scintillators signals are negligible, the only unknown being t_{phase} since the trigger was asynchronous with respect to the MDT read-out clock. To measure t_{phase} it was used a TDC of the MDT read-out system to encode the time of the trigger signal.

In this case, with respect to any triggered event, the use of the global time fit algorithm should ideally provide a constant value for the time offset within the resolution of the fitting method itself.

Starting from the $r(t)$ function derived by the standard autocalibration technique, track fit were performed both with the standard method described in Sec. 5.2 and with the global time fit method. The results are summarized in fig. 6.3 for the three tubes per layer illuminated by the trigger. In the top-left panel the correlation between the track parameters of (5.19) are shown, the angular coefficient a is in the interval ± 0.27 rad and the horizontal beam profile at the center of the chamber has a r.m.s. width of $\sim$2 cm. The top-right panel shows the distribution of the *time offset* parameter. The distribution is well fitted with a Gaussian with r.m.s. width of 1.4 ns, that convolutes the time resolution of the trigger and the intrinsic precision of the method itself. The same distribution without the trigger information is widened by the t_{phase} effect; it should be stressed that the distribution of t_{offset} reflects the jitter of the reference time, while the actual value of t_{offset} found event-by-event does not. The bottom panels show the differences in the fitted track parameters as obtained with the two tracking algorithms. The r.m.s. width are 70 μrad for the slope a and 10 μm for b, with no significant shift of the average values; to be compared with the MDT resolution of $\delta_a = 200$ μrad and $\delta_b = 20$ μm due to the single tube intrinsic space resolution.

6.2.1 Autocalibration with the Global Time Fit

A concern of the method is whether the global time fit algorithm can only be used once the $r(t)$ function is known, or whether such a track fitting algorithm can be used *in* the autocalibration procedure to derive the "correct" $r(t)$ relation. It will be shown that the same autocalibration procedure can be adopted with the global time fit method, i.e. starting with a trial $r(t)$ relation without an a priori knowledge of the t_0's, and that it results in a stable solution. ig. 6.4(top) shows the difference of the $r(t)$ function calculated with the two methods: a clear discrepancy is observed on the verticale scale. Such a large difference can be explained by a relative shift along the time-axis of the two $r(t)$ functions. As a matter of fact, the shape of the difference looks like the TDC spectrum of fig. 5.1. This happens when comparing two $r(t)$'s which differ by a time shift δt. In fact, the difference $\delta r(t)$ is

$$r(t + \delta t) - r(t) \simeq \frac{dr(t)}{dt}\ \delta t$$

and dr/dt is proportional to the drift time distribution dn/dt,

$$\frac{dn}{dt} = \frac{dn}{dr}\ \frac{dr}{dt},$$

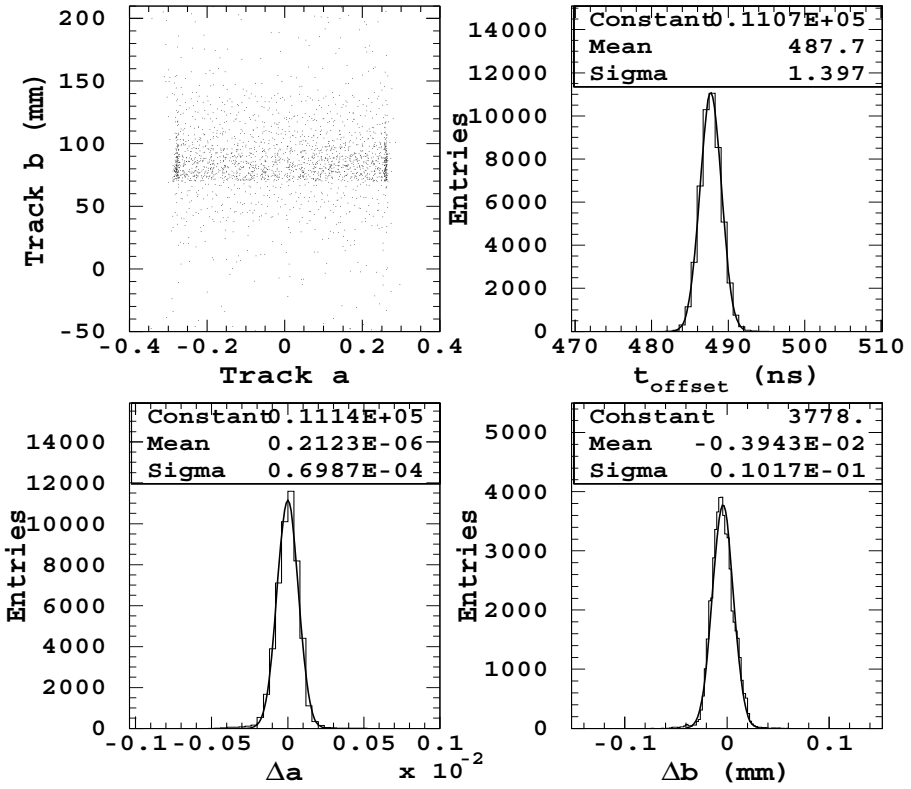

Figure 6.3: Top left: correlation between the track parameters a and b of (5.19). Top right: distribution of t_{offset}. Bottom: difference of the track parameters computed with the two fit methods.

if the tubes are uniformly illuminated, i.e. if dn/dr is constant, as was approximately the case with the tubes illuminated by the beam trigger.

Hence the two $r(t)$ functions show a time shift between them; this is, however, an expected result. In the standard tracking method, the definition itself of t_0 (e.g. the parameter p_5 in fig. 5.1) is somehow an arbitrary choice of the origin of the time axis. The definition is not necessarily the same for an algorithm which does not make any use of t_0 information. In order to check whether the only difference between the two $r(t)'s$ is a time relative shift, both functions have been fitted with a Chebyshev polynomial and then the difference was computed as a function of a global shift δt. fig. 6.4(bottom) shows the results for $\delta t \simeq 7$ ns: differences are at the micron level.

6.3 Application to Cosmic Rays

A BIL chamber was used for a study with cosmic rays in the production site. The trigger device described in 4.1.2 (fig. 4.5) was used in the configuration shown

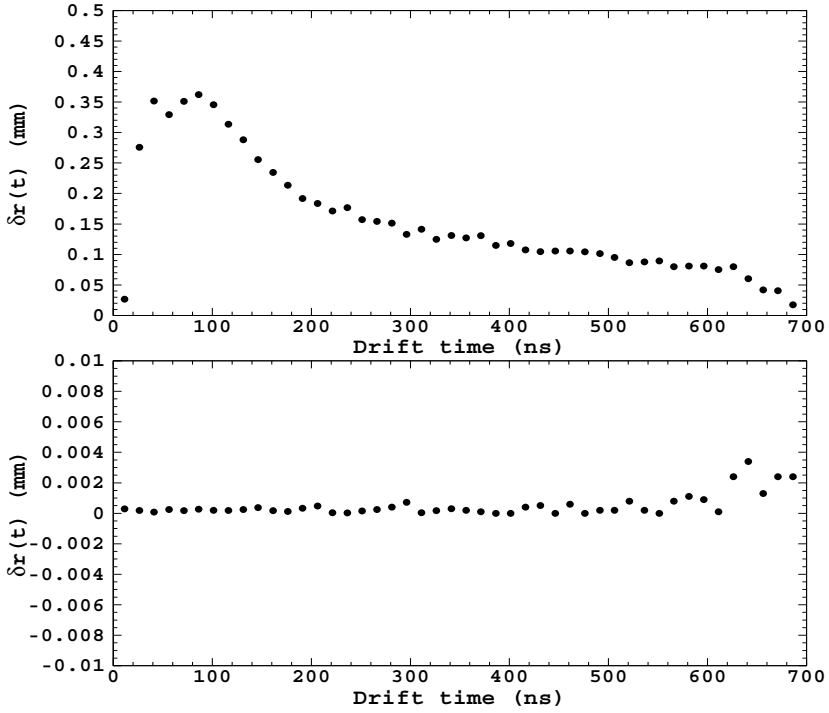

Figure 6.4: Top: differences of the $r(t)$ function as determined with the two track fit methods. Bottom: the same difference $\delta r(t)$ after a time shift.

in fig. 6.5: two scintillator paddles and a trigger coincidence $(S_1 \times S_2) \times (S_3 \times S_4)$

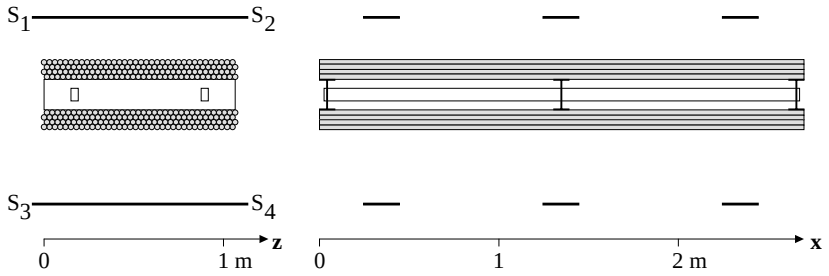

Figure 6.5: Setup to trigger on cosmic rays in the laboratory. The two trigger scintillators were placed in turns in the three positions shown in the figure.

where S_i are the signals of the PMT's in Fig. 6.5. The trigger timing was defined by the signal of S_4 delayed with respect to the other signals in order to depend on the track impact point on the bottom scintillator. Data were taken with the trigger scintillators in three positions, in the center of the BIL chamber, and displaced by about ± 100 cm.

6.3.1 Trigger time delay

With the scintillators in fixed position, the only variable term in (5.2) is $t_{trig,prop}$, the trigger propagation time. This depends on the light signal velocity in the scintillators. The track impact point along the scintillators was measured by the tubes traversed by the cosmic ray and $t_{trig,prop}$ by the t_{offset} computed as in Sec. 6.1. The correlation is shown in fig. 6.6: the signal velocity in the scintillator determined in this way is 13.5±0.3 cm/ns in good agreement with an independent measurement.

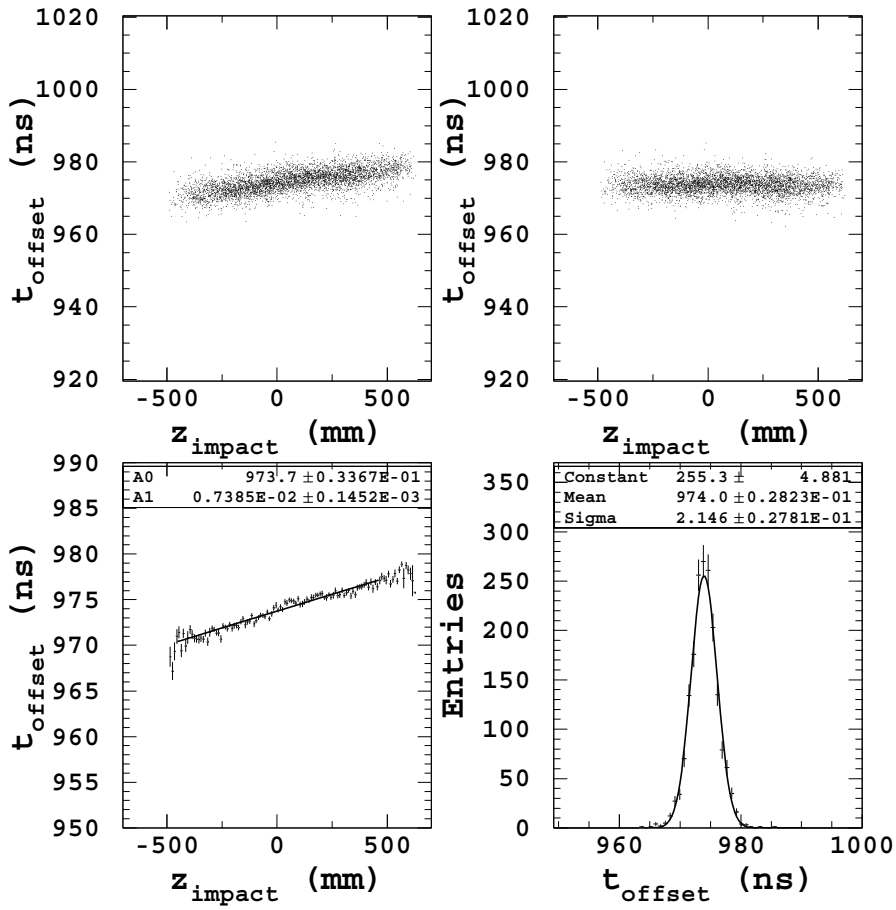

Figure 6.6: Top: t_{offset} as a function of the track impact point on the scintillators (z_{impact}) before (left) and after (right) correction for the light signal propagation time. Bottom-left: fit of t_{offset} as a function of z. Bottom-right: distribution of t_{offset} after correction.

Once the signal velocity in the scintillator is known, the trigger delay can be calculated event-by-event and subtracted to t_{offset}. The distribution of t_{offset} is shown in fig. 6.6 after correcting for this effect; the r.m.s. width of the distribution, 2.1 ns, is not as good as measured with the muon beam (Sec. 6.2) and this

is due to more than one reason:

i) a common $r(t)$ function for all 288 drift tubes in the chamber was used, while only 24 drift tubes were studied with the beam;

ii) data were taken over longer periods of time with temperature variations in the laboratory that were not accounted for in the calibration;

iii) the time resolution of the cosmic ray trigger was worse than with the beam;

iv) the algorithm assumes a straight track fit, while in the laboratory there was no selection of high momentum cosmic rays and the multiple coulomb scattering of low momentum tracks deteriorates the track fit.

6.3.2 Space Resolution

The effect of the trigger time delay on the measurement of the tube space resolution is reported in Sec. 7.3 and compared with the results achievable with the proposed algorithm.

6.3.3 Propagation Time Along the Tube

The corrected t_{offset} was determined for the three positions of the trigger scintillators shown in fig. 6.5. The t_{offset} distributions have the same width but different mean value for different positions. This reflects the delay due to the propagation of the signal along the wire, the term t_{wire} in (5.1). The dependence of the t_{offset} on the average trigger position was used to measure the propagation velocity along the wire: $v = (28.6 \pm 0.6)$ cm/ns. Hence, if a a time resolution of 1.3 ns is assumed, as determined with the beam data, it is possible to measure the position of the track in the tube direction with a precision of about 37 cm. In the ATLAS experiment there are chambers with drift tubes as long as 5 m and the "second" coordinate is measured by independent detectors, the trigger chambers. This method could be useful during the phase of detector commissioning to check the association of tracks in the coordinate parallel to the tube direction.

6.4 Trigger-less operation of a MDT chamber

Finally, to test the potentiality of the global time fit method, it has been tested the data acquisition of cosmic ray tracks in a BIL chamber *without* requiring an external track trigger. The rate of cosmic rays in the laboratory crossing the chamber was about 300 Hz. The data acquisition was the same as for the measurements described in Sec. 6.3, but the trigger was asynchronous provided by a 250 Hz clock, the rate being limited by the data acquisition system and the

on-line filter used for this measurement. During normal data taking (with the cosmic rays or with the beam trigger), the time window of the TDC was set to 1.6 μs; for this measurement it was set to the maximum value of 102 μs to improve the read-out duty cycle. In these conditions, the probability to reconstruct a cosmic ray track in the chamber was $\sim$3%.

Without any additional requirement on the data acquisition, the correlation of the number of drift tubes that gave a signal over threshold in the two multilayers is shown in fig. 6.7. A clear correlation is present with a peak at 4×4 hits corresponding to a track crossing the chamber in one tube in each layer. Then, an on-line filter was applied on the size of the read-out buffer requiring at least two tubes over threshold per multilayer; this reduced almost completely the number of events without a track. The data were then analyzed using the global time fit

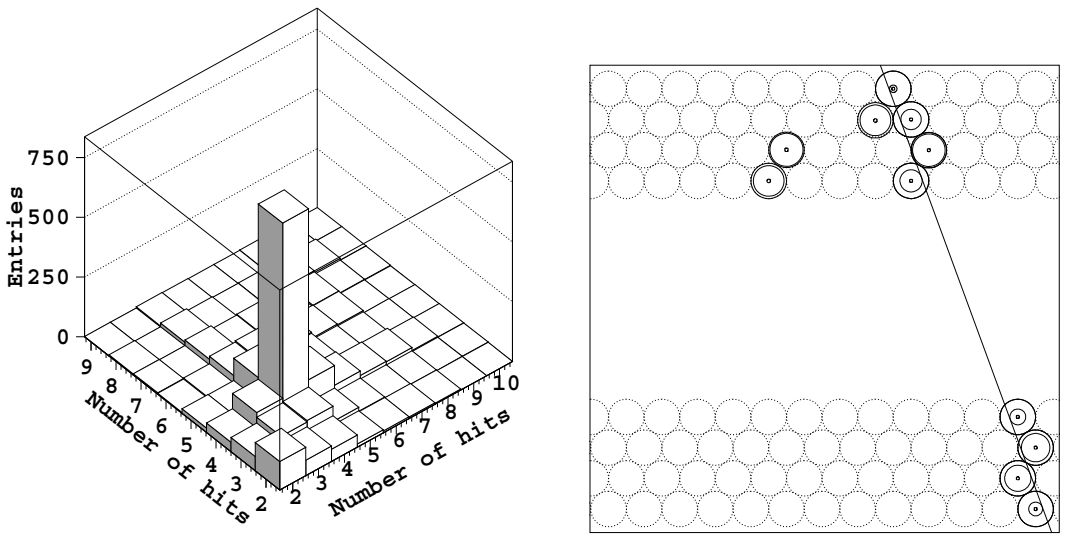

Figure 6.7: Left: Correlation of the number of drift tubes that give a signal over threshold in the two multilayers of the MDT chamber operated with a random trigger. To avoid the large number of "empty" events, only events with at least two hits per multilayer are shown.
Right: Example of a cosmic ray track recorded with a random trigger.

algorithm applying the $r(t)$ relation determined previously with the cosmic ray trigger. It is important to note that the initial pattern recognition is only based on tube hits and is independent on the $r(t)$ function, and that the autocalibration algorithm is able to find the "correct" $r(t)$ relation even if the input function is only approximate, i.e. if the actual operation of the chamber (temperature, pressure, ...) differ slightly from the nominal conditions. In fact, it was found that the drift tube resolution and the efficiency, as determined from the tracks reconstructed with the global time fit applied to this sample of events, do not

differ from those measured with the external cosmic ray trigger. As an example, fig. 6.7 shows an event with a cosmic ray track and few uncorrelated hits in the time window defined by the global time fit.

6.5 Conclusions

It has been presented a global time fit algorithm for general use in tracking detectors made of regular arrays of drift cells. The algorithm was tested with the geometry of the Monitored Drift Tube chambers that equip the Muon Spectrometer of the ATLAS experiment. The interesting features of this method are:

i) it allows for proper track segments reconstruction and autocalibration regardless of the knowledge of the individual drift cell t_0's;

ii) it is well suited to experiments with an asynchronous trigger, if the trigger does not provide a sufficiently good time resolution as required by a precise drift time measurement;

iii) in particular for cosmic ray experiments made of large arrays of drift detectors;

even in the case of experiments with a synchronous trigger, as e.g. ATLAS at the LHC, where the t_0's are constrained by the detectors position and the particles velocity, the method can be useful

iv) when triggering the experiment with cosmic rays, for commissioning, maintenance, special calibration runs;

v) to improve the calibration of the detector response;

vi) to derive a (coarse) measurement of the coordinate along the drift tube, independent on other detectors.

This algorithm applied to the track-segment reconstruction for particles traversing the MDT muon chambers can be considered as an interesting complement to the standard track finding algorithm under particular operation conditions of the experiment.

Chapter 7

Resolution studies

7.1 Single tube resolution

The single tube resolution is the spatial intrinsic accuracy of a drift tube and depends, in general, on the drift radius. For a sample of N of tracks, traversing an MDT in a distance d from the wire, the resolution is the r.m.s., around the mean d, of the distribution of the drift radius $r(t_i)$ derived from the measured drift time of the $i\text{-}th$ hit (Ch. 5,6).

$$\sigma^2(d) = \sum_{i=1}^{N} \frac{(d - r(t_i))^2}{N}; \tag{7.1}$$

7.2 Tube resolution determination without external reference

To calculate the tube resolution directly according to equation 7.1, the track position d with respect to the wire must be known accurately. This is, for example, the case if d is measured independently by a high precision external reference tracker. If no such detector is available the distance d had to be determined from the MDT data itself. In this case, since the distance d calculated from the equation of the fitted track, depends on the resolution itsef, an iterative procedure is needed.

The following iterative procedure has been used to derive the resolution $\sigma(r)$ as a function of the radius r.

1. Patterns belonging to a track with a defined number of hits are selected; default is 8 for a 8 layers chmaber.

2. One tube from the track is excluded and a straight line is fitted to the remaining hits according to equation **??**, using an estimated resolution $\sigma_n(r)$ with $n = 0$ for the first iteration, so as to calculate the track parameters a_n and b_n. A cut on the χ^2 can be applied.

3. The fitted track distance r_{fit} to the center (wire) of the excluded tube is calculated,

$$r_{fit} = (a_n \cdot z_w + b_n - y_w)/\sqrt{a_n^2 + 1},$$

where (z_w, y_w) are the coordinates of the wire of the excluded tube, as well as the residual.

$$\delta = \delta(r_{fit}) = r_{fit} - r_{drift} \tag{7.2}$$

and the fit extrapolation error in r_{fit} for the excluded tube

$$\sigma^2_{extr}(r_{fit}) = \left(\frac{\partial r_{fit}}{\partial a}\right)^2 \sigma^2_{a_n} + \left(\frac{\partial r_{fit}}{\partial b}\right)^2 \sigma^2_{b_n} + 2\left(\frac{\partial r_{fit}}{\partial a}\right)\left(\frac{\partial r_{fit}}{\partial a}\right) cov_{a_n,b_n}. \tag{7.3}$$

4. Steps from 1 to 4 are executed for all the tracks of the analyzed sample

5. The distributions of the residual $\delta(r)$ for different radius slices, 1 mm wide, are fitted with a Gaussian with width σ_δ. The average of the distribution of the extrapolation error $\overline{\sigma}_{extr}$ in the same slice is calculated as well; these distributions can be produced per single tube or per layer (multilayer, ...) to compute average quantities. An example is shown if fig. 7.1,7.2.

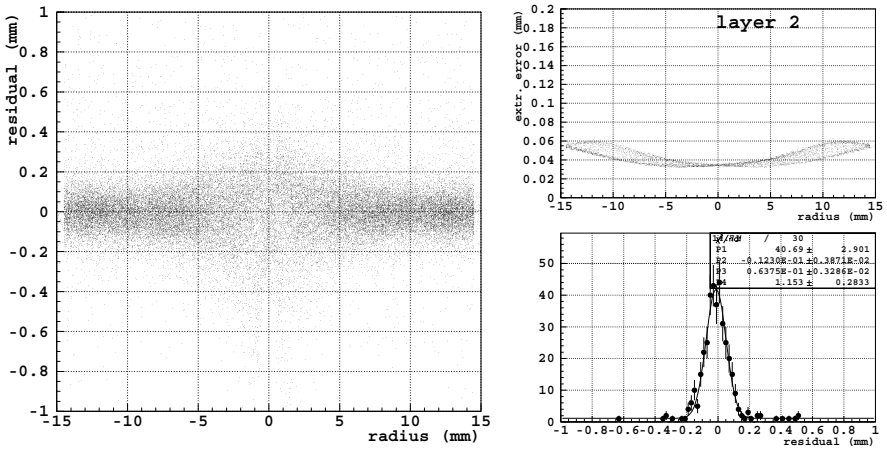

Figure 7.1: Results for a sample of simulated tracks in the angular range ±0.3. Residual (left) and extrapolation error (right top) distribution versus signed radius for the tubes on the second layer. The right bottom plot shows the residual for the range 9 $mm < r < 10$ mm.

6. A new estimate for the tube resolution is derived as

$$\sigma_{n+1}(r) = \sqrt{\sigma_\delta(r)^2 - \overline{\sigma}_{extr}(r)^2}. \tag{7.4}$$

7. A parametrization of the relation $\sigma_{n+1}(r)$, derived through a fit with the three parameter exponential function

$$\sigma(r) = p_1 + p_2 \cdot e^{-\frac{|r|}{p_3}}, \tag{7.5}$$

is used as input to the next iteration (fig. 7.2).

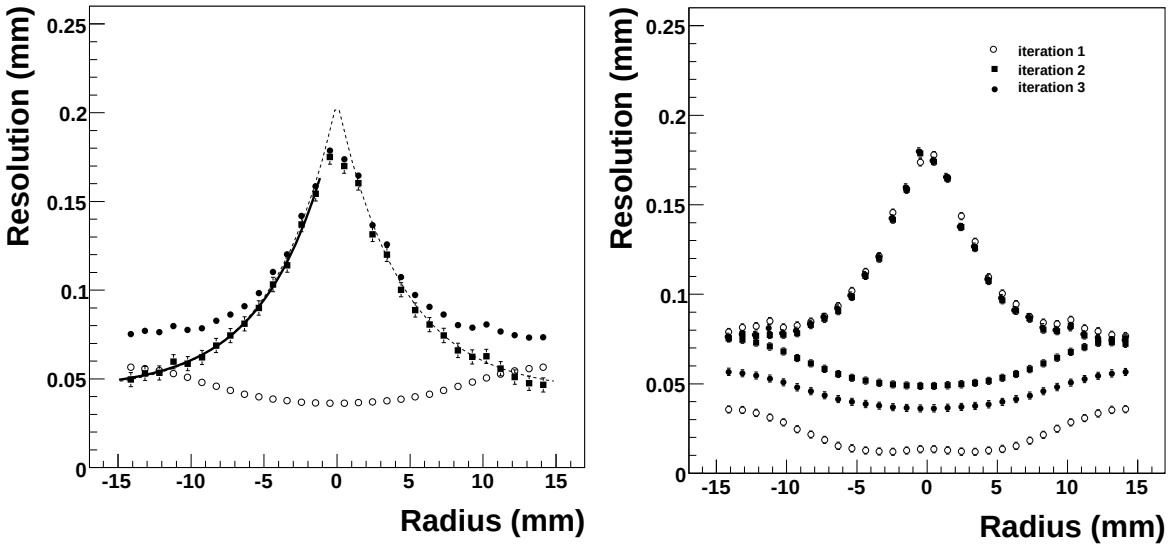

Figure 7.2: *Left* : Distribution of the residuals (full dots), the average extrapolation error (open dots) and of the resolution as a function of the radius. The bold line represents the fit to the function 7.5 while the superimposed dashed line shows the resolution function used at the generation level. *Right*: Distribution of the residuals and the average extrapolation error for different iterations.

8. Iteration 2 to 7 until σ_{n+1} equals σ_n within few microns.

The 7.4 can be derived according to the following considerations. Let r_0 be the "true" trajectory distance from the wire of the excluded tube . Then

$$\sigma_\delta^2 = < (r_{drift} - r_{fit})^2 > = < (r_{drift} - r_0 + r_0 - r_{fit})^2 > \tag{7.6}$$

$$= < (r_{drift} - r_0)^2 > + < (r_{fit} - r_0)^2 > \ + 2 < (r_{drift} - r_0) \cdot (r_{fit} - r_0) > .$$

The last term vanishes since r_{drift} and r_{fit} are statistically independent: r_{drift} is not used to fit the track used to calculate r_{fit}. Hence

$$\sigma_\delta^2 = < (r_{drift} - r_0)^2 > + < (r_{fit} - r_0)^2 > = \sigma^2 + \overline{\sigma}_{extr}^2, \tag{7.7}$$

that is the 7.4.

7.2.1 Validation. Effect of the angular range.

The reliability of the method has been verified analyzing a sample of 10^5 events. The results are reported in fig. 7.2. Events have been generated within the angular range corresponding to $a = [-0.3, +0.3]$ and with a known resolution function (dashed line in the plot) parametrized according to the 7.5 (Sec. 4.5) and similar to the one derived from the Test Beam data (see Sec. 5.4). The resolution converges after few (usually from 3 to 6 depending on the starting resolution $\sigma_0(r)$: point n. 2) iterations to a solution wich differs from the one used as the input to the simulation within few microns. From fig. 7.2 can be noticed that the convergence of the calculated resolution is mostly due to the convergence of the extrapolation error. The extrapolation error in fact is more sensitive to the resolution parametrization used at track fitting level with respect to the residual distribution. This is a consequence of the weak dependence of the autocalibration on the initial resolution function used (Sec. 5.3.2,5.5). No significant dicrepancies has been arised between the resolution computed for different layers. The method

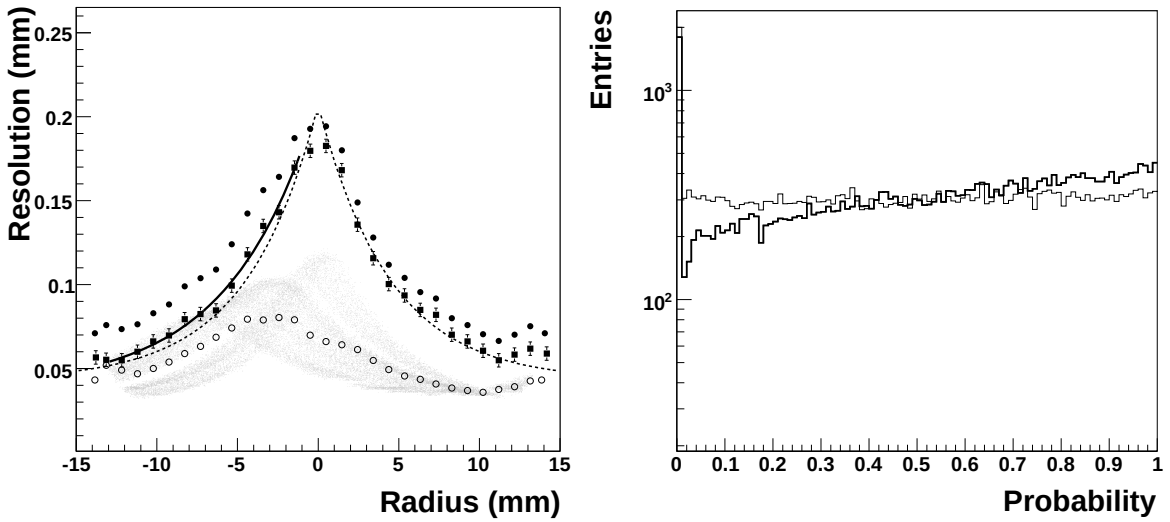

Figure 7.3: *Left* : Distribution of the residuals (full dot), the average extrapolation error (open dot) and the resolution (squared marker) has a function of the radius. The gray area represents the scatter of the extrpolation error vs the radius. The bold line is the fitted resolution function while the dashed line is the input to the simulation. The slope range is $a = [0.4, 0.6]$. *Right*: The χ^2 probability compared to the case (thin line) $a = [-0.3, 0.3]$.

has been tested to be robust for simmetrical angular range up to $a = [-0.6, 0.6]$.

In fig. 7.3 instead, the results obtained for a sample of tracks in the range $a = [0.4, 0.6]$. The method converge to a solution significantly different from the

expected one. This is due to the fact that the algorithm do not take into account the spread of the extrapolation error but only a mean value. In the case reported the resolution function is overestimated as demonstrated by the distribution of the χ^2 fit probability in fig. 7.3(right). This suggests that, if the probability distribution spots a bias in the measurement result, the procedure can be refined conceiving a minimization algorithm to find the parametrization which flattens the fit probability distribution.

7.2.2 The Test Beam resolution

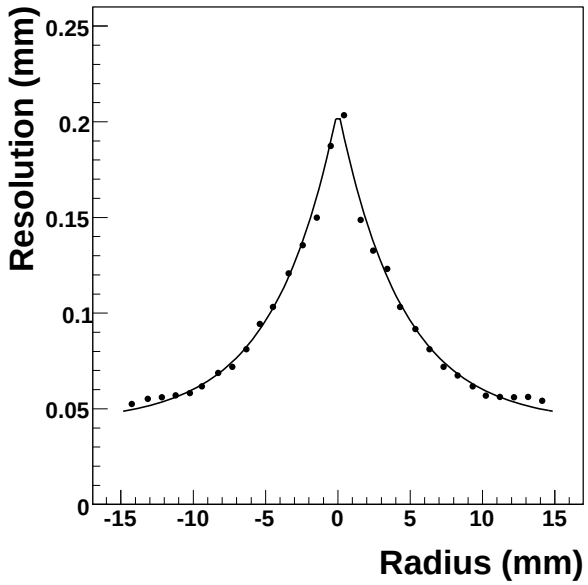

Figure 7.4: Tube resolution measured at the Teast Beam along with an exponential fit.

The method described above has been used to measure the resolution on a Test Beam data sample (Sec. 4.2). It is a *BILrot*-type sample of about 10^5 events. The discriminator threshold is 40 mV.

Fitted values for the resolution function are:

$$\begin{aligned} p_1 &= 0.043 \pm 0.007\ mm, \\ p_2 &= 0.164 \pm 0.005\ mm, \\ p_3 &= 4.431 \pm 0.078\ mm \end{aligned} \tag{7.8}$$

that means a resolution $\sigma(r = 0) = p_1 + p_2 \simeq 200\ \mu m$ close to the wire and of about 50 μm, roughly equal to p_1, close to the tube wall. The rise at small radii reflect the increase of the drift velocity in the vicinity of the anode wire (Ch. 3).

7.3 Contributions to the resolution

As a preliminary test, both fit algorithms, the standard (Sec. 5.2) and the global time fit (Sec. 6), were used to analyze the Test Beam data, starting with the same trial $r(t)$ relation and resolution function. The results are swhon in fig. 7.3(left) and do not differs significantly; an expected results since in the Test Beam setup, has already mentioned, the reference time provided by the trigger was not affected by any important smearing contribution.

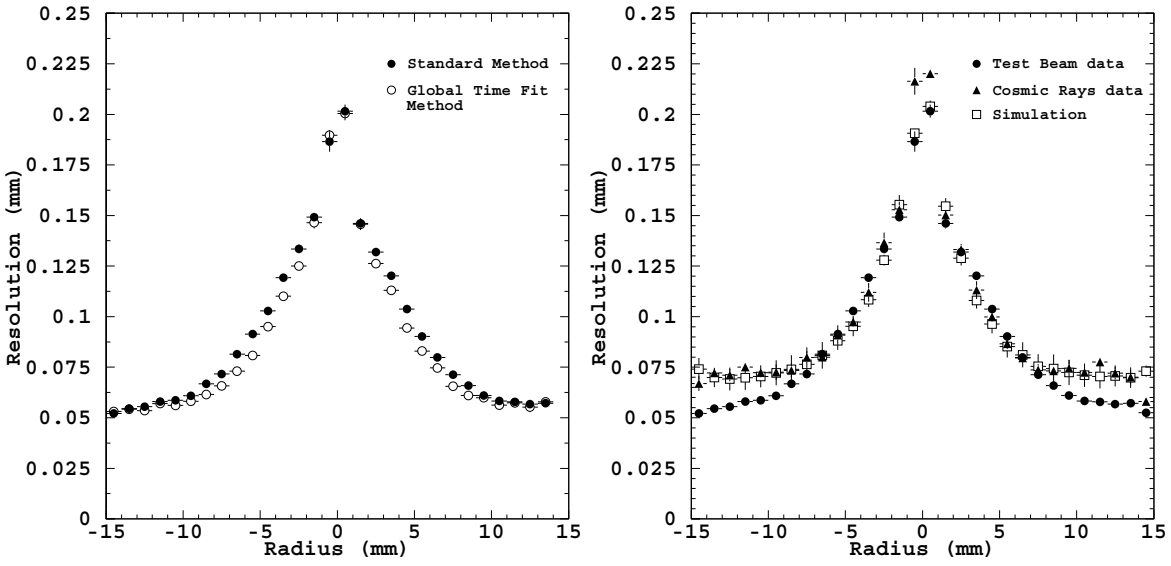

Figure 7.5: *Left* : space resolution function obtained with the standard and the global time fit tracking method from the analysis of Test Beam data. *Right* : comparison of the resolution obtained with the global time fit method from the anlysis of cosmic ray data. The differences are due to the multiple scattering as shown by the reults a Monte Carlo simulation.

Then, the resolution function was determined using the cosmic ray tracks (Sec. 4.1,6.3) and applying the global time fit method. The result, shown in fig. 7.3(right), differs significantly from the one obtained using the high energy Test Beam tracks. This discrepancy can be understood considering that the main differences in the experimental condition of the cosmic ray setup with respect to the Test Beam one are

1. trigger time delay due to signal propagation in the trigger plane.
2. multiple Coulomb scattering of low momentum particles.

Since the global time fit algorithm correct sproperly for trigger time jitter related effects, as described in Sec. 6, the worsening of the resolution should be attributed

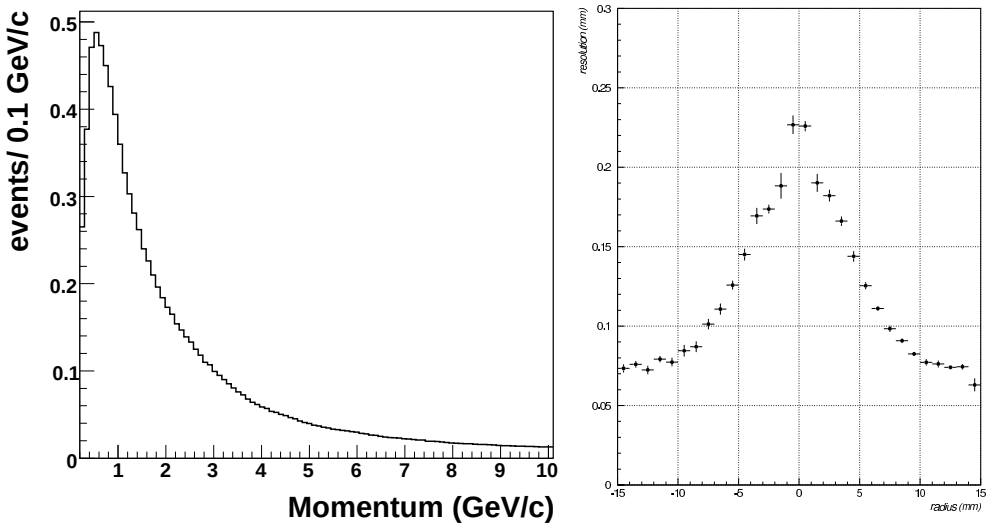

Figure 7.6: *Left* : Momentum spectrum of cosmic rays at the earth surface. *Right* : Resolution measured with a cosmic rays data hodoscope with the global time fit method.

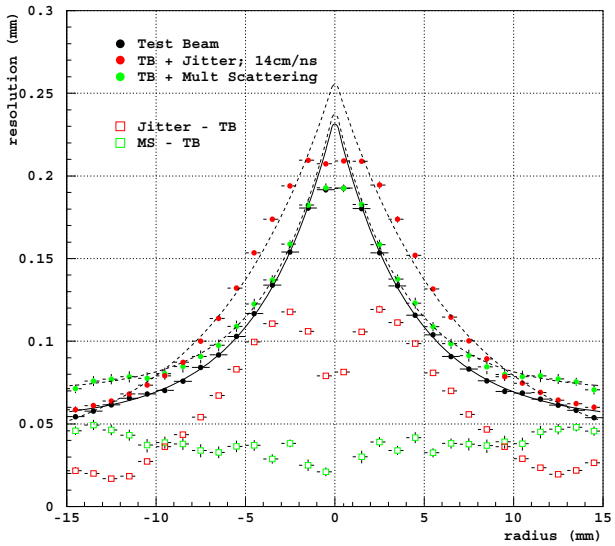

Figure 7.7: Contribution to the Test Beam high energy muons resolution (TB in the figure) of the multiple scattering (MS) and trigger time delay (jitter) (assuming a signal propagation of 14 cm/ns).

to the multiple scattering[1].

This interpretation was verified using the Monte Carlo described in 4.5. The propagation velocity inside the trigger plane (about 1 m long) was measured to

[1]from the 4.1 results that for a 1 GeV/c muon the standard deviation of the deflection angle in the tube wall is of the order of the *mrad*

be about 14 cm/ns and this value used as input to the simulation. Multiple scattering of muons with the momentum distribution and angular distribution of cosmic rays have been enabled. In particular, muon momenta are generated according to the distribution shown in fig. 7.6(left)[44] while the angular distribution as assumed to be proportional to $cos^2\theta$ if the θ is the direction with respect to the zenith [10].

The result is reported in fig. 7.7:

- the multiple scattering contribution is almost flat (radius independent) as expected; hence affects mostly the resolution at large radii while the effect of the trigger is more important close to the wire where the drift velocity is higher.
- Adding those two contributions to a Test-Beam-like resolution a resolution very similar to the one measured once the standard algorithm is applied to cosmic rays data, fig. 7.6(right), is obtained.

Chapter 8

Background studies

Large radiation doses are expected for detectors at the LHC experiments. Compared, for example, to the previous experiments at the LEP, HERA and the B-factories, the increase in the background particle rates is up to four orders of magnitude. Hence a significant increase in radiation hardness is required which implies not only careful selection of materials but also the definition of precise procedures for chamber assembly and operation.
In the era of LHC and forecasting an upgrade for $SLHC$ (SuperLHC) it is crucial to test the detector robustness in the harsh background environment.
The expected background conditions in the $ATLAS$ hall have been described in the section 3.4: simulations give a maximum total count rate of about 500 Hz/cm^2 under nominal LHC operation that can be 10 times higher under $SLHC$ operation. This corresponds to an accumulated charge of about 5 C/cm/wire in 10 years of $SLHC$ operation.

A degradation of wire chamber performances after extended operation in a high-rate environment is usually caused by the formation of deposits on the anode wire. These deposits can result from polymerization of the operating gas components or from contaminants in the mixture.
Considering also that, due to the complexity of the whole apparatus architecture, detector element replacement would be decidedly unconvinient, a study of the factors limiting their lifetime is particularly important.

Two prototypes of Monitored Drift Tubes chambers have been built and equipped with the standard gas distribution system, high voltage distribution and front-end electronics. Two test have been performed:

1. a gamma irradiation test accumulating a total charge of 4.8 C/cm/wire (which corresponds to about 10 years at $SLHC$ luminosity).
2. a neutron irradiation test integrating 1.4×10^{12} neutrons/cm^2 (equivalent to about 30 years of $SLHC$ assuming the expected neutron rate of

5 kHz/cm^2, 3.4).

An overview of different chamber aging mechanisms is reported in section 8.1. The gamma irradiation facility and the experimental setup are described in sections 8.2 and 8.3 respectively, while data taking and slow control are described in sections 8.5 and 8.6. The analysis of the drift time and collected charge spectra and tracking performance are discussed in sections 8.7 and 8.8. The result of electronic microscopy of the wires is summarized in section 8.9. It follows the description of the test performed at the neutron irradiation facility. The work presented here has been published in [66].

8.1 Wire chamber aging mechanisms

Aging effects observed in wire chambers [45, 46, 47, 28] are normally due to deposits on either the anode or the cathode surface. Already thin coatings on the anode wire, which can be either electrically insulating or not, lead to a loss in gas gain. As an example, consider an MDT wire with an original diameter of 50 μm which is increased by 2 μm due to the deposition of a conducting film of material; by substituting the different radii into Diethorn's formula and using the Diethorn parameters for $Ar : CO_2$ (93 : 7), as specified in 3.2.3, one finds a corresponding gain reduction of 23%.

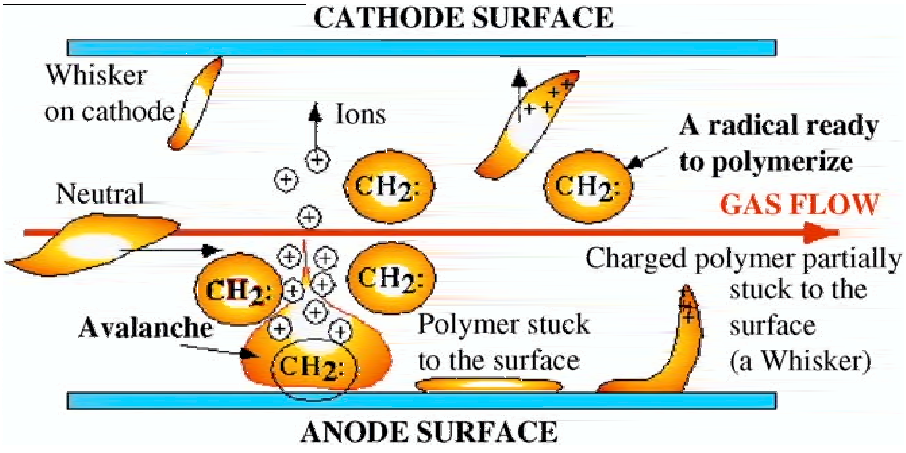

Figure 8.1: Schematic of process leading to wire chamber aging.

Deposits on the cathode have no direct impact on the gas gain; they can however be the cause for spontaneous discharges and self-sustained currents via a mechanism known as the Malter effect: if the cathode is coated by a thin film of insulating material, the neutralization of positively charged ions, produced either by a traversing particle or in the gas amplification

process, is impeded. A positive charge builds up at the boundary between the insulating layer and the operating gas of the drift tube; the consequence is an electric field perpendicular to the cathode surface which can be strong enough for electrons to be liberated from the cathode material by field emission. These electrons then drift to the anode wire where they undergo gas amplification, producing more ions which in turn move towards the cathode, contribute to the space charge and close the cycle. The result is a self-sustained current. Once the Malter effect manifests itself in a drift tube, its use for particle detection is very limited due to the large number of (fake) pulses and the degradation of the electric drift field caused by the large number of drifting ions.

Deposits, especially on the anode, can take the form of whiskers, droplets or a uniform coating; they can be both solid or liquid, brittle or viscous (fig. 8.1). One generally assumes that their formation is a polymerization process which involves either the molecules of the operating gas itself or a contaminant. In both cases the deposition of material on the wire surface competes with etching or ablation effects. Etching in this context is the process in which molecules are transferred from a solid phase (wire deposit) into the gas phase by a bombardment with electrons (from the gas amplification). Particular mixtures containing fluorine, e.g. in the form of CF_4, are known for their large potential for removing material from the anode wire of drift tubes; they are therefore sometimes deliberately used to prevent chamber ageing or as a cleaning gas. Aging effects can in some cases also be avoided by adding water or an alcohol to the gas mixture.

The mechanism by which these additives work is not yet fully understood. Since the ionization potential of most alcohols A is relatively low, one may speculate that charge transfer reactions $X^+ + A \rightarrow A^+ + X$ play a role by neutralizing a molecular ion X^+ in a more 'gentle' way than by the recombination process $X^+ + e^- \rightarrow X$ taking place at the cathode, with the result that the molecule is prevented from breaking up. Water on the other hand might produce radicals of the form $HO\cdot$, which can saturate the polymerization process before chains become so long that they are no longer volatile and attach themselves to the cathode or, with greater harm, to the anode.

Aging from gas polymerization

Most drift detector gases containing hydrocarbons tend to polymerize under high irradiation. A hypothetical polymerization reaction, showing the involved processes and starting from methane, is

$$CH_4 + e^2 \rightarrow CH_3 \cdot + H \cdot + e^- \quad (1)$$

$$\mathrm{CH_4} + e^- \rightarrow CH_2 : + H_2 + e^-$$

$$\mathrm{CH_2} : + CH_2 : \rightarrow C2H4 + 2H2 \quad (2)$$

$$\mathrm{CH_2}\cdot + C_2H_4 \rightarrow C_3H_7\cdot \quad (3)$$
$$\mathrm{C}_3H_7\cdot + C_2H_4 \rightarrow C_5H_{11}\cdot$$
$$\ldots$$
$$\mathrm{C}_nH_{2n+1}\cdot + H\cdot \rightarrow C_nH_{2n+2} \quad (4)$$
$$\mathrm{C}_nH_{2n+1}\cdot + C_mH_{2m+1}\cdot \rightarrow C_{n+m}H_{2(n+m)+2}$$

In (1) a methane molecule loses one or two of its hydrogen atoms due to the bombardment with electrons. The result is a radical with at least one unpaired electron, denoted by the "·" symbol, in the shell of the C-atom. Radicals are a very reactive species; they try to reach a stable, i.e. saturated, electron configuration by forming chemical bonds. The product of reaction (2) is the chemical compound ethylene, C_2H_4, in which two Carbon atoms are connected by a double bond ($C = C$). Both free radicals and molecules with a double (or triple) bond are needed for the actual polymerization process (3). The unpaired electron of the radical and one of the electrons from the $C = C$ double bond form a new single bond; the radical gets attached to the molecule which grows in size. The result of many such reactions is a hydrocarbon chain whose overall length is determined by the frequency with which one of the termination processes (4) occurs. Hydrocarbons above a certain size are normally non-volatile; if this size is reached in a drift detector, they will condense on the available surfaces which leads to the deposits responsible for ageing.

Results from different studies ([64, 65]) confirmed that this aspect is the main reason for not using hydrocarbon compounds as the operating gas for the ATLAS MDTs.

Aging from gas contaminants

Every drift detector contains non-metallic components which harbour the risk of polluting the operating gas. The main mechanisms by which contaminants are produced are

- Outgassing: Plastic materials often contain traces of non-polymerized monomers left from their production. Since these are not firmly bound to other molecules they can over time evaporate from the material. Outgassing can be particularly severe in glues, if they are not cured properly, and in plastics containing softeners.
- Dissociation and material breakdown under irradiation: chemical substances that are very stable under normal conditions can rapidly deteriorate if they are exposed to ultraviolet or ionizing radiation. In the case of organic compounds, this will mainly lead to the outgassing of H_2, though a substantial amount of heavier and more deadly molecules can also be produced. Certain chemical groups increase the radiation resistance of a material. Among them are aromatics like the phenyl

group $-C_6H_5$. These groups can absorb large excitation energies and hence prevent a molecule from dissociating; the yield for the production of radicals is low. Examples for plastic materials suitable for use in a high radiation environment are polyimide (KaptonR) and polyether-ether-ketone, PEEK.

– Evaporation: Valves in a detector gas system are often greased to prevent them from getting stuck. Soft sealants are used to achieve gas tightness and oils may be present in bubblers used to monitor the gas flow. In each of these cases molecules will evaporate from the surface of the liquid or (semi)solid material until the concentration in the gas phase equals the vapour pressure of the given substance.

– Improper cleaning: A variety of oils, lubricants and cooling fluids is used in the production and machining of both plastics and metals. They have to be thoroughly removed from the components of a drift detector before its assembly in order to avoid uncontrolled contamination of the operating gas.

From the above list it is evident that materials used in the construction of gaseous detecors to be operated under high rates need to be carefully chosen in order to guarantee an adequate lifetime. The mechanism by which contaminants cause ageing in a wire chamber is, as in the case of ageing due to the operating gas, the formation of deposits either on the anode or the cathode. Molecules with a large dipole moment are attracted to the anode wire by the inhomogeneous electric drift field. If they are heavy, they can stick to the wire surface and gradually build up an insulating or conducting layer of material. Once attached to the wire they are exposed to an intense bombardment with electrons from the gas amplification process. In many cases they will therefore polymerize and form heavily macro-molecules. If ageing is caused by a pollutant, it is not guaranteed that a higher gas flux will reduce the effect. On the contrary, the growth rate of a deposit will increase with the gas flow if the probability for impurities to be captured by the anode wire is high, since in this case a larger number of molecules is transported into the detector volume in a given time [30]. An element found as a deposit on the anode wire in numerous ageing studies is silicon (Si). Silicon belongs to the same group of the periodic table as carbon. Their chemical reactions are therefore similar. Silicon can polymerize, both with carbon and with oxygen. The result are macro-molecules either

```
   |     |     |                 |   |   |   |   |
— Si — O — Si — O — Si —   or   — Si — C — Si — C — Si —
   |     |     |                 |   |   |   |   |
```

as their backbone. A 3-dimensional cross-linking is also possible. The

simplest, purely inorganic structure in this case is $(SiO_2)_n$, which has a crystalline consistency and is found in silica glass and sand.
Silicon atoms found in a drift chamber usually stem from silicone materials, which are either used in its construction or present in the gas system. Silicones are chemical substances in which organic compounds are attached to a $(SiO)_n$ chain. The most basic silicone is poly-dimethylsiloxane $(Si(CH_3)_2O)_n$,

$$\begin{array}{ccccccccc} & & CH_3 & & CH_3 & & CH_3 & & \\ & & | & & | & & | & & \\ — & O & — & Si & - & O & - & Si & — & O & — \\ & & | & & | & & | & & \\ & & CH_3 & & CH_3 & & CH_3 & & \end{array}$$

from which all others are derived by replacing some of the methyl groups. Silicones are common sealants, e.g. as RTV (room temperature vulcanization) resins; they are also used as *o-rings* (silicone rubber), mould release agents and for lubrication.

8.2 The Calliope gamma facility

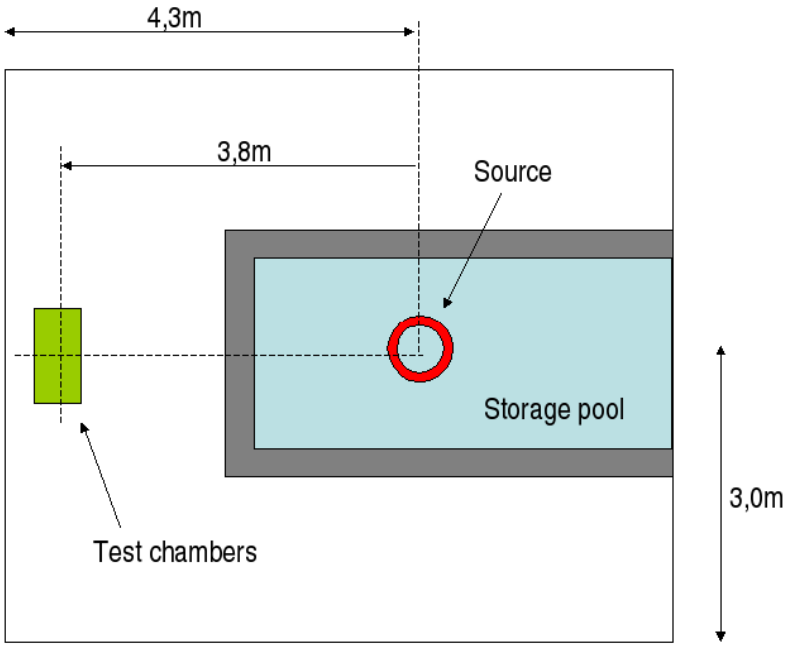

Figure 8.2: Schematic drawing of the Calliope facility.

The Calliope gamma facility at the ENEA Research Center near Rome [48] consists of a high intensity ^{60}Co source in a large volume shielded cell. The ^{60}Co isotope undergoes the beta decay $^{60}_{27}Co \rightarrow ^{60}_{27} Ni^* + e^- + \bar{\nu}_e$ with a half

life $t_{1/2}$ of 5.24 years. The subsequent Nichel de-excitation produces two photons of 1.17 MeV and 1.32 MeV. These values fall in the middle of the photon energy spectrum 3.22. The beta electron is emitted with an energy up to 317 keV and travels less then 1 m in air.

The activity of the source is reported to be R'_γ =6.72×10^{14}(±5%) Bq at 1/1/2005. Hence, at the time of the test, about six months later, the activity used to be

$$R_\gamma = R'_\gamma \cdot e^{-\frac{\Delta T}{\tau}} = 6.3 \times 10^{14}\, Bq. \tag{8.1}$$

with $\Delta T \sim 0.5\, y$ and $\tau = t_{1/2}/ln2$ is the nuclide average lifetime. The

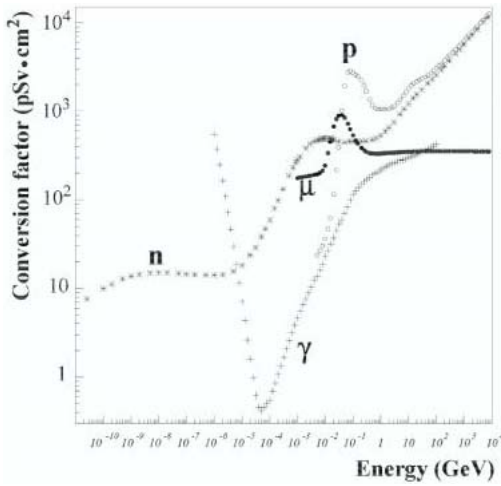

Figure 8.3: Conversion between energy and dose for different particles species.

detectors under irradiation were placed at about 3.8 m from the center of the source (fig. 8.2). The photon flux Φ_γ at the detector surface can be evaluated (neglecting photons attenuation in air) as

$$\Phi_\gamma = 2 \times \frac{R_\gamma}{4\pi d^2} = 7.0 \times 10^8\, photons/cm^2 s \tag{8.2}$$

with R_γ from the 8.1, and $d = 380\, cm$.

As a check, the average absorbed dose rate in air at the detector location was measured. The value obtained is 15.0 Gy/h (10% uncertainty). The relation between the absorbed dose rate and the photon flux can be deduced from the fig. 8.3: the average photon energy, 1.25 MeV, corresponds to about 6 $pSv\, cm^2$. Since for the photon Sv and Gy are equivalent the relation can be translated as: 1 Gy/s corresponds to $1.66 \cdot 10^{11}$ $\gamma/cm^2 s$. This implies that 15.0 Gy/h corresponds to $6.9 \cdot 10^8$ $\gamma/cm^2 s$, in good agreement with the value estimated from the source activity.

8.3 Experimental setup

8.3.1 The test detectors

A set of 48 identical drift tubes, 470 mm long, were built and tested following the standard $ATLAS$ wiring and quality control procedure [49]. The two 6×4 drift tubes chambers (bundles) were built gluing together six tubes (placed one next to the other with a separation of 0.02 mm) to form each layer and then gluing the different layers one in top of the other. The wire pitch is expected to be 30.035 mm and the uncertainty on the wire position with respect to the pitch to be about 20 μm. The bundles were equipped with the $ATLAS$ on chamber gas distribution system components. The gas inlet and outlet to each bundle were provided by two aluminum manifolds connected to the tubes by stainless steel capillaries of different length. Each capillary supplies gas to three tubes in the same layer connected in series with plastic rings. The gas mixture $Ar : CO_2$ (93 : 7) was supplied from a bottle of certified premixed gas. The pressure and the flux of the gas mixture were regulated and measured using a pressure controller and a mass flow meter, respectively. The gas tightness of MDTs in the bundles as estimated by the pressure drop rate either before and after the irradiation period. The gas leak of both bundles was found well below the $ATLAS$ standard limits (2×10^{-8} $bar \cdot l/s$ per tube). The gas flow during the test period was 3.5 l/h per chamber, corresponding to about 10 complete volume exchanges per day.
It is useful to introduce here a tube numbering scheme that will be used in the following. The tubes are numbered from 1 to 24 counting from left to right from the read-out side starting from the first layer which is the lower one (that is, the tube in the lower left corner of the test chamber is tube 1 and the one in the upper right corner is tube 24).

8.3.2 Front-end and DAQ electronics

The MDT electronics is described in 3.3 and 4.1.1. Each test chamber, consists of 24 tubes, hence is read out by a single *mezzanine* board. The information from the ADC has been recorded and used in the following analysis as a diagnostics for monitoring the chamber gas gain. The sensitivity of the full analog signal chain (pre-amplifier to shaper) for the expected signal range amounts to 12 mV/fC. The integration gate has been set to 25 ns and the discrimination threshold corresponds to the collection of the first 20 primary electrons (pe). From previous studies on this front-end electronics emerges that the sensitivity of this ADC at the working point, in terms of electrons collected at the anode wire, is about 1 $ADC_{ch}/0.85$ $pe = 1$ $ADC_{ch}/2.7$ fC.

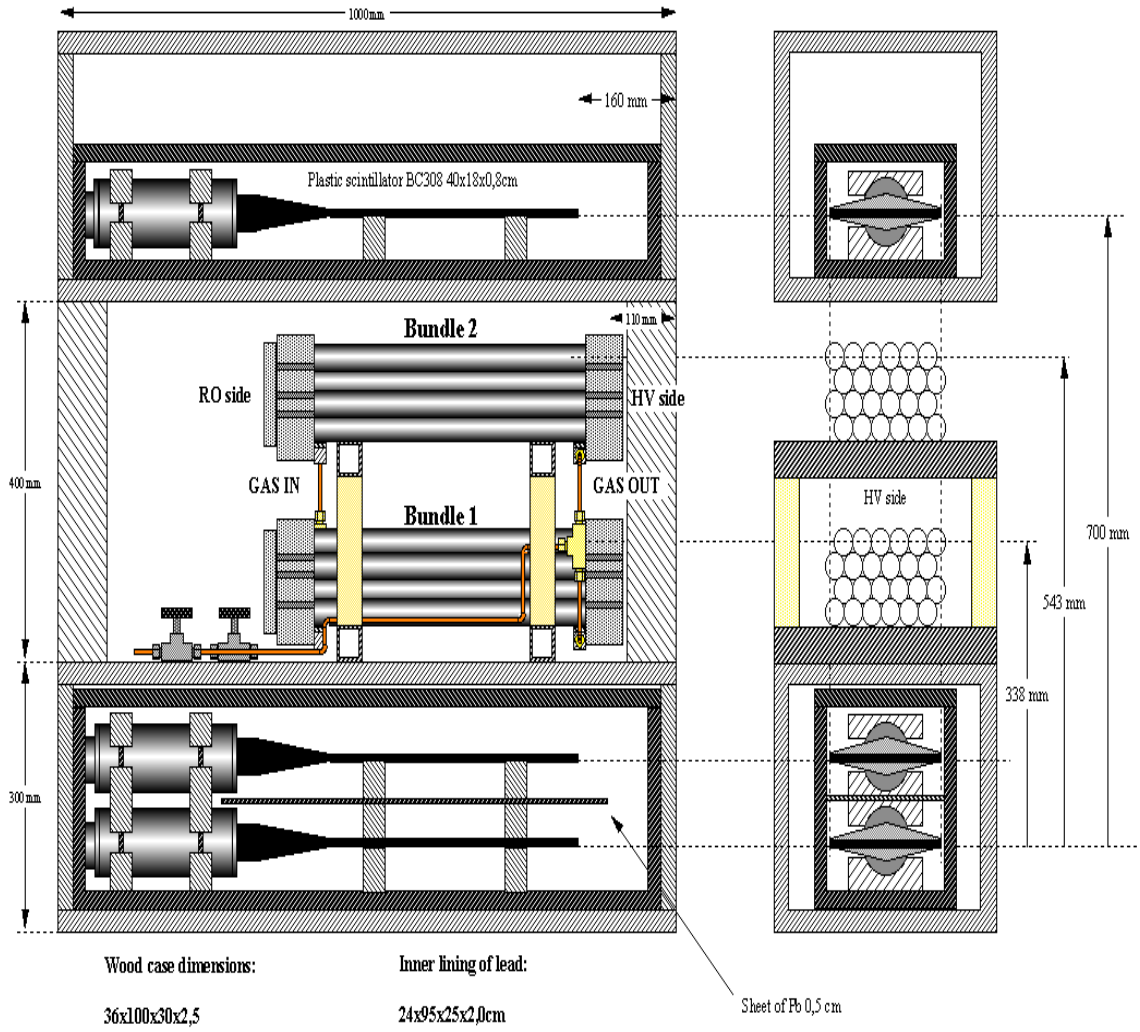

Figure 8.4: Side and front view of the setup showing the two bundles and the scintillator counters in the shielded boxes.

Note that each *pe* produces an avalanche with a multiplication factor G equal to $2 \cdot 10^4$ at the *ATLAS* working point.

8.3.3 Trigger

A coincidence of three scintillator counters was used as a trigger for cosmic rays. The counters were placed into two boxes (two in the box below the test chambers and the other in the one above) and completely wrapped with a 2 *cm* thick layer of lead in order to prevent PMT damage during the irradiation. Fig. 8.3.1 shows the set up.

8.4 Choice of the working point

Since the aim of the test is to study MDT performance with increasing accumulated charge it's important to avoid gas gain drop related to space charge effects. This would reduced significantly the accumulated charge in a given irradiation time (Sec. 3.4.2). In the following is described a calculation to optimize the working point to accumulate the maximum charge during the irradiation campaign.

The maximun ion drift time t_{max} was already derived in 3.2.4. In the approximation $r_0 << b$:

$$t_{max} = t(b) = \frac{ln(b/a)}{2\,\mu V} b^2. \tag{8.3}$$

In the above formula the electric field

$$E(r) = \frac{V}{ln\frac{b}{a}} \cdot \frac{1}{r} \tag{8.4}$$

of the "undisturbed" tube is used. For high rates, the field will change and the maximum ion drift time has to be corrected as well. For the ion mobility the value 1.7 cm^2/Vs (at the atmospheric pressure) is assumed (Sec. 3.2.2, fig. 3.7). The mobility scales linearly with the pressure p: $\mu = \mu(p_0) \cdot p_0/p$. Assuming a uniform tube irradiation, it can be demonstrated the ion density ρ has the following expression [53, 30]:

$$\rho(r) = \rho = n_p \cdot G \cdot t_{max} \cdot \frac{1}{\pi b^2} \cdot \frac{R}{L}. \tag{8.5}$$

where n_p is the number of primary ion pairs, G the gas gain and R/L is the counting rate per wire length (Sec. 3.4.1). It results that the ion density is independet of the radial distance r from the wire. The two photons emitted by the Calliope source mostly produce Compton electrons in the Al tube wall. The energy of these electrons ranges from zero to 883 keV (where there is a peak) and the average value is 550 keV. The average number of ion-electrons pairs produced by these Compton electrons into the gas volume can be estimated from the equation 3.46 at the atmospheric pressure (~ 1 bar), the result is $n_p \sim 300$.

In the general case of a non zero charge density, the potential $\Phi(r)$ can be calculated with the Poisson's equation

$$\Delta\Phi(r) = -\frac{\rho e}{\varepsilon_0} \tag{8.6}$$

and the boundary conditions $\Phi(a) = V$, $\Phi(b) = 0$. The solution over the active lenght L is:

$$\Phi(r) = \frac{V ln\frac{b}{r}}{ln\frac{b}{a}} + \frac{\rho e}{4\varepsilon_0} \cdot \left((b^2 - r^2) - \frac{(b^2 - a^2) ln\frac{b}{r}}{ln\frac{b}{a}} \right). \tag{8.7}$$

The electric field is then

$$E(r) = -\frac{d}{dr}\Phi(r) = \frac{V}{ln\frac{b}{a}} \cdot \frac{1}{r} + \frac{\rho e}{4\varepsilon_0} \left(2r - \frac{b^2 - r^2}{ln\frac{b}{a}} \frac{1}{r} \right). \tag{8.8}$$

As expected, in the absence of a space charge ($\rho = 0$) the second term vanishes and the equation 8.8 reduces to the first term that is the 8.4.

For gas gain estimation it is sufficient to use the field in the amplification region, this implies $r << b$ (Sec. 3.2.3) and

$$E(r) \simeq \frac{V - \delta V}{ln\frac{b}{a}} \cdot \frac{1}{r} \tag{8.9}$$

defining

$$\delta V = n_p \cdot G \cdot t_{max} \frac{e}{4\pi\varepsilon_0} \frac{R}{L}. \tag{8.10}$$

The electric field in the avalanche region behaves as if the effective potential was $V - \delta V$. It is important to notice that the t_{max} in the 8.10 is not given by the 8.3 which is valid for $\rho = 0$. Using the general expression 8.8 for the electric field in the Ramo's formula 3.32 the general expression for the maximum ion drift time is

$$t_{max} = \frac{\varepsilon_0}{\mu\rho e} ln \left(1 + \frac{\rho e b^2 ln\frac{b}{a}}{2\varepsilon_0 (V - \delta V)} \right). \tag{8.11}$$

The gas gain G can be estimated by the Diethorn formula 3.31 which depends on the potential V and can be written as

$$G = exp \left(\frac{V ln2}{\Delta V ln\frac{b}{a}} \cdot ln \frac{V}{E_{min} \frac{\rho}{\rho_0} a\, ln\frac{b}{a}} \right). \tag{8.12}$$

The meaning of the parameters ΔV and E_{min} is explained in 3.2.3. The values used are the measurements reported there.

The orignal purpose was to calculate the actual gain at a given rate R/L. This cannot be simply achieved by replacing $V - \delta V$ to V in the 8.12 because δV itself depends on the gain. Hence the two equations 8.12 and 8.10 have been solved iteratively.

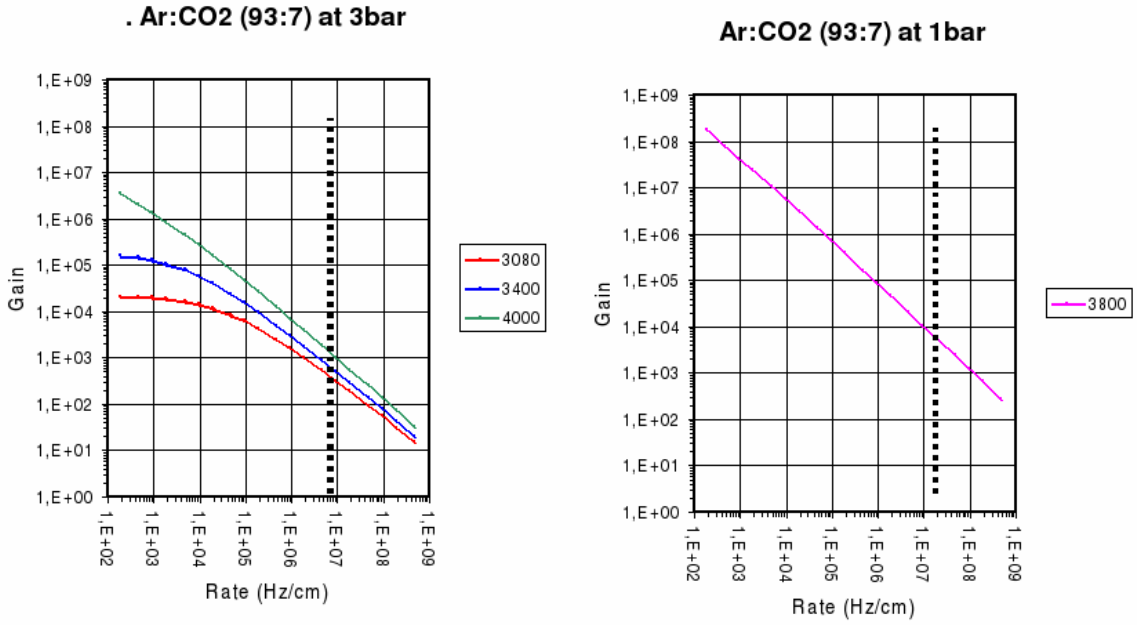

Figure 8.5: Gas gain with respect to the photon background rate. In the left plot the middle curve corresponds to 3400 V and the lower one to 3080 V. The vertical dotted line indicates the count rate at Calliope: $2 \times 10^7 Hz/cm$

The sensitivity ε_γ to photons of about 1 MeV is nedeed: the value used here is 0.0087 (fig. 3.23(a)). The counting rate per wire length is then

$$\frac{R}{L} = \Phi_\gamma \times L \times \varepsilon_\gamma \sim 2 \times 10^7 \frac{Hz}{cm} \tag{8.13}$$

where L is the tube diameter (3 cm).

The behaviour of the gas gain with increasing rate has been computed for the stantard gas at three different settings of the anode-cathode voltage: 3080 V, 3400 V and 4000 V. The results are shown in fig. 8.5. The gain is below the nominal value of 2×10^4 even at a voltage as high as 4000 V. To increase the gain is necessary to reduce the pressure as reported in the plot on the right where the pressure is 1.1 bar and the voltage 3800V.

Rate (Hz/cm)	V(kV)	P (bar)	I (μA)	$I_{EXP}(\mu A)$
2.0 $\times 10^7$	3.8	1.1	220	180
2.0 $\times 10^7$	4.0	3.0	59	50
3.8 $\times 10^6$	4.0	3.0	49	41
3.8 $\times 10^6$	3.08	3.0	14	15

Table 8.1: Comparison between the measured current and the calculated value.

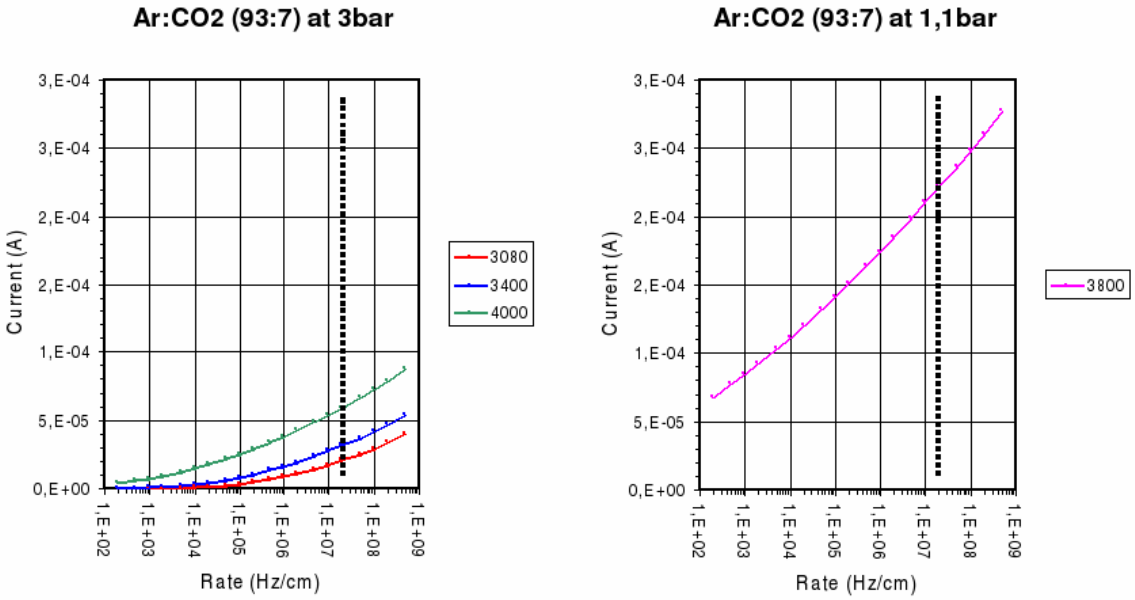

Figure 8.6: Iduced current with respect to the count rate for different tube operation settings. In the left plot the curve in the middle corresponds to 3400 V and the lower one to 3080 V. The vertical dotted line indicates the count rate at Calliope: 2×10^7 Hz/cm.

The current induced on the wire can be estimated

$$I = \frac{R}{L} n_p \cdot G \cdot e \cdot L. \tag{8.14}$$

The current dependence on the tube settings and count rate is shown in fig. 8.6. The current drawn by the chamber during the irradiation has been measured at different values of pressure and applied voltage and the photon flux[1]. From the values reported in tab. 8.1 the agreement between data and predicted values is rather good (10% level).

Operating the chamber at 3800 V and 1 bar gas pressure it is possible to operate in avalanche mode ($G \sim 0.5 \times 10^4$) even at a counting rate of the order of $10^7 Hz/cm$. With this configuration the current drawn is of about 200 μA which makes possible to accumulate the target value of 5 C/cm or so during the scheduled irradiation campaign.

run number		total events	accumulated charge	note
*Roma*3 sample	61	704×10^3	0 C/cm	
	168	401×10^3	4.8 C/cm	
	182	401×10^3	4.8 C/cm	changed read-out electronics
Calliope sample	68+69	78×10^3	0 C/cm	
	71	43×10^3	0.8 C/cm	
	74	43×10^3	1.3 C/cm	
	78	49×10^3	3.2 C/cm	
	79	300×10^3	4.8 C/cm	

Table 8.2: List of the runs used in the analysis.

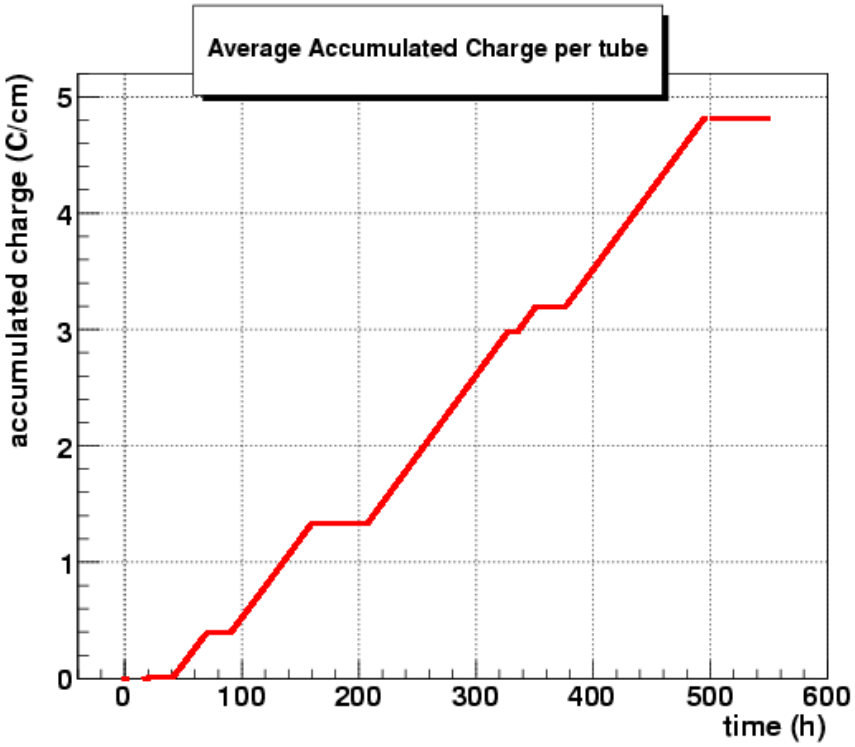

Figure 8.7: Accumulated charge during the irradiation campaign.

8.5 Data samples

After assembly, the bundles have been tested with cosmic rays in the Roma Tre laboratory (Sec. 4.1) The two test chambers were then moved to the Calliope plant to perform the aging test. Another test, consisting in two runs, was performed in the Roma Tre laboratory after the irradiation period.

[1]For a short period some radioactive elements have been removed from the source and the dose rate measured again.

In the last run, the read-out electronics was changed. Before starting the irradiation campaign, a run with cosmic rays trigger was taken and used as reference. While the ^{60}Co source was switched on, the chambers were operated at 3800 V, 1.1 *bar* according to the considerations reported in the previous Section. By rising the voltage and lowering the pressure, the current drawn by each tube could reach 180 μA resulting in an accumulated charge of 4.8 C/cm/wire at the end of the whole irradiation period.
Periods of gamma irradiation were followed by data taking with the cosmic rays trigger (the source was turned off) with MDTs operated in the ATLAS standard conditions for performance monitoring. Five different runs are available for the analysis corresponding to an average accumulated charge per tube of 0.0, 0.8, 1.3, 3.2, 4.8 C/cm. From now on these data and the data acquired in the Roma Tre laboratory will be named *Calliope* and *Roma*3 samples respectively. Details of cosmic rays trigger runs are summarized in Table 8.2.

The increase of the accumulated charge is shown in fig. 8.7.

The periods in which the source was turned off for cosmic data taking are clearly visible.

8.6 Slow control

8.6.1 Environmental parameters

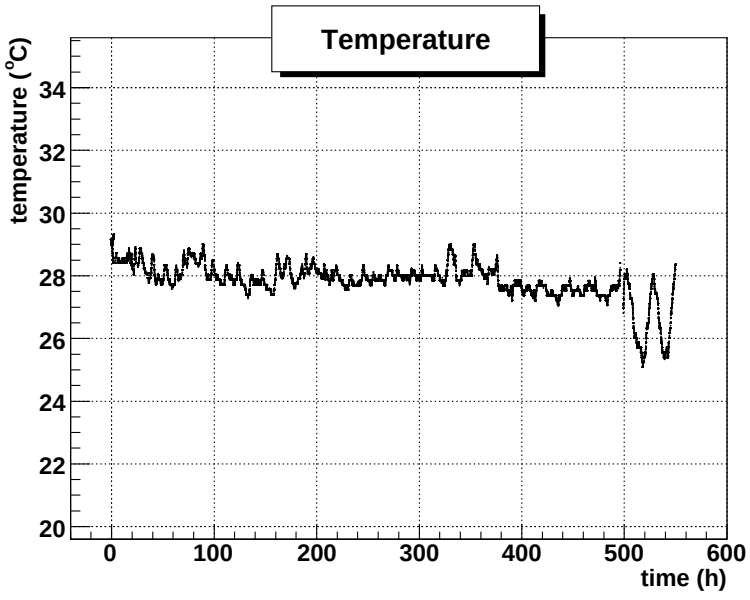

Figure 8.8: Temperature measured during the whole period.

During the test, gas temperature (T), flow and absolute pressure (P) were continuously recorded. The absolute values of T and P are known within $\pm 0.2\ K$ and $\pm 3\ mbar$ respectively. Data were corrected offline for both temperature and atmospheric pressure variations [67]. The temperature during the whole period is shown in fig. 8.8.

Temperature instability in the last part is due to the fact that for the last cosmic run the setup was moved from the irradiation cell, in which the temperature was almost constant, to another room.

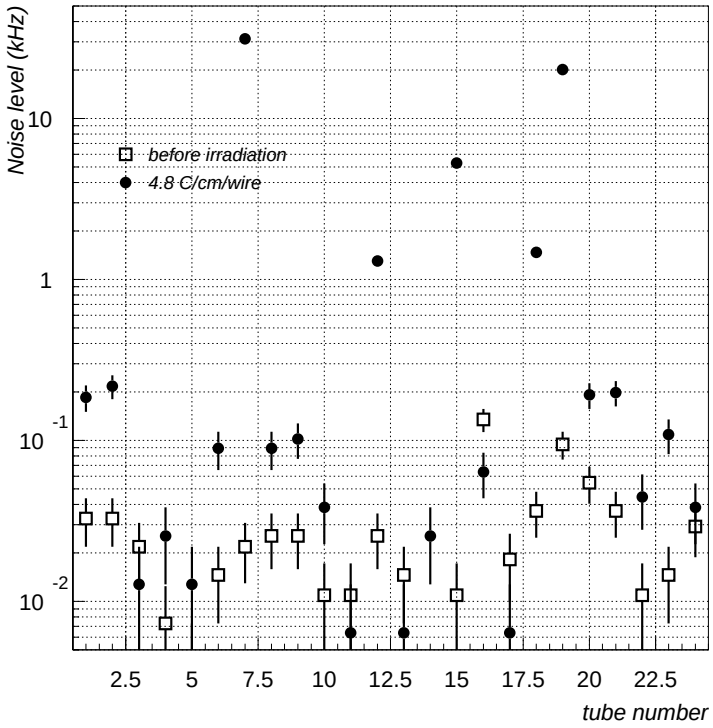

Figure 8.9: Noise level for the tubes of the first test chamber in the two runs of the *Roma*3 sample.

8.7 Drift parameters

In this section the analysis of single tube behavior is presented focusing on noise level, rise time distribution of the drift time spectra and collected charge. These quantities can give an insight on the status of the detector during irradiation and reveal aging effects (the rise time and the ADC spectra are the quantities which are the most sensitive to gain variation).

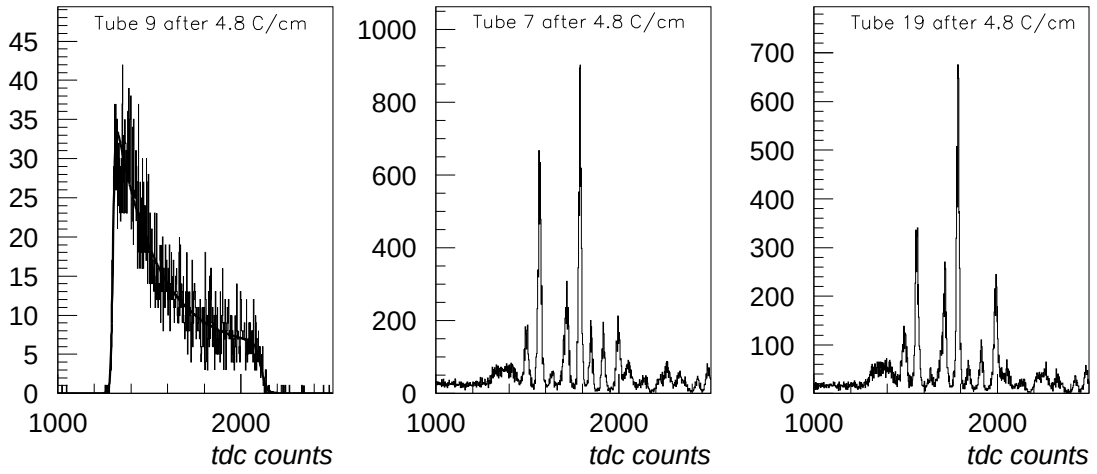

Figure 8.10: Drift time distribution for tubes 7 (center) and 19 (right) and for a good one (left) shown here for comparison.

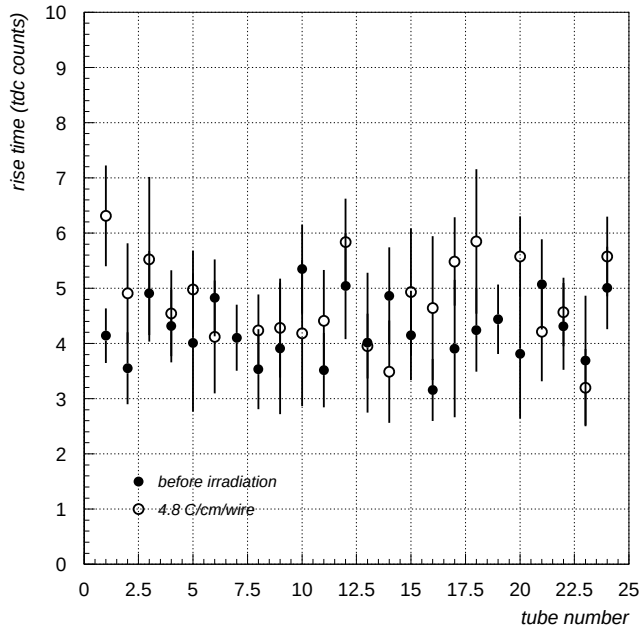

Figure 8.11: Rise time for the tubes of the first test chamber in the two runs of the *Roma*3 sample.

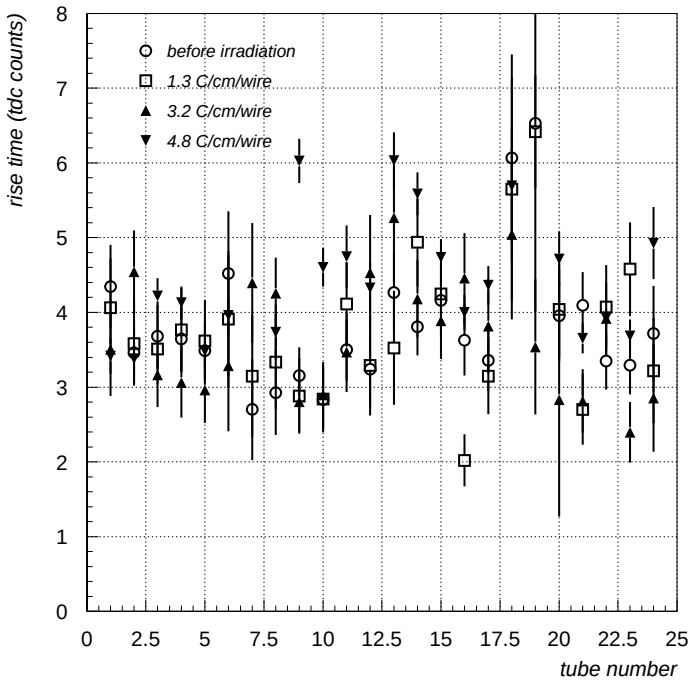

Figure 8.12: Rise time for the tubes of the first test chamber in the runs of the *Calliope* sample.

8.7.1 Drift time analysis

The noise level for all the tubes of the first test chamber is shown in fig. 8.9 for the two runs in the *Roma*3 sample. As can be seen the noise level is higher after irradiation for all drift tubes.

As it has been experienced several times in the past, this difference can be easily explained with minor differences in the electronics connection and grounding as the setup has been mounted several times. For two tubes in particular (namely tubes 7 and 19), the noise level showed a major increase.

The drift time distribution for these tubes is shown in fig. 8.10 (center and right respectively) together with a good drift time distribution for another MDT shown for comparison (fig. 8.10 left). As can be seen these tubes have a drift time distribution completely different and also a distorted charge distribution as will be shown in next Section.

Another parameter of the drift time distribution that can give insight on tube aging is the rise time which is closely related to the space resolution. The rise time for all the tubes of the first test chamber is shown in fig. 8.11 for the two runs in the *Roma*3 sample. Tubes 7 and 19 are not included for the run after the irradiation period as a fit to their drift time distributions

is meaningless. No clear effect of signal degradation can be found for the other tubes.

The same study on the rise rime stability has been performed on the same test chamber for the different runs in the *Calliope* sample and is shown in fig. 8.12. The rise time shows to be constant as the accumulated charge increases.

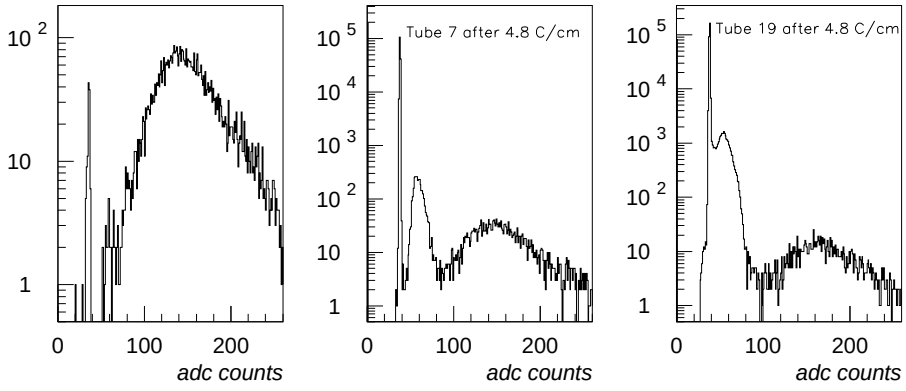

Figure 8.13: Collected charge distribution for tubes 7 (center) and 19 (right) and for a good one (left) shown here for comparison.

8.7.2 Collected charge analysis

The measure of the collected charge (raw charge, Sec. 4.3) can be very useful to investigate variation in the tube gain and in the overall tube response signal. The distribution of the collected charge is shown in fig. 8.13 for a typical tube (left) and for the two tubes already highlighted in the previous section (center and right).

As can be seen the distribution for those tubes is rather distorted. In the last run of the *Roma*3 sample the read-out electronics was changed; this resulted in an improvement of the ADC response for these two tubes as shown in Fig. 8.14 (left) only for tube 7 as an example. The noise induced peak pedestal is still rather high. The drift time distribution obtained requiring an ADC value larger than 50 ADC counts (in order to suppress the noise induced peak pedestal) has the expected shape as shown in fig. 8.14. For collected charge studies is necessary to fit the ADC distribution with a representative function where the mean value and width can be derived analytically. To fit the central region of the collected charge distribution,

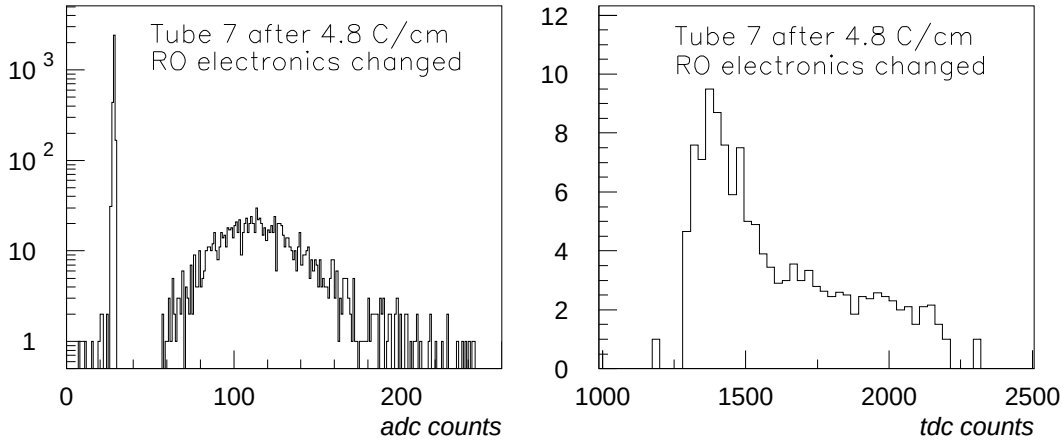

Figure 8.14: Collected charge distribution (left) and drift time spectra after applying the cuts on the ADC values (right) for tube 7 after changing the read-out electronics.

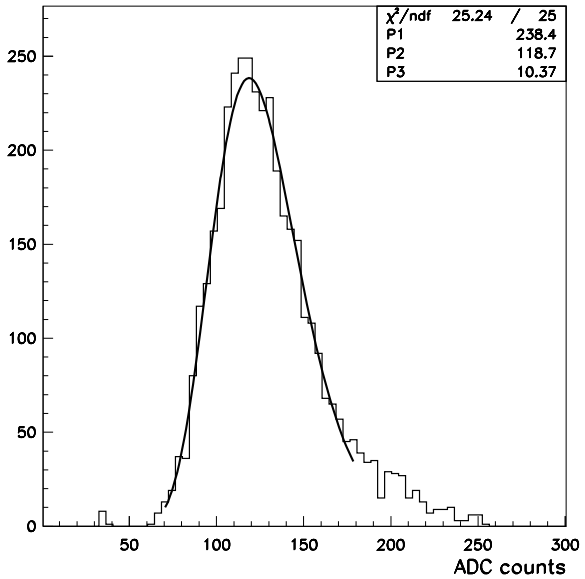

Figure 8.15: ADC spectrum fitted width the function 8.15.

excluding the peak pedestal,

$$f(x) = p_1 e^{-\frac{(x-p_2)^2}{xp_3}}, \tag{8.15}$$

has been constructed which is a gaussian width a non-constant sigma, suitable for quasi-symmetric distribution. The parameter p_2 is the value corre-

sponding to the maximum of the distribution and the width can be described by the $FWHM$ given by

$$((p_3 ln2)^2 + 4p_2 p_3 ln2)^{1/2}.$$

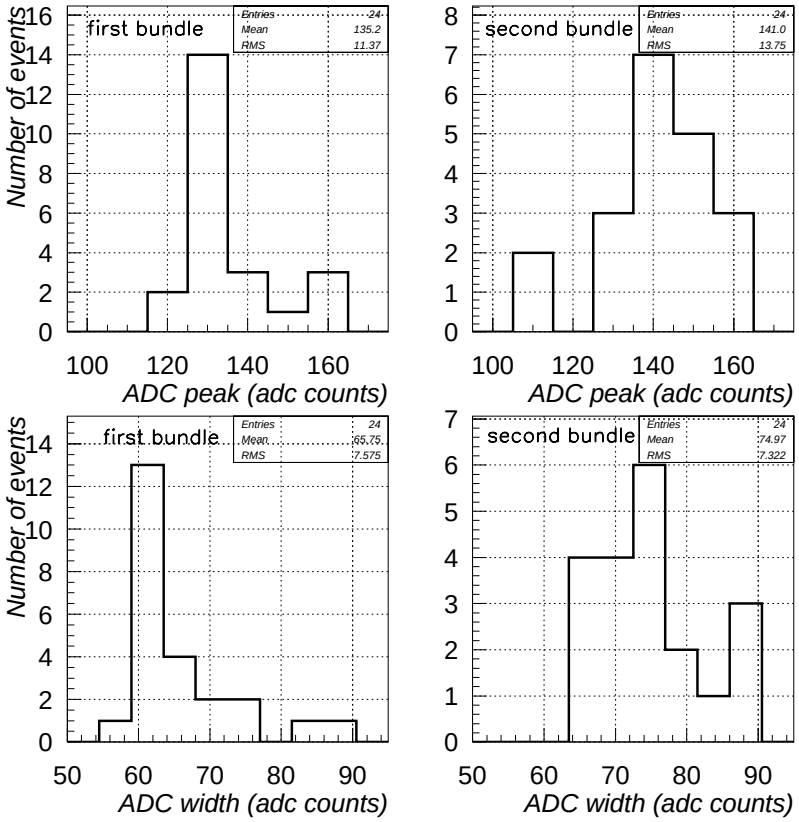

Figure 8.16: Distribution of the fit value of the ADC distribution peak value x_{max} and width $FWHM$ for the two test chambers before irradiation.

The gas gain is very sesitive to density variation, that is to say temperature and pressure, as the Diethorn formula states. From the 3.31, in the approximation $\Delta T << T$ and $\Delta P << P$:

$$G(T + \Delta T) = G(T) \cdot (1 + \Delta T/T)^{\alpha} \approx G(T)(1 + \alpha\ \Delta T/T) \tag{8.16}$$

$$G(P + \Delta P) = G(P) \cdot (1 + \Delta P/P)^{\alpha} \approx G(P)(1 - \alpha\ \Delta P/P) \tag{8.17}$$

where T is the absolute temperature expressed in Kelvin and $\alpha \approx 9.857$ for $Ar : CO_2(93{:}7)$ at 3 bar. It was thus decided to correct the peak value

x_{max} to take into account temperature and pressure variations in each run with temperature T=$T_0 + \Delta T$ and pressure P=$P_0 + \Delta P$, with respect to the reference temperature and pressure of the first run T_0 and P_0.

The corrected $x_{max}^{T_0,P_0}$ value has been obtained applying in turn a temperature and a pressure correction:

$$x_{max}^{T_0,P} = x_{max}^{T,P}\left(1 - 9.86\frac{\Delta T}{T_0}\right), \tag{8.18}$$

$$x_{max}^{T_0,P_0} = x_{max}^{T_0,P}\left(1 + 9.86\frac{\Delta P}{P_0}\right). \tag{8.19}$$

The distribution of the corrected value of x_{max} and $FWHM$ for all the tubes of the two bundles for the first run at the Calliope plant are shown as an example in Fig. 8.16. These values have a spread of about 10% as already reported in (Chap. 6).

The mean value of the distributions in fig. 8.16 and of the analogous distributions for all the other runs are shown with respect to the accumulated charge in fig. 8.17. It can be seen that both values are almost constant.

8.8 Tracking analysis

8.8.1 Space-time relation

The dependence of $r(t)$ relations on accumulated charge has been investigated to understand MDTs tracking properties after intensive gamma irradiation. The *Calliope* data sample has been used to evaluate possible differences in the $r(t)$s as the accumulated charge is increasing. A $r(t)$ relation has been calculated for each single run. Because of their dependence on gas, temperature and composition, only data with temperature spread within 1.5 $°C$ and pressure variation within few *mbar* have been analyzed. All $r(t)$s have been normalized to the same temperature of 28 °C, applying appropriate corrections as described in [52] and [58] and then compared with reference data taken before irradiation. Fig. 8.18 shows the differences between the $r(t)$ computed for the reference run and the $r(t)$ computed for each other run.

A small increase of the difference between the $r(t)$s with increasing accumulated charge is visible. It is less than 100 μm for large radii even after the total accumulated charge of 4.8 C/cm/wire. Such a variation is corrected in the standard calibration of the $r(t)$ relations (calibrations have to be performed regularly to take into account environmental parameters variations that can give effect of the same size).

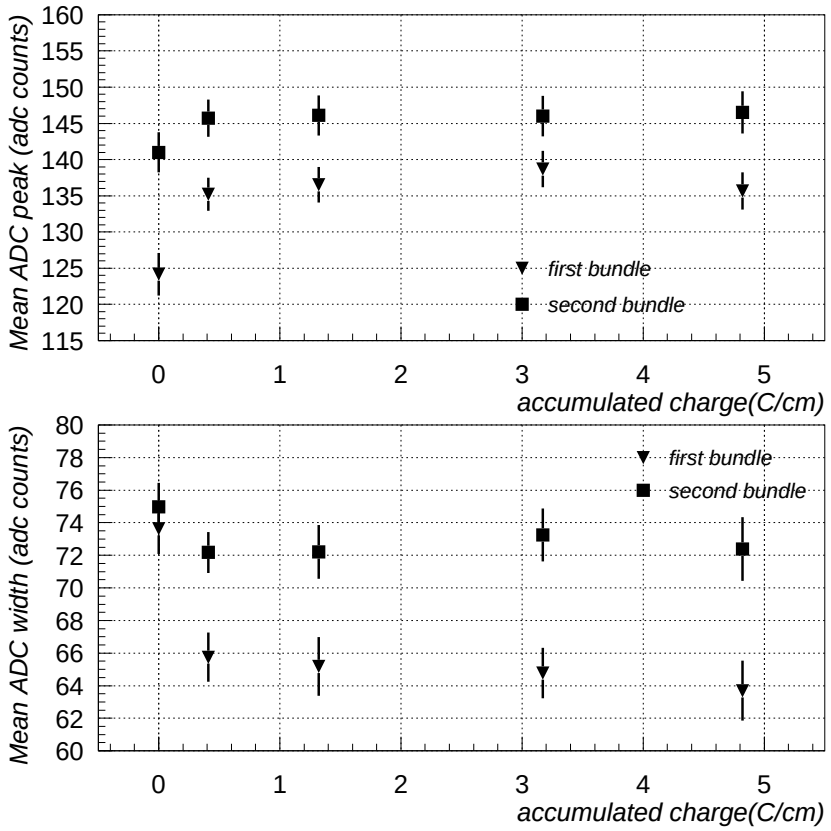

Figure 8.17: ADC distribution mean peak value x_{max} and mean width $FWHM$ (averaged over all the tubes of one test chamber) with respect to the accumulated charge for the two test chambers.

8.8.2 Tube efficiency

Two definitions of efficiency can be given for drift tubes: *hit efficiency* is the probability to register a hit for a muon track crossing the tube, irrespective of the measured drift time. The *n-σ efficiency* instead, is the probability that the drift radius r_{drift}, derived from the drift time, does not differ from r_{extr}, the radius extrapolated from the other tubes, more than n times the single tube resolution in r_{extr}. Tracks with at least three hits on tubes different from the one under observation are selected; then a drift radius r_{extr} is extrapolated on that tube. If residual with respect to the track differs less than 5σ the hit is considered a "good hit": efficiency is then computed as the ratio between the number of good hits and the number of tracks that crossed the tube. An optimal calculation of the *n-σ efficiency* cannot be achieved with the present setup. The non perfect grounding caused a slightly high

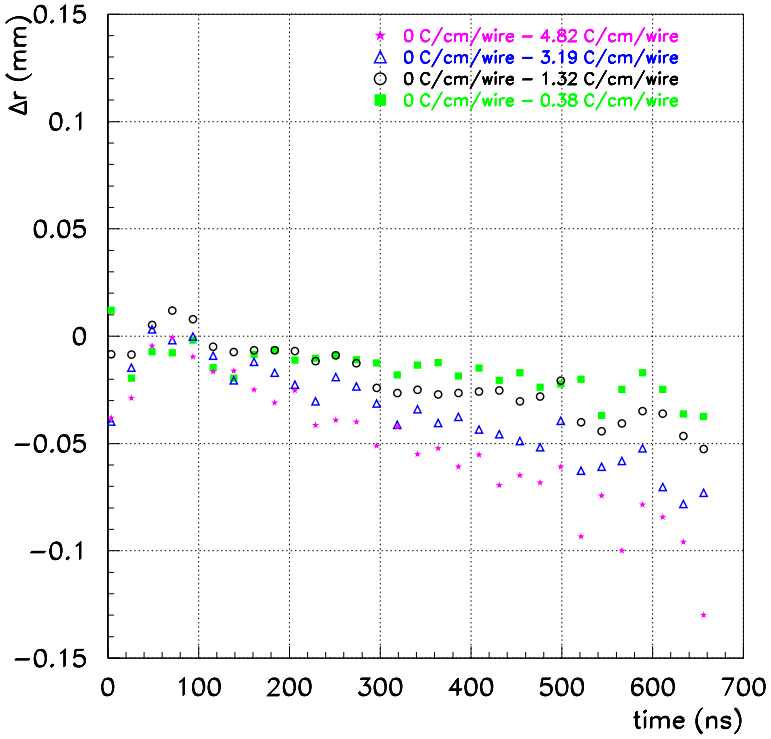

Figure 8.18: Comparison between the $r(t)s$ for the different runs with respect to reference data.

noise level in some tubes. This is a problem for the n-σ *efficiency* because of the 600 ns dead time fixed in the read-out electronics. Furthermore, for some angular configurations, the determination of the track parameters with only three drift circles suffers from an ambiguity that can affect the track extrapolation to the last tube. The best way to compute efficiency in the MDT chamber is to use the whole chamber, i.e. two multilayers, but this was not possible because the two bundles were not aligned. These effects are taken into account by normalizing the efficiency to the *hit efficiency*. The value of the efficiency for all the tubes of the first test chamber is shown in fig. 8.19 for the five different cosmic runs. In the last run, after the last irradiation period, tubes 7 and 19 showed the behavior described in the previous sections and their *hit efficiency* suddenly drops to less than 0.5 and their efficiency is not shown in the figure.

As it is shown in fig. 8.20 for some tubes of layer 3 as an example for all the other tubes, efficiency proved to be constant with respect to the accumulated charge.

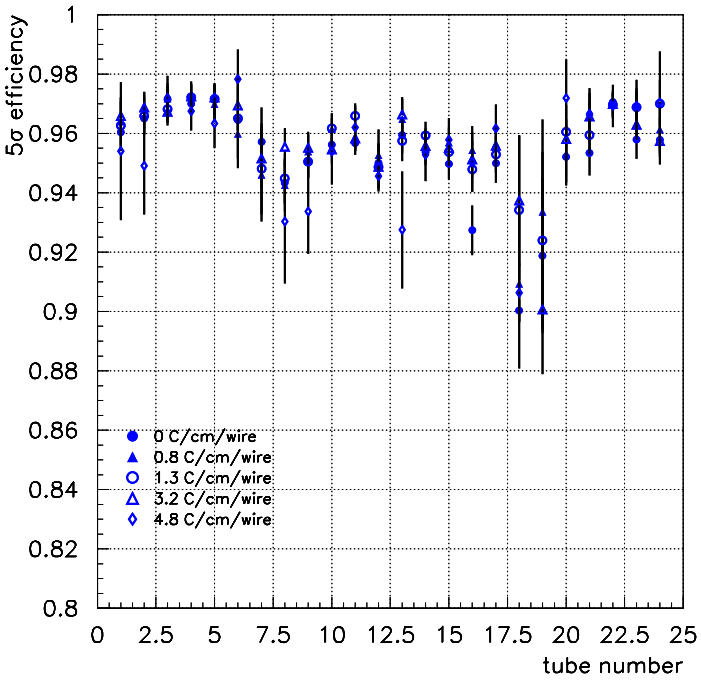

Figure 8.19: Efficiency for all the tubes of the first test chamber for the five cosmic runs.

The efficiency for tubes 7 and 19 has been controlled in the run of the *Roma*3 sample, in particular in the two runs after the irradiation campaign. After changing the read-out electronics the *hit efficiency* rises back to the initial value of 0.98±0.01 for tube 7 and to 0.95±0.02 for tube 19. This observation, in addition to the one in Sec. 8.7.2 and to the wire analysis in the next section, suggests that a part of the read-out electronics suffered a damage during irradiation.

8.9 Wire analysis

After the two irradiation campaigns some anode wires of the two test chambers were removed in order to perform chemical and sufrace analysis. The aim of the wire examination was to reveal some pollution and to analyze their composition.
Two techinques heve been used:
Scanning Electron Microscopy (SEM): Scanning Electron Microscopy or SEM makes it possible to resolve sub-micrometer details on the wire surface. This is done by moving a thin electron beam in a controlled way over the material under study and recording the number of electrons reflected.

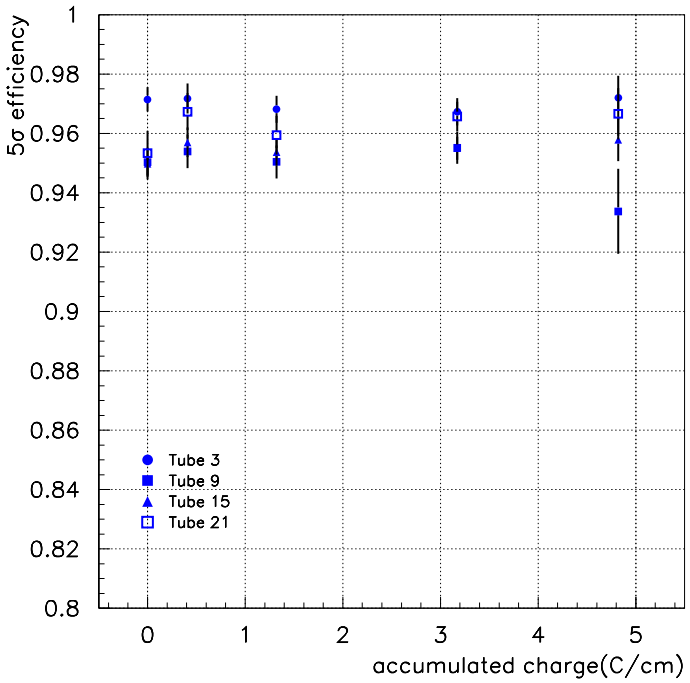

Figure 8.20: Efficiency for four central tubes (one for each layer) of the first test chamber versus accumulated charge.

From the contrast of the SEM picture it is also possible to deduce whether a material is electrically conducting or not.

Energy Dispersive X-ray analysis (EDX): Energy Dispersive X-ray (EDX) analysis is a method usually combined with SEM. When hit by the scanning electron beam, atoms are left in an excited state with energy E_i; they return to their ground state E_0 or a lower intermediate state E_j by emitting X-rays with a frequency proportional to the energy difference $E_i - E_j = E_{ij}$. Since the values of E_{ij} are characteristic for each chemical element, the chemical composition of a material can be identified by recording the X-ray spectrum; this is usually done with the help of a semi-conductor detector. EDX is sensitive to all elements except hydrogen; the volume of material probed is usually of the order 1 μm^3. With the instrument used for this thesis a volume of $0.5 \times 0.5 \times 0.5\,\mu m^3$ was analysed; material on the surface of another substance could be detected if its thickness exceeded $0.2\,\mu m$.

Four analyzed wires were taken from tubes of the test chamber n. 1, which was also irradiated with neutrons (Sec. 8.11), one from each layer. In particular, the wires from MDT tubes n. 3, 9, 13 and 20 were extracted. The

first two tubes accumulated a charge of 4.82 C/cm (5261 Gy), while tubes 13 and 20 accumulated a charge of 3.19 C/cm (3471 Gy) and 1.32 C/cm (1419 Gy) respectively. The other three wires were extracted from MDT tubes n. 3, 10 and 19 (the one that showed the worst response) from the test chamber n. 2. From previous aging tests ([59], [60] and [61]) it is known that pure $Ar : CO_2$ (93 : 7) doesn't show any evidence of aging up to an accumulated charge of 1.2 C/cm. Nevertheless some aging effects can appear if the gas is polluted with sealing material used for valves or chemicals that enters the drift tube by outgassing of components that are in contact with the gas system (e.g. cleaning agent). Since the on-chamber gas distribution is serial-parallel (three tube series) the wires were chosen in order to have at least one tube for each position in the gas series. The wires were extracted from the tubes and analyzed. A detailed description of the employed technique to extract the anode wire is given in [61].
Each extracted wire was divided in three samples of 4 cm length each: one at 2 cm from the beginning of the wire (gas inlet side), one in the middle and one at 2 cm from the end of the wire (gas outlet side). Each sample was analyzed and no deposits on the wire surface has been observed. Three additional samples (reference wires) of 4 cm length each, taken directly from the same wire spool employed for the test chamber tubes, were analyzed for comparison.

Fig. 8.21 shows a micro-photo and the analysis of one reference wire. The surface is everywhere clean besides some black spots and white particles, both with an important amount of Carbon. The surface of the irradiated wires appears similar to the reference one: mostly clean, with some regions with black stains (C-O-Si-Al-Ca) and other regions with white particles (Al-Cl-F). Fig. 8.22 shows two micro-photos as examples of irradiated wires with black stains (left) and white particles (right).

In conclusion the whole set of analyzed wires shows the same pollution detected on the reference one.

8.10 Summary

A intensive photon irradiation test was performed on final MDT-like test chambers. After a full accumulated charge of 4.8 C/cm per tube, a good behavior of the chamber is observed.
The pressure drop rate before and after the irradiation campaign was measured and it turned out to be constant (1×10^{-8} $bar \cdot l/s$, a value that fits with the ATLAS requirements). This implies a stable behavior of o-rings, end-plugs and all the different gas distribution elements.
Two tubes showed a distorted drift time spectra and a sudden drop in ef-

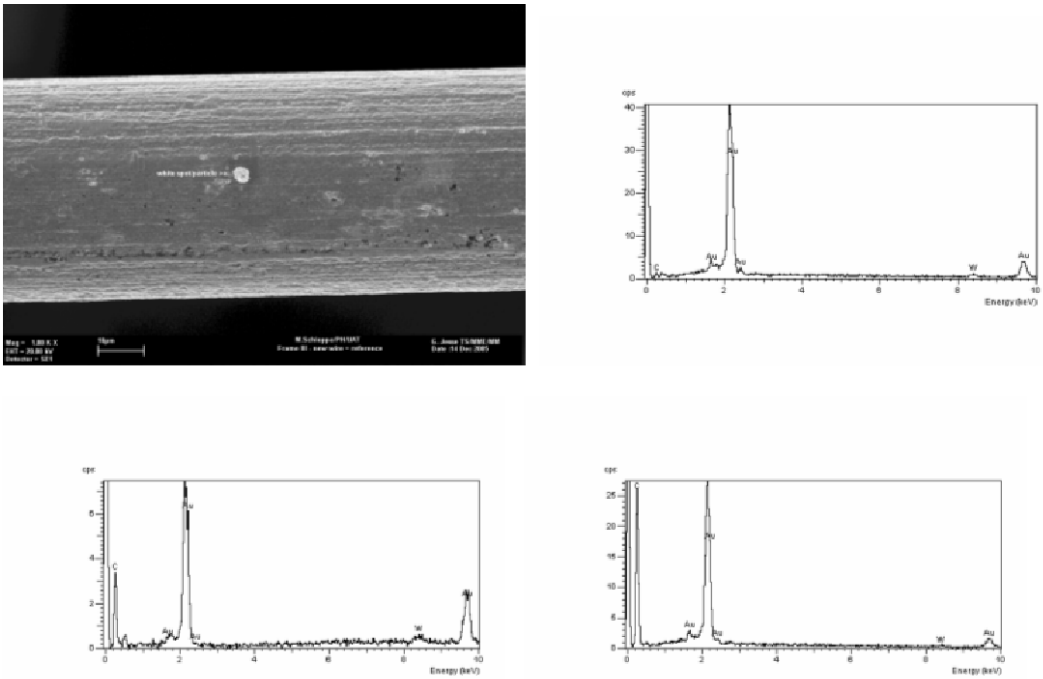

Figure 8.21: Micro-photo of the reference wire. EDX analysis related to the clean surface of the wire (top right), black spot (bottom left) and white particle (bottom right).

ficiency after 4.8 C/cm was accumulated. The hit efficiency improved by changing the read-out electronics, suggesting a damage to some electronic component. The SEM/EDX analysis shows no evidence of damages on the wires. It has to be underlined here that the ASD and the TDC chip have been tested under irradiation [62],[63] and proved to tolerate an irradiation equivalent to 10 years of LHC operation. However, in this test the irradiation was much higher than in earlier studies.
No significant gain drop is observed looking at the measured charge deposit and negligible variations of the drift properties result from drift time spectra and space-time relation studies for all the tubes of two bundles.
The single tube efficiency remains constant with increasing accumulated charge.
No evidences of deposits or damages on the surfaces of the wires resulted from chemical analysis.

8.11 Neutron irradiation test

Another test was performed by exposing a drift chamber to the neutron flux originated form a nuclear reactor. Neverthelss the detector sensitivity to neutrons is one oder of magnitude lower compared to photons, the neutron

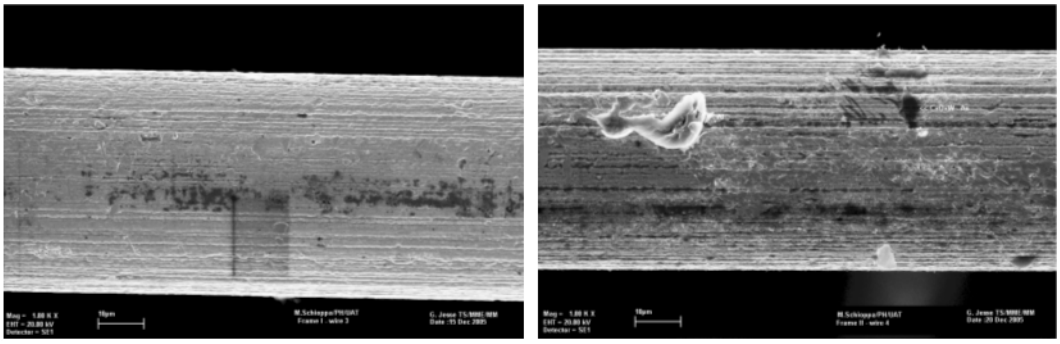

Figure 8.22: Micro-photo of the irradiated wire 20 (left) and wire 3 (right).

background can also affect critically the device performance and stability being the main source of radiation damage of the detector components i.e. bulk damage of the electronics.

8.11.1 Tapiro nuclear facility

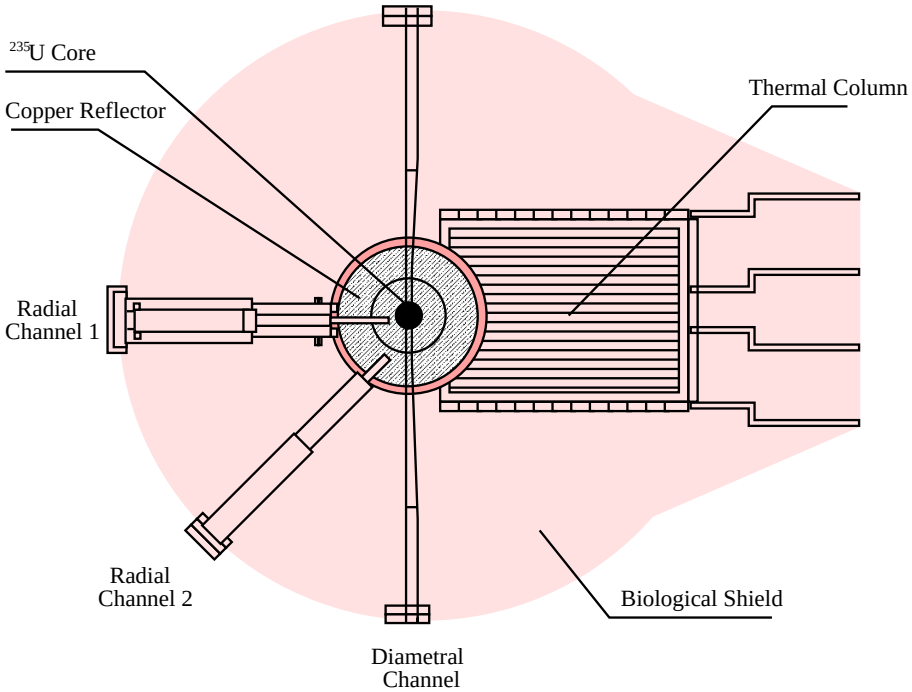

Figure 8.23: Schematic layout of TAPIRO reactor with a view of the experimental channels and of the thermal column cave.

The Tapiro nuclear reactor is a high-enriched ^{258}Uranium copper reflected fast neutron source at the ENEA research center. The reactor core has a cylindrical core with radius of 6.2 *cm* and a height of 10.87 *cm*. The fuel is

a metal alloy (U 98.5%, Mo 1.5%) with a fully enriched ^{235}Uranium (93.5%). Its critical mass is 21.46 kg. The maximum neutron flux at the core center is 2.2×10^{12} neutrons/$cm^2 s$ at the nominal thermal power of 5 kW. The reactor is surrounded by borate concrete shielding about 170 cm thick.

Several channels of different dimension and depth which penetrate the reactor shielding are present. They are used for locating apparatus to be irradiated (fig. 8.23). The largest cave available, the thermal column cave (fig. 8.23) the one used for the test, has dimensions $110 \times 110 \times 160\, cm^3$.

The neutron energy spectrum in the thermal cave is shown in fig. 8.24. It

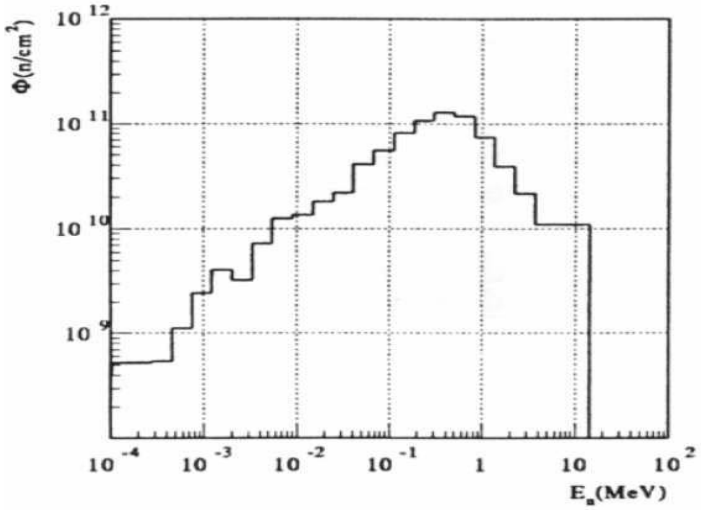

Figure 8.24: Neutron energy spectrum at the nuclear reactor source.

is rather consistent with the one expected in ATLAS, i.e. fig. 3.23.

The neutron flux at the detector surface have been measured by means of an activation tecnique, utilising bare and cadmium-shielded gold foils. The values measured at the reactor thermal power of 200 W are: 2.23×10^7 Hz/cm^2 at the surface which is upstream with respect to the source and 1.07×10^7 Hz/cm^2 at the opposite side of the detector (uncertainties are at 10% level).

8.11.2 Trigger system and setup

The experimental setup is the same assembled for the test at the photon facility 8.2. One chamber only has been used because of the small volume of the experimental cavity. The bundle used had already being irradiated with photons without significant performance degradation. The trigger scintillators have been further shielded with Borum powder to suppress the neutron

background.

The chamber has been irradiated for about 6-8 hours integrating from 1.68×10^{11} n/cm^2s to 1.48×10^{12} n/cm^2s by varying the reactor power between 100 W to 400 W. During the irradiation the trigger was switched off. Currents drawn by the tubes varies from 5 μA to 8 μA. To monitor the chamber response four cosmic ray data sample have been taken, during the campaign, while the reactor was off. A run was taken before starting the test to be used as reference.

8.11.3 Analysis

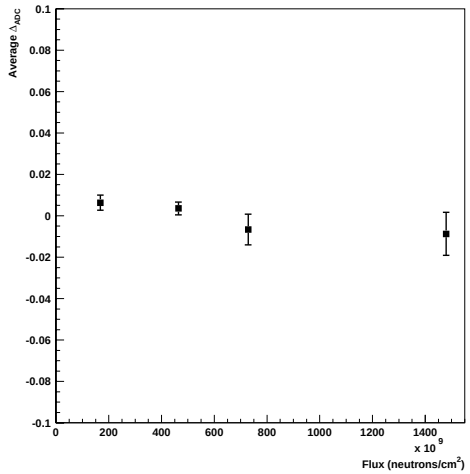

Figure 8.25: ADC peak mean relative variation with respect to the reference run for different neutrons integrated flux.

Three major tools were used to investigate the MDT response: *ADC* spectra, $r(t)$ relation and efficiency (see previous Sections). In fig. 8.25 the mean relative variation of the *ADC* with respect to the neutron integrated flux. Deviation from the reference value are whitin 2 %. The $r(t)$ relation was computed for each of the four mentioned runs and compared to the $r(t)$ obtained from the reference run (fig. 8.26): differences are whithin $\pm 25\,\mu m$. Results from efficiency measurements are reported in fig. 8.26: differences seems not to be significant.

The results of the wire analysis are described in Sec. 8.9.

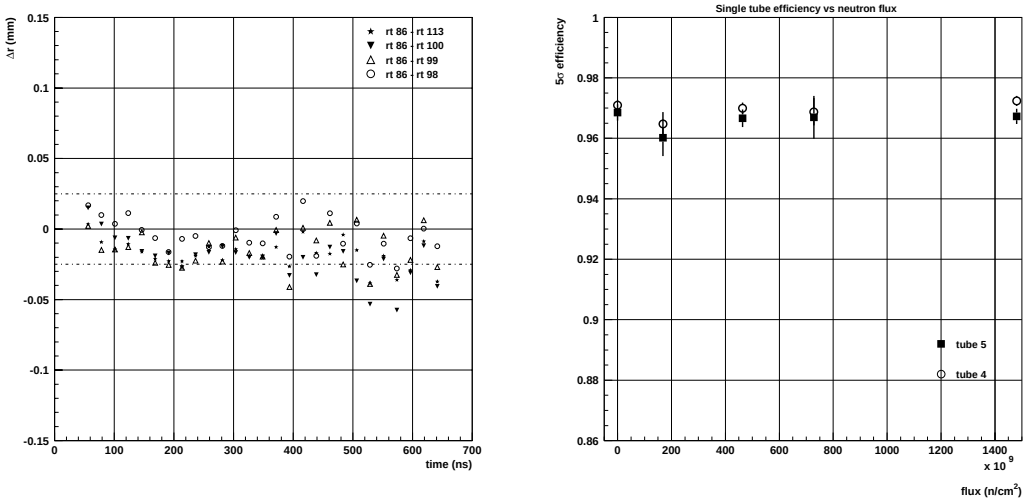

Figure 8.26: *Left*. r(t) differences with respect to the reference for different runs. *Right*: five sigma efficiency for the various runs (for two tubes only).

.1 Geometrical (orthogonal) distance least square fitting

The minimization of the function 5.22

$$\chi^2(a,b) = \sum_i \omega_i \, \frac{(a\ y_i + b - z_i)^2}{1+a^2} \tag{20}$$

with respect to the parameters a and b implies

$$\frac{\partial \chi^2}{\partial b} = \frac{2}{1+a^2} \sum_i \omega_i \left[a\ y_i + b - z_i\right] = a\ \frac{\sum_i \omega_i y_i}{\sum_i \omega_i} - \frac{\sum_i \omega_i z_i}{\sum_i \omega_i} + b = 0 \tag{21}$$

that is

$$b = \frac{\sum_i \omega_i z_i}{\sum_i \omega_i} - a\ \frac{\sum_i \omega_i y_i}{\sum_i \omega_i} = \bar{z} - a\ \bar{y} \tag{22}$$

and

$$\frac{\partial \chi^2}{\partial a} = \frac{2}{1+a^2} \sum_i \omega_i y_i \left[a\ y_i + b - z_i\right] - \frac{2a}{(1+a^2)^2} \sum_i \omega_i \left[a\ y_i + b - z_i\right]^2 = 0 \tag{23}$$

which can be expanded as[2]

$$\begin{aligned} (1+a^2)\Big(a\ \sum \omega y^2 + b\ \sum \omega y - \sum \omega y z\Big) \\ - a\ \Big(a^2 \sum \omega y^2 + b^2 \sum \omega + \sum \omega z^2 \\ -2a \sum \omega y z - 2b \sum \omega z + 2ab \sum \omega y\Big) = 0 \end{aligned} \tag{24}$$

It can be written as (the terms proportional to m^3 vanishes)

$$\begin{aligned} b^2\Big(-a \sum \omega\Big) + b\Big((1-a^2) \sum \omega y + 2a \sum \omega z\Big) \\ + a^2 \sum \omega y z + a\Big(\sum \omega y^2 - \sum \omega z^2\Big) - \sum \omega y z = 0. \end{aligned} \tag{25}$$

Inserting the 22 in the 25 the first two terms become

$$\begin{aligned} \Big[\Big(\frac{\sum \omega z}{\sum \omega}\Big)^2 + a^2 \cdot \Big(\frac{\sum \omega y}{\sum \omega}\Big)^2 - 2\ a\ \frac{\sum \omega z \cdot \sum \omega y}{(\sum \omega)^2}\Big]\Big(-a \sum \omega\Big) \\ + \Big(\frac{\sum \omega z}{\sum \omega} - a\ \frac{\sum \omega y}{\sum \omega}\Big)\Big(\sum \omega y - a^2 \sum \omega y + 2a \sum \omega z\Big) = \\ = -a\ \frac{(\sum \omega z)^2}{\sum \omega} - a^3\ \frac{(\sum \omega y)^2}{\sum \omega} + 2\ a^2\ \frac{\sum \omega z \cdot \sum \omega y}{\sum \omega} \end{aligned}$$

[2]Hereinafter the summation symbol may be omitted, *e.g.* $\sum_{i=1}^{N} \omega_i z_i y_i \equiv \sum \omega z y$.

$$+\frac{\sum \omega z \cdot \sum \omega y}{\sum \omega} - a^2 \ \frac{\sum \omega z \cdot \sum \omega y}{\sum \omega} + 2 \ a \ \frac{(\sum \omega z)^2}{\sum \omega} - a \ \frac{(\sum \omega y)^2}{\sum \omega}$$

$$+a^3 \ \frac{(\sum \omega y)^2}{\sum \omega} - 2a^2 \ \frac{\sum \omega y \cdot \sum \omega z}{\sum \omega}.$$

Adding the last two terms of the 25

$$a^2 \ \Big(\sum \omega yz - \frac{\sum \omega y \cdot \sum \omega z}{\sum \omega}\Big) +$$

$$+m \ \Big(\sum \omega y^2 - \frac{(\sum \omega y)^2}{\sum \omega} + \frac{(\sum \omega z)^2}{\sum \omega} - \sum \omega z^2\Big)$$

$$+\frac{\sum \omega y \cdot \sum \omega z}{\sum \omega} - \sum \omega yz.$$

Which can be rewritten

$$a^2 + a \ \frac{+\frac{(\sum \omega z)^2}{\sum \omega} - \sum \omega z^2 - (\sum \omega y^2 - \frac{(\sum \omega y)^2}{\sum \omega})}{\sum \omega yz - \frac{\sum \omega y \cdot \sum \omega z}{\sum \omega}} - 1 = 0.$$

or

$$a^2 + a \ \frac{\sum \omega z^2 - \sum \omega \bar{z}^2 - (\sum \omega y^2 - \sum \omega \bar{y}^2)}{\sum \omega \bar{z} \bar{y} - \sum \omega yz} - 1 = 0$$

with $\bar{z} = \sum \omega z / \sum \omega$ and $\bar{y} = \sum \omega y / \sum \omega$.

Defining

$$A = \frac{1}{2} \ \frac{\sum \omega z^2 - \sum \omega \bar{z}^2 - (\sum \omega y^2 - \sum \omega \bar{y}^2)}{\sum \omega \bar{z} \bar{y} - \sum \omega yz}$$

the solutions are

$$a_{\pm} = -A \pm \sqrt{A^2 + 1}.$$

The Muon Spectrometer of the ATLAS detector, which is currently under construction at the CERN laboratory, relies on Monitored Drift Tubes (MDTs) for precise muon track reconstruction. In this thesis are reported results achieved on the study of the MDT response and calibration.

An accurate knowledge of the MDT calibration constants and a longterm response uniformity and stability are mandatory to fully exploit the high mechanical precision of the detector and the good spatial resolution of the drift tubes.

Measurements were carried out using different experimental setups, developing and assembling ad-hoc detector and/or trigger devices in some cases. Some analysis alghoritms, to be used for calibration optimization and improvement and which have been implemented in the official software packages, have been developed and tested with both simulated and experimental data.

A dedicated algorithm for the simulation of the detector response has been also implemented for algorithm validation and interpretation of some experimental results.

A study of the systematic errors in the calibration procedure has been carried out analysing test beam data samples, data from cosmic rays setup, and simulation. The track fit task has been developed in detail. The variuos sources of uncertainties and the most critical factors affecting the determination of the MDT calibration constants (i.e. t_0 and the space-to-time $r(t)$ relation) and their impact on the track parameters have been put in evidence. A modified version of the standard procedure, which can also be used for the measurement of the position of the track in the wire direction in regions of the spectrometer where the information on the secoond coordinate is missing is presented as well. A section is dedicated to the description of the resolution determination algorithm and the possible optimizations quantifying the effects of the multiple scattering and of the trigger signal delays.

A degradation of the wire chamber performance after extended operation in a high-rate environment is the main factor limiting the detector lifetime. Two scaled-down MDT chambers have been build and equipped with the standard gas distribution system, high voltage distribution and front-end electronics to study their response under photon irradiation accumulating a total charge of 4.8 C/cm/wire corresponding to about 10 years of LHC operation at the highest luminosity. A neutron irradiation test was also performed. No significant drop in gain was observed neither significant variations variations in the drift properties. The visual and spectroscopic analysis of the anode wires confirmed these results.

Acknowledgements

I would like to thank Prof. F. Ceradini, Prof. F. Pastore and Prof. O. Ragnisco for the reason they know. I thank the Roma Tre ATLAS group for the nice and fruitful time spent together.

Bibliography

[1] F.Halzen,A.D.Martin, *Quarks and leptons: an introductory course in modern particle physics*, Wiley (1984).

[2] L.B.Okun; *Leptoni e quark*, Mir (1986).

[3] F.Mandl, G.Shaw, *Quantum Field Theory*, Wiley (1984).

[4] LEP Collaboration, LEP Electroweak Working Group and SLD Heavy Flavor and Electroweak Groups, *A combination of preliminary electroweak measurements and constraints on the standard model.*, hep-ex/0112021 , (2001).

[5] The LEP working group for Higgs boson searches, *Search for the Standard Model Higgs Boson at LEP*, CERN-EP/2001-055 (July 11, 2001)

[6] S.P.Martin, *A Supersymmetry primer*, CERN/90-10 ECFA/90-133, (1999).

[7] D.Denegri, *Aachen LHC workshop*, hep-ph/9709356 , (1990).

[8] Z.Kunszt, S.Moretti e W.J.Stirling, *Higgs production at LHC*, Z.Phys. C74, (1997) 479.

[9] A.Djouadi, D.Graudenz, M.Spira e P.M.Zerwas, *Higgs boson production at the LHC*, Nucl.Phys. B453, (1995)17.

[10] K. Hagiwara *et al.*, *Review of Particle Physics*, Physical Review D, 2002, 66, http://pdg.lbl.gov.

[11] ATLAS Collaboration; *ATLAS detector and physics performance Technical Design Report*, CERN-LHCC-99-14/15 (1999).

[12] B.Mellado; *Prospects of the Higgs physics at the LHC*, ATLAS internal note, ATL-CONF-2002-004 (2002).

[13] The LHC Study Group; *The LHC conceptual design report*, The Yellow Book, CERN/AC/95-05 (LHC).

[14] ATLAS Collaboration; *ATLAS Technical Proposal for a General Purpose p-p Experiment at the Large Hadron Collider at CERN*, CERN/LHCC/94-43,LHCC/P2 (1994).

[15] ATLAS collaboration; *Inner Detector Technical Design Report*, Volume 1, CERN/LHCC/97-16 (1997).

[16] ATLAS collaboration; *Liquid Argon Calorimeter, Technical Design Report*, CERN/LHCC/96-41 (1996).

[17] ATLAS collaboration; *Tile Calorimeter Technical Design Report*, CERN/LHCC/96-42 (1996).

[18] ATLAS Collaboration; *ATLAS detector and physics performance Technical Design Report*, CERN-LHCC-99-14/15 (1999).

[19] ATLAS Muon Collaboration, *ATLAS Muon Spectrometer Tecnical Design Report*, CERN/LHCC/97-22, ATLAS TDR-10 (1997).

[20] W.R. Leo, *Techniques for Nuclear and Particle Physics Experiments*, Spinger-Verlag, New York (1994).

[21] J.E. Moyal, *Theory of ionization fluctuations*, Phil. Mag. 46 (1955)

[22] F.Sauli, *Principles of operations of multiwire proportional and drift chambers*, CERN 77-09, May 1977.

[23] W.Blum, L.Rolandi, *Particle Detection with Drift Chambers*, Springer-Verlag (1993).

[24] L.G.Huxley and R.W.Crompton, *The Diffusion and Drift of Electrons in Gases*, Wiley, New York (1974).

[25] K. Kleinknecht, *Detectors for particle radiation*, Cambridge Univ. Press 1998.

[26] M. Aleksa, W. Riegler, *Non-linear MDT drift Gases like* Ar/CO_2, Atlas internal note, ATL-MUON-98-268.

[27] G. D. Alkhazov, *Statistics of elctron avalanches and ultimate resolution of proportional counters*, NIM 89, 155 (1970).

[28] S. Zimmermann, *High Rate and Ageing Studies for the Drift Tubes of the ATLAS Muon Spectrometer*,Ph.D. thesis, CERN-THESIS-2004-018;

[29] S. Horvat, *Study of the Higgs Discovery Potential in the Process* $pp \rightarrow H \rightarrow 4\ \mu$,Ph.D. thesis, CERN-THESIS-2005-036;

[30] M. Schioppa, private comunication.

[31] C.Posch, E.Hazen, J.Oliver, *MDT-ASD, CMOS front-end for ATLAS MDT*, ATLAS Internal Note, ATL-MUON-2002-003

[32] Y.Arai, *AMT-1 and 2 (ATLAS Muon TDC version 1 and 2) User's manual*, *http* : *//atlas.kek.jp/ arai*

[33] P.Branchini, F.Petrucci, *A platform-independent software for MDT front-end read-out with the CSM0*, ATLAS Internal Note, ATL-MUON-2002-001

[34] S. Baranov *et. al.*, *Estimation of Radiation Background, Impact on Detectors, Activation and Shielding Optimization in ATLAS*, ATL-GEN-2005-001.

[35] P.Branchini, F.Ceradini, M.Iodice, D.Orestano, F.Petrucci, E.Spiriti; *The cosmic ray hodoscope for the MDT chamber test site in Roma Tre*, ATLAS Internal Note, ATL-MUON-2001-007

[36] C.Bacci et al.;
Design of a cosmic test site for QAQC of MDT chambers, ATLAS Internal Note, ATL-MUON-98-241

[37] B.Ball, J.Chapman, J.Gregory, J Mann, J.Hollar;
CSM Users Manual, *http* : *//atlas.physics.lsa.umich.edu/docushare*

[38] E.Hazen;
ATLAS CSM 18-channel Adapter, *http* : *//bmc.bu.edu/bmc/CSM_adapter*

[39] P.Bagnaia, A.Baroncelli, M.Iodice, D.Orestano, L.Pontecorvo;
Calib: a package for MDT calibration studies - User Manual, ATLAS Internal Note, ATL-COM-MUON-2002-004.

[40] Saclay Muon Group;
Atlas Muon DataBase, *http*:*//atlas.web.cern.ch/Atlas/GROUPS/MUON /AMDB_SIMREC/amdb_simrec.html*.

[41] R.Veenhof, *GARFIELD - Simulation of gazeous detectors*, Cern Program Library W5050.

[42] Igor Smirnov, *HEED, program to compute energy loss of particles in gases*, Version 1.01, CERN Program Library.

[43] S. Biagi, *MAGBOLTZ, program to compute gas transport parameters*, Version 1.10, CERN Program Library.

[44] M. Gardener, Proc. Phys. Soc. 80 (1962) 697.

[45] J.A.Kadyk, Wire chamber aging, Nucl. Instr. and Meth. A 300 (1991) 436-479.

[46] J.Va'vra, Review of wire chamber aging, Nucl. Instr. and Meth. A 252 (1986) 547-563

[47] Proceedings of the Workshop on Radiation Damage to Wire Chambers, LBL-21170, (1986);
Proceedings of the International workshop on Aging Phenomena in Gaseous Detectors, Nucl. Instr. and Methods A515, (2003);
M.Titov et al, hep-ex/0204005, IEEE Trans.Nucl.Sci. NS49(4),1609 (2002);
J. Va'vra, Nucl. Instr. and Methods A515, 1 (2003).

[48] S.Baccaro et al., Gamma and neutron irradiation facility at ENEA-Casaccia Center, Report CERN-CMS/TN, 95-192 (RADH) 1995.
A.Tata et al., Radiation technology facilities operating at the Ital-

ian ENEA-Casaccia research center, ENEA RT/INN/98/1, CERN libraries, Geneva SCAN-9809001.

[49] A.Aprile et al., Production and test of monitored drift tubes for the muon spectrometer of the ATLAS experiment, IEEE Transactions on Nuclear Science, 49-3 (2002) 1077.
C.Bini et al., Nucl. Instr. and Meth. in Phys. Res. A461 (2001) 65.
P.Bagnaia et al., Nucl. Instr. and Meth. in Phys. Res. A546 (2005) 481

[50] J.E.Huth, J.Oliver, E.S.Hazen, C.Posch, J.T.Shank, Development of an octal CMOS ASD for the ATLAS Muon detector, Proceedings of the 5th Conference on Electronics for LHC Experiments, Snowmass, CO, 20-24 September 1999, p.436;
C.Posch, E.Hazen, and J.Oliver, MDT-ASD: CMOS front-end for ATLAS MDT chambers, ATL-MUON-2002-003; 7.6.2001,
`http://weblib.cern.ch/Home/ATLAS_Collection/ATLAS_Notes/Muon/`

[51] Y.Arai, Nucl. Instr. and Meth. in Phys. Res. A453 (2000) 365;
Y.Arai, Y.Kurumisawa and T.Emura, Development and a SEU Test of a TDC LSI for the ATLAS Muon Detector, Proceedings of the 7th Workshop on Electronics for LHC Experiments, Stockholm, Sweden, 10-14 September 2001, p.185.

[52] A.Baroncelli et al., Nucl. Instr. and Meth. in Phys. Res. A557 (2006) 421-435

[53] G.Scherberger et al, High rate performance of drift tubes, Nucl. Instr. and Meth. in Phys. Research A 424 (1999) 495-511.

[54] P.Bagnaia et al., `CALIB`: a Package for MDT Calibration Studies, ATL-COM-MUON-2002-004, 28.1.2002,
`http://weblib.cern.ch/Home/ATLAS_Collection/ATLAS_Notes/Muon/`

[55] G.Avolio et al., Nucl. Instr. and Meth. in Phys. Res. A523 (2004) 309

[56] W. Blum, L.Rolandi, Particle Detection with Drift Chambers, Springer, Berlin, 1994.

[57] P.Branchini et al., Study of the drift properties of high pressure drift tubes for the ATLAS muon spectrometer, IEEE NS Symposium Conference Record, 1 (2004) 427

[58] A.Aleksa, W.Riegler, Non-linear MDT drift gases like Ar-CO_2, ATL-MUON-98-268, 14.12.1998,
`http://weblib.cern.ch/Home/ATLAS_Collection/ATLAS_Notes/Muon/`.

[59] S. Kirche et al., Parameter of MDT Ageing and Reanimation, ATL-MUON-2001-012,
`http://weblib.cern.ch/Home/ATLAS_Collection/ATLAS_Notes/Muon/`.

[60] S.Zimmerman et al., MDT ageing studies - Results of the studies conducted at the Gamma Irradiation Facility GIF between autumn

2001 and summer 2003, ATL-MUON-2004-019,
`http://weblib.cern.ch/Home/ATLAS_Collection/ATLAS_Notes/Muon/`.

[61] C. Adorisio et al., Results from the 2004 ATLAS MDT ageing test in X5/GIF (Gamma Irradiation Facility) area, ATL-COM-MUON-2005-016,
`http://weblib.cern.ch/Home/ATLAS_Collection/ATLAS_Notes/Muon/`.

[62] C.Posch, E.Hazen, Total ionizing dose radiation hardness of the ATLAS MDT ASD and the HP-Agilent 0.5 micron CMOS process, ATL-ELEC-2002-001,
`http://weblib.cern.ch/Home/ATLAS_Collection/ATLAS_Notes/Muon/`.

[63] Y.Arai, M.Fukuda, T.Emura, Performance and irradiation tests of the 0.3 μm CMOS TDC for the ATLAS MDT, CERN-OPEN-2000-102,
`http://weblib.cern.ch/Home/ATLAS_Collection/ATLAS_Notes/Muon/`.

[64] M. Deile, J. Dubbert, M. Faessler, C. Gruhn, N.P. Hessey, A. Staude, *Test Beam Studies of the Gas Mixtures for Drift Tubes*, ATLAS Internal Note, MUON-NO-122, 1996.

[65] M. Kollefrath *et al*, *Aging Studies for the Atlas Monitored Drift Tubes*, Nucl. Instr. and Meth. A 419 (1998), 351-356.

[66] G. Avolio, S Di Luise. *et al*, *Monitored Drift Tubes aging under intensive gamma irradiation*, Nucl. Instr. and Meth. A 568 264 (2006).

[67] A. Baroncelli em et al, *Study of temperature and gas composition effects in rt relations of ATLAS MDT BIL Chambers*, ATASl Internal Note ATL-COM-MUON-2004-0011.